



UNIVERSITY OF
BIRMINGHAM

Finite Element Modelling of Multi-Point Forming

By
Mohamed Abosaf

A thesis submitted to
The University of Birmingham
For the degree of

DOCTOR OF PHILOSOPHY

Department of Mechanical Engineering
The University of Birmingham
July 2017

UNIVERSITY OF
BIRMINGHAM

University of Birmingham Research Archive

e-theses repository

This unpublished thesis/dissertation is copyright of the author and/or third parties. The intellectual property rights of the author or third parties in respect of this work are as defined by The Copyright Designs and Patents Act 1988 or as modified by any successor legislation.

Any use made of information contained in this thesis/dissertation must be in accordance with that legislation and must be properly acknowledged. Further distribution or reproduction in any format is prohibited without the permission of the copyright holder.

ABSTRACT

The need for sheet metal forming using reconfigurable dies has increased due to rapid changes in part design to meet customer requirements, especially in the automotive industry. Reconfigurable dies have relatively low manufacturing cost compared with solid dies and the same tool can be readily changed to produce different parts. As in solid dies, defects can occur in parts produced using multi-point forming dies. These defects have negative effects on the quality characteristics of fabricated parts, such as deviation from target shape, wrinkling, and thickness variation. The general aim of this study is to develop a 3-D FE model for multi-point forming dies using ABAQUS software and use this to study the effect of process parameters related to tool geometry such as radius of curvature of deformed parts, pin size, elastic cushion thickness and coefficient of friction. Doubly curved parts will be investigated in this research. The material properties for two blanks were determined for use as required parameters for the simulation analysis. Finite element models of the doubly curved forming process were developed and validated for two materials: DC05 steel sheet and 5251-O aluminium sheet. The mesh sensitivity, reliability of the numerical model, suitable blank holder force, effect of gap distance between punch and blank holder on the thickness distribution, and the corner defect were studied. A parametric study was carried to investigate the effect of certain parameters on the deviation from target shape, wrinkling, and thickness variation. A test rig for the experimental work was designed and manufactured. In parallel, experiments with the forming of doubly curved parts were conducted to validate the simulation results. The numerical analysis results were compared with the experimental results and good agreement was generally found. The methodology

developed in this research could help to build a reliable numerical model to predict the common defects in sheet forming using the multi-point forming process.

ACKNOWLEDGEMENTS

I would like to express my special appreciation and thanks to my lead supervisor Professor Duc Pham for encouragement, assistance, inspiration, guidance on the all aspects and interest shown in the work. I would like also to thank Dr Khamis Essa for his co-supervision and good advises. Dr Robert Cripps, Many thanks for your brilliant comments and suggestions. Also, I am deeply indebted to Professor Trevor Dean for his support and help in experimental work.

A special thanks to my parents, my family and my friends for their endurance, serenity, love and support in every possible way during my PhD study.

Contents

1. Introduction	1
1.1 Background on multi-point forming	1
1.2 Aims and objectives	2
1.2.1 General aims.....	2
1.2.2 Main objectives	3
1.2.3 Contributions.....	3
1.3 Methodology	4
1.4 Outline of thesis	5
2. LITERATURE REVIEW.....	6
2.1 Reconfigurable pin tooling.....	7
2.1.1 Shape of pin cross-section.....	7
2.1.2 Shape and material of pin tip.....	8
2.1.3 Pin density	10
2.1.4 Methods of pin adjustment	12
2.1.5 Pin clamping.....	15
2.2 Surface regularity	19
2.2.1 Elastomeric interpolating layer	19
2.2.2 Machining surface treatment.....	21
2.3 Multi-point forming defects	22
2.3.1 Dimpling	22
2.3.2 Wrinkling	24
2.4 Analytical methods.....	32
2.4.1.1 Static equilibrium method	32
2.4.1.2 Energy method	34
2.4.1.3 Initial imperfection method	35
2.4.2 Numerical method	36
2.4.2.1 Eigenvalue method.....	37
2.4.2.2 Static implicit finite element method	38
2.4.2.3 Dynamic explicit finite element method	39
2.5 Summary and research gaps.....	41
3. MULTI-POINT FORMING TOOLING DEVELOPMENT AND MEASUREMENT APPARATUS.....	43
3.1 Flexible die design	45

3.1.1 Pins.....	46
3.1.2 Main plate.....	48
3.1.3 Pin support.....	49
3.1.4 Pin fixing sheet.....	51
3.2 Blank holder	52
3.3 The guide.....	53
3.4 The springs	53
3.5 Specification of press machine.....	55
3.6 Specification of data logger, load cell, and distance transducer.....	56
3.7 Master curves	60
3.8 Faro arm (3-D laser scanner).....	60
3.9 Summary	61
4. DETERMINATION OF THE MECHANICAL PROPERTIES OF SHEET MATERIALS AND PROCESS MODELLING	62
4.1 Determination of the mechanical properties of sheet materials	64
4.2 Finite element modelling of multi point-forming.....	67
4.2.1 Explicit dynamic finite element modelling	67
4.2.2 Numerical investigation of multi-point forming	72
4.2.2.1 Effect of the element number in sheet thickness on forming force.....	73
4.2.2.2 Reliability of numerical model.....	74
4.2.3 FE modelling of MPF using blank holder	75
4.2.3.1 Determination of suitable blank holder force to eliminate flange wrinkling	76
4.2.3.2 Effect of gap distance on the thickness distribution.....	78
4.2.3.3 Reduced corner defect in doubly curved shape and effect on thickness	80
4.2.4 Validation of the finite element model without blank holder.....	83
4.2.5 Validation of the finite element model with blank holder.....	84
4.3 Parametric study.....	85
4.3.1 Effect of pin size on wrinkling, shape accuracy and sheet thickness.....	86
4.3.2 Effect of radius of curvature of the formed part on wrinkling, shape accuracy and	91
thickness variation.....	91
4.3.3 Effect of elastic cushion thickness on wrinkling, shape accuracy and thickness variation.....	94
4.3.4 Effect of coefficient of friction on wrinkling, shape accuracy, and thickness variation	97
4.4 Summary	100
5. OPTIMIZATION OF MULTI-POINT FORMING PROCESS PARAMETERS	102

5.1 Methodology of the study	103
5.2 Procedure for the Design of Experiments	103
5.3 Design of Experiment (DoE).....	105
5.3.1 Description of factor levels	105
5.3.2 Design of experiment (DoE) plan	106
5.3.3 Quantitative response variable	107
5.4 Numerical modeling of multi point forming and material data.....	108
5.4.1 Model types.....	108
5.4.2 Element types and boundary conditions.....	109
5.4.3 Material data.....	110
5.5 DoE results	112
5.5.1 Wrinkling	114
5.5.2 Maximum shape deviation	116
5.5.3 Thickness variation	117
5.6 Prediction of each quality characteristic	120
5-7 Optimisation of process parameters.....	121
5-8 Summary	123
6. INVESTIGATION OF THE RELATION BETWEEN WRINKLING AND THICKNESS: MODELLING AND EXPERIMENTAL RESULTS	124
6.1 Numerical investigation of the relation between wrinkling and thickness variation	125
6.1.1 Stress distribution on deformed sheet without blank holder	125
6.1.2 Thickness distribution and material flow of deformed sheets without blank holder.....	127
6.1.3 Wrinkling and deformed sheets without blank holder	131
6.1.4 Simulation results of deformed sheets with blank holder	134
6.2 Experimental work	135
6.2.1 Experimental set-up.....	137
6.2.1.1 Tooling pins adjustment	137
6.2.1.2 Distance introducer calibration	137
6.2.1.3 Data logger calibration	138
6.2.1.4 Load cell connection	139
6.2.1.5 Installation of die on the press.....	139
6.2.2 Experimental forming without blank holder	140
6.2.3 Experimental forming with blank holder	141
6.3 Comparison of simulation and experimental results with target profile	142

6.3.1 Results for deformed parts without blank holder	142
6.3.2 Results for deformed parts using blank holder.....	147
6.3.3 Thickness distribution on deformed parts without and with blank holder	150
6.4 Summary	152
7. CONCLUSIONS AND PROPOSALS FOR FUTURE WORK.....	153
7.1 Conclusions	153
7.2 Suggestions for future work	157
APPENDIX A	158
APPENDIX B	165
Refrences.....	178

List of Figures

Figure 1.1 Doubly curved part	2
Figure 1.2 Work flow and methodology	4
Figure 2.1 Literature review chart.....	6
Figure 2.2 (a) Discrete die with separated pins (b) Densely packed pins [11].....	7
Figure 2.3 Pin cross-sections: (a) Hexagonal cross-section [15], (b) Square cross-section.....	8
Figure 2.4 Pin tip shapes (a) Hemisphere, (b) Partial hemisphere,	8
Figure 2.5 Reconfigurable rubber tipped pins [21]	9
Figure 2.6 Various pin tip concepts [23, 24].....	10
Figure 2.7 (a) Pin tooling with uniform space (b) Pin tooling without space	11
Figure 2.8 Types of pin arrangements [26]	12
Figure 2.9 Pin size effect on die pin density [20].....	12
Figure 2.10 Using numerical control for pins adjustment [29]	13
Figure 2.11 Using master model [29].....	13
Figure 2.12 Schematic illustrating computer control of forming machine [30].....	14
Figure 2.13 Lead screw pin [31]	14
Figure 2.14 A cross-sectional view of a hydraulically-actuated reconfigurable	15
Figure 2.15 Pin fixing using low-temperature moldable backing material [25]	16
Figure 2.16 Types of clamping force generation mechanisms [15](To be continued).....	17
Figure 2.17 Square cage to pin clamping [38]	19
Figure 2.18 Methods of using elastic layers [13, 36, 42]	20
Figure 2.19 The Boeing Company's composite forming structure [44]	21
Figure 2.20 Milling surface treatment [45]	21
Figure 2.21 Dimpling forms (a) surface dimpling (b) enveloping dimpling [46]	22
Figure 2.22 Dimpling (a) clear dimpling, and (b) no dimpling using 10 mm pin size [20]	23
Figure 2.23 Forming paths a- Multipoint forming die b- multi-point press forming [1]	24
Figure 2.24 Sketch of sectional multi-point forming [1].....	24
Figure 2.25 Wrinkle growth (a) spherical shape, and (b) saddle shape [47].....	26
Figure 2.26 Normalised critical stress vs. normalised binder pressure for.....	27
Figure 2.27 Normalised wavelength vs.	27
Figure 2.28 Normalized critical stress vs.	27
Figure 2.29 Normalised wavelength vs.	27
Figure 2.30 Critical buckling stress vs.	28
Figure 2.31 Normalised wavelength vs.	28
Figure 2.32 Normalised critical stress vs. anisotropy parameter R at a wrinkling wavelength of 10t [53].....	28
Figure 2.33 Different meshes number used for the 160 mm blank diameter, SPCE material, and 0.7mm thickness: (a) 608 elements, (b) 1680 elements, and (c) 1956 elements [54]	29
Figure 2.34 Results of finite element analysis simulation for three meshes sizes, 608, 1680, and 1956 elements [54].....	29
Figure 2.35 Comparison of numerical and experimental results wave wrinkling shape [54]	30
Figure 2.36 Mechanism of wrinkling initiation.....	31
Figure 2.37 Rectangular thin plate under in-plane compression [57]	32
Figure 2.38 Use of implicit and explicit code in sheet metal forming	40

Figure 3.1 Sheet metal forming tooling model without blank holder	44
Figure 3.2 Sheet metal forming tooling model with blank holder	44
Figure 3.3 Tool components assembled and disassembled	45
Figure 3.4 Pin tip	46
Figure 3.5 Pin cap	47
Figure 3.6 Pin screw	47
Figure 3.7 Main plate	48
Figure 3.8 Forces acting on tool pins	49
Figure 3.9 Pin supports	50
Figure 3.10 Drawing for short and long pin supports	51
Figure 3.11 Pin fixing sheet	51
Figure 3.12 Blank holder	52
Figure 3.13 Main parts of pin guide	53
Figure 3.14 Spring on blank holder	54
Figure 3.15 The four columns downstroke hydraulic press E200 from Mackey Bowley	55
Figure 3.16 Omega OM-CP-QUADVOLT-30V data logger	57
Figure 3.17 Load cell	58
Figure 3.18 Distance transducer position on tool	59
Figure 3.19 Master curves	60
Figure 3.20 3D laser scanner	61
Figure 4.1 Samples cutting directions	62
Figure 4.2 Stress-strain curves for DC05 steel and Aluminium 5251-O	65
Figure 4.3 Yield stress and ultimate tensile stress for DC05 steel and aluminium 5251-O	65
Figure 4.4 Elongation for DC05 steel and 5251-O aluminium	65
Figure 4.5 Nominal compression stress – strain relationship for polyurethane A-90	67
Figure 4.6 Mass-spring-damper system under external force	67
Figure 4.7 Finite element model of tool (Quarter of die)	73
Figure 4.8 Punch force distribution in Y-direction with different numbers	74
Figure 4.9 Effect of mesh element size on the maximum force and simulation time.	74
Figure 4.10 The energy curves of finite element solution	75
Figure 4.11 Finite element model of tool with blank holder (Quarter die)	76
Figure 4.12 Flange wrinkling waves	77
Figure 4.13 Flange wrinkling amplitude over path CB for four levels of blank holder force	77
Figure 4.14 Flange wrinkling amplitude over path AB for four levels of blank holder force	77
Figure 4.15 The gap between punch and blank holder	78
Figure 4.16 Sheet thickness distribution using 5 mm gap between blank holder and die	79
Figure 4.17 Sheet thickness distribution using 10 mm gap between blank holder and die	79
Figure 4.18 Sheet thickness distribution using 15 mm gap between blank holder and die	79
Figure 4.19 Thickness distribution over paths OA and OC at centre of deformed sheet	80
Figure 4.20 Doubly curved shape with corner defect	81
Figure 4.21 Doubly curved shape after elimination of corner defect	81
Figure 4.22 Comparison of corner profile at path ML before and after increasing distance between sheet and die	81
Figure 4.23 Thickness distribution on doubly curved shape with corner defect	82
Figure 4.24 Thickness distribution on doubly curved shape after eliminating corner defect	82

Figure 4.25 Thickness distributions over path DB.....	83
Figure 4.26 Comparison of predicted and experimental force for multi-point forming without blank holder.....	84
Figure 4.27 Comparison of predicted and experimental force for multi-point forming model with blank holder.....	85
Figure 4.28 Effect of pin size on wrinkling at Path AB and CB.....	86
Figure 4.29 Effect of pin size on formed profile along path OA	87
Figure 4.30 Effect of pin size on formed profile along path OC.....	87
Figure 4.31 Pressure distribution on deformed sheet using 10, 15, 20 mm size pins	88
Figure 4.32 Thickness distribution of deformed sheet using different pin sizes	89
Figure 4.33 Effect of pin size on thickness distribution on short path OA	90
Figure 4.34 Effect of pin size on thickness distribution on long path OB	90
Figure 4.35 Effect of the radius of curvature on wrinkling along paths AB and CB	91
Figure 4.36 Effect of the radius of curvature on profile of the deformed sheet along paths OA and OB	92
Figure 4.37 Thickness distribution of deformed sheet using different radii of curvature	93
Figure 4.38 Effect of the radius of curvature on thickness distribution along paths OA and OB.....	94
Figure 4.39 Effect of elastic cushion thickness on wrinkling at paths AB and CB.....	94
Figure 4.40 Effect of elastic cushion thickness on profile of deformed sheet along paths OA and OC	95
Figure 4.41 Thickness distribution on deformed sheet using different elastic cushion thickness (To be continued).....	96
Figure 4.42 Effect of elastic cushion thickness on thickness distribution along paths OA and OC ...	97
Figure 4.43 Effect of the coefficient of friction on wrinkling along paths AB and CB.....	98
Figure 4.44 Effect of the coefficient of friction on deformed profile over paths OA and OC.....	98
Figure 4.45 Thickness distribution on deformed sheet using different coefficients of friction (To be continued).....	99
Figure 4.46 Effect of coefficient of friction on thickness distribution along paths OA and OC.....	100
Figure 5.1 Quantification of wrinkling (see Eq. 5.5)	107
Figure 5.2 Measure of maximum deviation from the target shape.....	107
Figure 5.3 Three pin matrix configurations.....	108
Figure 5.4 The pin shapes and dimensions for the three pin configurations	109
Figure 5.5 Element mesh type and boundary conditions	110
Figure 5.6 Experimental stress-strain results for DC05 sheet steel and fitted curve.....	111
Figure 5.7 Nominal compression stress–strain relationship for polyurethane A-90	112
Figure 5.8 Effect of pin size and radius of curvature on wrinkling.....	115
Figure 5.9 Pressure distributions on upper and lower sides of formed sheet	115
Figure 5.10 Effect of pin size and radius of curvature on maximum shape deviation	116
Figure 5.11 Pressure distribution on the formed sheet for small and large pin sizes (radius of curvature =400mm)	117
Figure 5.12 Effect of coefficient of friction and pin size on thickness variation	118
Figure 5.13 Effect of coefficient of friction and radius of curvature on thickness variation	118
Figure 5.14 Effect of interaction between cushion thickness and coefficient	119
Figure 5.15 Effect of interaction between cushion thickness and pin size on.....	120
Figure 5.16 (a) Multi-point forming die, (b) Fabricated part, and (c) Part cut into two halves	122

Figure 5.17 Comparison of formed shape with target shape.....	122
Figure 6.1 Wrinkling on double curved sheet	124
Figure 6.2 3-D FE model a) without blank holder b) with blank holder.....	125
Figure 6.3 Mises stress distribution for 5251-O aluminium sheet	126
Figure 6.4 Mises stress distribution for 5251-O aluminium sheet	126
Figure 6.5 Mises stress distribution for DC05 steel sheet (radius of curvature 400 mm)	127
Figure 6.6 Mises stress distribution for DC05 steel sheet (radius of curvature 800 mm)	127
Figure 6.7 Thickness distribution for 5251-O aluminium and DC05 steel sheets	128
Figure 6.8 Simulation results of thickness distribution at centre of deformed aluminium and.....	129
Figure 6.9 Logarithmic strain at centre of the sheet (area A) for deformed DC05 steel sheet and 5251-O aluminium sheet, $R = 400$ mm	130
Figure 6.10 Logarithmic strain at between the central region and edge of the sheet (area B) for deformed DC05 steel sheet and 5251-O aluminium sheet, $R = 400$ mm.....	131
Figure 6.11 Logarithmic strain at edge of the sheet (area C) on deformed DC05 steel sheet and 5251-O aluminium sheet, $R = 400$ mm	131
Figure 6.12 Thickness distribution and formed shape for both long and short sides of 5251-O aluminium sheet (radius of curvature, 400 mm)	132
Figure 6.13 Thickness distribution and formed shape for both long and short sides of DC05 steel sheet (radius of curvature, 400 mm).....	132
Figure 6.14 Thickness distribution and formed shape on both long and short sides of 5251-O aluminium sheet (radius of curvature, 800 mm)	133
Figure 6.15 Thickness distribution and formed shape on both long and short sides of DC05 steel sheet (radius of curvature, 800 mm).....	133
Figure 6.16 Thickness distribution for 5251-O aluminium and DC05 steel sheets (R = radius of curvature)	134
Figure 6.17 Thickness distribution and deformed shape on both long and short sides of aluminium sheet deformed using blank holder (radius of curvature, 400 mm).....	135
Figure 6.18 Thickness distribution and deformed shape on both long and short sides of steel sheet deformed using blank holder (radius of curvature, 400 mm)	135
Figure 6.19 Experimental plan	136
Figure 6.20 Pin adjustment using master curve	137
Figure 6.21 Distance transducer calibration using voltmeter	138
Figure 6.22 Window of data logger setup	138
Figure 6.23 Load cell – software main window	139
Figure 6.24 Tool setup on the press	140
Figure 6.25 Position of metal and elastic cushion sheets in discrete tool	140
Figure 6.26 Deformed sheets with different curvatures (without blank holder)	141
Figure 6.27 Sheet fixing into the blank holder.....	141
Figure 6.28 Aluminium and steel deformed sheets using blank holder	142
Figure 6.29 Target, simulated and deformed profiles over the section CD for 5251-O aluminium sheet (radius of curvature, 400 mm).....	142
Figure 6.30 Target, simulated and deformed profiles over the section AB for 5251-O aluminium sheet (radius of curvature, 400 mm).....	143
Figure 6.31 Target, simulated and deformed profiles over the section CD for DC05 steel sheet (radius of curvature, 400 mm).....	143

Figure 6.32 Target, simulated and deformed profiles over the section AB for DC05 steel sheet (radius of curvature, 400 mm).....	143
Figure 6.33 Simulated wrinkled profile, deformed shape and target profile over the section BC for aluminium sheet (radius of curvature, 400 mm)	144
Figure 6.34 Simulated wrinkled profile, deformed shape and target profile over the section AB for aluminium sheet (radius of curvature, 400 mm)	144
Figure 6.35 Simulated wrinkled profile, deformed shape and target profile over the section BC for steel sheet (radius of curvature, 400 mm)	144
Figure 6.36 Simulated wrinkled profile, deformed shape and target profile over the section AB for steel sheet (radius of curvature, 400 mm)	145
Figure 6.37 Target, simulated and deformed profiles over the section CD for aluminium sheet (radius of curvature, 800 mm).....	145
Figure 6.38 Target, simulated and deformed profiles over the section AB for aluminium sheet (radius of curvature, 800 mm).....	145
Figure 6.39 Target, simulated and deformed profiles over the section CD for steel sheet (radius of curvature, 800 mm)	146
Figure 6.40 Target, simulated and deformed profiles over the section AB for steel sheet (radius of curvature, 800 mm)	146
Figure 6.41 Wrinkling profile obtained from simulation results and deformed shape over the section BC for aluminium sheet (radius of curvature, 800 mm)	146
Figure 6.42 Wrinkling profile obtained from simulation results and deformed shape over the section AB for aluminium sheet (radius of curvature, 800 mm)	147
Figure 6.43 Wrinkling profile obtained from simulation results and deformed shape over the section BC for steel sheet (radius of curvature, 800 mm)	147
Figure 6.44 Wrinkling profile obtained from simulation results and deformed shape over the section AB for steel sheet (radius of curvature, 800 mm)	147
Figure 6.45 Target, simulated and deformed profiles over the section CD for aluminium sheet (with blank holder, and radius of curvature, 400 mm)	148
Figure 6.46 Target, simulated and deformed profiles over the section AB for aluminium sheet (with blank holder, and radius of curvature, 400 mm)	149
Figure 6.47 Target, simulated and deformed profiles over the section CD for steel sheet (with blank holder, and radius of curvature, 400 mm)	149
Figure 6.48 Target, simulated and deformed profiles over the section AB for steel sheet (with blank holder, and radius of curvature, 400 mm)	149
Figure 6.49 Experimental and simulated thickness distribution profiles over the sections AB and CD for aluminium sheet (without blank holder, and radius of curvature, 400 mm).....	150
Figure 6.50 Experimental and simulated thickness distribution profiles over the sections AB and CD for aluminium sheet (with blank holder, and radius of curvature, 400 mm).....	151
Figure 6.51 Experimental and simulated thickness distribution profiles over the sections AB and CD for steel sheet (without blank holder, and radius of curvature, 400 mm).....	151
Figure 6.52 Experimental and simulated thickness distribution profiles over the sections	151

List of tables

Table β-1 Specification of steel die springs from Cromwell with external diameter 26mm and length 44mm [79].....	54
Table β-2 Press specification [80].....	56
Table β-3 Omega OM-CP-QUADVOLT-30V data logger specification [81].....	57
Table β-4 Specification of load cell [83].....	58
Table β-5 Distance transducer specifications [84]	59
Table 4-1 R_a in rolling, 0^0 , 45^0 and 90^0 orientations for DC05 steel	66
Table 4-2 R_a in rolling, 0^0 , 45^0 and 90^0 orientations for aluminium 5251-O.....	66
Table 5-1 Process parameters.....	105
Table 5-2 Design of experiment plan.....	106
Table 5-3 Mechanical properties of the sheet metal.....	110
Table 5-4 Simulated response results as a function of design parameters	113
Table 5-5 Significant factors and corresponding P-values.....	114
Table 5-6 Coefficient values corresponding to each response parameter	121
Table 5-7 Optimal work parameters.....	122
Table 5-8 Comparison of formed shape with target shape.....	122

Nomenclature

F_{clamp}	clamping force
F_{lm}	perpendicular force applied to the wall
P_o	hydraulic pressure
A_{cs}	cross section area of cylinder
K_f	force loss coefficient of the cylinder
θ	angle with x-axis
F_w	input force
Φ	wedge incline angle
μ_A	coefficient of static friction between A
μ_B	coefficient of static friction between B and the horizontal wall
V	voltage
L_p	length of lamination
W_p	width of lamination
T_p	thickness of lamination
g_{33}	coefficient of piezoelectric voltage
α_f	coefficient of linear thermal expansion of the frame material
E_f	elasticity modulus of the frame metal
A_f	total cross-sectional area of the element matrix in a plane normal to the loading
E_m	elasticity modulus of the discrete pins
T_0	temperature to which the frame is cooled
T	initial hot temperature of the entire discrete die
a	Plate radius
t	thickness
E_0	buckling modulus
E_p	strain-hardening modulus
σ_1^{cr}	critical stress
R	radius of curvature
p	critical binder pressure
α	loading factor
K	strength coefficient of material
ε_0	pre-strain
D	bending stiffness
w	deflection bending
Φ	function of stress
η	initial imperfection factor
w_o	initial imperfection
K_e	elastic stiffness matrix
λ_i	eigenvalues
K_g	differential initial stress
Φ_i	the i^{th} shape of buckling mode
\dot{u}	velocity
\ddot{u}	acceleration
M	lumped mass matrix
F	vector of externally applied forces
I	vector of internal element forces

R_a	normal anisotropy coefficient
r_0	plastic anisotropy in rolling direction
r_{45}	plastic anisotropy inclined 45° on rolling direction
r_{90}	plastic anisotropy perpendicular on rolling direction
M	mass
C	coefficient of damping
K	spring stiffness
Z	factor of viscous damping
ω	system frequency
L	element dimension
c_d	elastic wave speed
G	shear modules of elasticity
$ALLAE$	artificial strain energy
$ALLKE$	kinetic energy
$ALLIE$	internal energy
N	strain-hardening exponent
σ	yield stress
n	Poisson ratio
ε	true strain
C_{01}, C_{10}	temperature dependent material properties
I_1, I_2	First and second invariants of the deviatoric
$RMSE$	Root mean square error
z	maximum amplitude of wrinkling wave
\bar{x}	mean of the data set
q	response
$k0-k14$	process parameters coefficient
A	plastic cushion thickness
B	coefficient of friction
C	pin size
D	radius of curvature

List of Publications

1. **Abosaf**, M., Essa, K., Alghawail, A., Tolipov, A., Su, S. and Pham, D., 2017.
Optimisation of multi-point forming process parameters. *The International Journal of Advanced Manufacturing Technology*, pp.1-11.
2. **Abosaf**, M., Alghawail, A., Pham, D., Essa, K., Tolipov A. and Su, S. , 2017.
Effect of overhang between die and blank holder on thickness distribution in multi-point forming. The 39th MATADOR Conference.

Chapter 1

Introduction

1.1 Background on multi-point forming

Sheet metal forming is a manufacturing process in which a metallic sheet is deformed plastically by tools without metal removal. The main target of the sheet forming process is to produce semi-finished products with high quality and at low cost; such products include car body part and many others industrial components. In recent years, demand is changing from mass production toward batch production to be more compatible with market requirements and flexible manufacturing systems. Hence, there is much research being undertaken to develop discrete dies to replace solid dies, because the latter are not suitable for limited production, being more costly and time-consuming to produce, especially for complex die surfaces [1]. Multi-point forming is a method used for sheet metal forming utilising a press machine with a reconfigurable discrete die. The idea of constructing a die to form a sheet using discrete pins and surface shape control was initially presented nearly 50 years ago [2]. This initial die was composed of a matrix of square steel pins which were moved along their longitudinal axis using servo motors and then locked in place by applying pressure on the sides [3]. The contact between sheet and die is the pin points, this can lead to indents on the sheet which are called dimpling. To avoid dimpling, after the discrete die is clamped a sheet of elastic material such as ethylene vinyl acetate, which acts as an elastic cushion, is placed between the metal sheet and the pins. The material type and thickness has important effects on shape accuracy and product quality [4]. Wrinkling of the sheet metal can also occur on the deformed parts as the results of compressive stress as the punch pushes the sheet into the die cavity, this can be avoided by the use of blank holders.

To reduce the cost and cycle time in fabrication of the conventional stamping die, MPF die has been developed based on the discretization of the die. In MPF die, the fixed shape matched-dies of conventional stamping are replaced by a pair of opposed matrices of movable punch elements. Using multi-point matched-dies generated by punch matrices, a variety of three-dimensional sheet parts of different shapes can be produced. For that, this study will focus on investigating multipoint forming process and some defects to improve the deformed parts quality.

1.2 Aims and objectives

1.2.1 General aims

The multi-point forming process will be numerically simulated using finite element (FE) modelling and the model will be validated against experimental data. The general aim of this research is to develop a 3-D FE model for a discrete die using ABAQUS software. This model will be used to study the effect of certain of the process parameters related to tool geometry and their effect on wrinkling phenomenon (such as radius of curvature, pin size, elastic cushion thickness, and coefficient of friction). In parallel, an empirical model will be developed to predict wrinkling, maximum deviation from target shape and thickness variation for doubly curved parts. Figure 1.1 shows a doubly curved part.

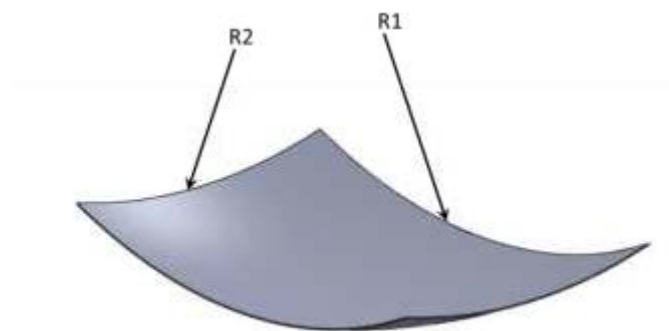


Figure 1.1 Doubly curved part

1.2.2 Main objectives

- a. Develop a multi-point forming die with square pin size 10 mm to validate the numerical models (Details of dimension are shown in Appendix A).
- b. Determine the mechanical properties and anisotropy coefficients for DC05 steel sheet and 5251- aluminium alloy sheet.
- c. Develop 3-D numerical models for the multi-point forming process to study wrinkling, deviation from target shape, and thickness variation in doubly curved parts.
- d. Study the influence of main tool surface parameters which are represented in radius of curvature, friction, elastic cushion thickness, and pin size on the wrinkling, deviation from target shape, and thickness.
- e. Develop an empirical model to predict wrinkling, maximum deviation from target shape and thickness variation for the doubly curved sheet forming process.
- f. Investigate the relationship between the wrinkling phenomenon and thickness variation on deformed sheets.
- g. Compare the simulation results and experimental results.

1.2.3 Contributions

- a. The development of a more detailed Finite Element modelling for Multi-point Forming process.
- b. Clarify the effect of pin size on quality characteristics, by using small pin cross section in MPF process.
- c. Using the simulation to predict the quality characteristics of MPF process products.
- d. Illustrate the effect of the thickness variation on the wrinkling initiation.

1.3 Methodology

Figure 1.2 shows the work flow and methodology of this study in stages.

Stage 1: Develop a multi-point forming tool with pin size 10 mm. The total number of pins is 600, arranged as a matrix of 20x30 pins.

Stage 2: Determine the mechanical properties of the material to be used in the experimental work using the Zwick tensile test machine.

Stage 3: Develop a numerical model for the multi-point forming process with and without a blank holder using ABAQUS software.

Stage 4: Carry out the experimental work using the developed tool to validate the numerical results.

Stage 5: Compare numerical and experimental results.

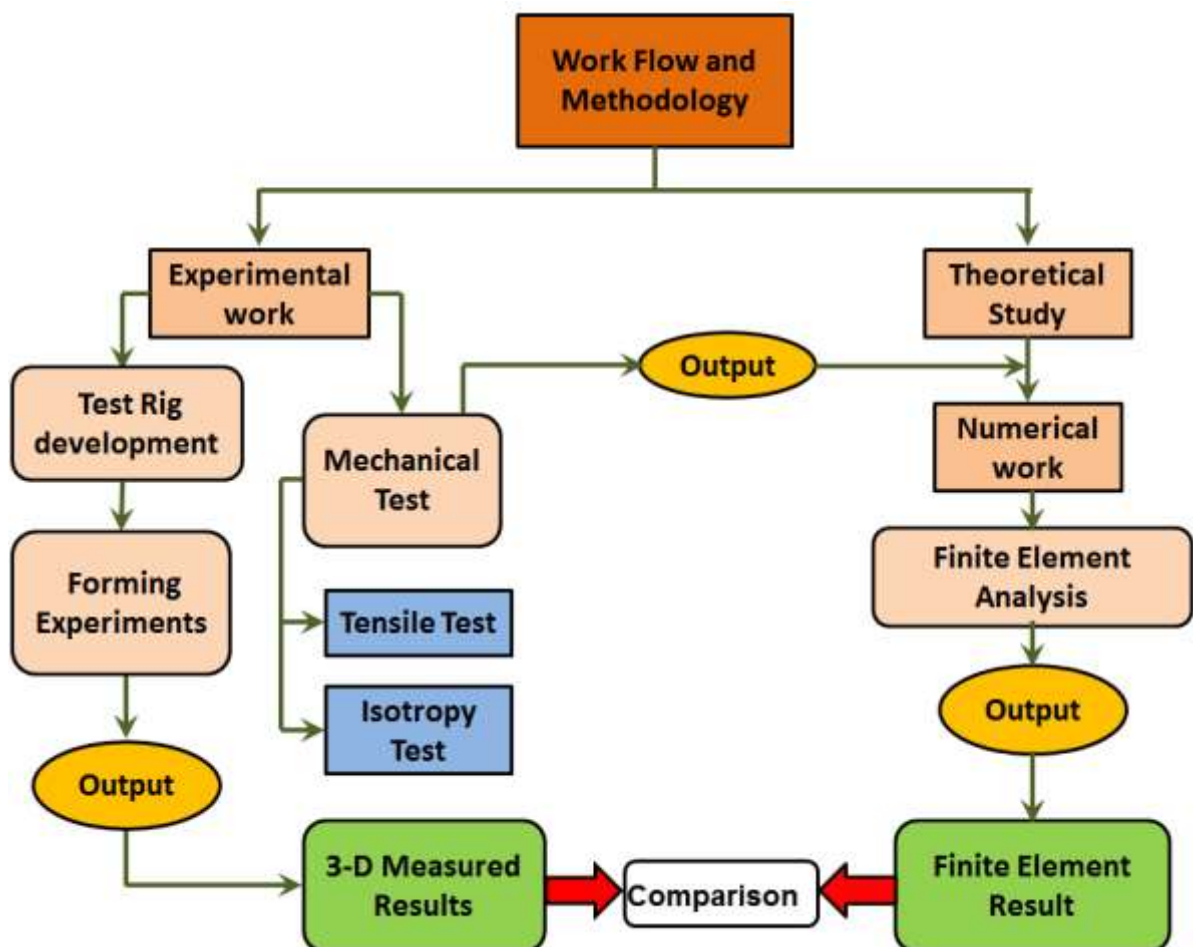


Figure 1.2 Work flow and methodology

1.4 Outline of thesis

The thesis is divided into seven chapters. Following this introduction chapter, chapter 2 gives an overview of multi-point forming which includes reconfigurable pin tooling, surface regularity, multi-point forming defects, and analytical approaches. Chapter 3 explains the development of the design of multi-point forming tooling and the measurements apparatus which is used to evaluate the deformations of deformed parts. Chapter 4 presents the results of tests made to determine the behaviour of DC05 steel sheet and 5251-O aluminium sheet under tensile load, plastic anisotropy, and behaviour of polyurethane shore A-90 under uniaxial compression test. It also presents the numerical simulation used to study the effect of process parameters. Chapter 5 covers the optimisation of process parameters radius of curvature, friction, elastic cushion thickness, and pin size to determine which one of them has the most effect on wrinkling, deviation from target shape and thickness variation. The chapter develops an empirical model to predict the wrinkling, maximum deviation from target shape, and thickness variation for the doubly curved sheet forming process. Chapter 6 relates to a numerical study of wrinkling and thickness variation, and the relation between them. The results of the experimental work are reported and numerical and experimental results are discussed and compared. Chapter 7 summarises this investigation, draws conclusions and makes recommendations for future work.

CHAPTER 2

LITERATURE REVIEW

With the technological development of production processes in sheet metal forming and the requirement to reduce manufacturing costs, it became necessary to find a flexible process suitable for batch production of products of different shapes. Thus, flexible tooling designs have been developed, such as, the discrete die [5, 6], flexible stretch forming [3, 7, 8], and the use of rubber pad forming [9, 10]. One important development is the Multi-Point Forming (MPF) process, an advanced technology for the manufacturing of 3-D sheet metal parts, which has become a necessity in the metal forming industry. A MPF tool is complex and its design must pass through many different stages before it is finally assembled. This chapter will present a summary of previous research in MPF and Figure 1.1 shows the four main sections of the literature review. Included are: reconfigurable pin tooling, surface regularity, multi-point forming defects, and analytical approaches.

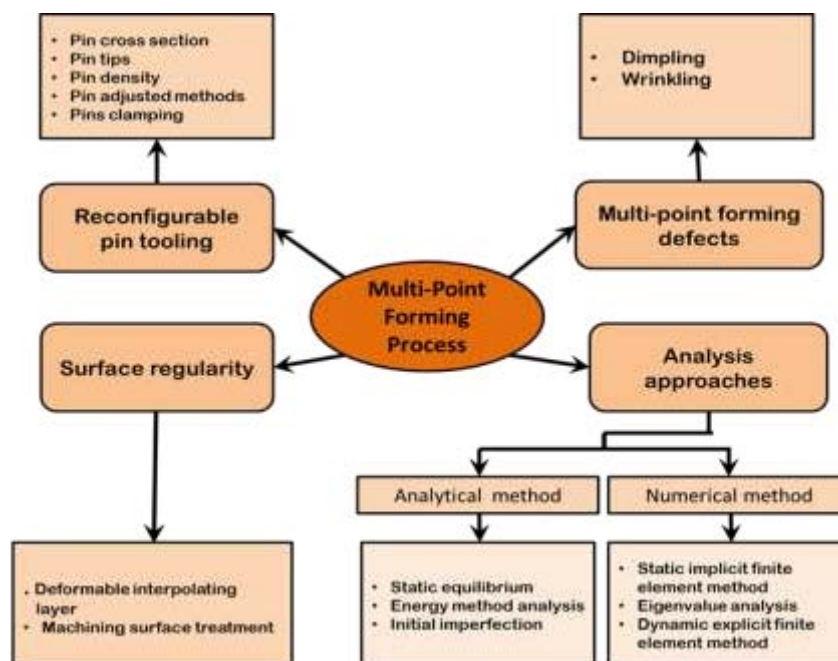


Figure 2.1 Literature review chart

2.1 Reconfigurable pin tooling

A reconfigurable die is a flexible tool that can be used in forming the 3-D surface of sheet metal, and the same tool can be readily changed to produce different parts. The concept of reconfigurable tooling for flexible production was suggested by Hardt of Massachusetts Institute of Technology [1, 2]. The die is formed from different parts, such as the pins which move perpendicularly on the fixing plate, the pin fixing plate and pin supports. There are two main types of reconfigurable die constructions: the separated pin matrix and the densely packed pin matrix as shown in Figure 2.2 [11, 12].

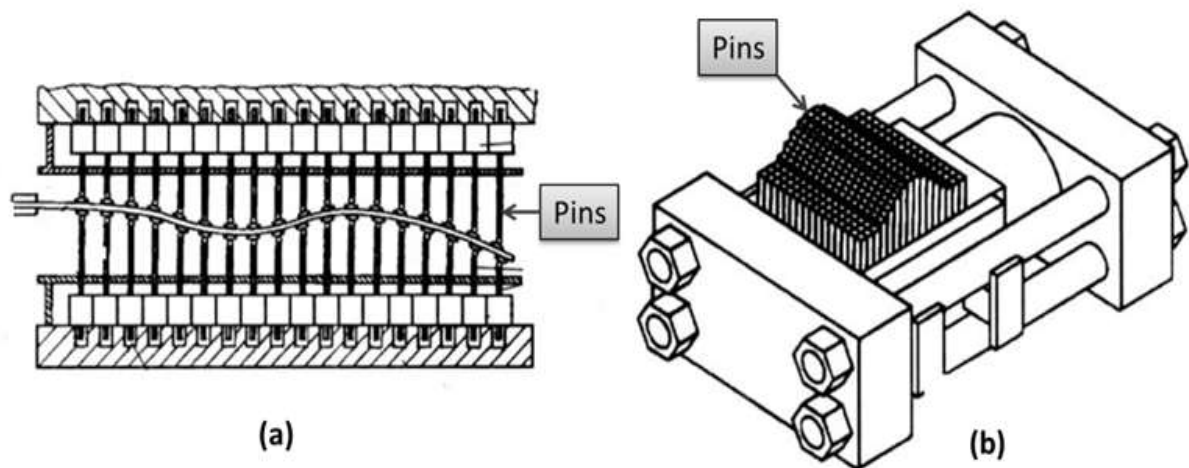


Figure 2.2 (a) Discrete die with separated pins (b) Densely packed pins [11]

2.1.1 Shape of pin cross-section

The pins are an important element of the MPF die and can have different cross-sectional shapes. Four cross-sectional shapes used by previous investigations are: hexagonal cross-section [12, 13], square cross-section [11, 14], triangular cross-section [15] and circular cross-section [16, 17] as shown in Figure 2.3. Threaded circular cross-section pin [18], have also been used.

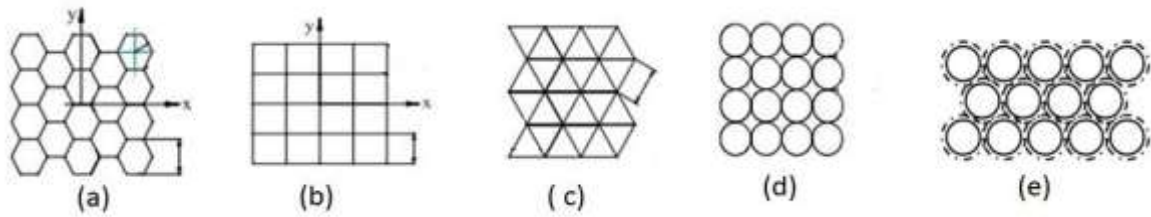


Figure 2.3 Pin cross-sections: (a) Hexagonal cross-section [15], (b) Square cross-section [15], (c) Triangle cross section [15], (d) Circular cross-section [15], and (e) Threaded cross section [18]

Pin cross-section has a significant effect on quality of fabrication because if the pin cross-sectional shape means the pins tessellate well they can be clamping together in a matrix without gaps between them, e.g. square pins, while with circular and threaded pins there are small gaps. Reducing the gaps between pins make the die more rigid and better able withstand forming forces.

2.1.2 Shape and material of pin tip

The geometrical shape of pin tips has a significant effect on the product surface quality. The contact between the die pins and metal sheet is point-to-surface contact so the tip of the pin must be smooth to avoid making any unwanted marks in the sheet during forming. The radius of the pin tip must be at least equal to the half dimension of the pin's cross-section [11]. For that, the pin tip shape should be hemispherical, a partial hemisphere or a hemi-ellipsoid, as shown in Figure 2.4 [19].

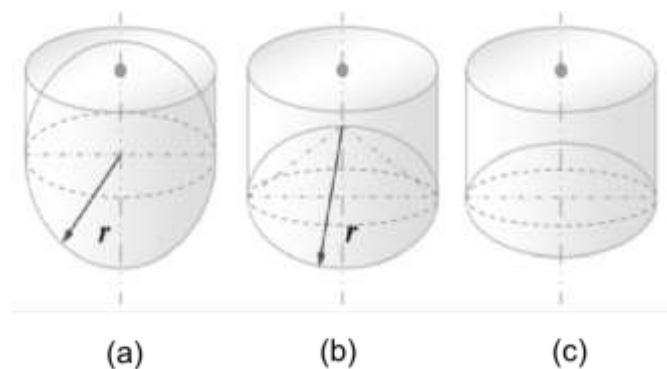


Figure 2.4 Pin tip shapes (a) Hemisphere, (b) Partial hemisphere, (c) Hemi-ellipsoid [19]

However, producing a hemispherical pin tip is easier than producing a hemi-ellipsoidal tip, but the dimpling would be observed more easily [19]. Moreover, the variety of possible die curvatures will be limited if the radius of pin tip is larger [20].

It is possible that some pin tips can be replaced and/or reconfigured as required by the surface shape. Inserts can be threaded into the tips of hollowed out pins and placed in key positions as required [18], and reconfigurable rubber tipped pins are shown in Figure 2.5 [21].

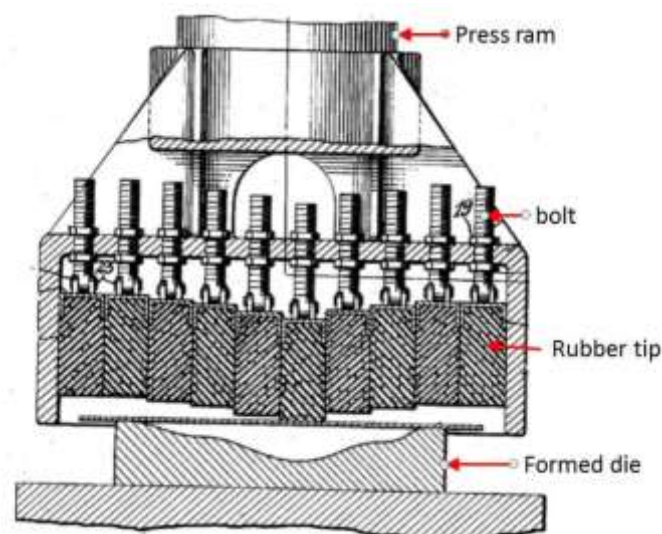


Figure 2.5 Reconfigurable rubber tipped pins [21]

Another method for improving pin tip performance is the provision for cold/hot gases flow through the honeycomb panel between the pins and through holes on the pin tip itself [22]. To increase the forming efficiency and avoid damage to products, Papazian [23] improved the tip of the pin by fabricated it from rubber, these pins could be concave or convex in shape, or have a cavity which contained pressurised gas or a spring. Some pin tips use a swivel ball, which is suitable for use when the direction of the force is not vertical on the surface. Figure 2.6 shows various pin tip concepts [23, 24].

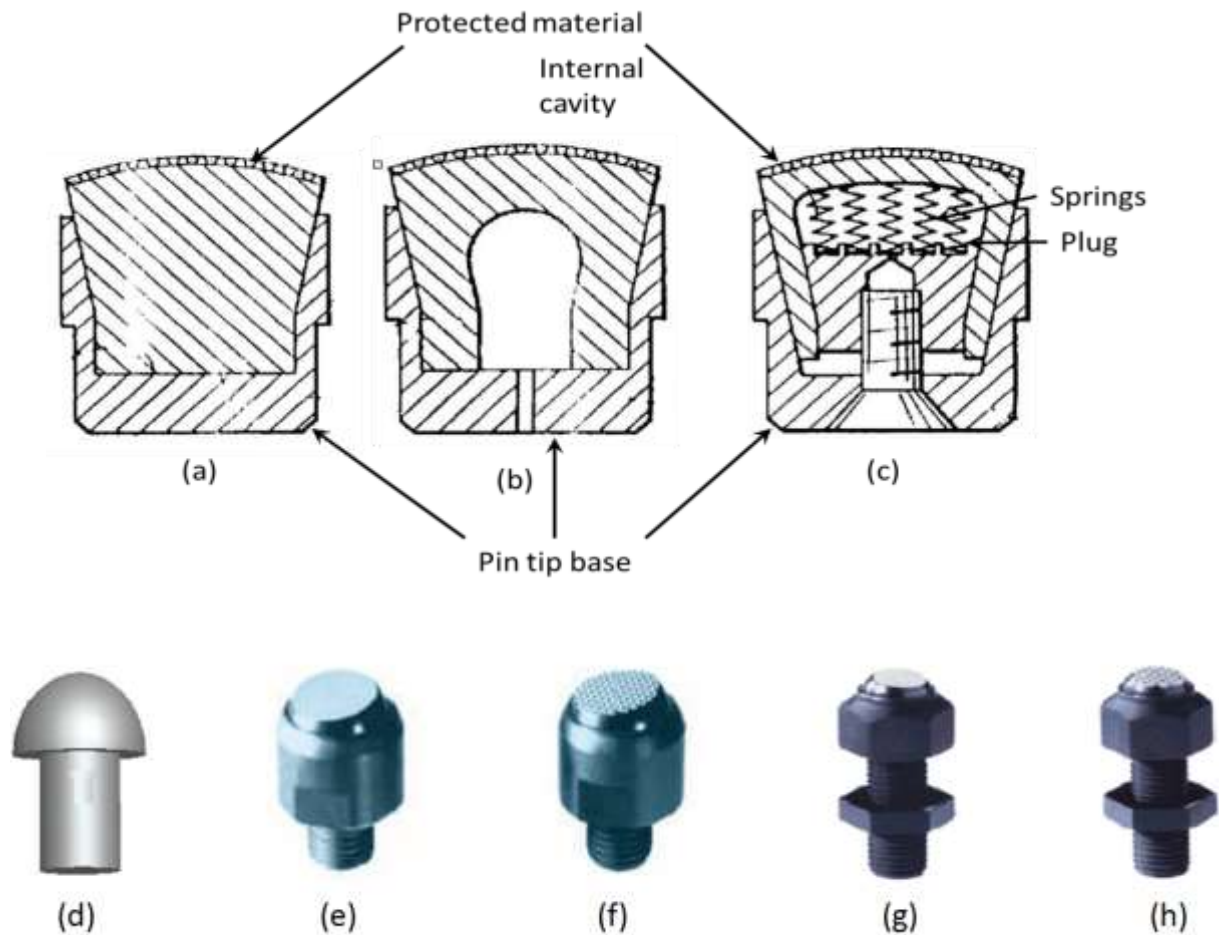


Figure 2.6 Various pin tip concepts [23, 24]
a- Rubber tip (Solid), b- Rubber tip (Cavity), c- Rubber tip (with springs), d- Metal tip (Spherical), (e, f, g, and h) Metal tips with swivel ball

2.1.3 Pin density

Pins density is the number of pins in a unit area of the multi-point forming die. There are two factors affecting die pin density, pin arrangement, and pin shape and size. According to previous investigations, pins arrangements for multi-point tooling can be divided into two groups: a matrix of separated pins and matrix of densely packed pins. Figure 2.7 shows pin tooling with a uniform space between circular pins (matrix of separated pins), and without space between circular pins (matrix of densely packed pins). In matrix of densely packed pins it is obvious that for pins of the same shape and size the density of pins is higher than for a matrix of separated pins. Thus the shape of the die pin has an essential role in

determining pin density. All pin cross-section shapes can be arranged as a close-packed matrix because in such an arrangement the pins support each other and are better able to withstand high forming loads. However, the gaps between pins are different from one cross-section to another. However, the lack of separation between pins makes adjustment of individual pins more difficult.

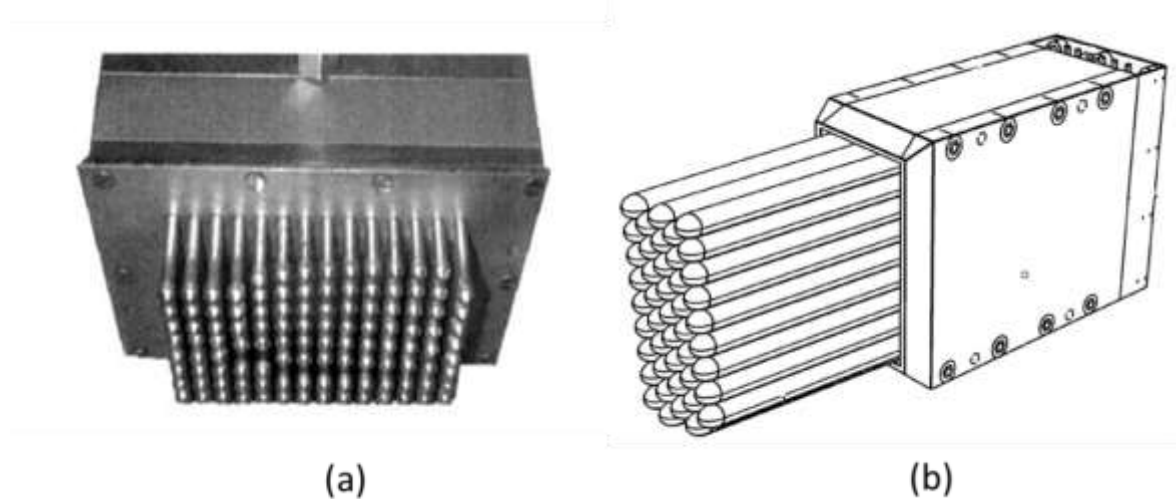


Figure 2.7 (a) Pin tooling with uniform space between pins [25]

(b) Pin tooling without space between pins [17]

Common close-packed pin arrangements are; hexagonal (or diagonal) packing and square (or rectangular) packing, see Figure 2.8. Rectangular packing is more suitable for square and circular cross-section pins, however, FE analysis showed that for a reconfigurable die, diagonal packing is the more efficient arrangement [26]. Increasing the number of pins per unit area may reduce both dimpling and error in the deformed shape [20]. Figure 2.9 shows how the size of the pin has effects the pin density, obviously, the pin density increases with smaller size pins.

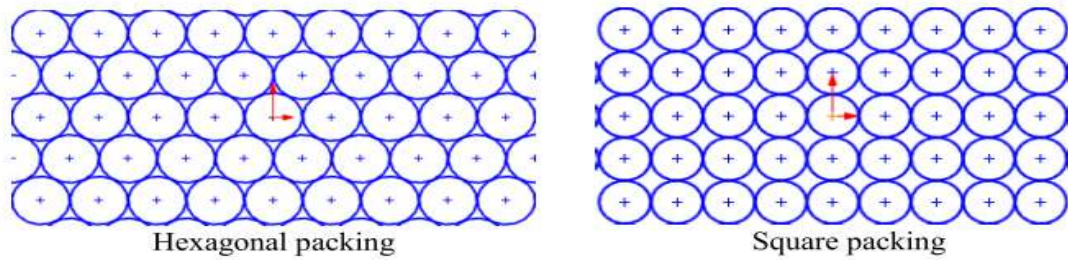


Figure 2.8 Types of pin arrangements [26]

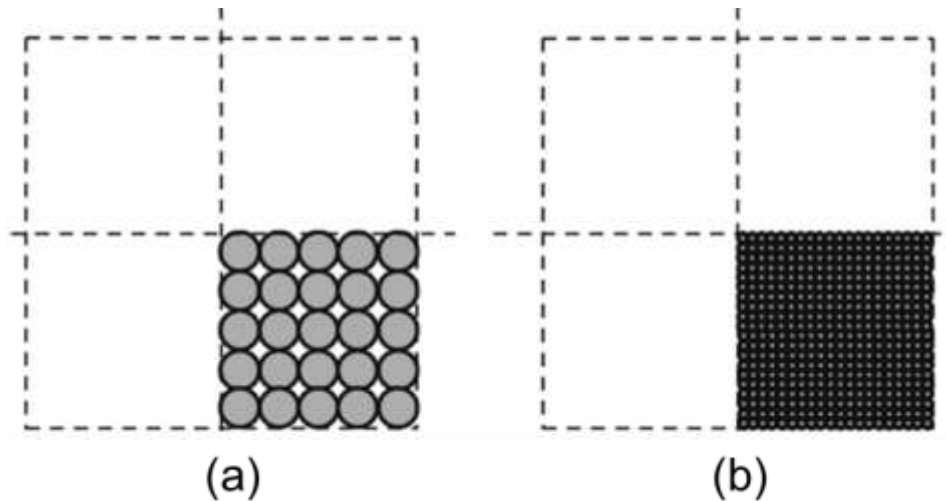


Figure 2.9 Pin size effect on die pin density [20]

2.1.4 Methods of pin adjustment

Different methods have developed for pins adjustment; mechanical (lead screw) and fluid pressure (hydraulic or pneumatic) methods need numerical control to set the shape of the pins before they are clamped as a rigid tool. Pin actuation includes manual and automatic methods. The first use of the manual method was as a 2-D forming device which was used with uniformly spaced adjustable pins in two opposed rows [27]. This idea was developed to 3-D by using many rows for sheet forming [28]. Nakajima used two methods to generate a curved surface; point to point control (individual pins) and sweep control (groups of pins) to push the pins to the desired positions, see Figure 2.10 [29], using a numerically controlled milling machine.

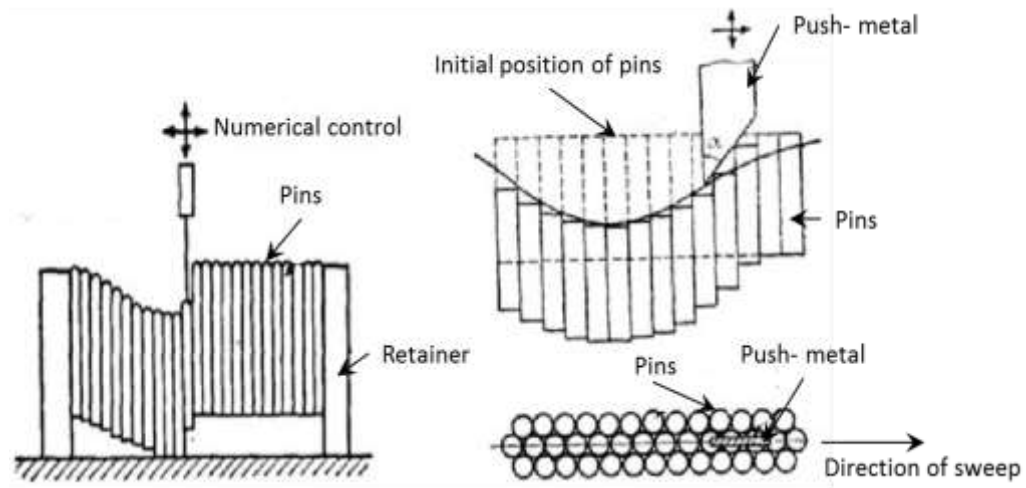


Figure 2.10 Using numerical control for pins adjustment [29]

The master model was used to set the pins into final shape as shown in Figure 2.11.

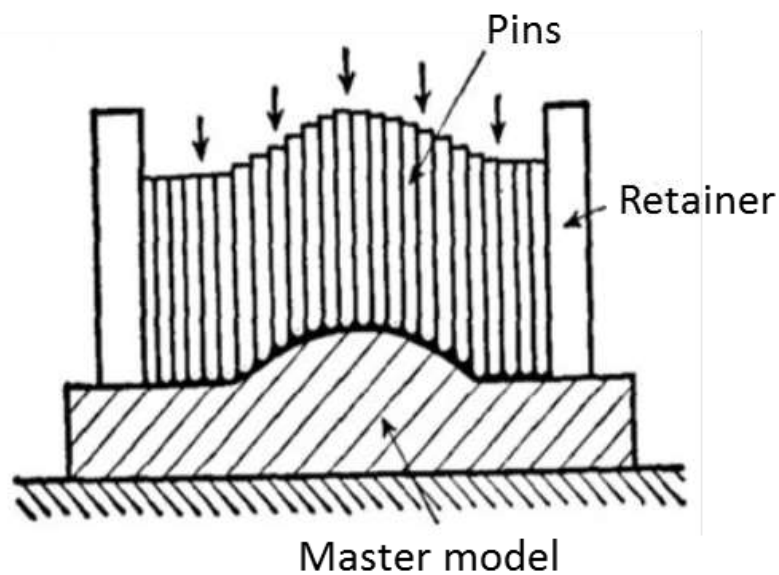


Figure 2.11 Using master model [29]

The first 3-D reconfigurable pin tooling with self-automatic control by computer was developed by Pinson, here each pin was connected with a servo-actuator as shown in Figure 2.12 [30].

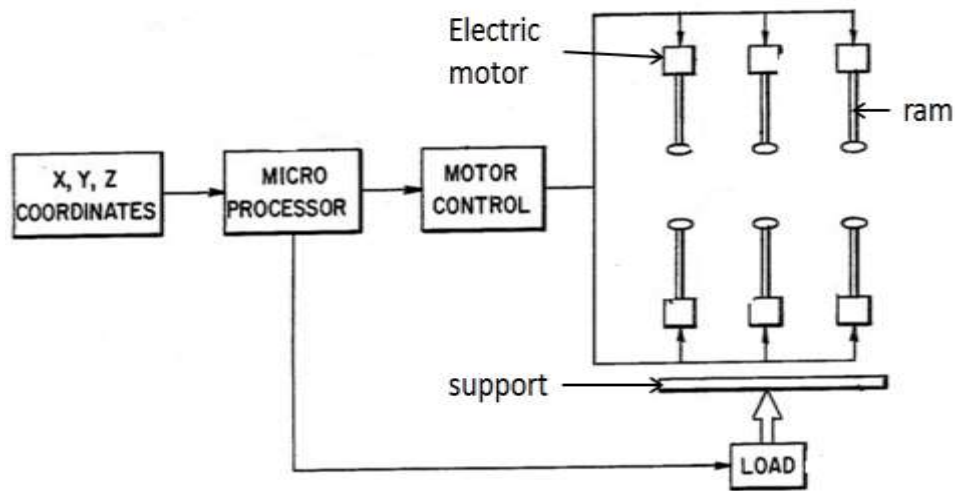


Figure 2.12 Schematic illustrating computer control of forming machine [30]

An effective mechanical method to adjust MPF tooling is the lead screw pin, Figure 2.13 shows the design and the pin's main parts. All parts are supported by the plate at the bottom. The height of the pin can be adjusted by rotating the lead screw on its thread till it reaches the specified position. After adjusting all pins as required by the design, the die will function as a solid die.

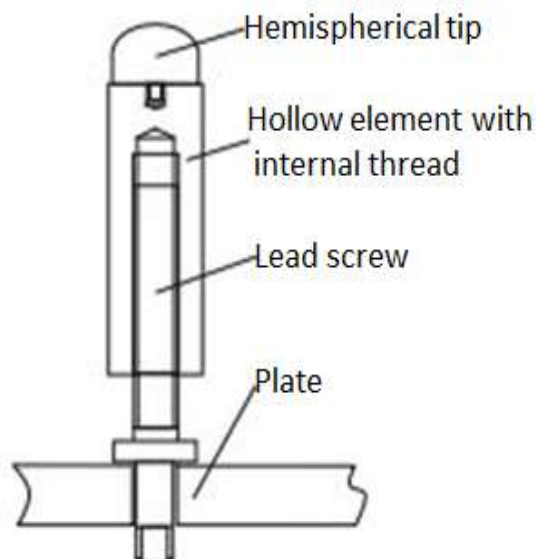


Figure 2.13 Lead screw pin [31]

Haas, et al., used a shaft-driven lead screw to adjust a 42x64 pin matrix [14, 32]. Boas used the same technique to adjust 16 elements at a time of a 48x72 pin matrix. After that, all pin elements were moved simultaneously using a group of motors [31, 33].

A hydraulic method to adjust the pins is shown in Figure 2.14. Every pin works as a hydraulic cylinder and each pin is controlled separately [11, 34].

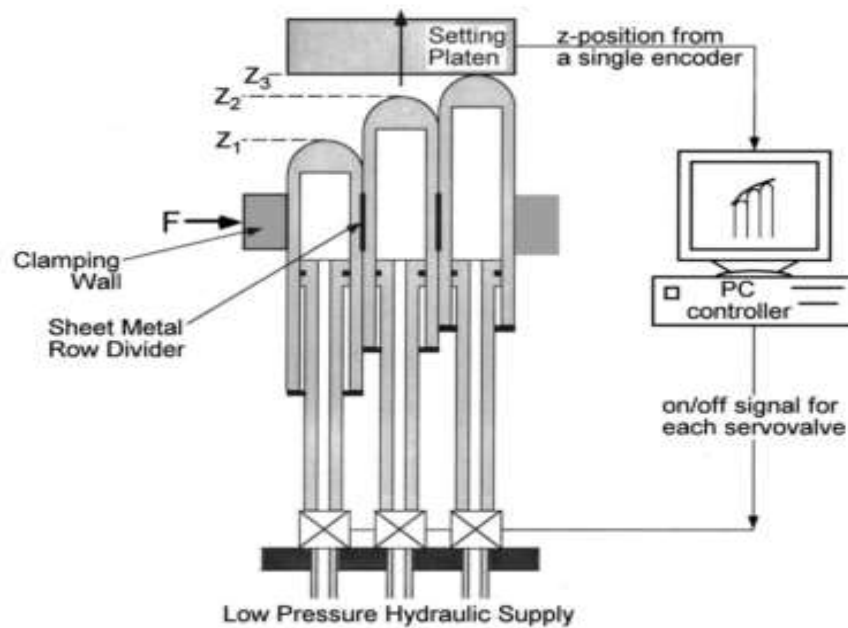


Figure 2.14 A cross-sectional view of a hydraulically-actuated reconfigurable discrete die [34]

As a result of performance comparison among leads crew-driven pins, hydraulic adjustment pins, and shaft-driven lead screw, it was clear that all the systems could achieve or surpass the main performance criteria such as speed of setting, the accuracy of pin position, and maximum forming force [35].

2.1.5 Pin clamping

Pin clamping is a crucial step after the pins are locked into position which helps the pins to withstand the high forming force that gives the target its shape. There are three ways to make sure the pins remain in position: firstly; a self-locked method which is used with large

pins where lead screw parts or hydraulic parts are used to support the pin [31, 36]. The second way is to fill the non-forming pins side with low-temperature moldable backing material, such as tin, bismuth, lead, or cadmium. The low-melt temperature of these materials should allow a local heat source to melt the material so that when the material re-solidifies it will hold the pin in place [25]. Figure 2.15 shows the essential mechanism of this method.

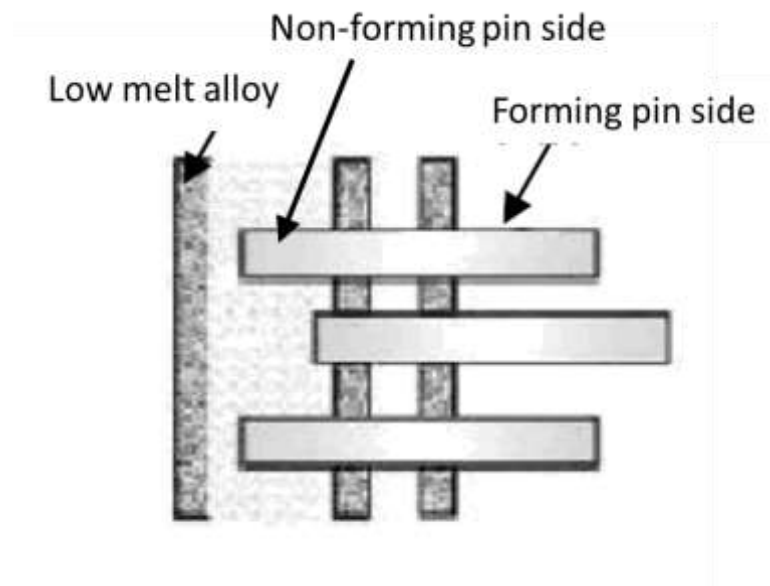
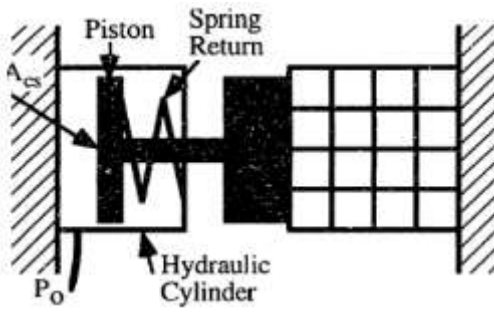
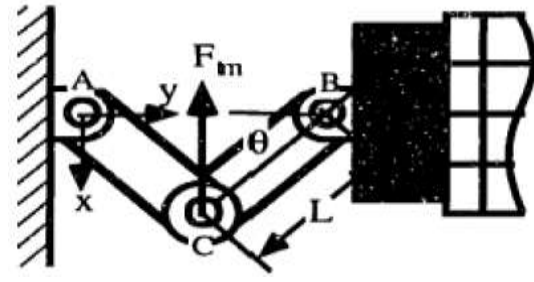


Figure 2.15 Pin fixing using low-temperature mouldable backing material [25]

Thirdly, side wall clamping uses a force normal to the side wall to prevent the pins from slipping during the forming process. The friction force due to the clamp must be greater than the forming force. To create a clamping force of sufficient magnitude, Walczyk used three traditional methods: a simple hydraulic actuator, a toggle mechanism, and mechanical wedge method; and suggested two non-traditional methods, a stack of piezoelectric laminations and thermally-induced contraction of a reconfigurable die frame [37] . Figure 2.16 illustrates the five clamping force mechanisms.



a- Hydraulic actuator



b- Toggle mechanism

$$F_{\text{clamp}} = P_o \cdot A_{cs} \cdot (1 - K_f)$$

P_o =hydraulic pressure

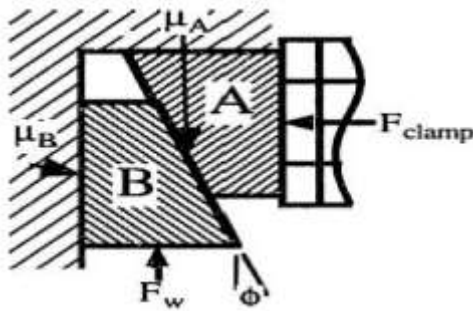
A_{cs} =cross section area of cylinder

K_f =force loss coefficient of the cylinder

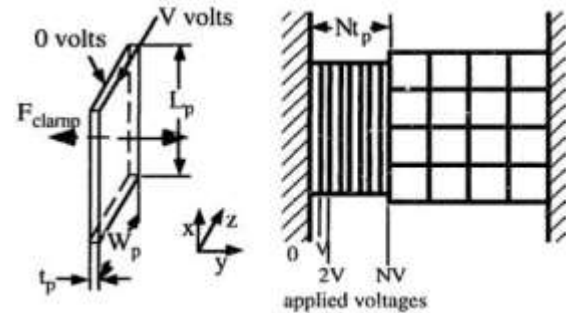
$$F_{\text{clamp}} = \frac{F_{lm}}{2 \cdot \tan \theta}$$

F_{lm} = perpendicular force applied to the wall

θ =angle with x-axis



c- Mechanical wedge



d- Stack of piezoelectric lamination

$$F_{\text{clamp}} = \frac{F_w \cdot (\cos \phi - \mu_A \sin \phi)}{[(\mu_A + \mu_B) \cdot \cos \phi + (1 - \mu_A \mu_B) \cdot \sin \phi]}$$

F_w =input force

Φ =wedge incline angle

μ_A = coefficient of static friction between A and B

μ_B = coefficient of static friction between B and the horizontal wall

$$F_{\text{clamp}} = \frac{V \cdot L_p \cdot W_p}{t_p \cdot g_{33}}$$

V =voltage

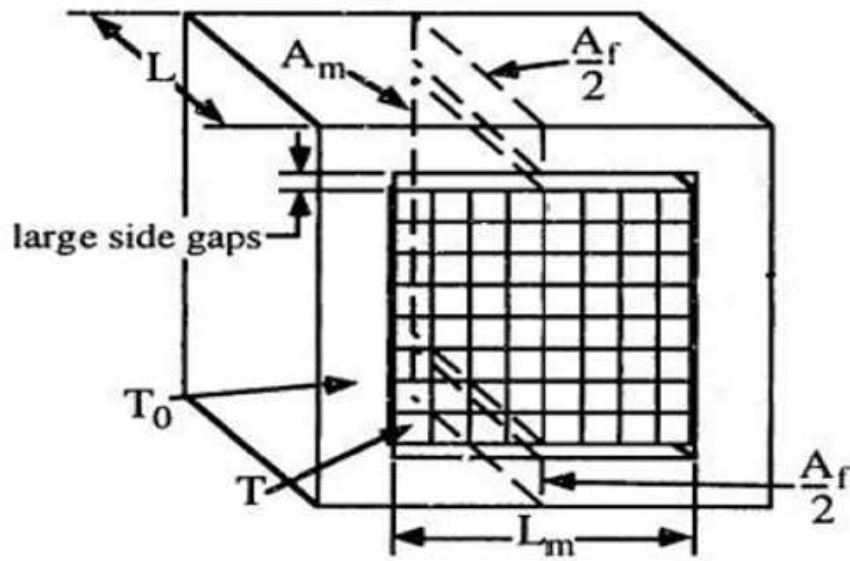
L_p =length of lamination

W_p =width of lamination

T_p =thickness of lamination

g_{33} = coefficient of piezoelectric voltage

Figure 2.16 Types of clamping force generation mechanisms [15](To be continued)



e- Thermally-induced contraction of discrete dies frame

$$F_{\text{clamp}} = \frac{\alpha_f \cdot (T - T_0)}{\left[\frac{1}{A_m E_m} - \frac{1}{A_f E_f} \right]}$$

α_f = coefficient of linear thermal expansion of the frame material

E_f = elasticity modulus of the frame metal.

A_f = is the total cross-sectional area of the element matrix in a plane normal to the loading direction

A_m = is the cross-sectional area of the element matrix in a plane normal to the loading direction

E_m = elasticity modulus of the discrete pins

T_0 = temperature to which the frame is cooled

T = initial hot temperature of the entire discrete die.

Figure 2.16 Types of clamping force generation mechanisms

A square cage is used to clamp the square pin matrix with one of the sides movable, thus the effect is of a force on the pin matrix from one side due to the rotation of the clamping screw which passes through a support plate as shown in Figure 2.17 [38].

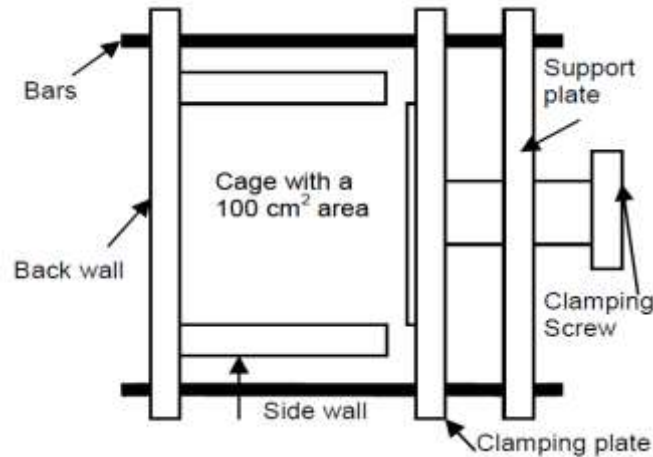


Figure 2.17 Square cage to pin clamping [38]

2.2 Surface regularity

The non-smooth surface of reconfigurable tooling leads to defects emerging on the surface of the products such as dimpling, which is caused by the presence of discrete pin tips. Previous research has developed different methods to eliminate such defects, for instance, the insertion of a deformable elastic layer, deformable pin tips, and surface machining.

2.2.1 Elastomeric interpolating layer

An elastomeric interpolating layer (an “interpolator”), is placed on top of the hemispherical forming ends of the die elements to prevent dimpling, as a continuous flexible (rubber) sheet gives more continuity to the discrete die surface, see Figure 2.18 [3, 12,[39]. This is the same, in principle, as the so-called elastic cushion method, which uses a rubber or polyurethane pad to protect the metal sheet from dimpling in sectional multi-point forming [40]. In the stamping process, the metal sheet is sandwiched between two rubber-polyurethane sheets, placed between the two parts of the tool to avoid dimpling defects [31]. The thickness of the plastic layer has an effect on the sheet formability, a thicker elastic

layer leads to a reduction of stress in the elastic material which affects the blank deformation negatively [41].

Figure 2.18 a, b, and c shows the use of elastic layers.

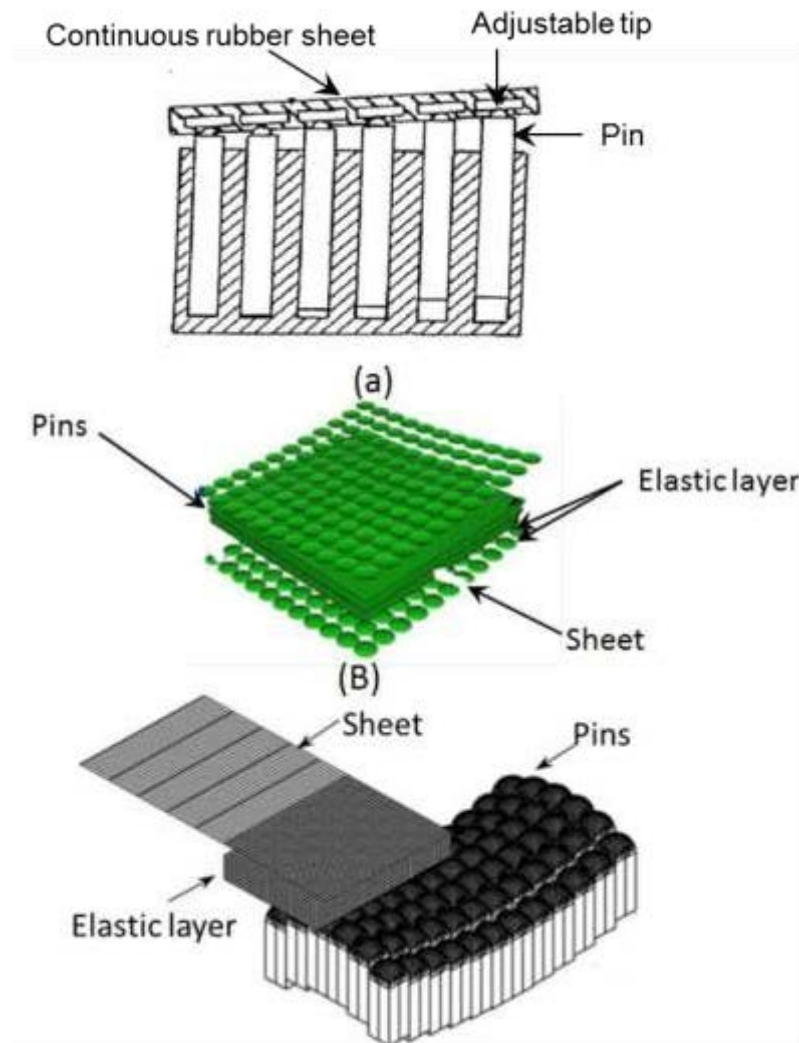


Figure 2.18 Methods of using elastic layers [13, 36, 42]

Quan et al., [43] investigated effect of elastic cushion thickness on the formability of AZ31B magnesium alloy, and showed that the formability of AZ31B was improved by using the elastic cushion, with the optimal thickness of elastic cushion being 4 mm for the multi-point bending of 2 mm thick AZ31B sheet. The Boeing Company used the deformable pin tip technique to prevent dimpling appear on the deformed sheet surface in sheet metal forming [30]. A composite tool was built containing two opposed sets of rams placed in matrix

arrays, with the surface of the tips rounded to get a better surface quality on the deformed part. Figure 2.19 shows the tool construction.

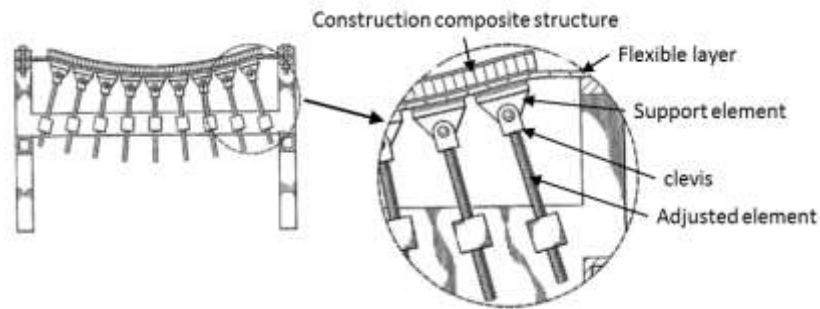


Figure 2.19 The Boeing Company's composite forming structure [44]

2.2.2 Machining surface treatment

Surface machining incorporates two approaches of treatment to generate a smooth surface, subtractive pin tooling (SPT) technology and near-net-shape pin tooling (NPT) technology. For SPT the top ends of the pins are machined to match the target surface, for NPT the pin ends are filled using an appropriate filler in the liquid phase and machining it after becomes solid. In the first approach, the machining is of only the pins' material, and in the second approach, machining is mostly of the filler. Figure 2.20 shows the two approaches of machining surface treatment.

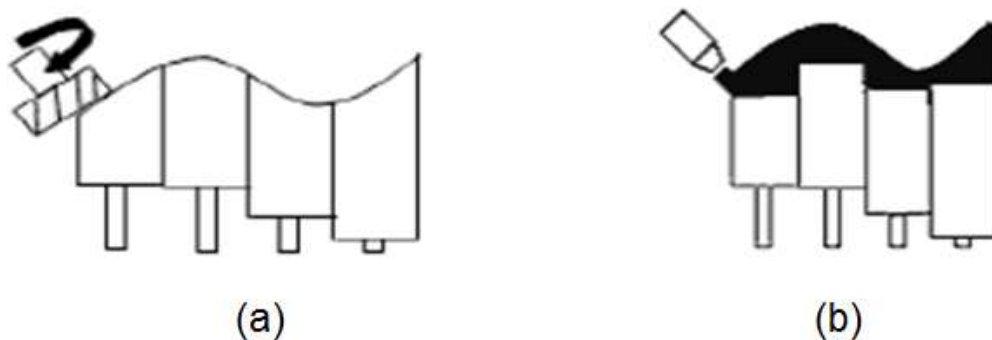


Figure 2.20 Milling surface treatment [45]
(a) Subtractive pin tooling, and (b) Near-net-shape tooling

2.3 Multi-point forming defects

As with solid dies, many defects can appear in discrete dies, and negatively effect product quality, especially where a smooth finish is needed for paint. The most common defects in the MPF process are dimpling and wrinkling.

2.3.1 Dimpling

In MPF, the deformation force from the pins on the metal sheet is concentrated on the contact points. Due to the small contact area between the pin and sheet, the contact pressure is large and can lead to localised plastic deformation, this deformation is named dimpling. Dimpling appears on one side of the metal sheet during Multi-Point Stretch Forming, and on both sides during Multi-Point Stamping Forming.

Dimpling has two main forms; surface dimpling and enveloping dimpling. The use of an elastic pad in multi-point forming can significantly reduce dimpling by ensuring more uniform contact pressure distribution. Variable path multi-channel multi-point forming technology is also capable of suppressing dimpling as well as allowing the realisation of large deformations by increasing the forming limit [46]. Figure 2.21 shows surface and enveloping dimpling.

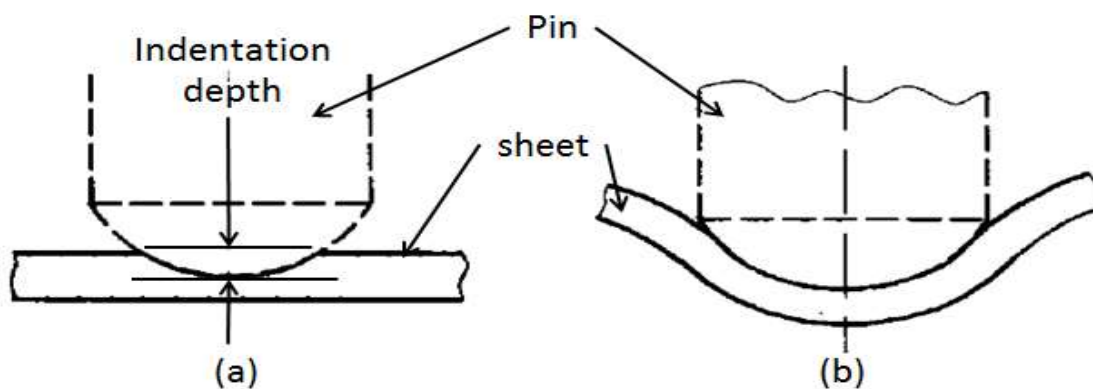


Figure 2.21 Dimpling forms (a) surface dimpling (b) enveloping dimpling [46]

The forming force is one of the major factors influencing dimpling. An excessive forming force will lead to serious dimples on the formed part [47]. The numbers of pins and pin tips radius have an effect on dimpling. A numerical analysis has been carried out on forming spherical and saddle shaped parts using multi-point stretch forming with a 400 mm x 400 mm die with different numbers pins; 10x10, 20x20, 32x32, 40x40, 50x50, and 80x80 pins respectively [20]. The results show that increasing the number of pins but maintaining the area constant helps to eliminate dimpling. Figure 2.22 shows the dimpling on the metal sheet formed by using the largest and smallest pin cross sections.



Figure 2.22 Dimpling (a) clear dimpling, and (b) no dimpling using 10 mm pin size [20]

Li et al. [1] investigated dimpling and wrinkling defects and found that these defects can be eliminated using the proper design of the deformation path. Figure 2.23 a, and b shows the multi-point forming die and multi-point press forming. Additionally, the section by section part forming technique allows fabrication of large size products using a small die [48]. Figure 2.24 shows a sketch of sectional multi-point forming.

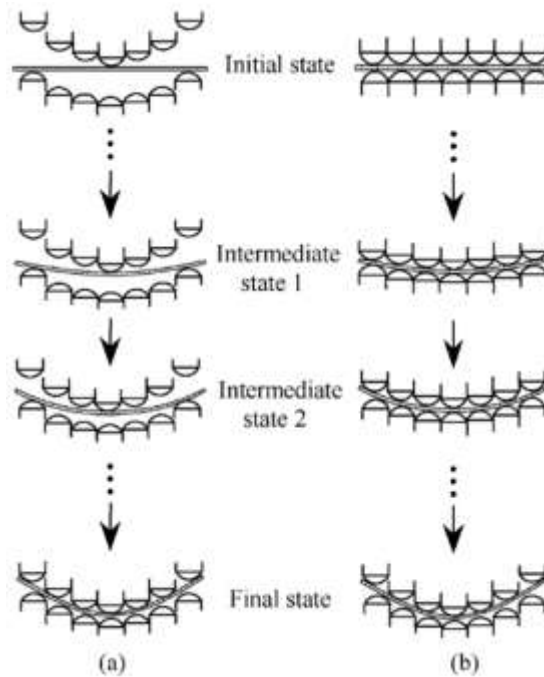


Figure 2.23 Forming paths a- Multipoint forming die b- multi-point press forming [1]

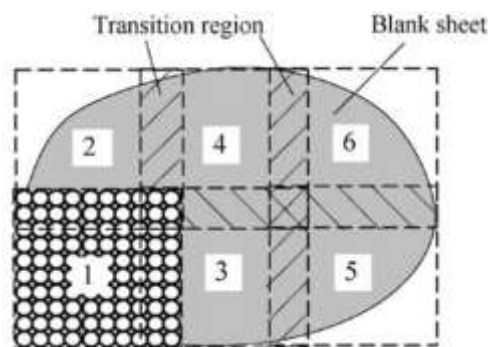


Figure 2.24 Sketch of sectional multi-point forming [1]

2.3.2 Wrinkling

Wrinkling is usually undesired in sheet metal parts for both aesthetic and functional reasons, and it is especially unacceptable in the outer skin parts where appearance is crucial. Wrinkling on mating surfaces can adversely affect the part assembly and part functions, such as sealing and welding. Previous investigations have focused on studying the wrinkling defect to predict and prevent it. One study was of the wrinkling on circular plates of mild

steel with radius to thickness ratios of between 30:1 and 60:1, using a stamping hemispherical solid die, and focused on the relation between wrinkling and punch force. This study showed that increasing punch force may reduce wrinkling, and for thin plates wrinkling did not appear when the ratio between plate radius and thickness was less than the value given in Equation 2.1 [49] :

$$\frac{a}{t} < 1.68 \left(\frac{E_0}{y} \right)^{0.5} \quad (2.1)$$

Where a is a circular plate radius, t is plate thickness, y is yield stress, and E_0 is buckling modulus which is calculated from equation 2.2.

$$E_0 = \frac{4EE_p}{(\sqrt{E} + \sqrt{E_p})^2} \quad (2.2)$$

Where E_p is strain hardening modulus

T X YU et al. [50] used double curved dies to stamp rectangular plates of mild steel, copper and aluminium without clamping. The punch force, contact areas, final shape were studied for different die curvature ratios and plate size, and compare the results with theoretical analysis.

This work showed that the wrinkling appears if the ratio of half-length of a rectangular plate to the thickness of a plate was large, and the aspect ratio between the lengths of rectangular sides of the metal sheet was close to unity [50].

Cai et al. [47] studied wrinkling on spherical and saddle shaped parts and found the wrinkling appeared in the middle of the sheet edges for the spherical parts and in middle of the sheet for the saddle parts. The results of the study showed that initiation of wrinkling starts when the punch reached a critical value. Wrinkling continues to increase with punch movement until it reaches a maximum value, after that, the maximum wrinkle height decreases until the punch reaches the final point of its travel. Figure 2.25 shows wrinkle growth on spherical and saddle shapes.

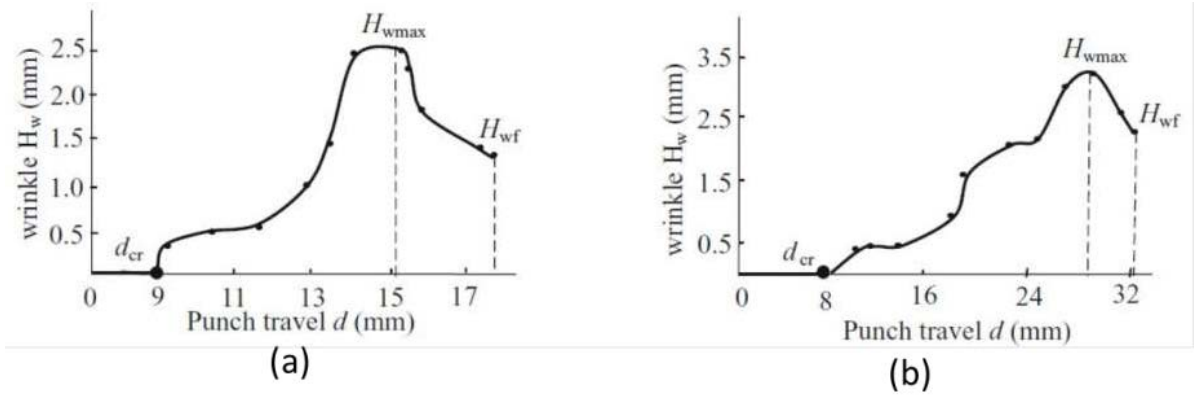


Figure 2.25 Wrinkle growth (a) spherical shape, and (b) saddle shape [47]

Wrinkling formation in double curved thin sheets has been studied using plastic bifurcation theory for thin plates and shells, and the study showed that the wrinkling condition depends on the geometrical ratio of sheet thickness to radius of curvature of deformed part and on strain hardening. Equation 2.3 shows the relation between critical stress and geometrical parameters with strain hardening [51].

$$\sigma_1^{cr} = \frac{2}{3} \frac{t}{R^2} \sqrt{E - E_t} \quad (2.3)$$

Where σ_1^{cr} is critical stress, t is thickness of the sheet metal, R is radius of curvature, E is modules of elasticity, and E_t is tangent modules.

The study of wrinkling behaviour is necessary to predict and prevent flange wrinkling. Cao and Boyce [52] suggested an analytical model based on the wrinkling condition. The critical buckling stress and wrinkling wavelength as a function of normal pressure on the plat surface have been calculated and experimentally validated for conical and a square cup forming. The critical buckling can be determined quantitatively from Equation 2.4 [53].

$$\sigma_{cr} = K^2 \sqrt{\frac{1+R}{1+\alpha^2+R(1-\alpha)^2}} (\varepsilon_o + c_1 \ln \left(1 - \frac{2u_{xcr}}{L} \right))^n \quad (2.4)$$

A parametric study has been completed by Jian Cao and Xi Wang [53] for the parameter group represented in Equation 2.5.

$$\sigma_{cr} = f(p, \alpha, n, K, R, \varepsilon_o) \quad (2.5)$$

Where σ_{cr} = critical buckling stress, p = critical binder pressure, α = loading factor, n = strain hardening exponent, K = strength coefficient of material, R = normal anisotropy, ε_0 = pre-strain (but it has been found that ε_0 does not affect the critical wrinkling conditions and wavelength), and the effect of the remaining parameters are shown in Figure 2.26 to Figure 2.32.

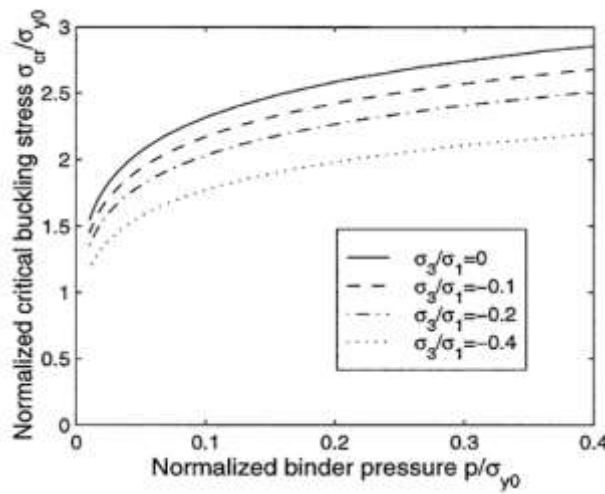


Figure 2.26 Normalised critical stress vs. normalised binder pressure for various σ_3 [53]

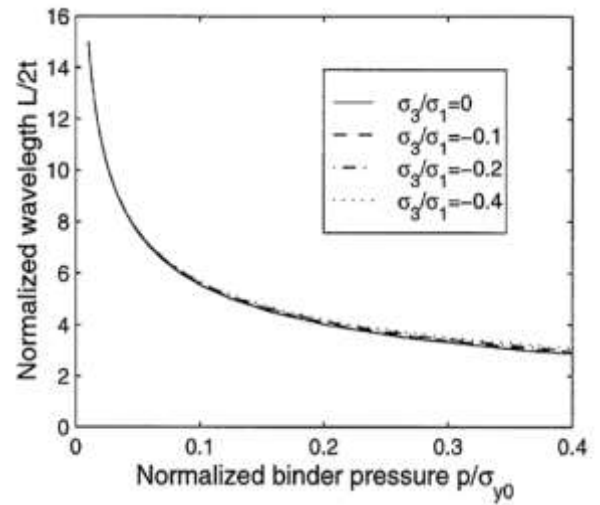


Figure 2.27 Normalised wavelength vs. normalised binder pressure for various σ_3 [53]

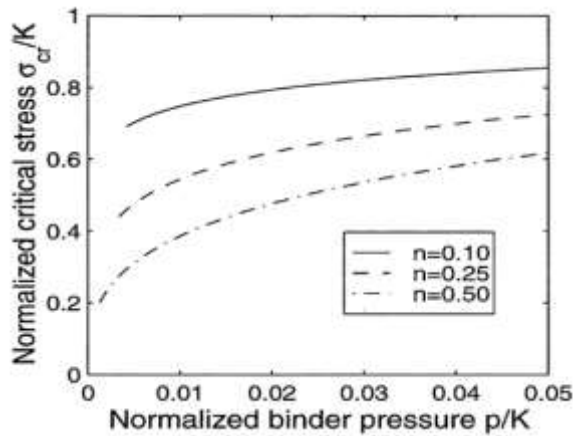


Figure 2.28 Normalized critical stress vs. normalized binder pressure for various n [53]

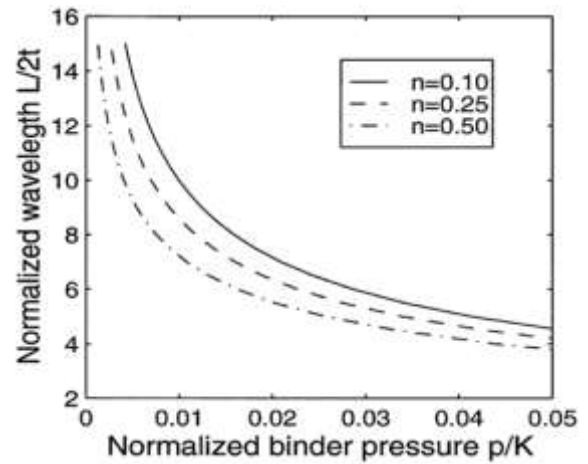


Figure 2.29 Normalised wavelength vs. normalized binder pressure for various n [53]

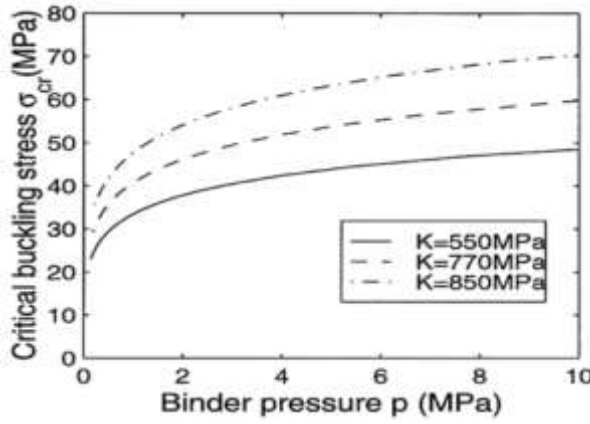


Figure 2.30 Critical buckling stress vs. binder pressure for various K [53]

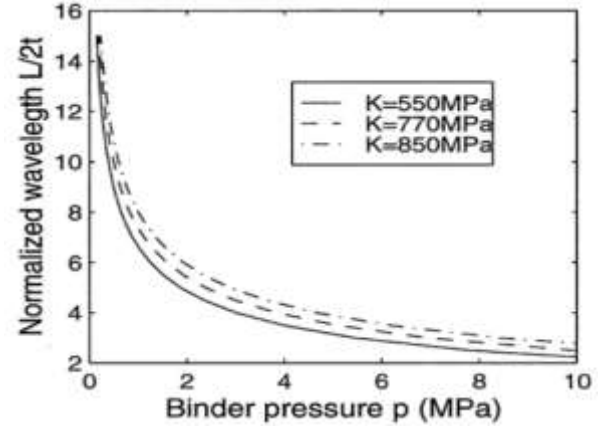


Figure 2.31 Normalised wavelength vs. pressure for various K [53]

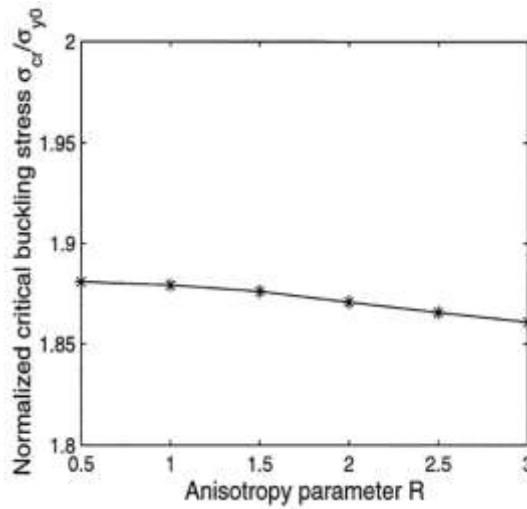


Figure 2.32 Normalised critical stress vs. anisotropy parameter R at a wrinkling wavelength of 10t [53]

FE analysis was used to study wrinkling to avoid the cost of experimental tests, however, there is a question over whether this method is reliable and accurate enough for precise wrinkling prediction. Kawka, et al. [54] compared experimental results for wrinkling obtained using the deep drawing process with a conical cup with numerical prediction using static explicit (ITAS3D) and dynamic ABAQUS/Explicit. The results showed that many parameters could impact on the wrinkling simulation results, the most important of which was the FE mesh size. To study the mesh effect, three mesh densities were used, see Figure 2.33.

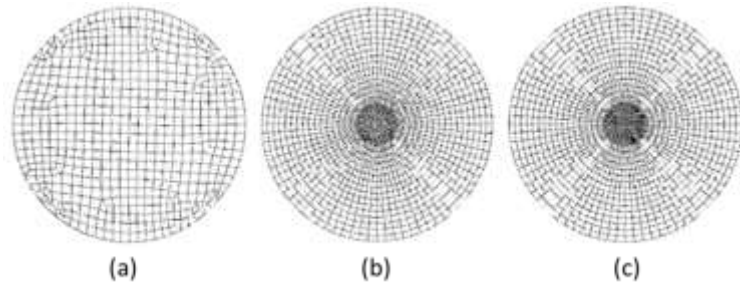


Figure 2.33 Different meshes number used for the 160 mm blank daimeter, SPCE material, and 0.7mm thickness: (a) 608 elements, (b) 1680 elements, and (c) 1956 elements [54]

Simulation results showed the high sensitivity to the mesh size, for example,

Figure 2.34 illustrate the different results obtained using 608 elements and 1956 elements in the two codes.

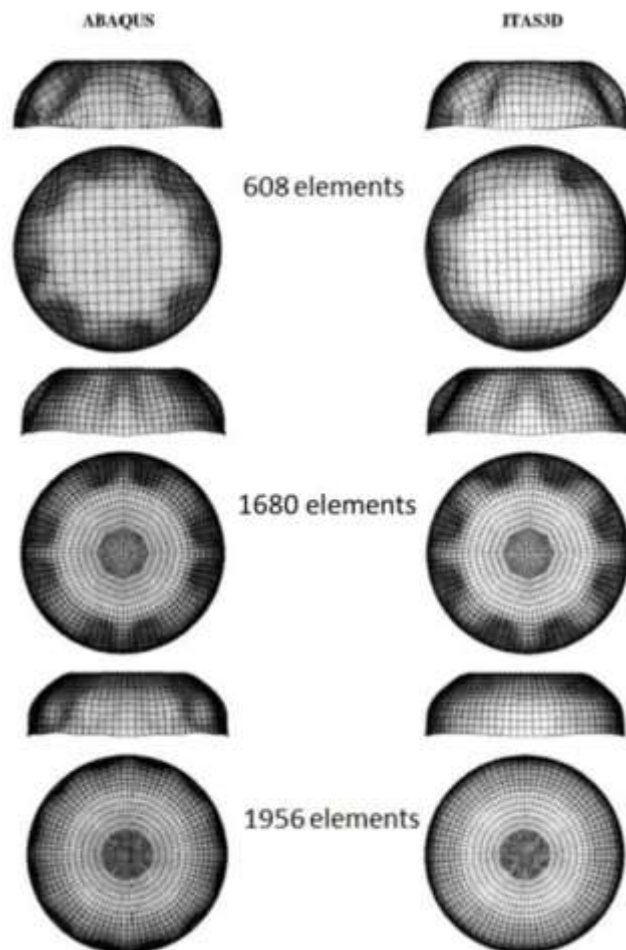


Figure 2.34 Results of finite element analysis simulation for three meshes sizes, 608, 1680, and 1956 elements [54].

The simulation results for the two codes (ABAQUS Explicit and ITAS3D) are compared with experimental results in Figure 2.35.

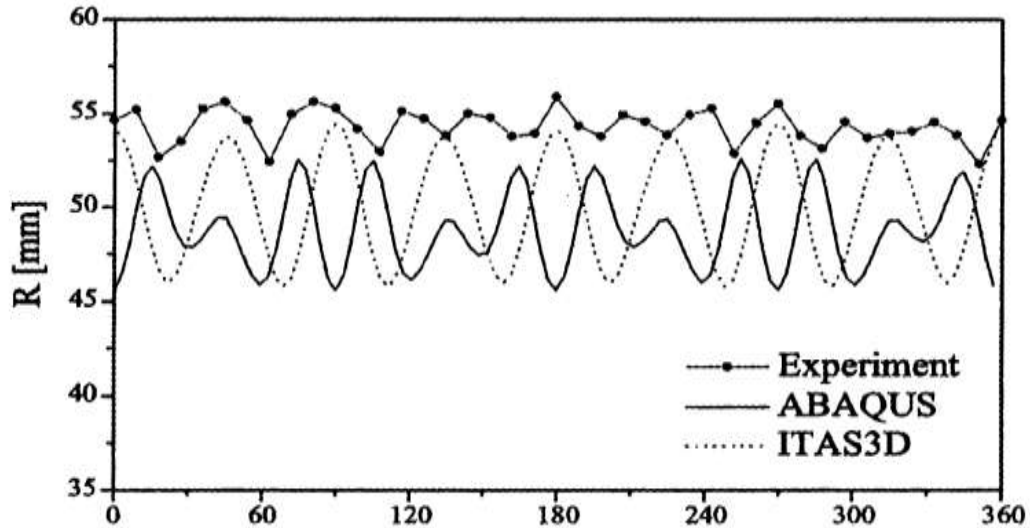


Figure 2.35 Comparison of numerical and experimental results wave wrinkling shape [54]

The two FEM codes not only differed between themselves but each code showed a high sensitivity to mesh size. More importantly, both codes predicted results that were markedly different from the experimental results. All this confirmed the necessity to do an experimental test to predict wrinkling.

Bifurcation algorithms have been used to study initiation and growth of wrinkling on the flange for a cylindrical cup in deep drawing, and taking into account factors which impact on wrinkling. Those factors are the mechanical properties of the sheet material, stress ratios, contact condition and geometry of the product. During forming, the lateral constraints reduce as a result of increasing the gap between the die and blank holder due to the reaction of the metal to deformation which gives rise to the so-called reaction forces, or thickening of the sheet edges, as shown in Figure 2.36 [55].

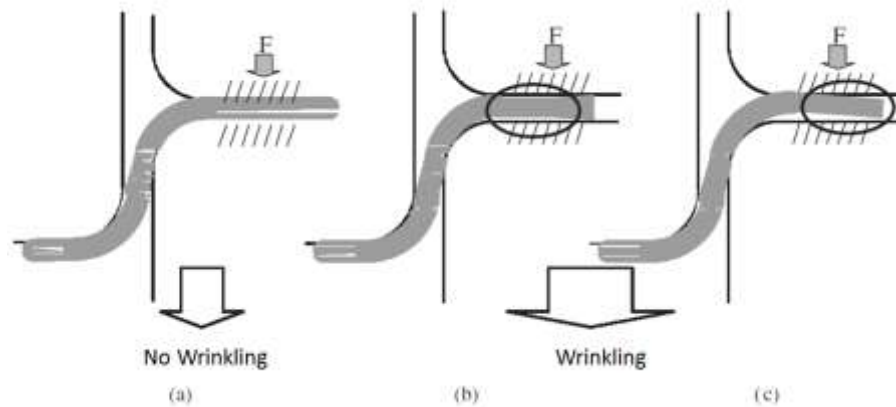


Figure 2.36 Mechanism of wrinkling initiation
 (a) full contact at the flange area; (b) loss of contact by thickening of the sheet; and
 (c) loss of contact by the reaction force of the sheet [55]

To analyse wrinkle growth, blank holder force control and the two face contact treatment technique are used. The analysis shows that thickening at sheet edges and reaction force have a significant effect on wrinkling initiation, which occurs more easily for sheet materials having a low normal anisotropic coefficient. The simulation results were compared with experimental results, and there was a good agreement, therefore the study of wrinkling initiation using FE analysis (bifurcation algorithm) is considered reliable. Yaser, et al., [56] have studied how to use MPF tooling to produce rectangular cups by means of the deep drawing method. Wall thickness, punch load, and process defects (wrinkling and pitting) were the main parameters which were analysed. An irregular rectangular cup was obtained without wrinkling using a properly adjusted blank holder force or blank holder gap.

2.4 Analysis approach

There are two general prediction approaches to the study of wrinkling initiation: first, analytical methods and secondly numerical methods such as the static implicit FE method, and the dynamic explicit FE method.

2.4.1 Analytical methods

For more than fifteen years analytical method has been used in sheet metal wrinkling studies. The analytical study of wrinkling is generally simplified by considering the buckling stability confined to a shell under laterally constrained conditions. For instance; the sheet metal forming process using stamping can be simplified to a thin sheet model. There are three main analytic methods; static equilibrium, initial imperfection and the energy method. [57].

2.4.1.1 Static equilibrium method

Consider the forming of thin plates under compressive loading N_x in the x-direction, N_y in the y-direction and N_{xy} in x-y plane. The stress of these forces acts in middle plane of the plate and, initially, the stress state across the thickness is uniform. If the width of the plate w and length L are as shown in Figure 2.37, then Equation 2.6 represents plate buckling [58].

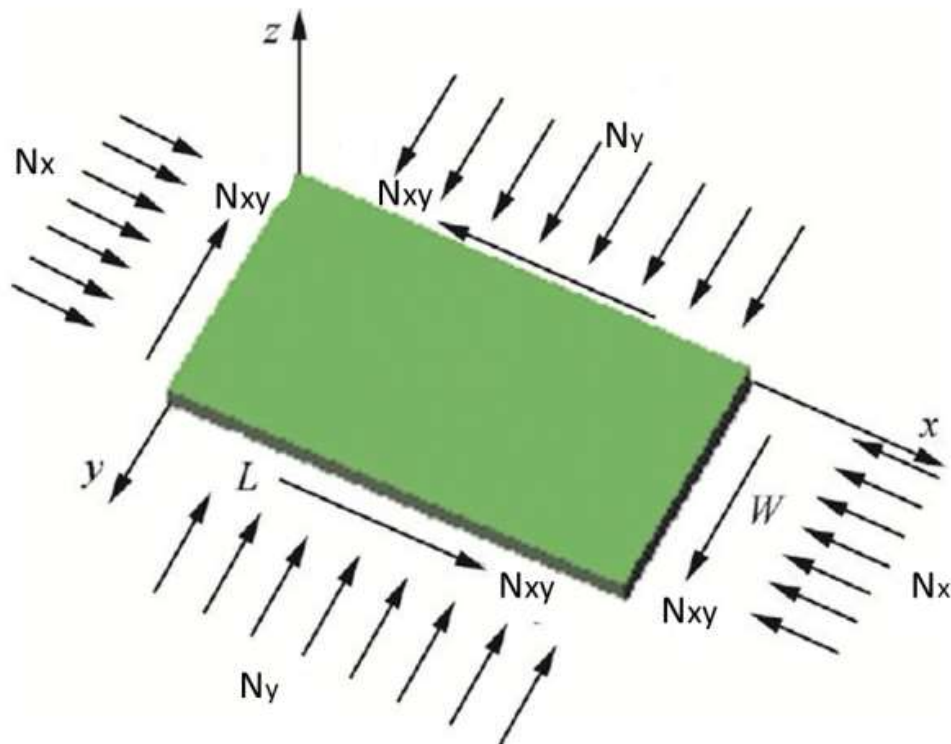


Figure 2.37 Rectangular thin plate under in-plane compression [57]

$$\frac{\partial^4 w}{\partial x^4} + 2 \frac{\partial^4 w}{\partial x^2 \partial y^2} + \frac{\partial^4 w}{\partial y^4} = \frac{1}{D} \left(N_x \frac{\partial^2 w}{\partial x^2} + N_y \frac{\partial^2 w}{\partial y^2} + 2 N_{xy} \frac{\partial^2 w}{\partial x \partial y} \right) \quad (2.6)$$

where w is the deflection bending, and D is bending stiffness.

The simplest case of this equation when N_x , N_y and N_{xy} are constant and it is supposed that there are particular ratios between the forces as follows; $N_y = \alpha N_x$, and $N_{xy} = \beta N_x$. Now it is possible to solve Equation 2.6 for the given boundary conditions, and the smallest value N_x is taken as the critical value. If the forces N_x , N_y , and N_{xy} are not constant, we can assume a common factor γ for the expressions of N_x , N_y and N_{xy} . The increase of γ helps to obtain the increase of loading.

In case of shell model with k_x and k_y as radius of curvature, the small deflection is represented by Equation 2.7 [57].

$$\begin{aligned} \frac{D}{t} \nabla^4 \nabla^4 w + E k_y^2 \frac{\partial^4 w}{\partial x^4} + 2 E k_x k_y \frac{\partial^4 w}{\partial x^2 \partial y^2} + E k_x^2 \frac{\partial^4 w}{\partial y^4} + P_x \nabla^4 \left(\frac{\partial^2 w}{\partial x^2} \right) + 2 P_{xy} \nabla^4 \left(\frac{\partial^2 w}{\partial x \partial y} \right) \\ + P_y \nabla^4 \left(\frac{\partial^2 w}{\partial y^2} \right) = 0 \end{aligned} \quad (2.7)$$

where E and t are modulus of elasticity of the shell material and thickness of shell plate respectively.

The static equilibrium method can provide an assessment in terms of general tendency and impact of parameters individually on wrinkling initiation. However, it is difficult to solve the above equations for complex problems when the shapes have irregular geometry and complicated boundary conditions. This because Equations 2.6 and 2.7 become partial differential equations with variable coefficients. This method has been used to investigate the critical load of a cylindrical shell simply supported with clamped end conditions. It presented a good solution and enabled critical load and the relative influence of the coefficients to be determined [59]. This method was also used to investigate the pure bending of a tube as generalised plane strain problem and the wrinkling initiation was

predicted as buckling modes, including a sinusoidal variety of the displacements along the length of the tube [60].

2.4.1.2 Energy method

The energy method is alternative analytical method that can be used to study wrinkling phenomenon. If a compressive force is applied to the centre of a bar, then, if the value of the applied force is smaller than the critical value then the compressed bar will remain straight (equilibrium state). If the force is increased slightly above critical value, theoretically there are two possible forms of equilibrium; one is the bar remains straight, and other is the bar buckles sideways. Experimental work has shown that the straight form is unstable and invariably the bar buckles under a load greater than the critical value [58]. This theory has been applied to study the elastic buckling of thin plates and shells with several boundary conditions. The energy method depends on balancing the internal energy ΔU and the work done by in-plane membrane forces ΔT . That is, the deflection increases ΔU in terms of the strain energy of the system, and load will move a small distance and do work equal to ΔU . Then the stability of the system depends on balancing between ΔU and ΔT as shown in Table 2.2.

Table 2.2 Stability conditions

Energy balance	Condition
$\Delta U > \Delta T$	Stable
$\Delta U = \Delta T$	Critical
$\Delta U < \Delta T$	Unstable

Buckling stress can be determined as plate properties, as a function of stress, and of shape. Wang, et al., [61] suggested developing energy equality and applying it to metal forming for the area under compression. The model could be used to study wrinkling assuming that the metal sheet was a flat or simply curved sheet. The model could be applied to forming

processes such as deep drawing with conical and square cups. Morovvati, et al., [62] used energy method analysis to study the prediction of wrinkling phenomenon initiation in two-layer aluminium-stainless steel sheets with the deep drawing process and compared the theoretical results and numerical with experimental results. Good agreement was obtained between analytical, FE and experimental results.

Shafaat et al., [63] used the energy method to investigate sidewall wrinkling for galvanised steel during the conical forming test. The effect of material anisotropy was studied and a new deflection function was developed to predict wrinkling.

Comparisons between experimental results and energy method results have shown good agreement, this was also the case for all previous studies. By using the energy method one can avoid solving partial differential equations. Because it focuses only on the beginning and end of deformation the energy method is suitable for dealing with problems which have more complex boundary conditions.

Kowsarinia et al., [64] applied the energy method and plastic bending theory to the analysis of flange wrinkling in high-velocity forming operations, such as explosive forming. The critical radial distance and wrinkling wave numbers were determined, and the effect of blank holder force, radii ratio and mechanical properties of the material on wrinkling were discussed. The validation has shown good agreement between analytical and experimental results.

2.4.1.3 Initial imperfection method

It has been shown that real cylindrical supports and shell structures in the membrane state buckle at loads significantly less than the theoretical buckling load [65]. This is also true for laboratory tests of axially compressed cylinders subject to simple supports, and there have been many studies focused on determining the reasons for the difference between theory and

experiment. Many studies have investigated imperfection sensitivity and shell buckling. These include Peek and Hilberink [66], Kyriakides and Corona [67], Hutchinson and He [68]. With initial imperfections, the partial differential equilibrium Equation 2.8 of a cylindrical shell has $k_x = 0$ and $k_y = 1/R$ and becomes [57]:

$$\left\{ \begin{array}{l} \frac{D}{t} \nabla^2 \nabla^2 w - \frac{1}{R} \cdot \frac{\partial^2 \Phi}{\partial x^2} = \frac{\partial^2 \Phi}{\partial x^2} \cdot \frac{\partial^2 w}{\partial s^2} - 2 \frac{\partial^2 \Phi}{\partial x \partial s} \cdot \frac{\partial^2 w}{\partial x \partial s} + \frac{\partial^2 \Phi}{\partial s^2} \cdot \frac{\partial^2 w}{\partial x^2} \\ \quad + \frac{\partial^2 \Phi}{\partial x^2} \cdot \frac{\partial^2 w_0}{\partial s^2} - 2 \frac{\partial^2 \Phi}{\partial x \partial s} \cdot \frac{\partial^2 w_0}{\partial x \partial s} + \frac{\partial^2 \Phi}{\partial x \partial s} \cdot \frac{\partial^2 w_0}{\partial x \partial s} \\ \frac{1}{E} \nabla^2 \nabla^2 \Phi = \eta \left[\left(\frac{\partial^2 w}{\partial x \partial s} \right)^2 - \left(\frac{\partial^2 w}{\partial x^2} \right) \left(\frac{\partial^2 w}{\partial s^2} \right) \right] - \frac{1}{R} \frac{\partial^2 w}{\partial x^2} \end{array} \right. \quad (2.8)$$

where R and L are the radius and length of the tube respectively, Φ is function of stress, x is the axial direction, s is the circumferential direction, t is sheet thickness, and η is the initial imperfection factor. The deflection function w is represented in Equation 2.9 [57]:

$$w = at \left(\cos \frac{m\pi x}{L} \cos \frac{ns}{R} + b \cos \frac{2m\pi x}{L} + c \cos \frac{2ns}{R} + d \right) \quad (2.9)$$

The initial imperfection w_0 is represented in Equation 2.10 [57]:

$$w_0 = a_0 t \left(\cos \frac{m\pi x}{L} \cos \frac{ns}{R} + b \cos \frac{2m\pi x}{L} + c \cos \frac{2ns}{R} + d \right) \quad (2.10)$$

where a , b , c , d , a_0 are constant.

Using the initial imperfection method, simplifications and assumptions concerning boundary and initial conditions and the geometry of the system, means that solutions obtained by analytic methods tend to be of limited applicability and reliability. The general case of buckling of real shells represented by non-linear partial differential equations which are sensitive to real geometric imperfections is too complex and difficult to solve.

2.4.2 Numerical method

The high computation capability of numerical methods means they can be used as a tool to study the wrinkling phenomenon. To select the best numerical procedures, whether the

eigenvalue, static-implicit FE, or dynamic explicit FE method, it is required to understand the advantages and disadvantages of each method.

2.4.2.1 Eigenvalue method

The main purpose of this method is to seek out the singular point of a structure stiffness matrix under a linear perturbation. Equation 2.11 is used to get the critical load and buckling modes by extracting the eigenvalue and eigenvectors [57].

$$(K_e + \lambda_i K_g) \phi_i = 0 \quad (2.11)$$

where λ_i are the eigenvalues; K_g is the differential initial stress and load stiffness matrix due to the incremental loading pattern matrix, K_e is the elastic stiffness matrix corresponding to the base state; ϕ_i is the i^{th} shape of buckling mode (eigenvectors); i refers to the i^{th} buckling mode. From Equation 2.10, increase in the value of λ lead to the equation having a non-zero solution (deflection form is in a stability position which is a type of buckling mode). These modes are the most useful result of the eigenvalue analysis, since they predict the likely instability modes of the structure. Thus, the imperfection has the form as in Equation 2.12[57].

$$\Delta x_i = \sum_{i=1}^N A_i \phi_i \quad (2.12)$$

In Equation 2.12, A_i is the associated scaling factor and N the order of the eigenvector.

The eigenvalue buckling analysis on ABAQUS was used by Wong and Pellegrino [69, 70] to predict the wrinkling modes of members subjected to a simple shear and a diagonal pair of opposite loads. They found the eigenvalue buckling can be applied only to elastic problems.

2.4.2.2 Static implicit finite element method

The implicit finite element method uses an automatic increment strategy based on the success rate of a full Newton iterative solution method as Equation 2.13 shows:

$$\Delta u^{(i+1)} = \Delta u^{(i)} + K_t^{-1} \cdot (P^{(i)} + I^{(i)}) \quad (2.13)$$

Where K_t is the tangent stiffness matrix, P is the applied load vector, I is the internal force vector, and Δu is the increment of displacement. The implicit FE analysis method iterates to find the approximate static equilibrium at the end of each load increment. It controls the increment by a convergence criterion throughout the simulation. There are two numerical procedures used in the FE method; the bifurcation analysis of a perfect structure, and non-bifurcation analysis with initial imperfection. Riks [71] proposed bifurcation analysis as continuation method, and used it to analyse post bifurcation behaviour of an elastic thin shell structure.

A 3-D rigid-plastic FE simulation system has been developed by Zhan, et al., [72] to study the bending process of a thin-walled tube. This investigation showed that 3-D FE simulation is a valid tool for analysing numerical control of the bending process of the tube. Bifurcation theory also used to study wrinkling in the sheet metal forming process and has shown that plastic buckling in high yield stress material is higher than in lower yield stress material [73]. In order to study wrinkling behaviour, many methods of including introductions of imperfection into FE models have been discussed, and this development has shown the ability to accurately simulate wrinkling behaviour under complicated boundary conditions [52]. All previous investigations were based on the implicit algorithm, and it has been concluded that the implicit method should usually be avoided to solve large complex contact problems.

2.4.2.3 Dynamic explicit finite element method

The explicit method was originally developed, and is still primarily used, to solve dynamic problems involving deformable bodies. A fully explicit procedure means that the state at time $(t+\Delta t)$ is determined based on information available at time (t) . During each increment, the initial kinematic conditions are used to calculate the conditions for the next increment. The nodal acceleration (\ddot{u}) can be calculated at the beginning of the increment based on dynamic equilibrium using Equation 2.14 [74], here the superscripts refer to the time increment.

$$\ddot{u}^{(i)} = M^{-1}(F^{(i)} - I^{(i)}) \quad (2.14)$$

Where M is the lumped mass matrix, F is the vector of externally applied forces and I is the vector of internal element forces. Since the explicit code uses a diagonal mass matrix, the acceleration at any nodal point is determined only through its mass and net acting force, without the need to solve simultaneous equations. Therefore each time increment is computationally inexpensive to solve. The term “explicit” refers to the fact that the state of the analysis is advanced by assuming constant values for the velocities (\dot{u}) and the accelerations (\ddot{u}) across intervals of half the time step. From a knowledge of the accelerations, the velocities (\dot{u}) and displacements (u) are advanced “explicitly” through each time increment (Δt) using the central difference rule, which is used in ABAQUS/Explicit code, as shown in Equations 2.15 and 2.16[74].

$$U^{(i+1)} = U^{(i)} + \Delta t^{(i+1)} \dot{U}^{(i+1)} \quad (2.15)$$

$$U^{(i+1/2)} = \dot{U}^{(i-1/2)} + 1/2(\Delta t^{(i+1)} + \Delta t^{(i)})\ddot{U}^{(i)} \quad (2.16)$$

where \dot{U} is the velocity and \ddot{U} is the acceleration, i refers to the increment number and $(i-1/2)$ and $(i+1/2)$ refer to mid-increment numbers.

Correia and Ferron [75] investigated wrinkling initiation in sheet metal forming analytically and numerically using FE ABAQUS/Explicit. The results were compared with the results of experimental work from the literature, and both analytical and simulation results gave good agreement. Waston and Long [76] used the commercial software ABAQUS/Explicit to investigate wrinkling failure mechanics, the results show that process parameter and material properties are important factors affecting wrinkling. Usually, implicit and explicit FEA codes are used for simulation of sheet metal forming. Figure 2.38 shows the use of implicit and explicit codes.

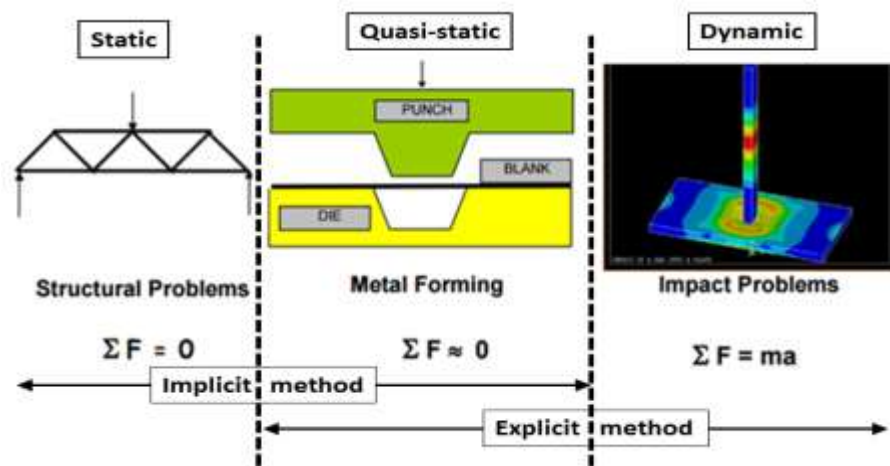


Figure 2.38 Use of implicit and explicit code in sheet metal forming

Abaqus/Standard is more efficient for solving smooth nonlinear problems; on the other hand, Abaqus/Explicit is the clear choice for a wave propagation analysis. There are, however, certain static or quasi-static problems that can be simulated well with either program. Typically, these are problems that would usually be solved with Abaqus/Standard but may have difficulty converging because of contact or material complexities, resulting in a large number of iterations. Such analyses are expensive in Abaqus/Standard, because each iteration requires a large set of linear equations to be solved. While Abaqus/Standard must iterate to determine the solution to a nonlinear problem, Abaqus/Explicit determines the solution without iterating by explicitly advancing the kinematic state from the previous

increment. Even though a given analysis may require a large number of time increments using the explicit method, the analysis can be more efficient in Abaqus/Explicit if the same analysis in Abaqus/Standard requires a large number of iterations. Another advantage of Abaqus/Explicit is that it requires much less disk space and memory than Abaqus/Standard for the same simulation. For problems in which the computational cost of the two programs may be comparable, the substantial disk space and memory savings of Abaqus/Explicit make it attractive [77]. For these reasons, ABAQUS/ Explicit was chosen to simulate the multi-point forming process which includes complicated contact problems.

2.5 Summary and research gaps

This chapter has outlined essential elements of sheet metal forming using a multi-point forming tool, for instance, reconfigurable pin tooling geometry, surface regularity, and has considered dimpling and wrinkling as multi-point forming defects, and corresponding analytic approaches. It was found from the literature that:

1. Multi-point forming tooling with pins of 10 mm or less has not been investigated. Therefore, the current study will develop a multi-point forming tool with 10 mm square pin dimension.
2. The literature review revealed that optimisation of process parameters has not been done. The current study will optimise the process parameters including elastic cushion thickness, pin size, coefficient of friction, and radius of curvature.
3. From the literature review, it is clear that many researchers have investigated wrinkling and most of those researchers used a solid die, however, the relation between wrinkling and thickness variation has not been investigated. Therefore, the current study will investigate the relation between wrinkling and thickness variation using a multi-point forming die.

4. Based on the literature review, and for those reasons mentioned in Section 2.4.2.3, the explicit FE method will be used for the sheet metal forming simulation and the wrinkling analysis.

Chapter 3

MULTI-POINT FORMING TOOLING DEVELOPMENT AND MEASUREMENT APPARATUS

This chapter presents the development of multi-point metal forming (MPF) tooling used to press hemispherical parts with different radii of curvature. Defects can occur during sheet metal forming when using MPF tooling, i.e., dimpling and wrinkling, as described in Chapter 2. These defects are influenced by a number of parameters as discussed in the literature review, some of them relate to the properties of the sheet material such as strength of material, sheet thickness and other dimensions, while others relate to tool geometry including pin size, pin tip radius, distance between adjacent pins and radius of curvature part, which should all be taken into account in the design of the forming tooling.

Thus, the main purpose of developed die is to validate the numerical analysis in this study, so that the influences of these factors on the phenomenon of wrinkling can be studied. The minimum and maximum die radii and blank holder force need to be taken into the account during the design of the forming die. The multi-point forming tooling was to be fixed on the 4 Column Downstroke Hydraulic Press in the Mechanical Laboratory in the School of Mechanical Engineering at the University of Birmingham, and the features of this machine were taken into consideration in the design of the tool. The main components of tooling are; the pins, upper base plate, lower base plate, blank holder, pin support, pin fixing sheet and guides, see Figure 3.1 and Figure 3.2.

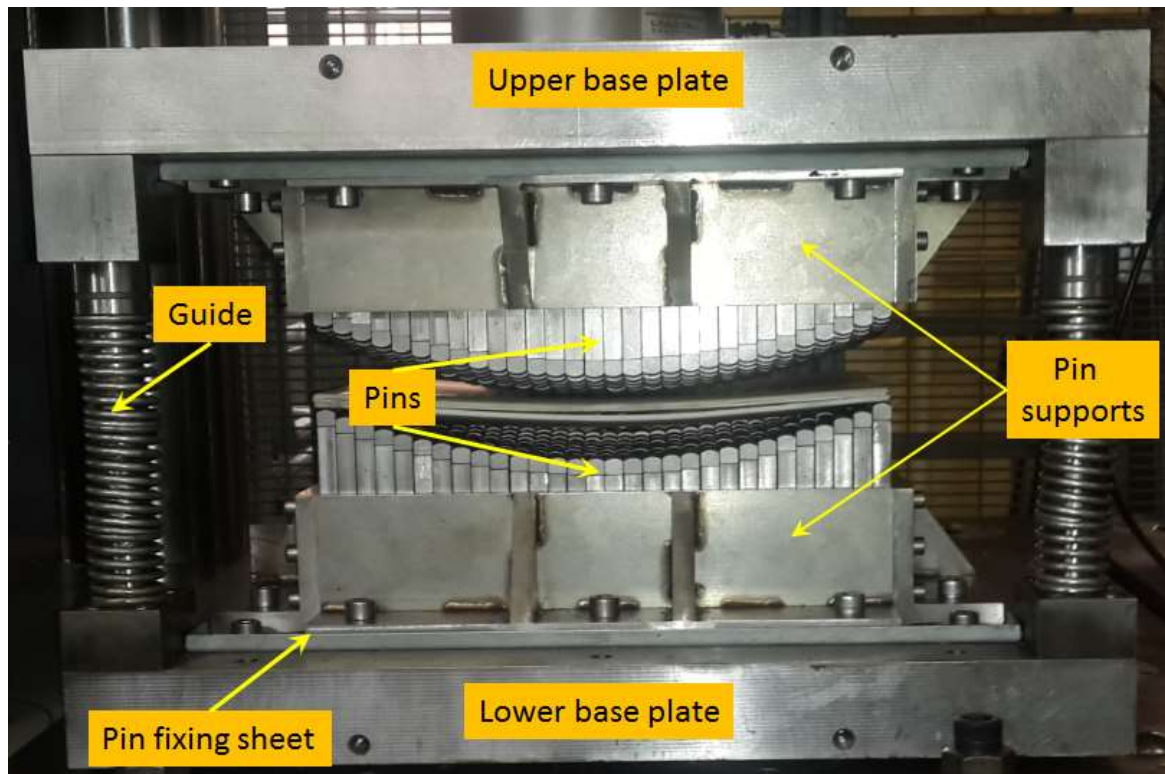


Figure 3.1 Sheet metal forming tooling model without blank holder

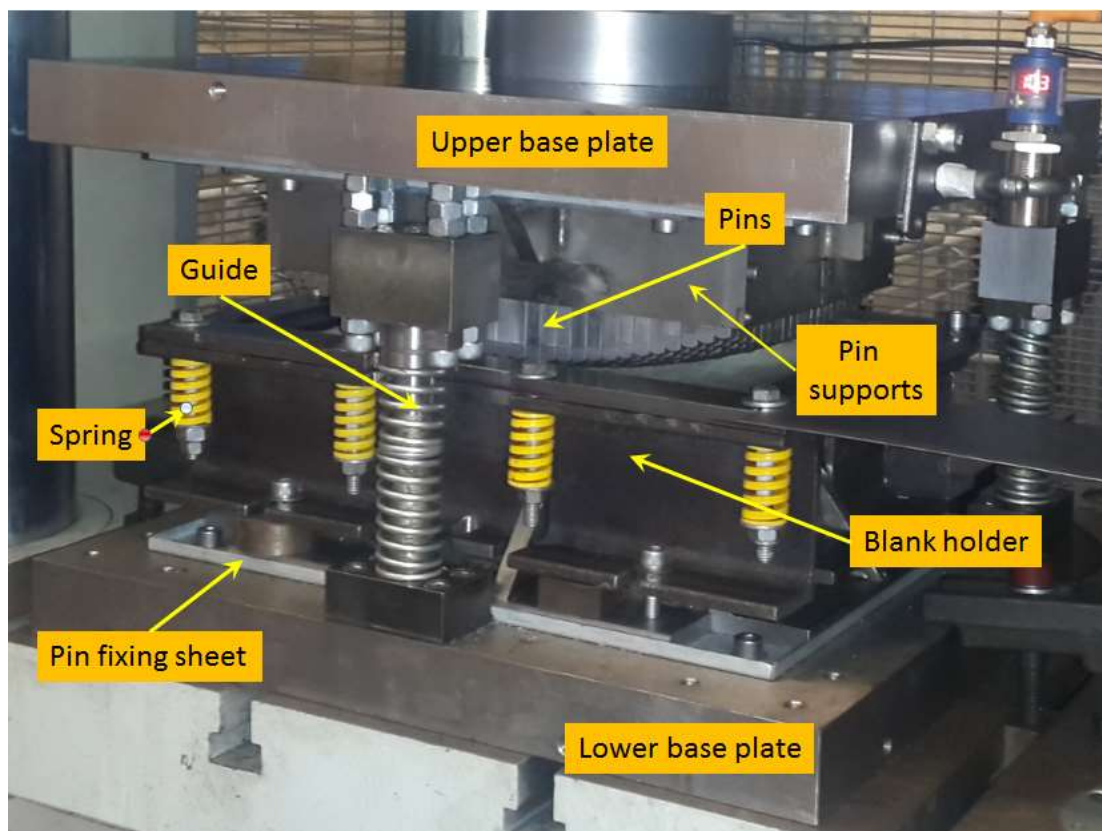
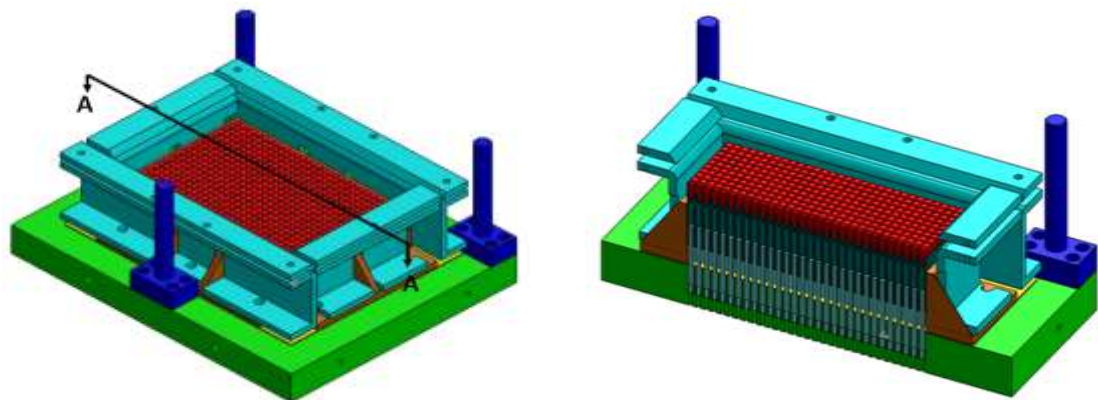


Figure 3.2 Sheet metal forming tooling model with blank holder

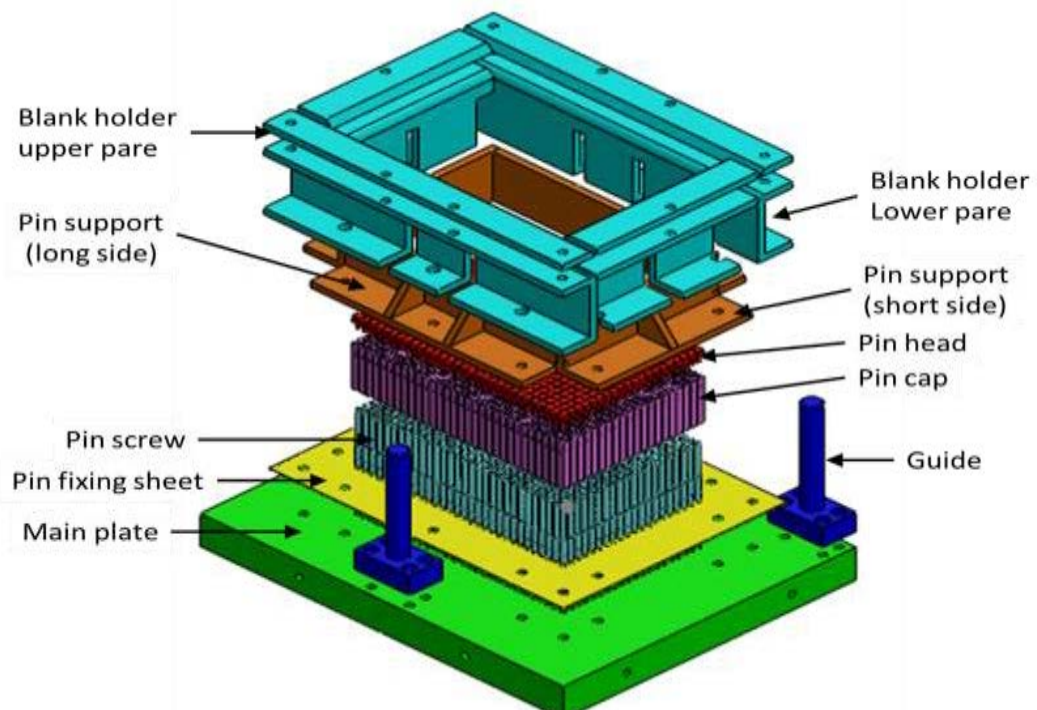
3.1 Flexible die design

In this study, flexible tooling is, basically, composed of two symmetrical parts; the upper and lower parts. The upper part working as a punch and lower as die, both parts include the same components, which are represented in the the main plate as pins, pin fixing sheet, and pin support. Figure 3.3 a, and b presents drawings of the main components of the assembled and disassembled tool and blank holder.



a- Assembled tool

Cross section A-A



b- Disassembled tool

Figure 3.3 Tool components assembled and disassembled

3.1.1 Pins

The pins are movable in a flexible tool; they move perpendicular on the main plate and compose the tool surface. In this case the pin height is adjusted by a screwing motion between the pin screw and cap, controlled by the number of revolutions of the screw. The pin consists of three parts; pin tip, pin cap, and pin screw. Figure 3.4 shows the pin tip. The tip radius is 10 mm, the pin cross-section is square cross section, of dimension 10 mm, and the length of the body of the pin is 80mm. The pin tip connects with the pin cap via a circular peg of 6 mm diameter, and 10 mm length, and the fit type is interference.

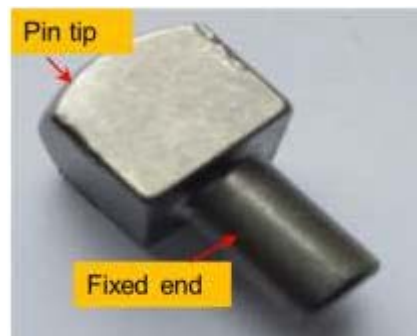


Figure 3.4 Pin tip

Figure 3.5 shows the shape of the pin cap, which is of square 10 mm cross-section and 70 mm length. A hole with 6 mm diameter and 11 mm depth is machined into the upper surface to fit the peg of the pin tip, and an internal thread M6 x 0.75, 55 mm deep is machined on the lower face to connect the pin cap with the pin screw, which is used to control the pin height. A 1 mm hole was machined on the cap pin side to release the air during pin adjustment.



Figure 3.5 Pin cap

Figure 3.6 shows the pin screw. The total length of pin screw is 85 mm, of which 50 mm has M6 x 0.75 external thread. On the other end of the pin screw is an internal thread of M5 x 0.8 (i.e. 8 mm diameter) into which fits a male threaded bolt with internal hexagonal head nut, which is used to for pin adjustment.



Figure 3.6 Pin screw

3.1.2 Main plate

The principal design of the main plate depends on the number of pins, dimensions of the pins and the distance between adjacent pins - which controls the distance between the centres of the holes in the main plate. The number of pins within a fixed forming area of a flexible tool is determined by the pin cross-section. For 600 pins of cross-section 10 mm x 10 mm arranged as 30 pins x 20 pins with clearance between two adjacent pins of 0.25 mm, the distance between hole centres is 10.25 mm. Figure 3.7 shows of the main plate, note the diameter of the holes are 8 mm and there are, of course, 600 holes. The forming die area as measured to the outside of the outer rows of holes is 307.25 x 204.75 mm².



Figure 3.7 Main plate

As shown in Figure 3.7, there were twenty-six M10 screw holes machined into the face of the main plate to fix pins supports, pins fixing sheet, blank holder and punch motion guides.

3.1.3 Pin support

The pin support is the side frame used to maintain the formation of the pin arrays and prevent pin bending due to any inclined component of the forming force. The forming force is not distributed uniformly over the pins but varies in magnitude and direction, especially for the outer pins which are loaded by inclined force F , see Figure 3.8, which has a horizontal component $F \cos \theta$. This force acts to bend the pins so the pin support must be capable of resisting at least this magnitude of horizontal force.

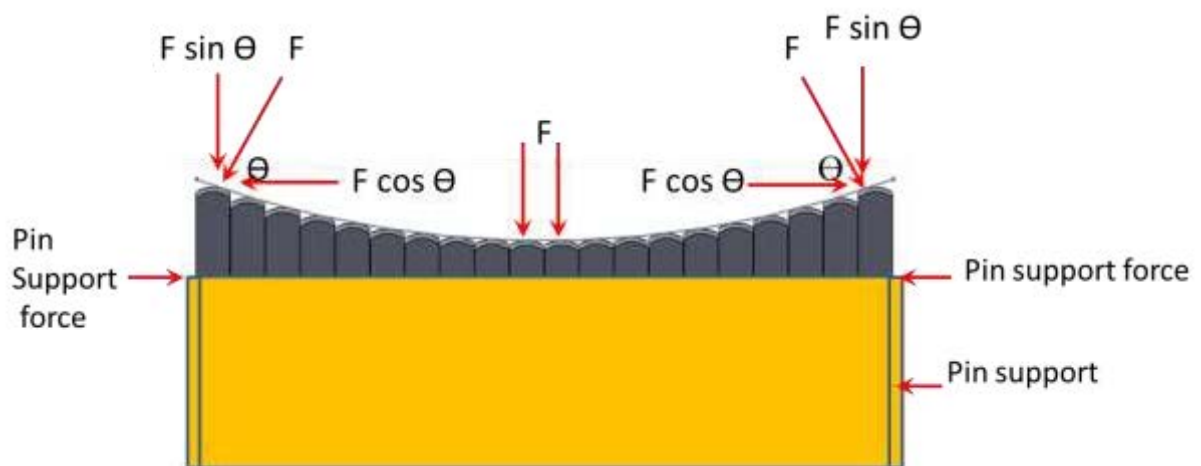
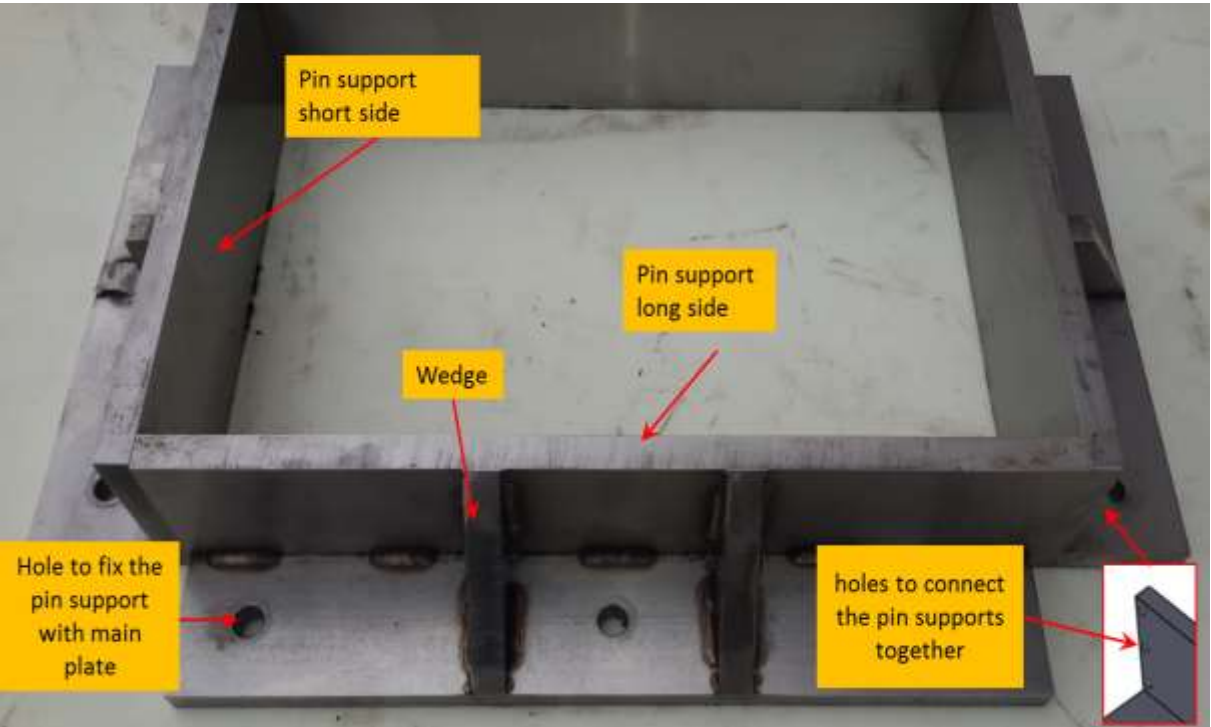


Figure 3.8 Forces acting on tool pins

Figure 3.9 shows the shape of the pin support for both short and long sides of the tool. The short sides of the pin support consist essentially of two rectangular plates and one wedge; the main dimensions of the two rectangular plates are 224.75 mm long and 10 mm thick. One is 65 mm width and the other is 50 mm width and one wedge for each side which is 65 mm high x 50 mm long x 10 mm thick as Figure 3.10 is shown. The pin supports for the long sides consist of two rectangular plates each 307.25 mm long and 10 mm thick, one being 65 mm width and the other being 60 mm width, and two wedges of height 65 mm x 50 mm depth x 10 mm thick behind each side as

Figure 3.10 is shown. Also Figure 3.10 shows that on each end of the short sides of the pin support there are three through holes of 5 mm diameter for bolts to connect the short and long sides together, and two through holes of 10 mm diameter for bolts to fix the short side pin support to the main plate. Figure 3.10 also shows than on the long sides of the pin supports there are six M5 holes to connect the pin supports together, and three through holes to fix each long side pin support to the main plate. More details are given in Appendix A.



Pins support short side



Pin support long side

Figure 3.9 Pin supports

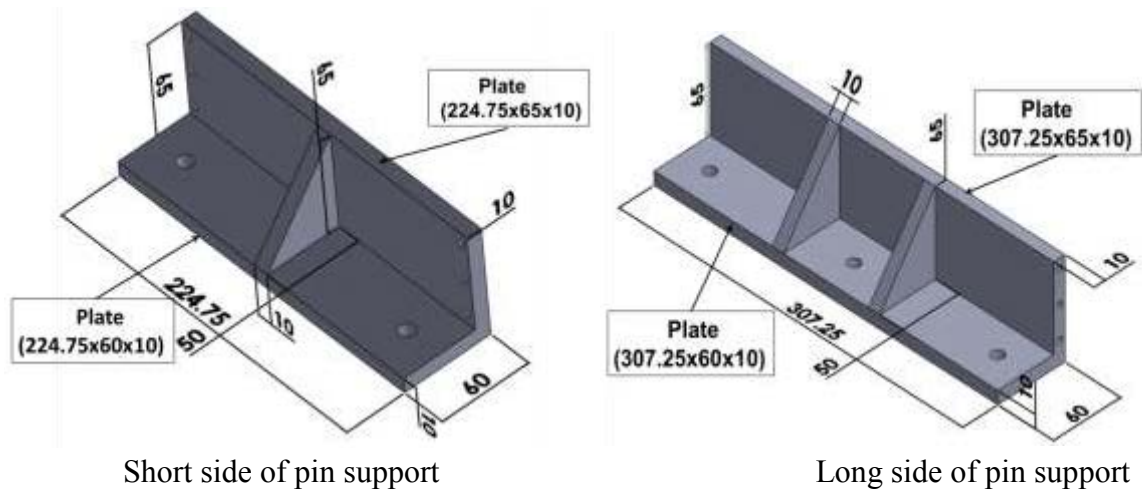


Figure 3.10 Drawing for short and long pin supports

3.1.4 Pin fixing sheet

A pin fixing sheet is used to fix the pins into the holes in the main plate for both halves of the tool. Figure 3.11 shows the pin fixing sheet with 600 through holes of 6 mm diameter machined to accept the threaded end of the pins, the diameter of these holes is less than the diameter of the non-threaded end of the pins, thus the pin fixing sheet retains the pins in the holes. The main dimensions of the pin fixing sheet are given in Appendix A.



Figure 3.11 Pin fixing sheet

3.2 Blank holder

The blank holder design is shown schematically in Figure 3.12. The blank holder consists of two parts, an upper part and a lower part. The upper part is connected with the lower part using 10 bolts with 10 springs to generate the force required to clamp the sheet. The bolts were placed to obtain an equal pressure distribution. The upper internal edge of the lower part was machined as a 5 mm curve to make the sheet metal flow more easily. All pieces of the upper part were welded together and lower part too.

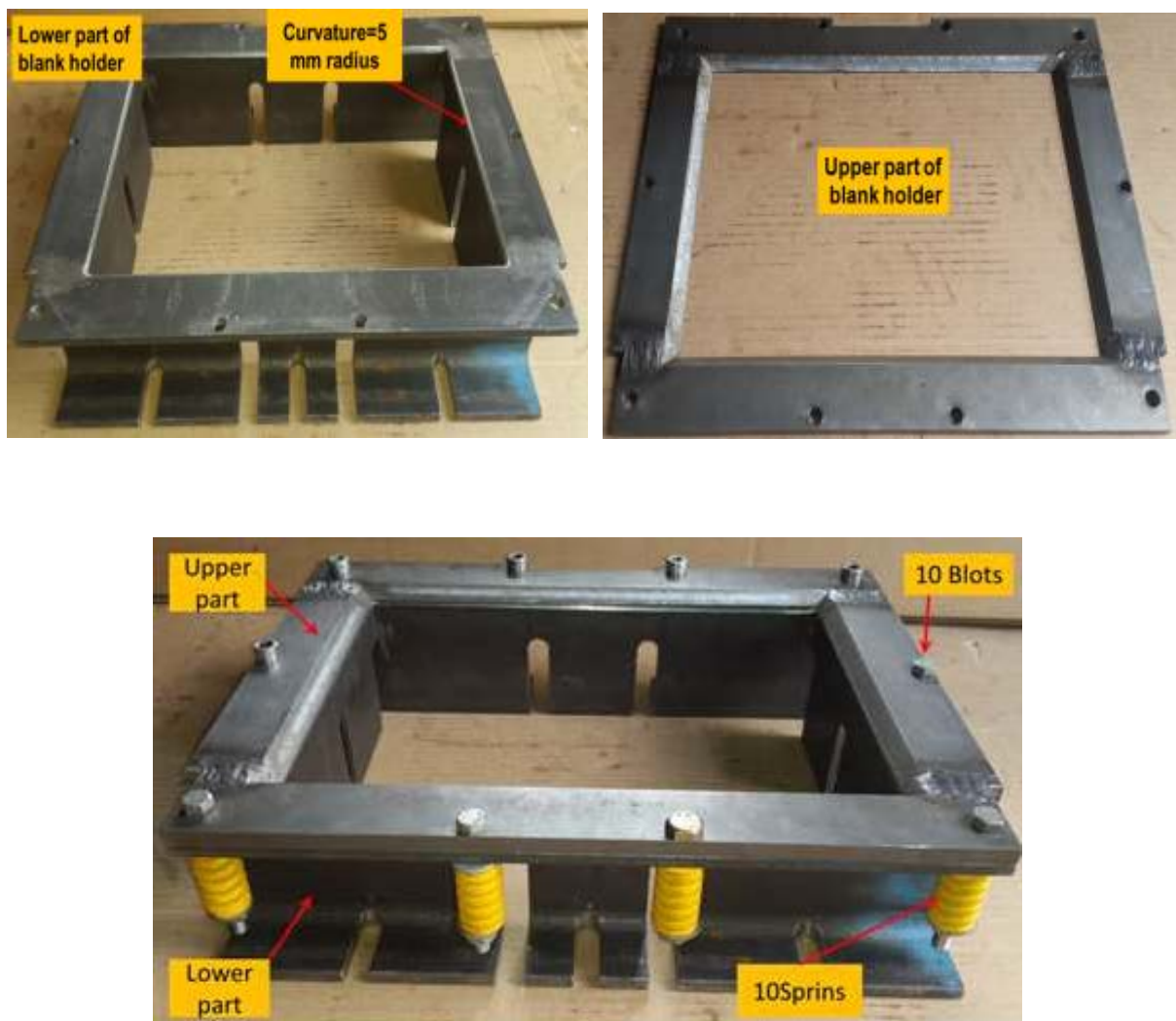


Figure 3.12 Blank holder

3.3 The guide

Guide pins are used to ensure alignment between the upper and lower halves of the die set. These provide for alignment of the two halves during the forming process, and are usually fabricated of hardened tool steel. The guide consists of two parts, a pin attached to the lower part of the tool and pin guide attached to the upper part of the tool, see Figure 3.13 which shows the main parts of the guide [78].

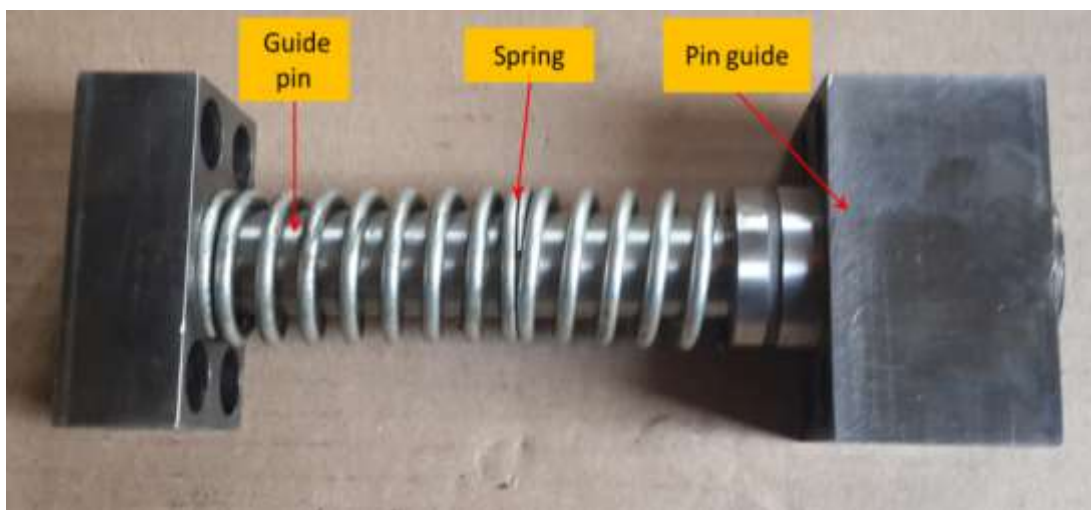
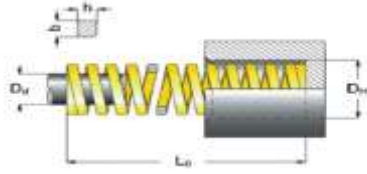


Figure 3.13 Main parts of pin guide

3.4 The springs

In this study, 10 steel die springs - extra heavy load from Cromwell with external diameter 26mm and length 44mm were used to generate the blank holder force by rotating the bolt and compressing the spring. **Error! Reference source not found.** and Figure 3.14 provide details of the springs. A washer was placed between the spring top and the bolt head. The force clamping the upper part of the blank holder to the lower part thus clamped the sheet to be formed.

Table β-1 Specification of steel die springs from Cromwell with external diameter 26mm and length 44mm [79]

				
External diameter (D_H) mm	Inner diameter (mm)	Free length (L_0) mm	Spring rigidity (N/mm)	Spring weight (g)
26	12.5	44	244	70

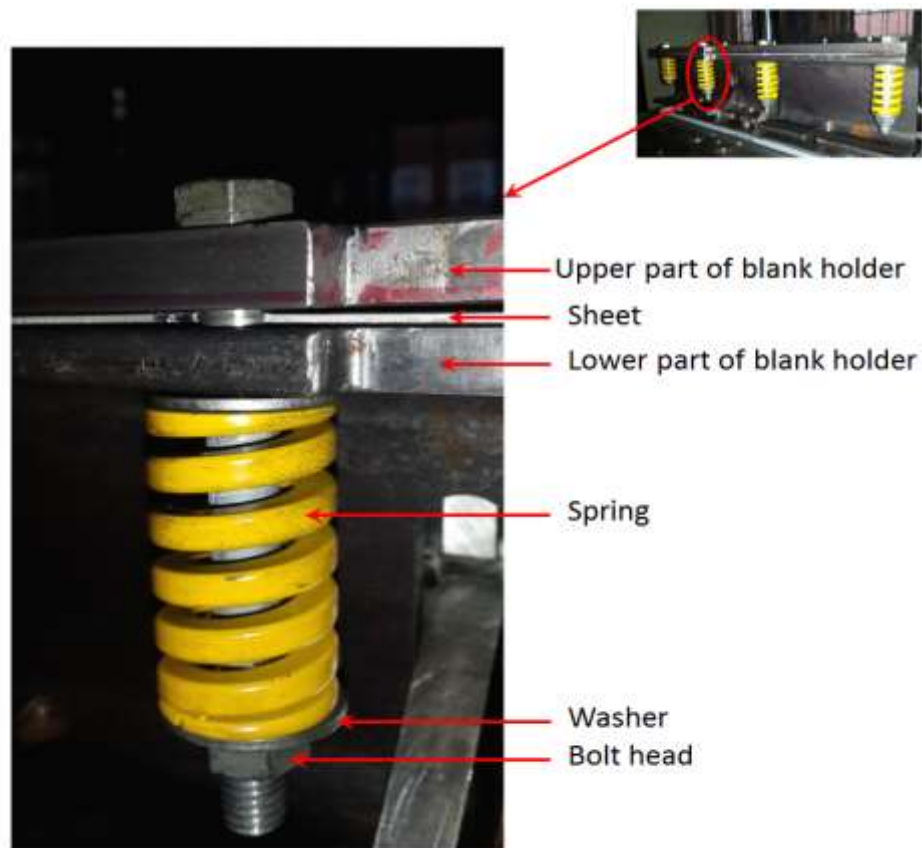


Figure β.14 Spring on blank holder

The Instron universal testing machine was used to measure the spring rigidity. It was found the spring rigidity (compressed 1 mm) is 244 N/mm, which was as stated by the supplier. For example, to generate a 15 kN blank holder force each spring would be compressed by 6.15 mm, and the total force for 10 springs is equal 15000 N (15 kN).

3.5 Specification of press machine

The four columns downstroke hydraulic press E200 from Mackey Bowley used in the experimental work was a 400 tonnes downstroke press of four columns construction with auto-control. The press provided a central punch ram of 200 tonnes and clamp table fitted with four 50 tonne rams.

Figure 3.15 shows the press, and the main specifications are shown in Table 3-2 [80]

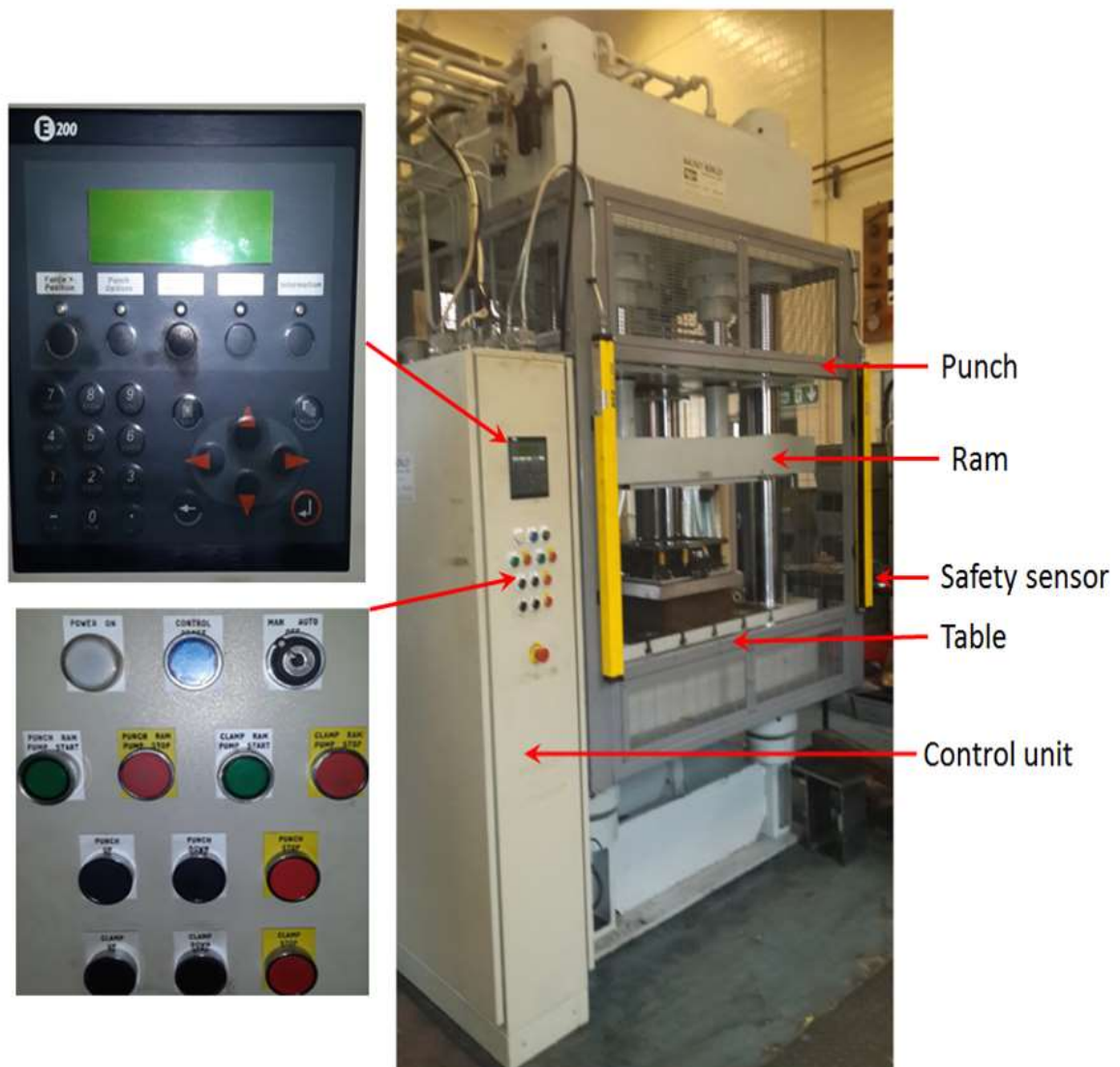


Figure 3.15 The four columns downstroke hydraulic press E200 from Mackey Bowley

Table 3-2 Press specification [80]

Description	Values
Combined maximum press load	400 Tonnes
Maximum clamp load	200 Tonnes
Minimum clamp load	20 Tonnes
Clamp close speed	5mm/sec to 14 mm/sec
Clamp Press speed	0 -3 mm/sec
Clamp return speed	25 mm/ sec
Punch close speed	5mm/sec to 18 mm/sec
Punch Press speed	0 to 6mm/sec
Punch return speed	30mm/sec
Maximum punch load	200 Tonnes
Minimum punch load	20 Tonnes
Maximum stroke clamp	350mm
Maximum stroke punch	350mm
Table height	1000mm
Bed area	1000mm x 1000mm
Electric motor power	15 kW +7.5 kW

3.6 Specification of data logger, load cell, and distance transducer

The Omega OM-CP-QUADVOLT-30V data logger was used to collect data during the forming process, such as force as a function of time, and distance with time to enable a study of the relation between force and distance. The main specifications of the data logger are stand - alone voltage input, high - resolution, and require low battery power, see Figure 3.16, and Table 3-3. It also allows the user to store user defined engineering units as well as scale factors and offset values. This enables the user to easily linearize and scale any transducer that provides a voltage to any user required units automatically.



Figure 3.16 Omega OM-CP-QUADVOLT-30V data logger

Table 3-3 Omega OM-CP-QUADVOLT-30V data logger specification [81]

Description	Values
Input ranges	OM-CP-QUADVOLT-30V
Input channels	4 channels
Nominal input range	0 to 30
Measurement range	-2.0 to 32.0 V
Resolution	1.0 mV
Accuracy	±0.1% FSR
Input impedance	>10kΩ
Overload protection	±48 V
Software	XP SP3/Vista and 7 (32-bit and 64-bit)
Operating environment	-40 to 80°C (-40 to 176°F)

A Low Profile Load Cell 100kN, see Figure 3.17 and Table 3-4, was used to measure and record force values with time during the forming process and store it on a computer. The output of the load cell was fed directly to a computer via the USB port using an in-line load cell amplifiers and load cell USB [82]. Power to the load cell is supplied by the USB port, so that no external power supply was needed. The data can be viewed and logged on the computer using Word Excel.

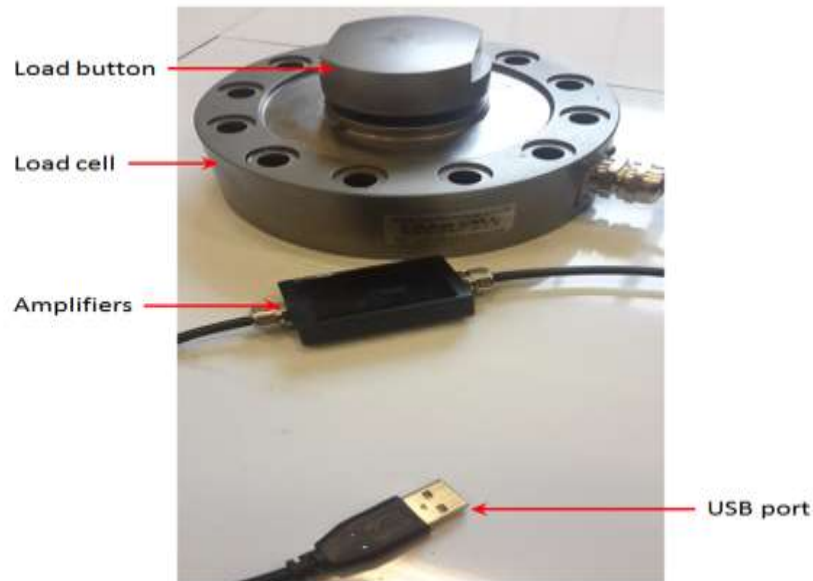


Figure 3.17 Load cell

Table 3-4 Specification of load cell [83]

Description	Values
Standard range	0 - 100 kN
Excitation voltage	10V (normal), 15V (maximum) DC
Sensitivity	2 mV/V (nominal)
Electric connection	Connector - Amphenol MIL Spec, or 2 m integral screened cable

The micro-sonic distance transducer (mic+25/IU/TC) was used to determine the punch position with time during the forming process. The distance transducer was fixed on the upper part of die using the holder and connected with the data logger using connected cable-M12 as shown in Figure 3.18.

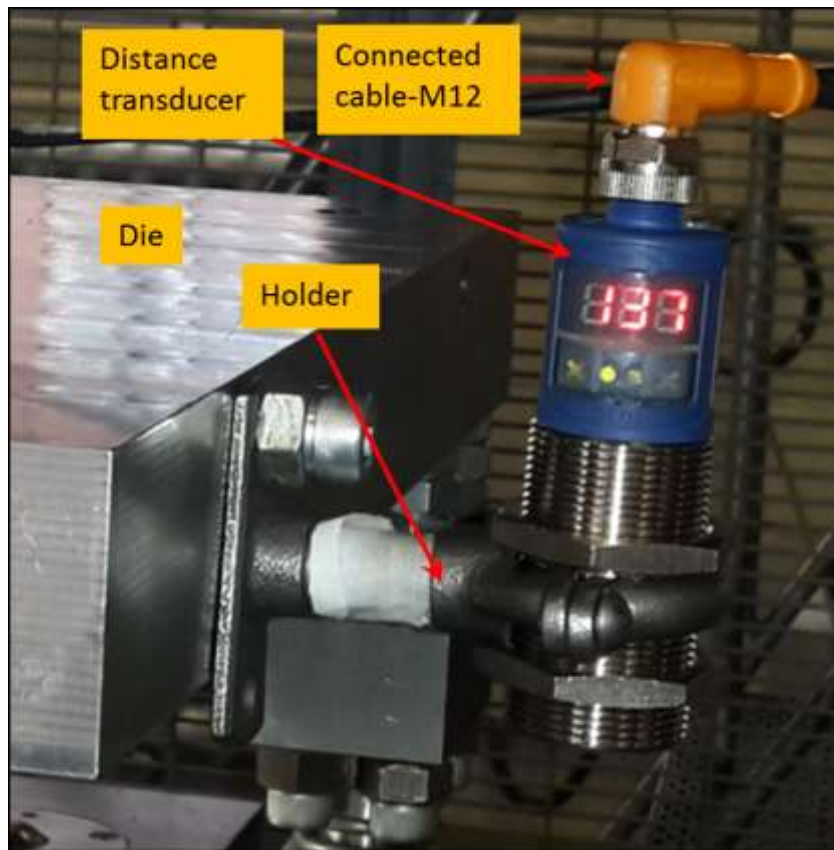


Figure 3.18 Distance transducer position on tool

The technical specification of micro-sonic distance transducer (mic+25/IU/TC) is shown in Table 3-5.

Table 3-5 Distance transducer specifications [84]

Description	Values
Operating range	30 - 350 mm
Design cylindrical	M30
Operating mode	Analogue distance measurements
Means of measurement	Echo propagation time measurement
Transducer frequency	320 kHz
Blind zone	30 mm
Operating range	250 mm
Maximum range	350 mm
Resolution/sampling rate	0.025 mm to 0.10 mm/ depending on the analogue window
Accuracy	$\pm 1 \%$
Operating voltage U_B	9 - 30 V d.c, reverse polarity protection
Voltage ripple	$\pm 10 \%$
Type of connection	= 5-pin M12 initiator plug

3.7 Master curves

To prepare for the experimental work, the press should be set up with the multi-point forming tool set for a specific shape using a master curve fabricated using a 3-D printer. The dimensions of the master curve take into account the thickness of the elastic cushion after compression. Figure 3.19 shows the two master curves used to set up the tool.

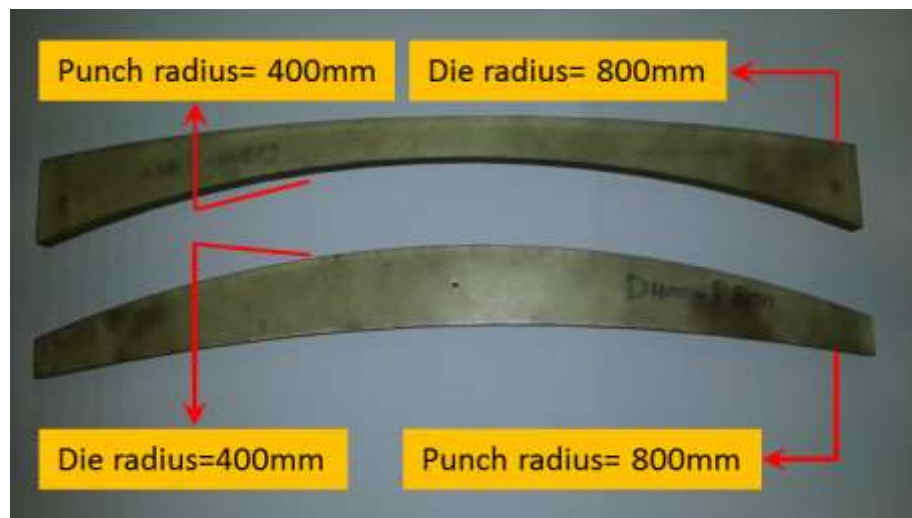


Figure 3.19 Master curves

3.8 Faro arm (3-D laser scanner)

A Faro arm (3-D laser scanner) as shown in Figure 3.20 was used to scan the deformed parts after the multi-point stamping process to build a 3-D representation of the surface. This representation was used to evaluate wrinkling waves, form profile, and thickness variation. A small vice was used to hold the specimen for scanning, as shown in Figure 3.20. The machine resolution is 0.025 mm which is sufficient for this kind of application [85]. The machine was calibrated prior to each test to minimise measurements errors.

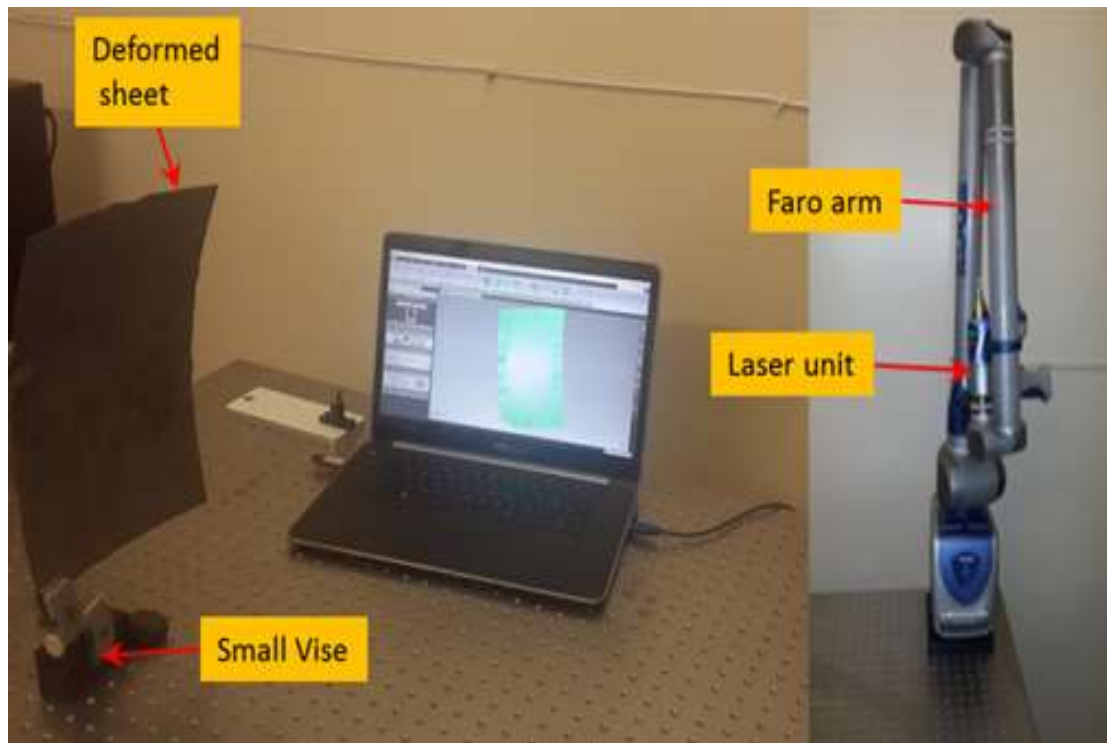


Figure 3.20 3D laser scanner

3.9 Summary

The main elements of the multi-point forming tool and apparatus specifications have been presented in this chapter. The description of the individual tool parts such as pin, main plate, pin support and plate holder have been shown in several figures, and more details about the dimensions of die parts are given in Appendix A. The features of the press, data logger, load cell and distance transducer have been listed and a short description given of the Faro arm 3-D laser scanner, used to scan the formed parts and produce a 3-D representation in order to study forming profile, wrinkling and thickness variation.

CHAPTER 4

DETERMINATION OF THE MECHANICAL PROPERTIES OF SHEET

MATERIALS AND PROCESS MODELLING

This chapter describes the tests that have been carried out to determine the material properties and behaviour (plastic anisotropy) of DC05 steel and 5251-O Aluminium materials, and also the mechanical properties of elastic cushion material under tensile load in a uniaxial compression test. It also describes the numerical simulation of the effect of certain of the process parameters which offers the opportunity for improving product quality and minimising defects.

The mechanical tests were performed using a Zwick tensile test machine in the Metallurgy and Materials Department - University of Birmingham. Different samples were cut at different angles regarding the material orientation (0° , 45° , and 90°) as shown in Figure 4.1 is shown, and sets of uniaxial tensile tests were carried out.

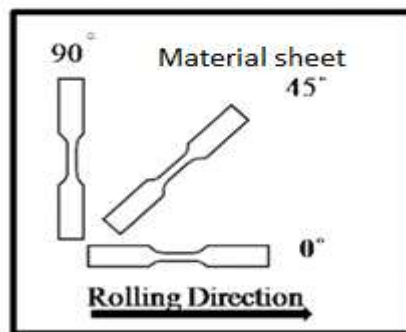


Figure 4.1 Samples cutting directions

Two sheets of materials were used in this investigation, 1 mm thick DC05 steel sheet and 1.25 mm thick 5251-O aluminium sheet. The DC05 steel sheet was considered representative of medium strength materials and the aluminium sheet representative of low strength materials. The experimental results will be incorporated into the FE models to

represent the material properties of these two materials and numerical modelling should then be able to provide important details of the deformation process that are not obtainable from experimental work. These details may then be used to reduce manufacturing costs.

The numerical study of sheet forming using the multi-point stamping forming technique was carried out using ABAQUS software on the central computer (blue bear). This has high-power computing facilities to complete the 3-D simulation models. For accuracy of the numerical outcomes, information on the materials being pressed, the movement of the punch, coefficient of friction (between metal sheet and elastic cushion, and pins and elastic cushion) and interaction between surfaces should all be precisely defined, thus, the mechanical properties of the given system need to be experimentally determined. The main objectives of this chapter are:

1. Determine mechanical properties of DC05 steel sheet and 5251-O aluminium sheet, such as the yield stress (σ_Y), the ultimate stress (σ_{UTS}) and the elongation (ΔL).
2. Determine the plastic anisotropy r_0 , r_{45} , and r_{90} in order to calculate the normal anisotropy coefficient (R_a) of DC05 steel sheet and 5251-O aluminium sheet.
3. Determine the behaviour of the elastic material which will be used as an elastic cushion.
4. Develop FE model for multi-point stamping forming in order to study the effects of a number of parameters on the forming force.
5. Determine a suitable blank holder force to eliminate flange wrinkling.
6. Study the effect of the gap between the die and blank holder on sheet thickness distribution.
7. Reduce the corner defect in double curved shapes, and assess the reducing process effect on thickness distribution

8. Study the effect of pin size, radius of curvature, elastic cushion thickness, and coefficient of friction on product quality, which is represented by the degree of wrinkling, shape accuracy and sheet thickness.

4.1 Determination of the mechanical properties of sheet materials

The specification of the tensile test machine used for the experimental work, the test specimen preparation, and the methodology of the uniaxial tensile test of metal sheets and uniaxial compression tests of polyurethane, and the anisotropy test metal sheets are explained in Appendix B.

Figure 4.2 shows the stress flow for DC05 steel sheet and 5251-O aluminium sheet which are to be used for the experimental work. The yield stress found for DC05 was about 210 MPa. For 5251-O aluminium, the yield stress was about 105 MPa. Figure 4.3 shows a comparison between yield stress and ultimate tensile stress for DC05 and 5251-O aluminium sheet materials at 0° , 45° , and 90° orientations. It can be observed that there is a big difference in yield stress and ultimate tensile stress between steel and aluminium sheet. From Figure 4.4, the aluminium sheet has the lower elongation which is equal to about 20%, while the higher elongation was for the steel sheet and equal to about 37%. The behaviour of materials was normal, nevertheless there was some fluctuation in aluminium stress –strain curve, which is called the Portevin-Le Chatelier effect (PLC effect). This variation in the stress-strain curve is normal in Al-Mg alloys [86-88], but it can effect material formability [89].

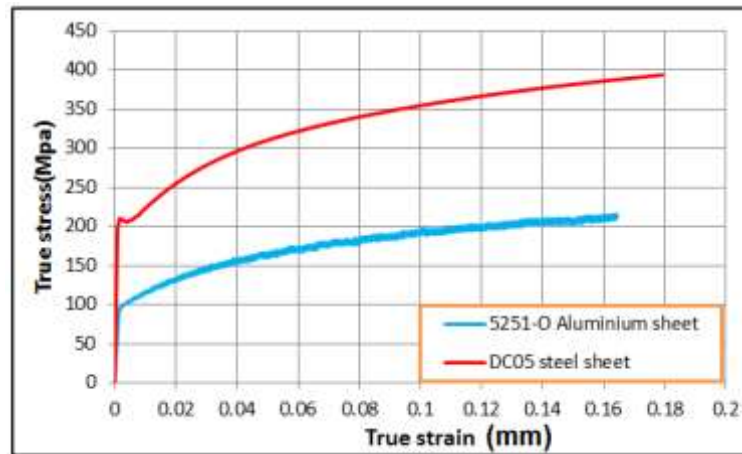


Figure 4.2 Stress-strain curves for DC05 steel and Aluminium 5251-O

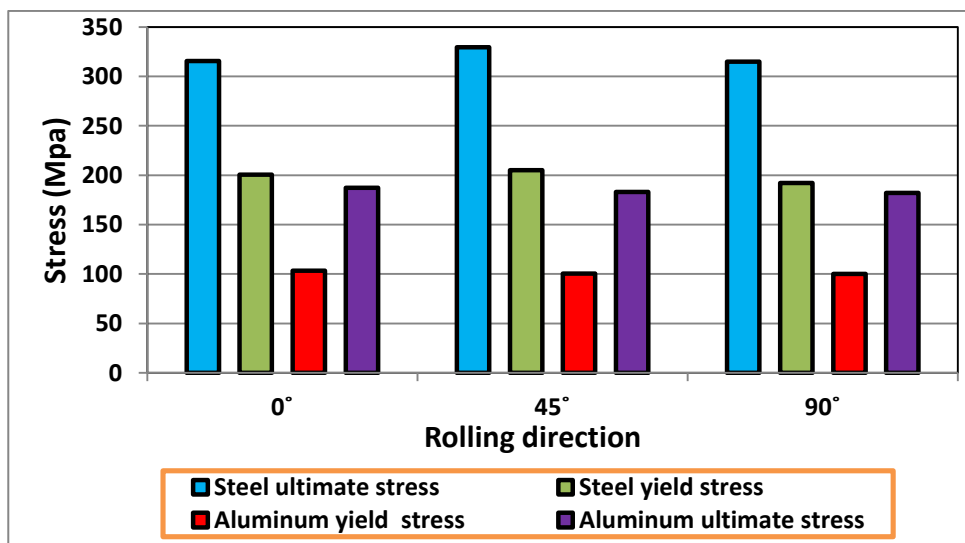


Figure 4.3 Yield stress and ultimate tensile stress for DC05 steel and aluminium 5251-O at 0°, 45°, and 90° to the rolling orientation

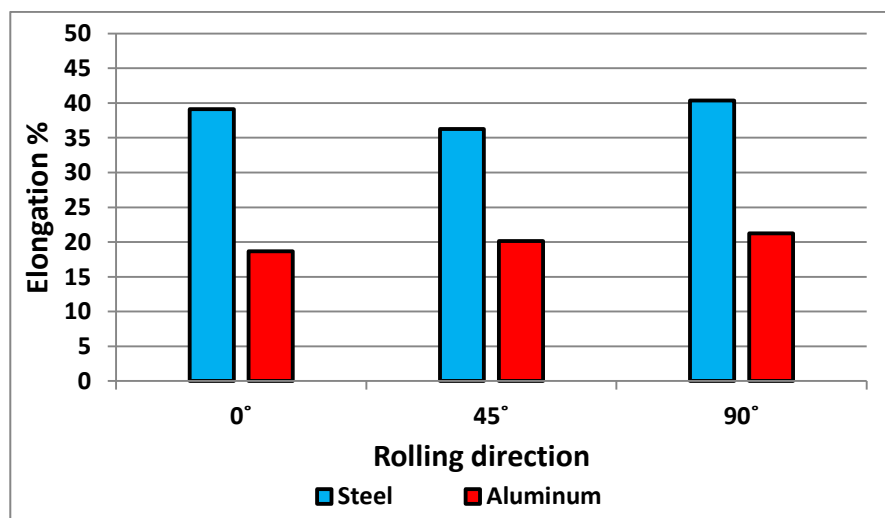


Figure 4.4 Elongation for DC05 steel and 5251-O aluminium at 0°, 45°, and 90° to the rolling orientation

Table 4-1 and Table 4-2 show plastic anisotropy (r) in three directions and the normal anisotropy coefficient (R_a) of DC05 steel and 5251-O aluminium sheets. It can be observed that the normal anisotropy of steel is greater than unity, while for aluminium it is less than unity. Thus, the risk of thinning of aluminium sheet is greater than the risk of thinning for steel sheet that is the ability to form aluminium sheet is less than for steel sheet. The values of plastic anisotropy r_0 , r_{45} , and r_{90} may be used as a guide to a suitable cutting direction for the steel and aluminium sheets to be used in the forming process.

Table 4-1 R_a in rolling, 0° , 45° and 90° orientations for DC05 steel

Orientation	No of samples	$r_a = \frac{\epsilon_w}{\epsilon_t}$	Average (r_a)	$R_a = \frac{r_0 + 2r_{45} + r_{90}}{4}$
0°	1 2	1.723 1.655	1.689	1.156
45°	1 2	0.831 0.810	0.821	
90°	1 2	1.205 1.381	1.293	

Table 4-2 R_a in rolling, 0° , 45° and 90° orientations for aluminium 5251-O

Orientation	No of samples	$r_a = \frac{\epsilon_w}{\epsilon_t}$	Average(r_a)	$R_a = \frac{r_0 + 2r_{45} + r_{90}}{4}$
0°	1 2	0.605 0.573	0.589	0.569
45°	1 2	0.521 0.533	0.527	
90°	1 2	0.604 0.668	0.636	

Figure 4.5 presents the flow stress for polyurethane A-90 calculated from experimental test results.

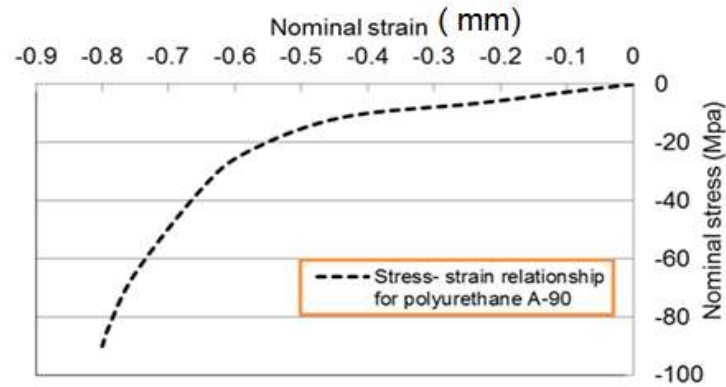


Figure 4.5 Nominal compression stress – strain relationship for polyurethane A-90

4.2 Finite element modelling of multi point-forming

4.2.1 Explicit dynamic finite element modelling

The dynamic explicit method is used in the study of the sheet metal forming process. In principle the system is modelled as a simple mass-spring-damper, see Figure 4.6.

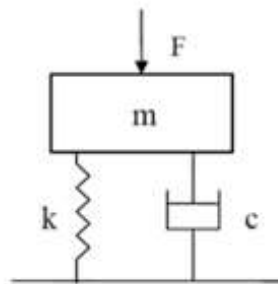


Figure 4.6 Mass-spring-damper system under external force

The free body diagram motion equation of the mass is represented by Equation 4.1

$$m\ddot{u} + c\dot{u} + ku = F(t) \quad (4.1)$$

where m is the mass of the body, c is the coefficient of damping for the damper, k is the spring stiffness, u is the mass displacement measured from the static equilibrium position, \dot{u} is the instantaneous speed of the mass at time t , \ddot{u} is the instantaneous acceleration of the mass at time t , and $F(t)$ is the external force as function of time.

Divided throughout Equation 4.1 by m it becomes,

$$\ddot{u} + 2\zeta\omega\dot{u} + \omega^2u = f(t) \quad (4.2)$$

where

$$\begin{cases} \omega = \sqrt{\frac{k}{m}} \\ \zeta = \frac{c}{(2\sqrt{mk})} \\ f(t) = \frac{F(t)}{m} \end{cases} \quad (4.3)$$

ζ is a factor of viscous damping, ω is the undamped natural frequency. The state of the system depends on ζ . If $\zeta > 1$, the system is over damped, the system is under damped if $\zeta < 1$ and critically damped if $\zeta = 1$.

The coefficient of damping is calculated from Equation 4.4

$$c = 2\omega m \quad (4.4)$$

The finite difference method is used to solve Equation 4.1 and it gives:

$$\begin{cases} \ddot{u}^t = \frac{1}{\Delta t^2} (u^{t+\Delta t} - 2u^t + u^{t-\Delta t}) \\ \dot{u}^t = \frac{1}{2\Delta t} (u^{t+\Delta t} - u^{t-\Delta t}) \end{cases} \quad (4.5)$$

The displacement at $(t + \Delta t)$ is found after substituting Equation 4.5 into Equation 4.3.

$$\left[\frac{1}{(\Delta t)^2} m + \frac{1}{2\Delta t} c \right] u^{t+\Delta t} = F(t) - ku^t + \frac{m}{(\Delta t)^2} [2u^t - u^{t-\Delta t}] + \frac{c}{2\Delta t} u^{t-\Delta t} \quad (4.6)$$

In this case, the solution of displacement at time $t + \Delta t$ depends on knowing the displacement at times t and $t - \Delta t$. This is known as the equation of motion with dynamic explicit integration. The important condition is that the time step should be less than the critical time step.

$$\Delta t_{cr} = \frac{T}{\pi} = \frac{2}{\omega} = 2\sqrt{\frac{m}{k}} \quad (4.7)$$

where T is the time period of the system to reach convergence.

Furthermore, for a 3-D deformable body, an inertia term can be added to the virtual work equation which becomes:

$$\int_V T_{ij} \delta u_{ij} dV = \int_A t_i \delta u_i dA - \int_V \rho \ddot{u}_i \delta u_i dV \quad (4.8)$$

where T_{ij} is the stress tensor, u_{ij} is the displacements gradient, \ddot{u}_i is the material acceleration, t_i is the traction vector, δ is the variational operator, and ρ is the density.

The discretization of this equation leads to;

$$[M]\ddot{u}^t = \{F^t\} - \{I^t\} \quad (4.9)$$

where $[M]$ is the consistent mass matrix, $\{F\}$ and $\{I\}$ are the external and internal forces at time t respectively. For stability reason, artificial damping $[C]$ is added to equation 4.9 which becomes;

$$[M]\{\ddot{u}^t\} + [C]\{\dot{u}^t\} = \{F^t\} - \{I^t\} \quad (4.10)$$

Using the central difference method given in equation 4.5 above equation can be time discretized to;

$$\frac{1}{(\Delta t)^2} [M] + \frac{1}{2\Delta t} [C]\{u^{t+\Delta t}\} = \{F^t\} - \{I^t\} + [M] \frac{1}{(\Delta t)^2} (2\{u^t\} - \{u^{t-\Delta t}\}) + \frac{1}{2\Delta t} \{u^{t-\Delta t}\} \quad (4.11)$$

The primary conditions at time (t=0) for nodal displacement, velocities, internal and external forces are given. Nevertheless, the displacement of the nodal at time - Δt , is necessary, and is calculated using:

$$\{u^{-\Delta t}\} = \{u^0\} - \{\dot{u}^0\}\Delta t - \frac{1}{2}\{\ddot{u}^0\}(\Delta t)^2 \quad (4.12)$$

where $\{\ddot{u}^0\}$ is given by

$$[M]\{\ddot{u}^0\} = \{F^0\} - \{I^0\} - [C]\{\dot{u}^0\} \quad (4.13)$$

The diagonal (lumped) matrix $[C]$ is assumed to be the linear combination of the mass matrix and stiffness matrix [90]

$$[C] = c_1[M] + c_2[K] \quad (4.14)$$

where $[M]$ is the lumped matrix and c_2 will be taken as zero because there are difficulties in getting the structure's damping properties. Also, c_1 can be approximated based on critical damping conditions [91]:

$$c_1 = 2\omega \quad (4.15)$$

Instead of $c_2=0$ Schewizerhof and Hallquist [92] suggest modifying equation 4.15 by using the approximation:

$$\{\dot{u}^t\} \approx \left\{ \dot{u}^{t-\frac{\Delta t}{2}} \right\} \quad (4.16)$$

to become,

$$\left(\frac{1}{(\Delta t)^2} [M] \right) \{u^{t+\Delta t}\} = \{F^t\} - \{I^t\} + \left(\frac{[M]}{2\Delta t} - [C] \right) \left(\frac{\{u^t\} - \{u^{t-\Delta t}\}}{\Delta t} \right) \quad (4.17)$$

In the case without damping,

$$\Delta t \leq \frac{2}{\omega_{max}} \quad (4.18)$$

and with damping,

$$\Delta t \leq \frac{2}{\omega_{max}} \left(\sqrt{1 + \zeta^2} - \zeta^2 \right) \quad (4.19)$$

Where ξ is the fraction of critical damping in the highest mode.

For a linear system, Equation 4.19 is valid. However, it can also be used for nonlinear systems such as elasto-plastic metal forming. For non-linear problems, the critical time step is estimated by equation 4.19 to be about 50-80% less than the time computed for the linear system [90]. For each element, the critical time step can be estimated by:

$$\Delta t \leq \frac{L}{c_d} \quad (4.20)$$

where L is the element dimension and c_d is the elastic wave speed of the material calculated from;

$$c_d = \sqrt{\frac{2G(1-\nu)}{(1-2\nu)\rho}} \quad (4.21)$$

The main advantages of the dynamic explicit method are that it is robust and does not consume large quantities of computer time, however, too small a time step can lead to a large number of increments, which make the dynamic explicit method non-applicable. To avoid this problem, and reduce the total process time the punch speed can be exaggerated or material density increased. The mass scaling technique can be used to reduce the computational time due to its significantly reducing the processing times while maintaining an acceptable computational accuracy [77, 93]. In multi-point forming, the mass scaling reduces the simulation time by increasing the density of the material. However, if mass scaling is too large, the inertial forces will affect the accuracy of the solution.

4.2.2 Numerical investigation of multi-point forming

In industry FE modelling has found a place because it can substantially reduce the costs and duration of the design and development process [94]. This is true of the FE modelling of multi-point forming process. The main dimensions of the multi-point forming tool model mentioned in Chapter 3 are used in the numerical investigation to study the wrinkling defect, formed sheet profile, and thickness variation. The DC05 steel sheet is used in this study as a blank material and polyurethane A-90 is used as the elastic cushion to protect the blank surface from dimpling. The mechanical properties of DC05 steel sheet and A-90 polyurethane sheet material were experimentally determined and reported in Section 4.1. When quasi-static forming analyses is used, the rigid bodies are ideally suited for modelling tooling, thus the die and punch were considered as a discrete rigid body [95], and the metal sheet as an elastic-plastic deformable body of homogeneous material, and the elastic cushion as a deformable body of hyper-elastic material [93, 96].

Considering the symmetry of the system, only a quarter of the die was simulated to reduce computation time. Displacement boundary conditions were used to fix the die in the x , y and z directions, and the punch in the x and z directions. In addition, symmetrical boundary conditions were applied to the elastic cushion and metal sheet.

The die and punch were meshed using linear quadrilateral elements (R3D4) with size 1 mm, the steel sheet and elastic cushion were both meshed using 3-D 8-node linear elements (C3D8R). To define the contact of parts one with another, general contact condition was used, this is simple and efficient way of creating interaction between model parts because ABAQUS itself finds and determines where contacts occur [97]. Figure 4.7 shows the FE model.

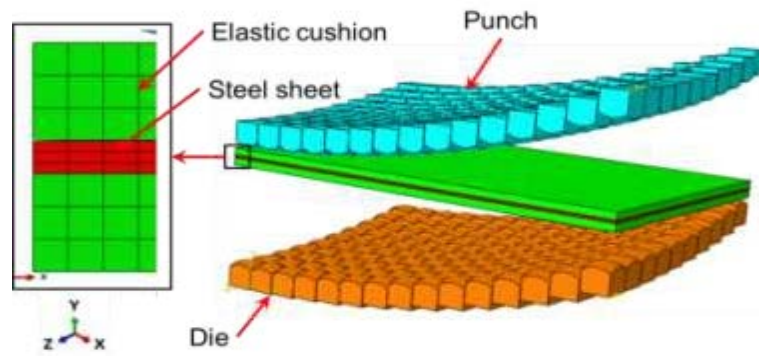


Figure 4.7 Finite element model of tool (Quarter of die)

4.2.2.1 Effect of the element number in sheet thickness on forming force

In this investigation, increasing the number of element in the direction normal to the plane of the steel sheet was undertaken to study the effect of mesh size (the thickness dimension of the mesh) on the forming force. By increasing number of elements across the sheet thickness, it should vary the aspect ratio of the mesh elements (where the aspect ratio is the ratio between its largest and smallest dimension) [98]. The mesh size was changed so that there were, sequentially, one, two and three mesh elements across the thickness of the metal sheet, see Figure 4.7. Figure 4.8 shows the punch forming force distribution in the Y-direction for one, two and three mesh elements across the thickness of the metal sheet. During these simulation tests the mesh element in the elastic cushion was maintained constant with an edge length of 1 mm. Figure 4.9 shows the predicted forming force and simulation time. It can be seen the maximum predicted punch force increased with decreasing thickness of the mesh elements. The maximum forming force for two and three elements were 56.39 kN and 58.67 kN respectively, it can be seen that the force in two cases converged. However, for only one element in the thickness direction, the maximum forming force was 49.36 kN. Thus, the thickness of the sheet was represented by three mesh elements in the model simulation for formed metal sheet, because the difference between the force values is small and was reasonable simulation time in cases of two and three elements.



Figure 4.8 Punch force distribution in Y-direction with different numbers of mesh elements in the thickness direction of sheet

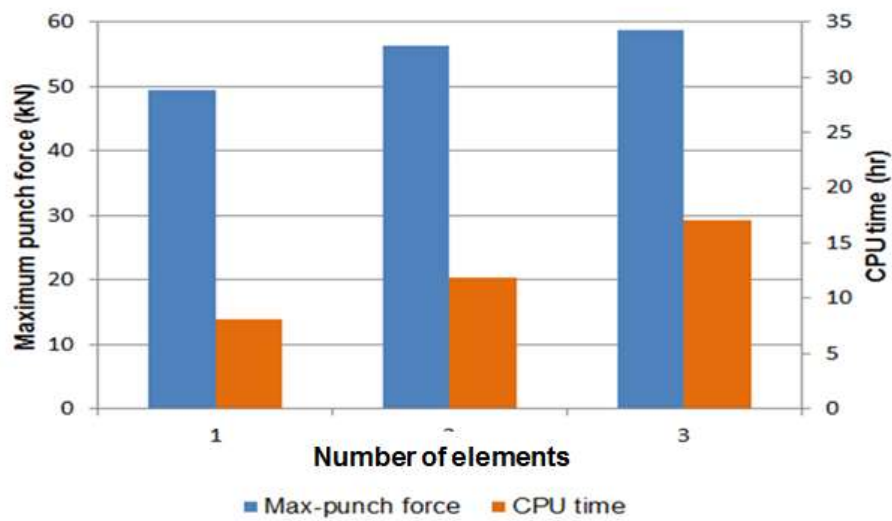


Figure 4.9 Effect of mesh element size on the maximum force and simulation time.

4.2.2.2 Reliability of numerical model

To ensure the validity of the FE model it is necessary to carry out an assessment of the stability of the numerical solution to ensure that the solution is close to quasi-static conditions. To be considered reliable the FE model must have artificial strain energy (ALLAE) and kinetic energy (ALLKE) less than the internal energy (ALLIE), at no more

than 10% of the internal energy, and the kinetic energy curve must be free of any fluctuations [99, 100]. Figure 4.10 shows the maximum values of ALLAR is 7.8%, and ALLKE is 0.7% of internal energy. Both energy parameters are within the suggested limit.

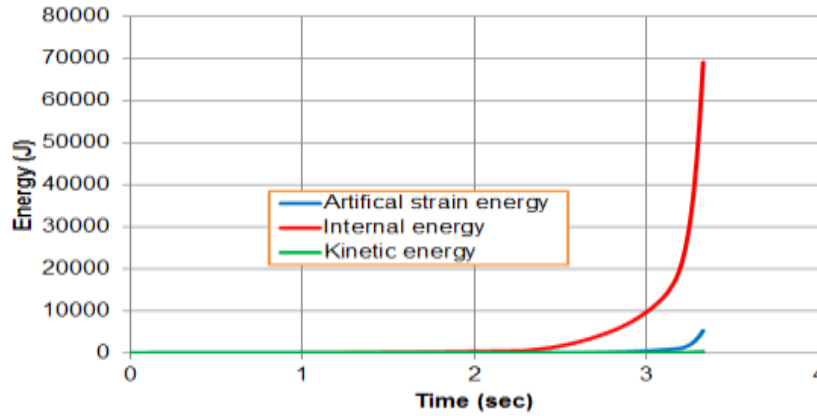


Figure 4.10 The energy curves of finite element solution

4.2.3 FE modelling of MPF using blank holder

In the forming of sheet metal by stamping a blank holder is used to reduce or eliminate wrinkling and improve shape quality. In the stamping process, a punch pushes a portion of the metal sheet into the die cavity until it takes its final shape. As a result of the forming process the pressed sheet assumes its radius of curvature, and wrinkling defects can emerge, especially in the middle of the edges and particularly at small radii of curvature such as 400 mm. To produce good quality parts, there should be control of material flow during the forming process, this is obtained using a blank holder [101].

This section presents the results of a numerical study using the blank holder to eliminate wrinkling, and the effect of blank holder force on flange wrinkling waves. The dimensions of the blank holder (534mmX334mmX50mm) will be used in process modelling. Figure 4.11 shows the FE model with blank holder. The same boundary conditions were applied to die, punch, elastic cushion, and metal sheet as given in Section 4.1.2. Additionally, displacement boundary conditions were applied to the blank holder, fixing the lower part of the blank holder in the x , y and z directions, and upper part in the x and z directions.

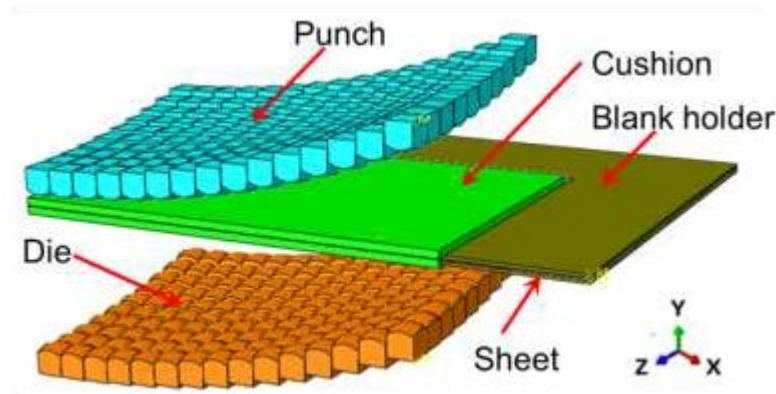


Figure 4.11 Finite element model of tool with blank holder (Quarter die)

4.2.3.1 Determination of suitable blank holder force to eliminate flange wrinkling

During the MPF process, the sheet inside the blank holder was pulled into the die cavity by the punch; as a result of compressive stress during the sheet forming wrinkling will be initiated if the Blank Holder Force (BHF) is insufficient, this is called flange wrinkling, see Figure 4.12. The BHF is an important parameter in the control of wrinkling. Thus, the initiation of wrinkling is studied for different values of BHF. The simulation is conducted with the values of 5 kN, 10 kN, 15 kN, and 20 kN for the BHF. The thickness of the sheet was 1 mm, and radius of curvature of part was 400 mm. It is observed from Figure 4.13 and Figure 4.14 that the flange wrinkling profile over path AB and CB used a different BHF for both sides of deformed sheet. It can be seen that the amplitude of the wrinkling is reduced by increase of BHF. The lowest value of wrinkling amplitude was with the largest BHF (20 kN).

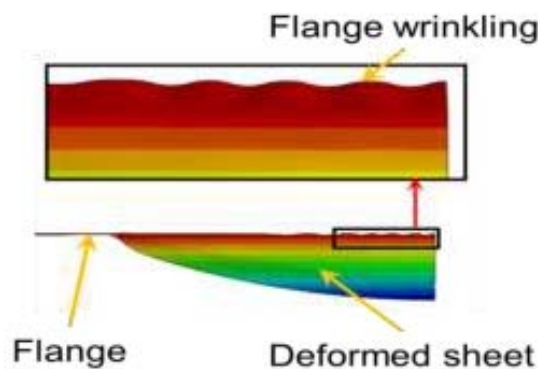


Figure 4.12 Flange wrinkling waves

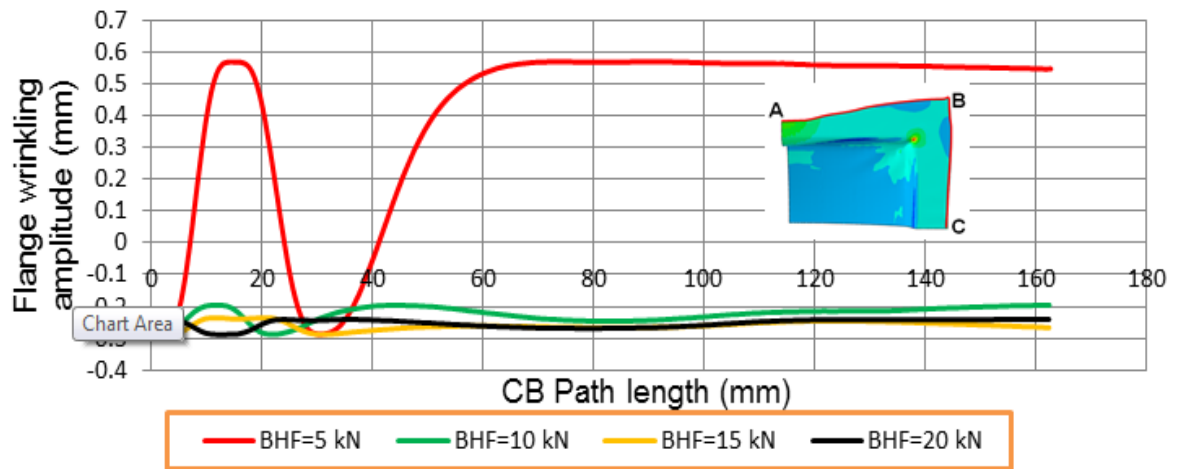


Figure 4.13 Flange wrinkling amplitude over path CB for four levels of blank holder force

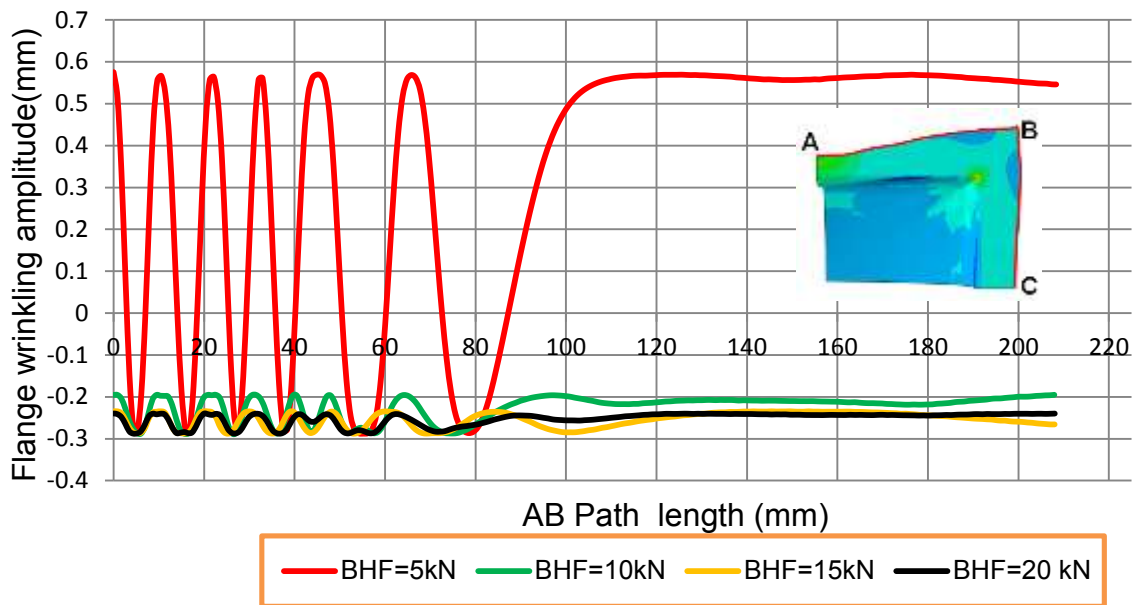


Figure 4.14 Flange wrinkling amplitude over path AB for four levels of blank holder force

4.2.3.2 Effect of gap distance on the thickness distribution

It is necessary to leave a small gap between blank holder and die to allow the sheet material to flow more easily during the forming process. Figure 4.15 shows the gap between punch and blank holder.

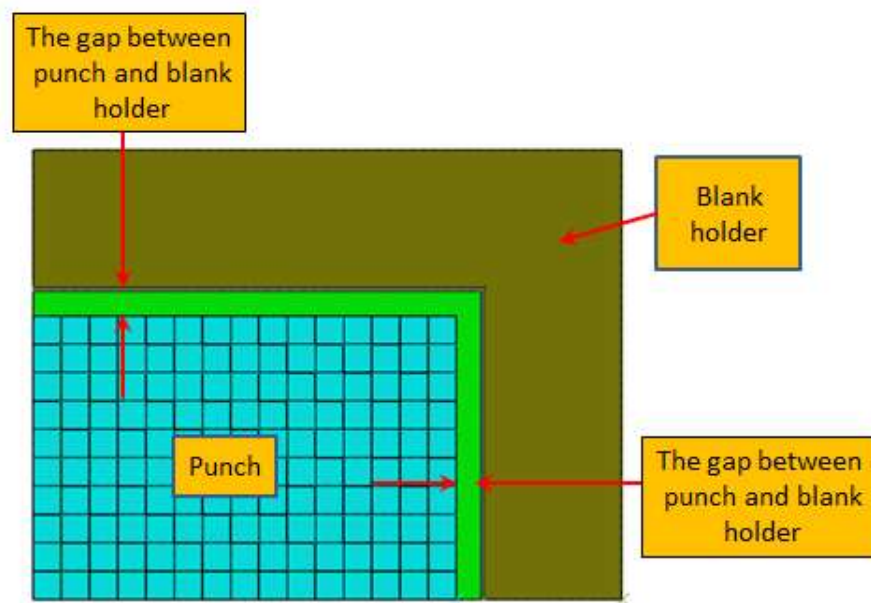


Figure 4.15 The gap between punch and blank holder

The magnitude of the gap has significant effect on the sheet thickness distribution and sheet lost (overuse). In this simulation study, 5 mm, 10 mm, and 15 mm gaps were used between die and blank holder. Figure 4.16, Figure 4.17, and Figure 4.18 show the corresponding sheet thickness distributions. In general, it can be seen that the thickness distribution was more uniform using the 10 mm gap, with maximum and minimum thinning in the overhang area obtained using the 5 mm and 15 mm gaps respectively. Figure 4.19 shows the thickness distribution over paths OA and OC across the centre of deformed sheet.

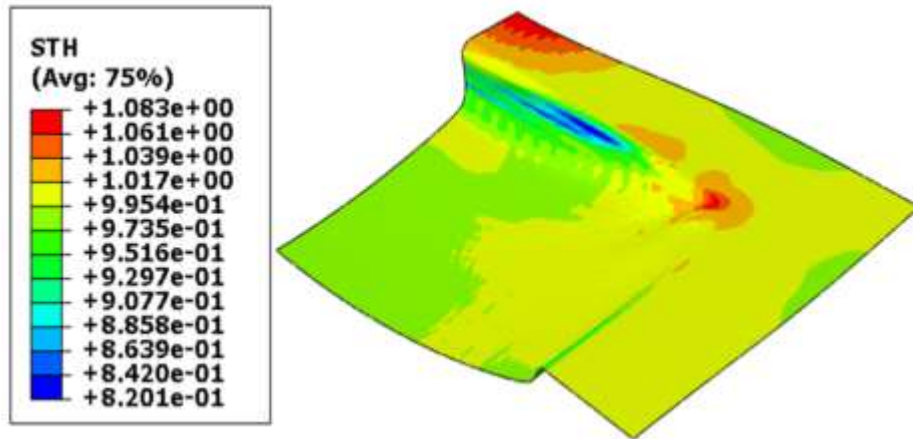


Figure 4.16 Sheet thickness distribution using 5 mm gap between blank holder and die

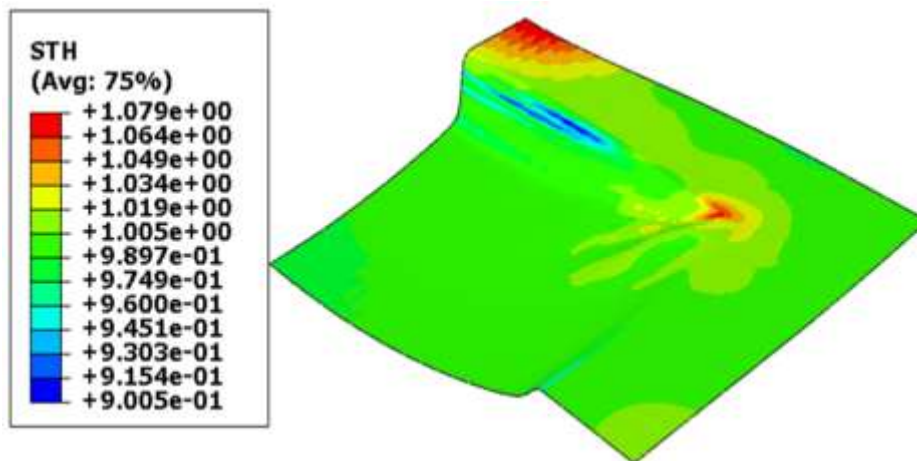


Figure 4.17 Sheet thickness distribution using 10 mm gap between blank holder and die

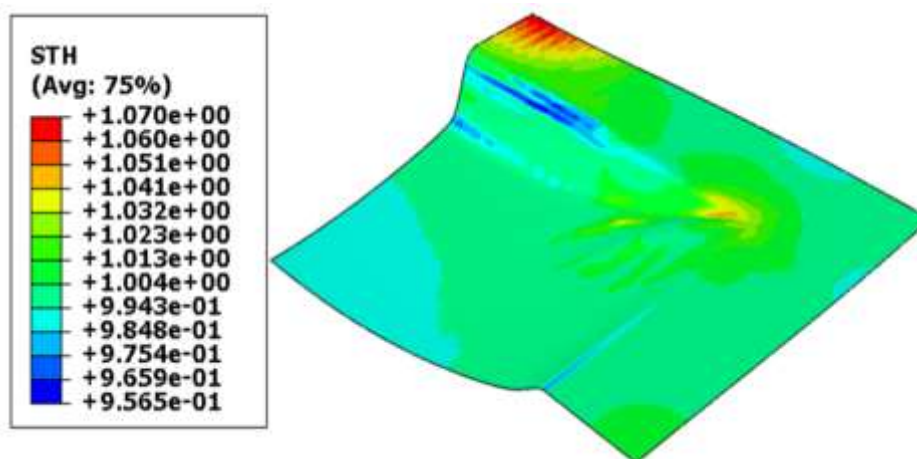


Figure 4.18 Sheet thickness distribution using 15 mm gap between blank holder and die

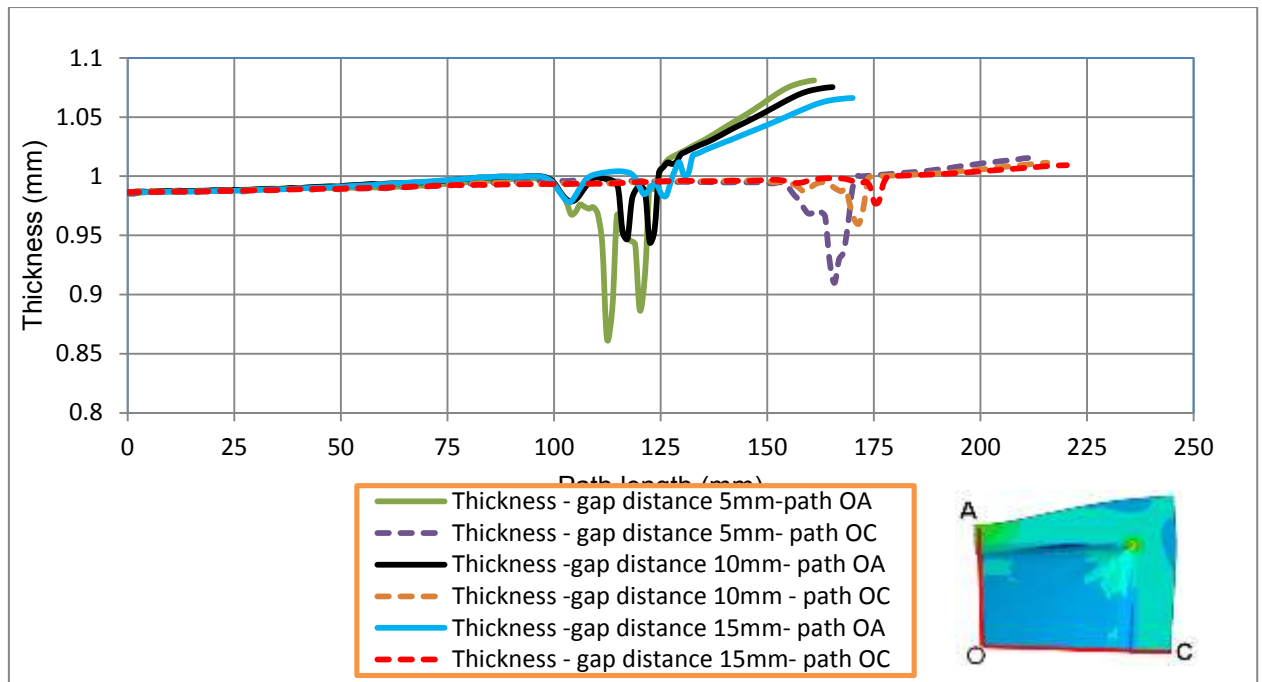


Figure 4.19 Thickness distribution over paths OA and OC at centre of deformed sheet

4.2.3.3 Reduced corner defect in doubly curved shape and effect on thickness

Using a blank holder to eliminate wrinkling in the forming of a double curved part from a flat rectangular sheet can lead to a geometrical defect in the corner as shown in Figure 4.20. This defect can be reduced by increasing the distance between the sheet and die, so that the punch stroke is increased. This lead to greater sheet stretching (semi-deep drawing), and reduces the geometrical defect as shown by the simulated results in Figure 4.21. Figure 4.22 illustrates the corner profile over path ML before increasing the distance between sheet and die. It can be seen that a wave profile is produced in the corner as a result of compression stress. By increasing the distance between the sheet and die the corner profile becomes more uniform, because the lateral compression stress is reduced as a result of sheet stretching in depth direction (direction of the movement of the punch).

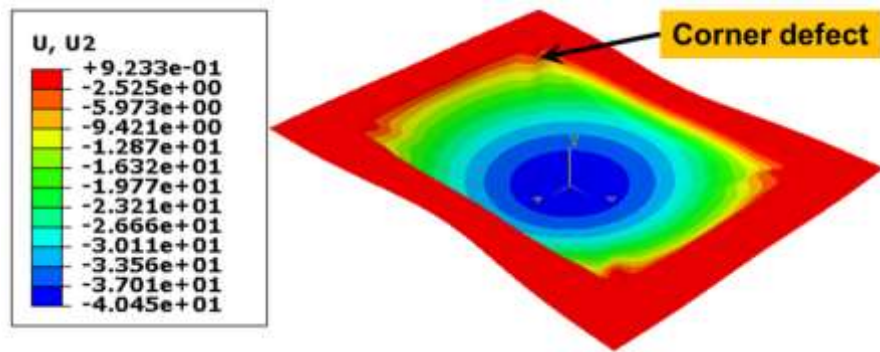


Figure 4.20 Doubly curved shape with corner defect

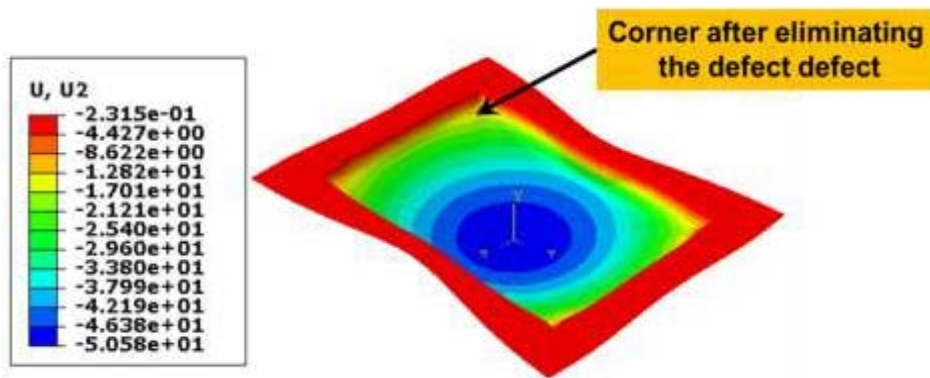


Figure 4.21 Doubly curved shape after elimination of corner defect

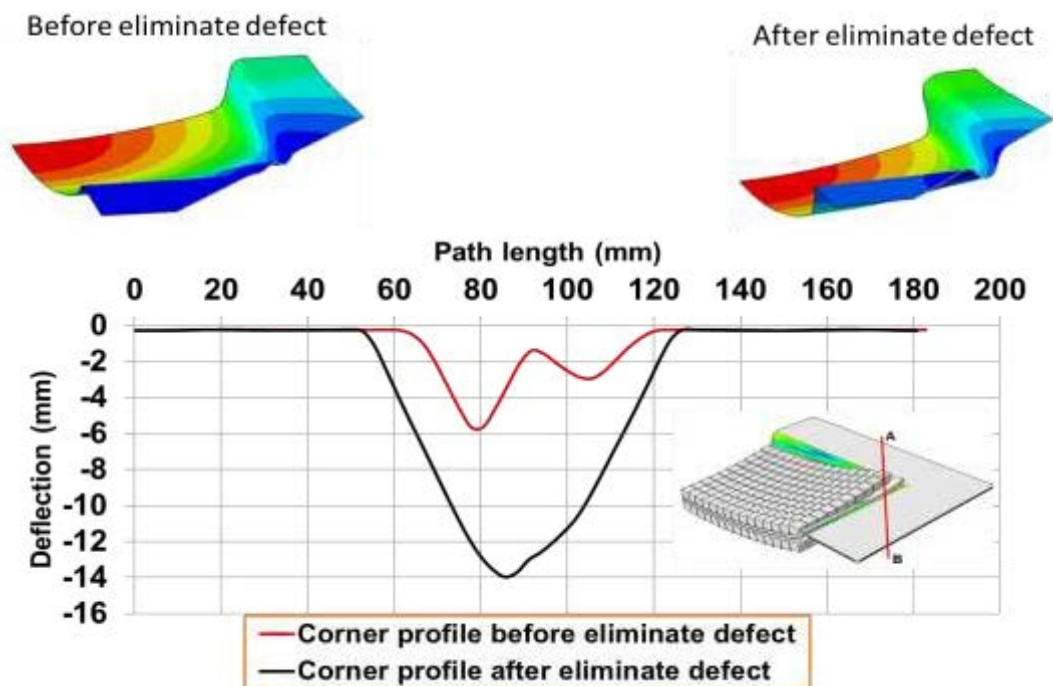


Figure 4.22 Comparison of corner profile at path ML before and after increasing distance between sheet and die

Increasing sheet stretching affects sheet thickness distribution. The results of two simulations in Figure 4.23 and Figure 4.24, respectively, show thickness distributions before and after treating the corner defect. It can be seen that the sheet thinning in the deformed area after reducing the corner defect is greater than before the reduction of the corner defect. This result is normal, because increasing the distance between sheet and die leads to an increase in the punch stroke, so that sheet thinning increases as a result of the sheet stretching.

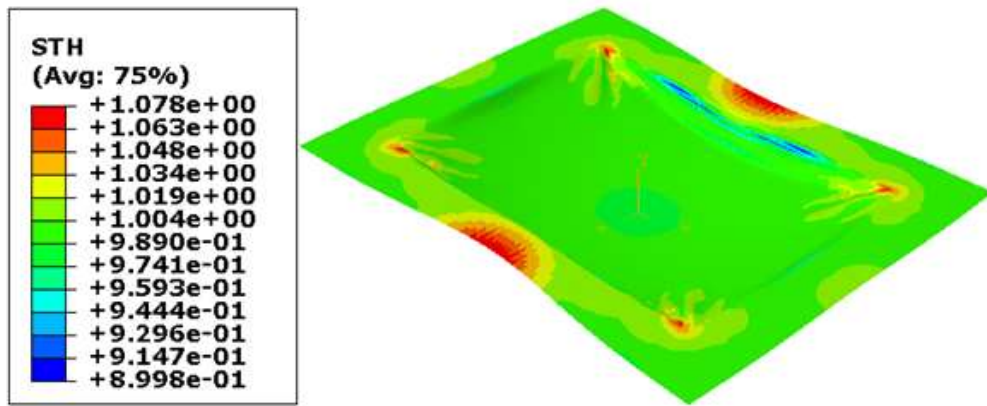


Figure 4.23 Thickness distribution on doubly curved shape with corner defect

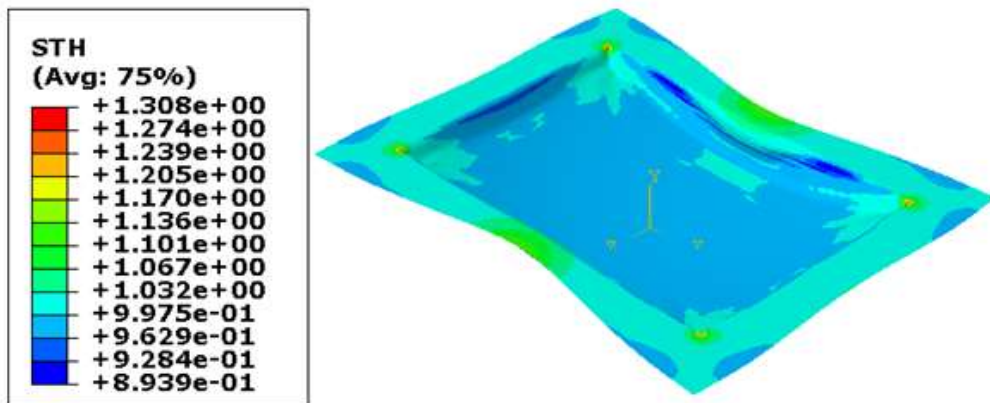


Figure 4.24 Thickness distribution on doubly curved shape after eliminating corner defect

Figure 4.25 shows the thickness along path BD. It can be seen that the thickness distribution is the same for all three condition up to about 50 mm along the path and from about 150 mm to the end of the path. However, there is difference in thickness distribution from about 50

mm to about 150 mm. Before reducing the corner defect there is slight increase in thickness along the path BD with a maximum at 75 mm. After reducing the corner defect there is a sharp but substantial increase in thickness at 65 mm after which the thickness quickly returns to 1 mm at about 80 mm. For both these conditions there is a slight thinning of the sheet beyond about 150 mm. Using a curved blank holder corner to reduce maximum thickening is effective, as shown in Figure 4.23. However the thickening takes place over a greater length of path BD, it starts from about 50 mm and extends until about 115 mm. Thus, the blank holder with angled corner will be used in the experimental work.

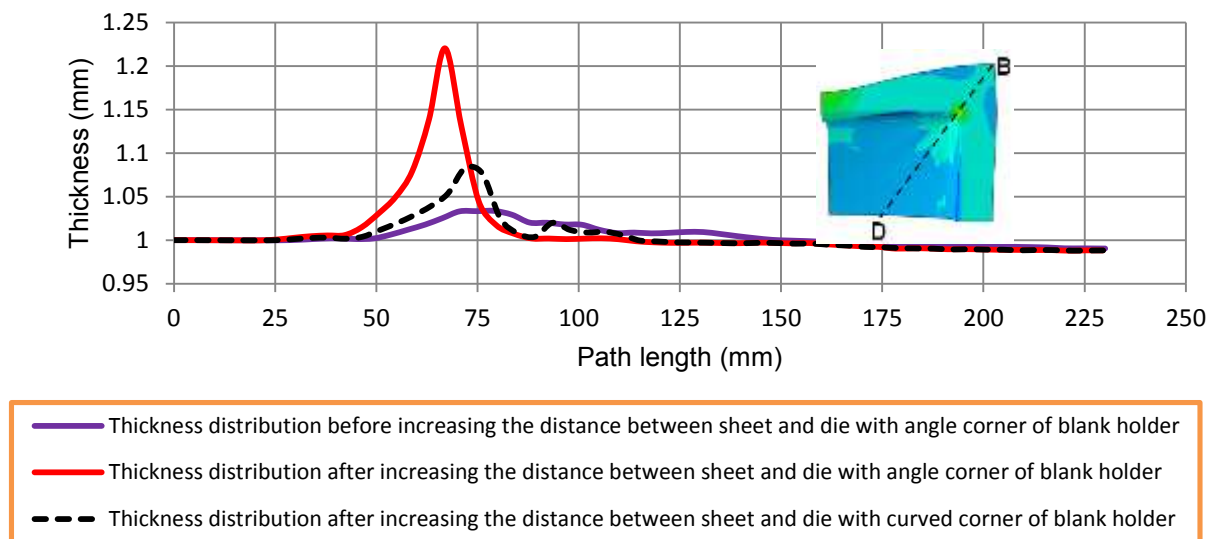


Figure 4.25 Thickness distributions over path DB

4.2.4 Validation of the finite element model without blank holder

The numerical model was validated against experimental results using the following parameters; a 1 mm thick steel sheet, 3 mm elastic cushion thickness, and pin size 10 mm to produce a shape with a 400 mm radius of curvature. The results are shown in Figure 4.26, the force remains approximately constant until the punch displacement reaches 25 mm. At this position, pins come into contact with the elastic cushion and plastic deformation starts to take place. After that, the force increases with plastic deformation due to strain hardening of the material till the punch reach 38 mm, after which the force increased rapidly with plastic

deformation again due to strain hardening of the material and compression of the elastic cushion until the steel sheet takes its final shape. The maximum predicted forming force was 58.6 kN when the upper and lower dies are closed and the measured force, which was 61.1 kN. This was considered good agreement as the error in the maximum force was about 4%.

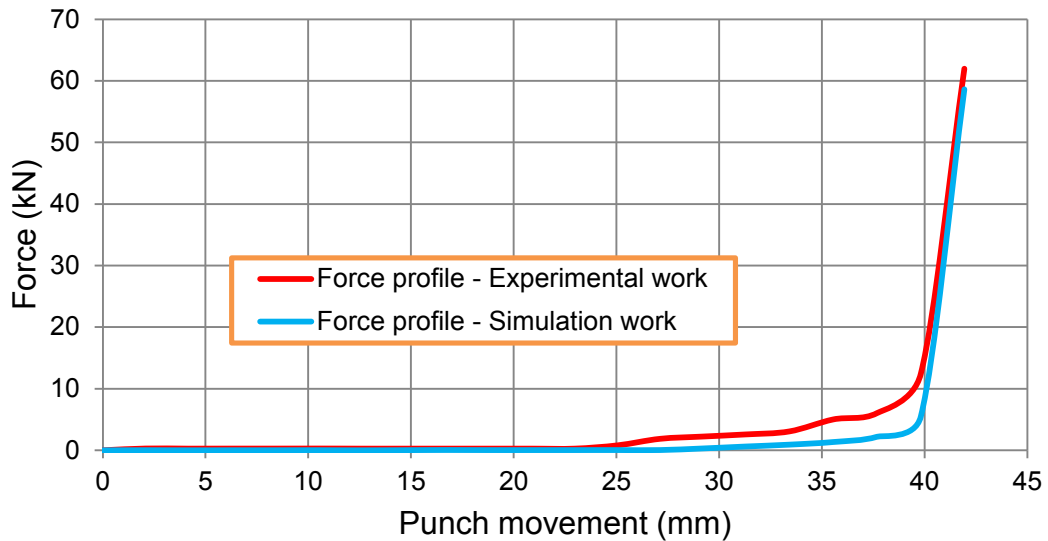


Figure 4.26 Comparison of predicted and experimental force for multi-point forming without blank holder

4.2.5 Validation of the finite element model with blank holder

The FE model with blank holder was also validated against experimental results using the following parameters; 1 mm thick steel sheet, 3 mm thick elastic cushion, pin size 10 mm, with 400 mm radius of curvature and BHF=20 kN. As shown in Figure 4.27, the simulated and experimental forces are the same until the punch displacement reached 3 mm, after which the force increases to overcoming the blank holder pressure until punch displacement reached 34 mm after which the force increased sharply with plastic deformation due to strain hardening of the material and compression of the elastic cushion. This continues until the steel sheet takes its final shape. The maximum predicted force is 72.96 kN when the upper

and lower dies are closed and the measured force was 75.23 kN, giving an error in the maximum force of approximately 3%.

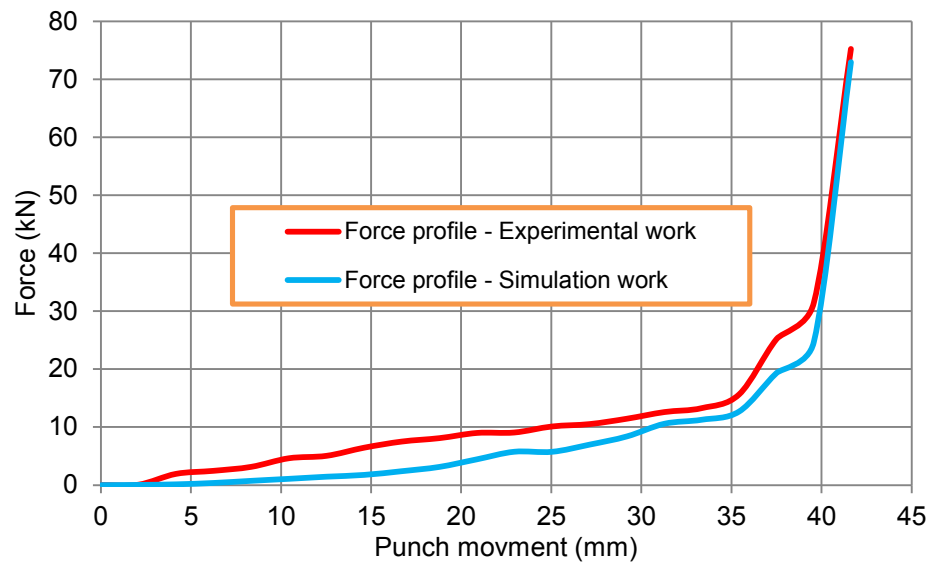


Figure 4.27 Comparison of predicted and experimental force for multi-point forming model with blank holder

The good agreement between the FE and experimental results gives confidence in the use of numerical simulations to study the effect of process parameters.

Next is the assessment of the influence of the pin size, radius of curvature of part that will be produced, elastic cushion thickness, and coefficient of friction on wrinkling, shape accuracy and thickness variation.

4.3 Parametric study

This section explains the investigation of the effects of the main parameters relating die shape to the surface quality characteristics of the parts formed. These parameters are the pin size, radius of curvature of part, elastic cushion thickness, and coefficient of friction. The quality characteristics of the parts formed include wrinkling, deviation from target shape and thickness variation

4.3.1 Effect of pin size on wrinkling, shape accuracy and sheet thickness

To study the effect of pin size on wrinkling, shape accuracy and variation in sheet thickness the remaining parameters such as the radius of curvature, elastic cushion thickness, coefficient of friction and sheet dimensions must be held constant. Figure 4.28 shows the effect of different pin sizes 10 mm, 15 mm, and 20 mm on the wrinkle wave form. In all three cases, wrinkling appears in the middle of both sheet edges. For path CB, the wrinkles differ in shape and amplitude depending on pin size. It can be seen the smallest wrinkle amplitude (difference between actual and target profiles) is for the smallest pin size (10 mm) and the largest wrinkle amplitude occurs for the largest pin size (20 mm). While for path AB, the 15 mm pin gives maximum amplitude of the wrinkle and largest number of wrinkle waves. The wrinkled profile using the 10 mm pin was closest to target profile.

It can also be seen from Figure 4.28 that the number of wrinkle waves on path AB is greater than the number of wrinkle waves on path CB, and the wrinkle wave amplitude for path AB is less than for path CB.

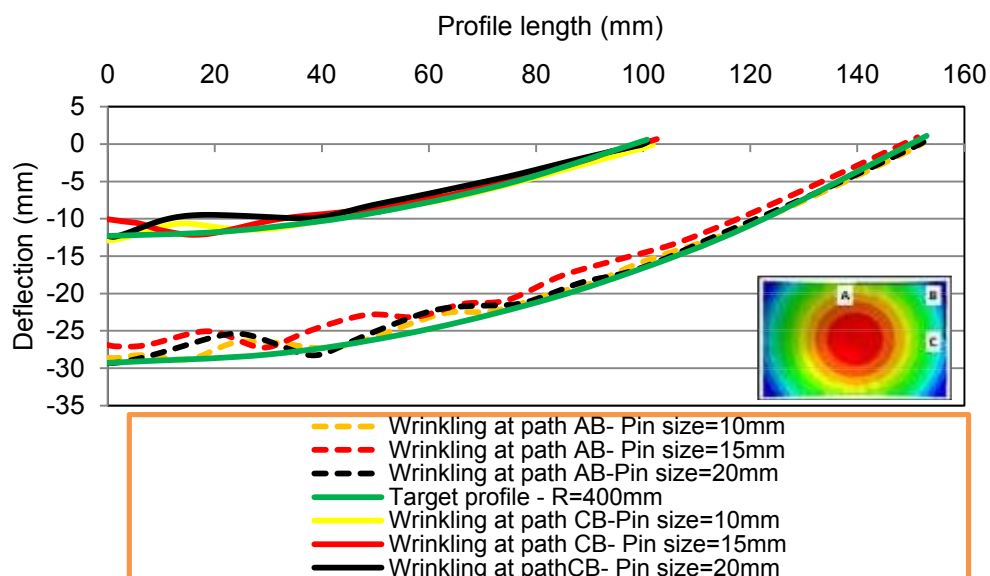


Figure 4.28 Effect of pin size on wrinkling at Path AB and CB

As shown in Figure 4.29 and Figure 4.30, for the mutually perpendicular paths both OA and OC, the formed profile using the 10 mm pin is close to the target profile until about 70 mm

along the length of the profiles, after that, there is clear deviation on both paths. The two profiles formed using pin sizes 15 mm and 20 mm were close together but neither was coincident with the target profile in the middle of the sheet. This deviation from target profile in the middle of deformed sheet was due to low pressure in the middle area of the deformed sheet, see Figure 4.31. For the same punch movement, the pressure is changed due to the different size gaps between pin tips.

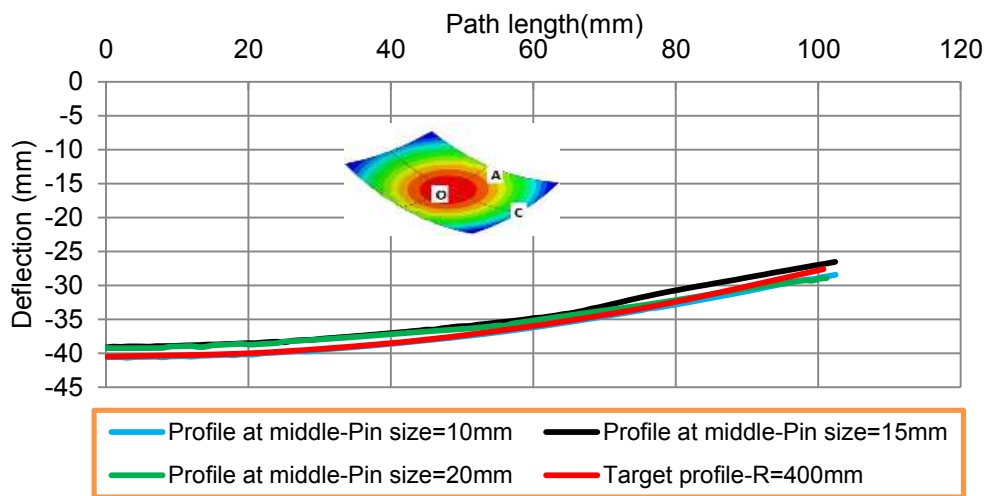


Figure 4.29 Effect of pin size on formed profile along path OA

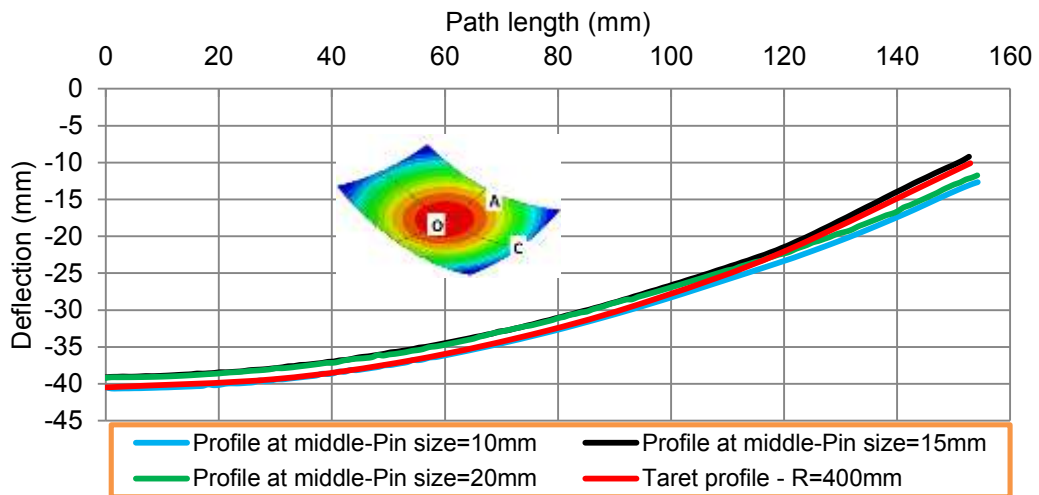
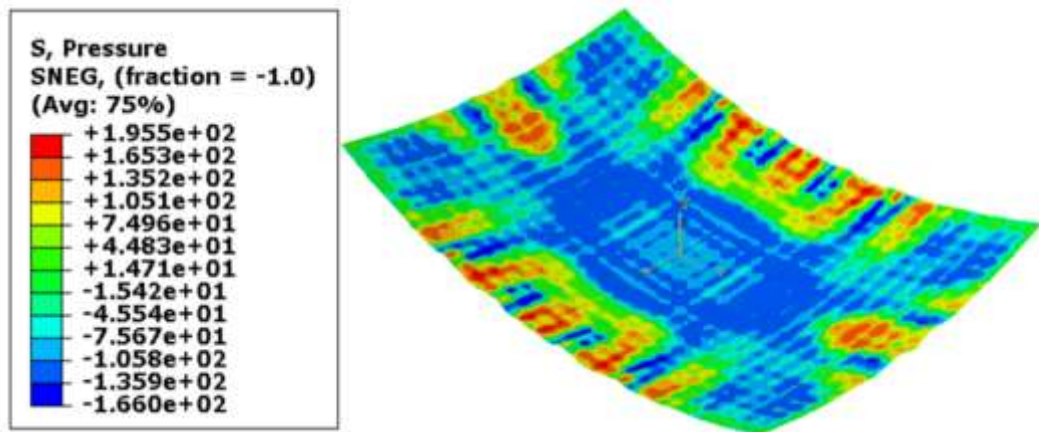
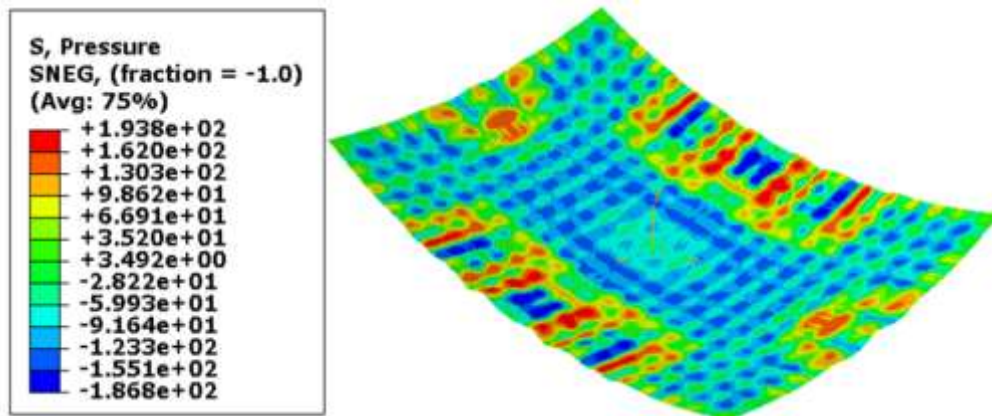


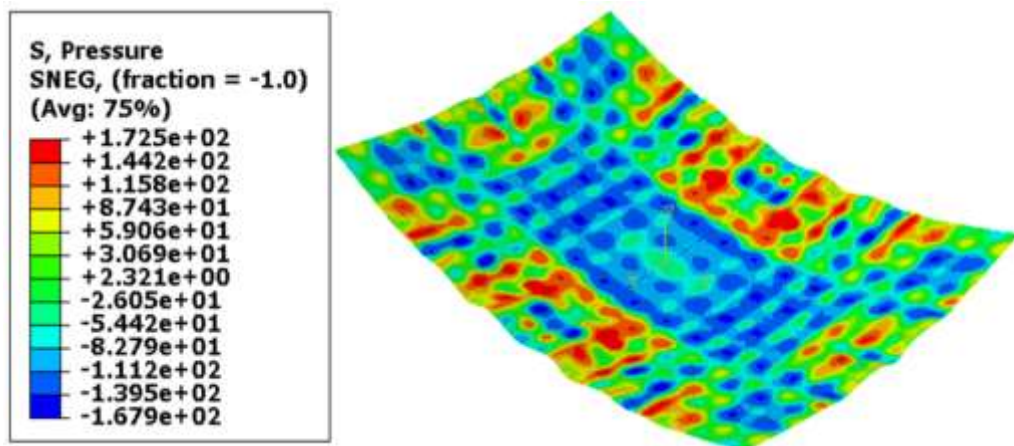
Figure 4.30 Effect of pin size on formed profile along path OC



a- Pressure distribution on deformed sheet using pin size 10 mm



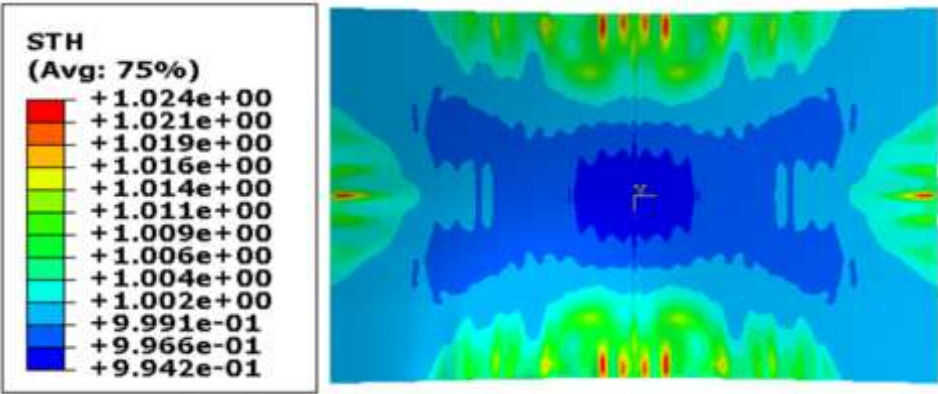
b- Pressure distribution on deformed sheet using pin size 15 mm



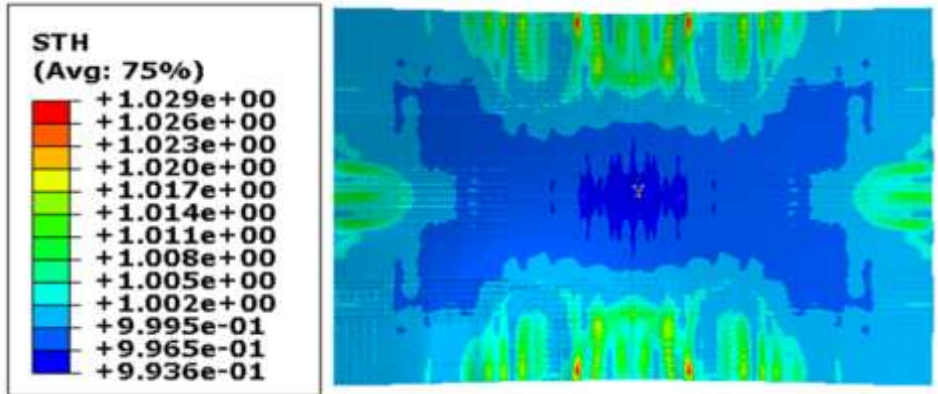
c- Pressure distribution on deformed sheet using pin size 20 mm

Figure 4.31 Pressure distribution on deformed sheet using 10, 15, 20 mm size pins

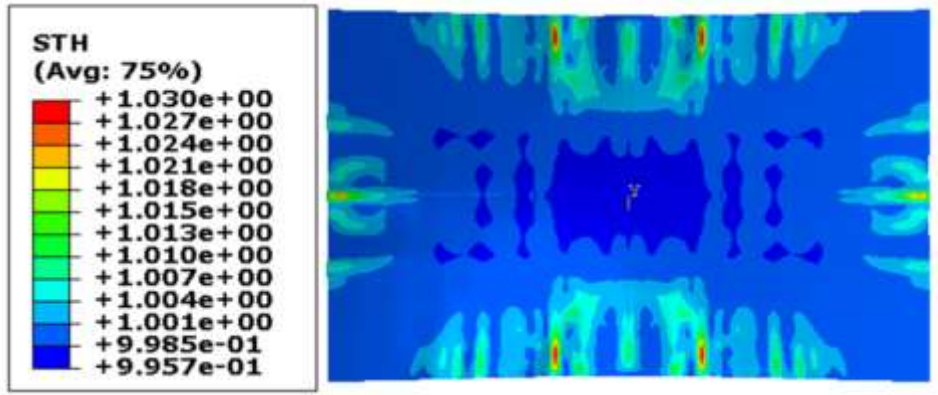
Figure 4.32 illustrates the thickness distribution of the deformed sheet using different pin sizes. In general, it can be seen clearly that the greatest thinning and thickening occur using pin size 20 mm, and least thinning and thickening occur using pin size 10 mm.



a-Thickness distribution (pin size =10 mm)



b-Thickness distribution (pin size=15 mm)



c-thickness distribution (pin size=20 mm)

Figure 4.32 Thickness distribution of deformed sheet using different pin sizes

The predicted thickness variation of the deformed sheet along paths OA and OB, for the three pin sizes, are compared in Figure 4.33 and Figure 4.34 . For all three pin sizes, for both paths, the thickness in the central region decreased and at edges increased. On path OB, the thickness variation is slightly more uniform than the thickness variation along path OA. However, while the thickness distribution around the middle of the deformed sheet was more uniform with the 10 mm pin, that pin tended to produce the greatest thinning at the centre and the greatest thickening at the edges.

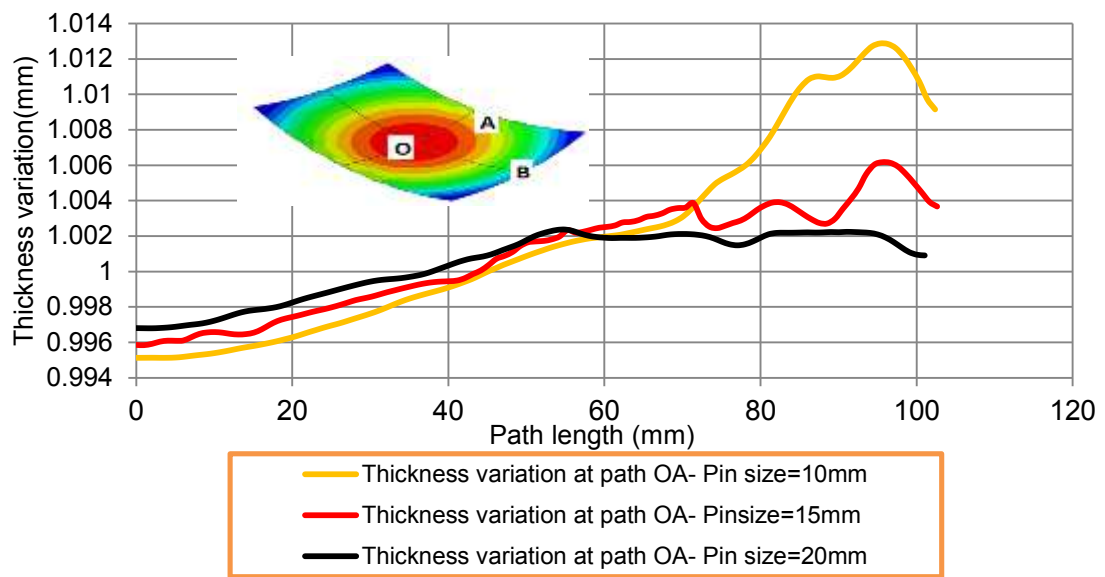


Figure 4.33 Effect of pin size on thickness distribution on short path OA

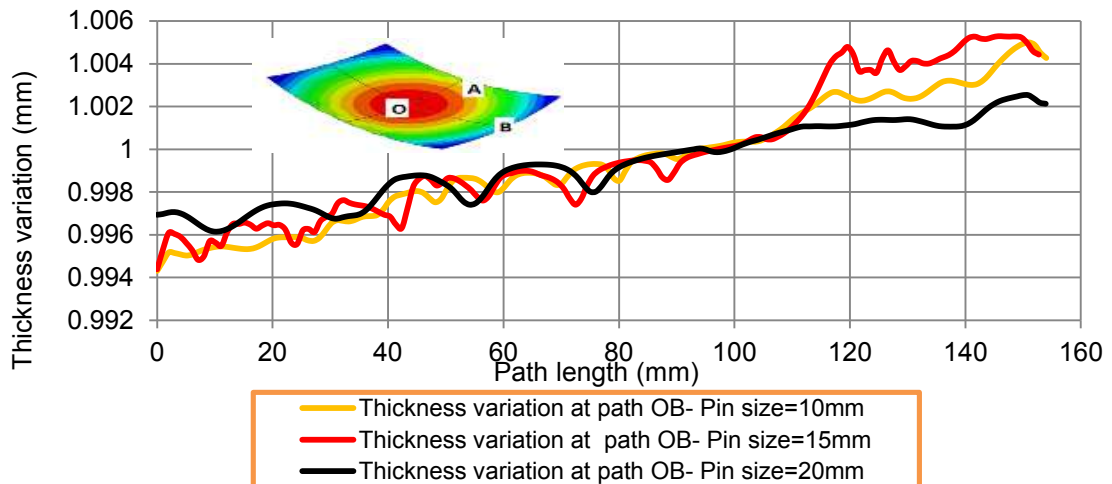


Figure 4.34 Effect of pin size on thickness distribution on long path OB

4.3.2 Effect of radius of curvature of the formed part on wrinkling, shape accuracy and thickness variation

To study the effect of curvature of the formed part on wrinkling, shape accuracy and thickness variation all other parameters must be constant. For a double curved part, different parameters effect deformed sheet quality, for instance, the geometry of the product which is representing by the radius of curvature. In this case, the radii of curvature of 400 mm, 600 mm, and 800 mm have been used. The deflection profiles along paths AB and CB are shown in Figure 4.35. The effect of radius of curvature on wrinkling can be seen. The lowest wrinkling occurs along paths AB and CB for radius of curvature 800 mm, and the highest wrinkling on both paths for radius of curvature 400 mm. This is believed to be due to the influence of the stress and strain distribution in the deformed sheet [47]. The general trend is for wrinkling to increase with decrease in radius of curvature.

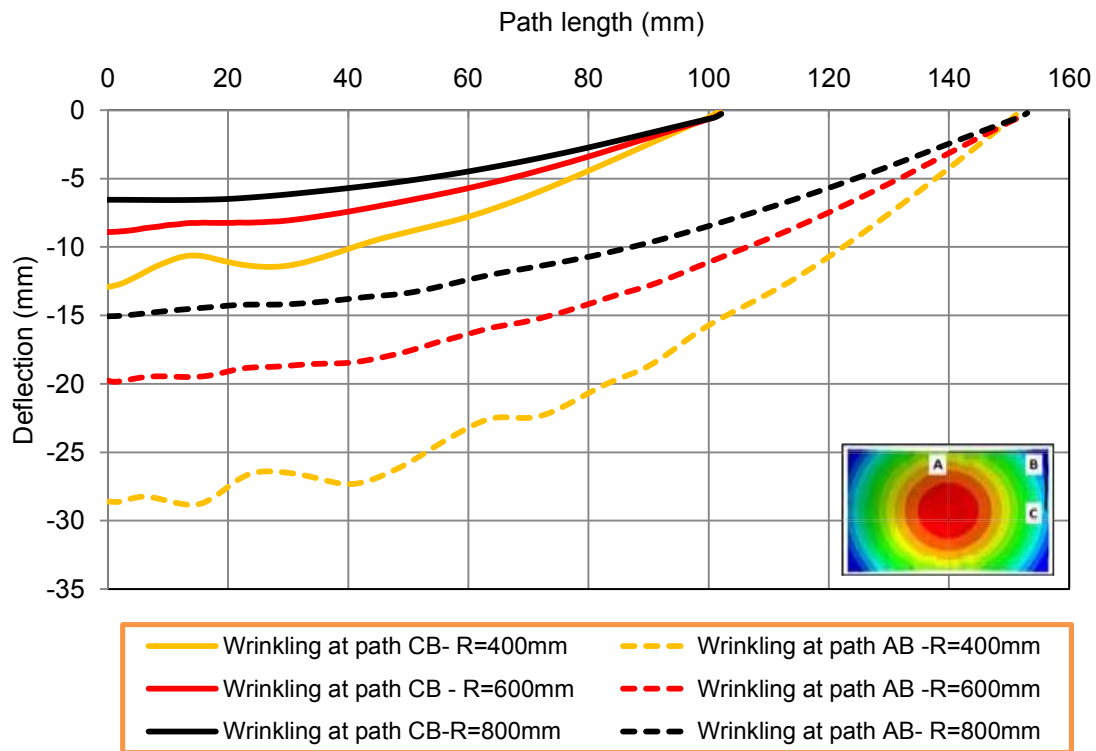


Figure 4.35 Effect of the radius of curvature on wrinkling along paths AB and CB

From Figure 4.36, the effect of curvature on deflection of the deformed sheet can be clearly seen. Decreasing the radius of curvature caused increased deviation between target profile and deformed profile. The highest deviation occurred for the 400 mm radius of curvature, particularly for paths lengths longer than 100 mm. The smallest deviations were obtained using the 800 mm radius of curvature; here the target profile and actual profile did not differ significantly. The accuracy of the deformed shape decreases with decrease in radius of curvature. The deviation between target shape and formed shape is thought to be due to the contact area between punch and sheet, when using 400 mm as the radius of curvature this area is smaller than the contact area when the radius of curvature is 800 mm. This means the material flow of the elastic cushion toward the edges of the sheet increases and prevents the sheet from reaching the target profile.

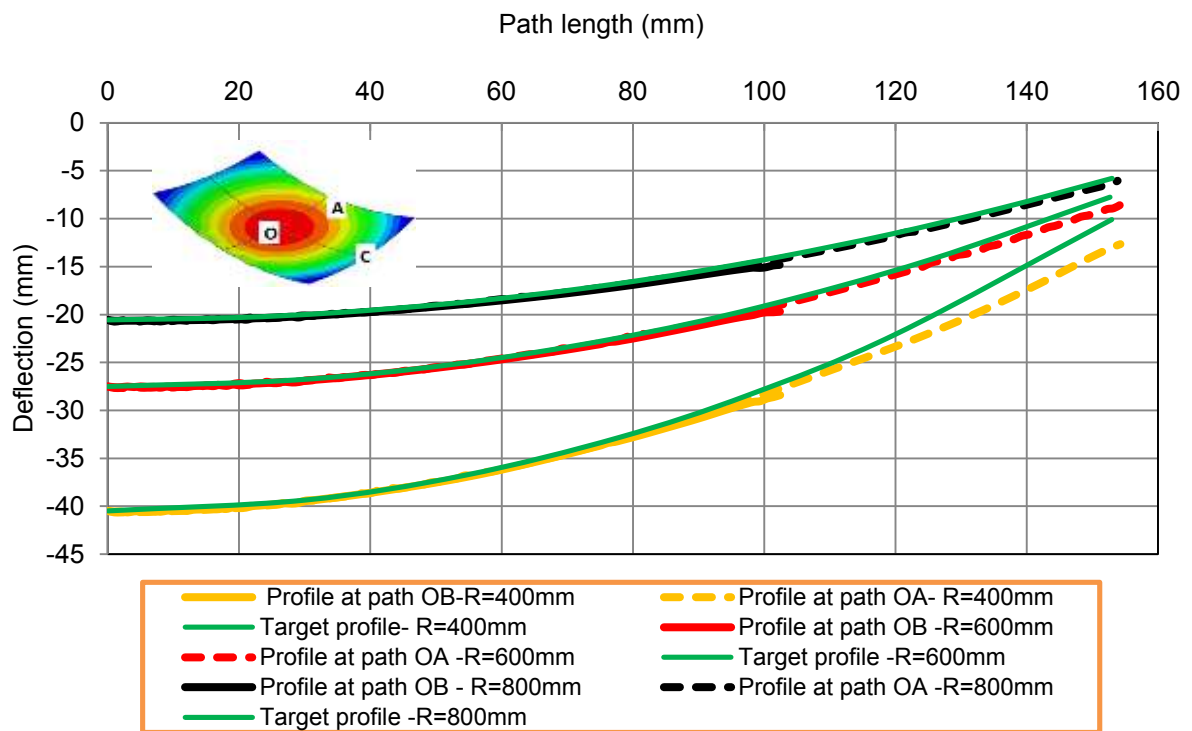
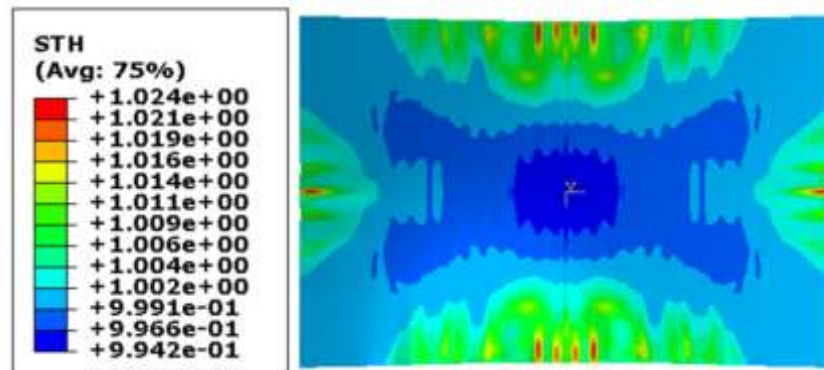
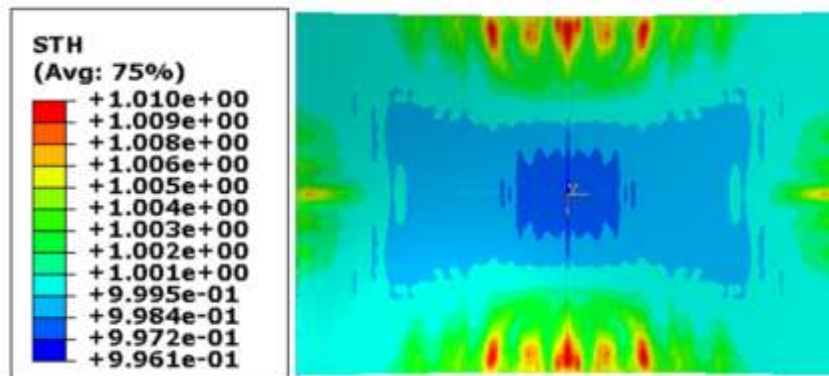


Figure 4.36 Effect of the radius of curvature on profile of the deformed sheet along paths OA and OB

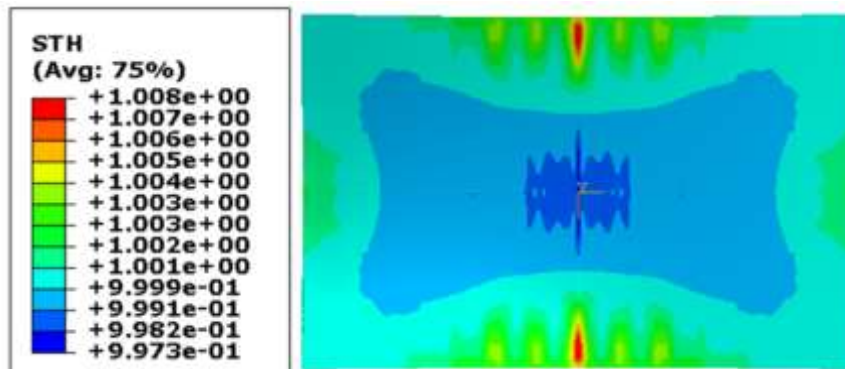
As can be seen in Figure 4.37 that the biggest reduction in thickness (thinning) and biggest increase in thickness (thickening) occur with the smallest radius of curvature, and the least thinning and least thickening occurs with the highest radius of curvature. Figure 4.38 shows the thickness distribution along paths OA and path OC. It can be seen that thinning occurs at the centre of the deformed sheet and thickening at the middle of the edges. This means that decreasing the radius of curvature causes an increase in thickness variation.



a-Thickness distribution (radius of curvature =400 mm)



b-Thickness distribution (radius of curvature =600 mm)



c-Thickness distribution (radius of curvature =800 mm)

Figure 4.37 Thickness distribution of deformed sheet using different radii of curvature

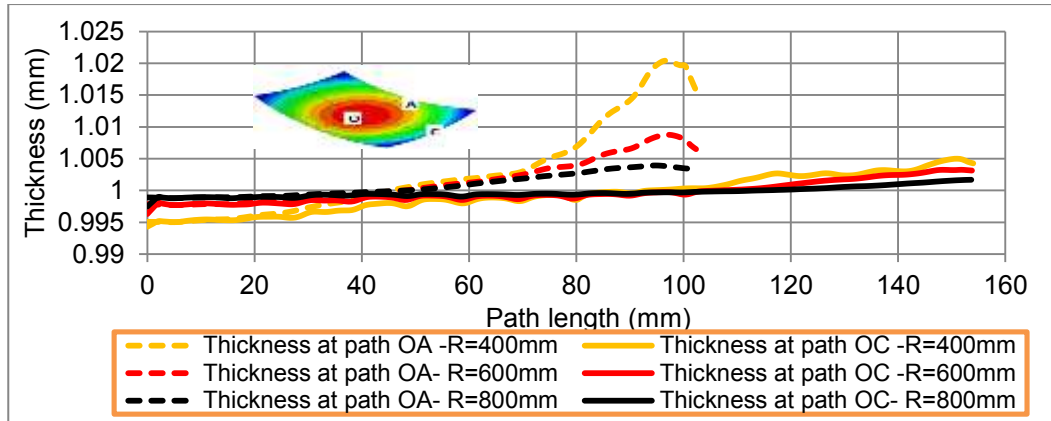


Figure 4.38 Effect of the radius of curvature on thickness distribution along paths OA and OB

4.3.3 Effect of elastic cushion thickness on wrinkling, shape accuracy and thickness variation

Figure 4.39 shows the effect of different elastic cushion thicknesses, 3 mm, 6 mm, and 9 mm on the wrinkle waveform. In all three cases, a wrinkle waveform appears at the centre of both sheet edges. On path AB, the wrinkle waves are different in shape and amplitude from those along CB, with the number of wrinkle waves on path AB more than on path CB. At path AB, it can be seen the smallest and biggest wrinkle wave amplitudes occur when using elastic cushion thicknesses of 3 mm and 9 mm respectively.

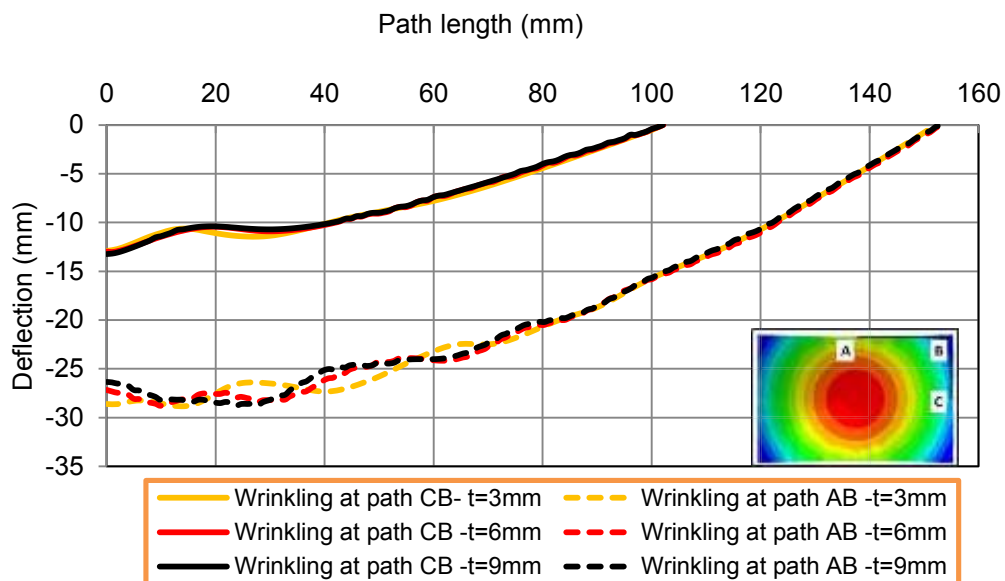


Figure 4.39 Effect of elastic cushion thickness on wrinkling at paths AB and CB

As can be seen in Figure 4.40, the effect of elastic cushion thickness on the deformed shape at its centre is not significant. The deviation between deformed profile and target profile for each of the three elastic cushion thicknesses; 3 mm, 6 mm, and 9 mm, was approximately equal. There is good agreement between target shape and deformed shape from the sheet centre till about 65 % of the distance (about 100 mm) along length of paths OA and OC.

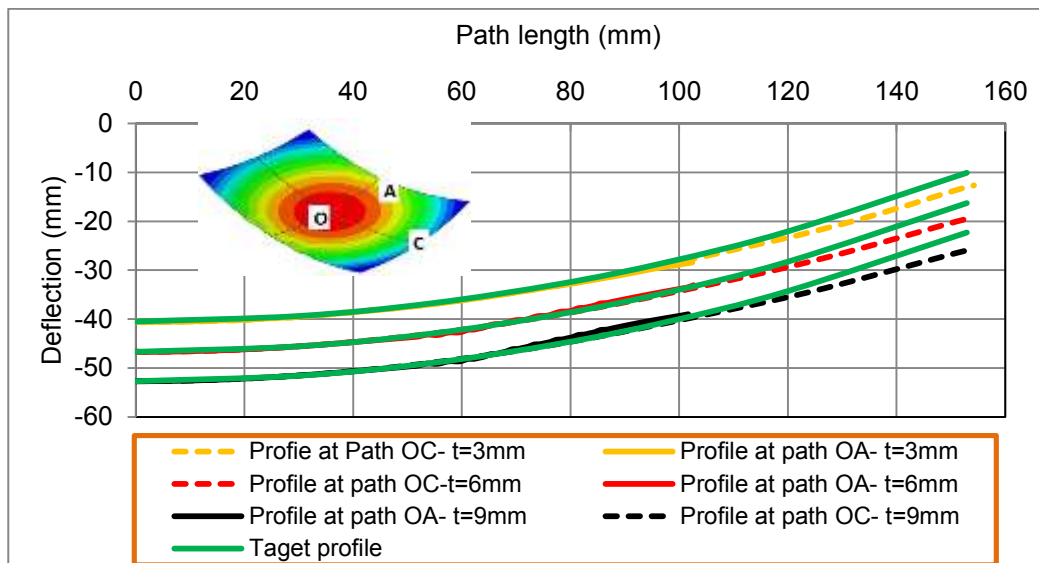
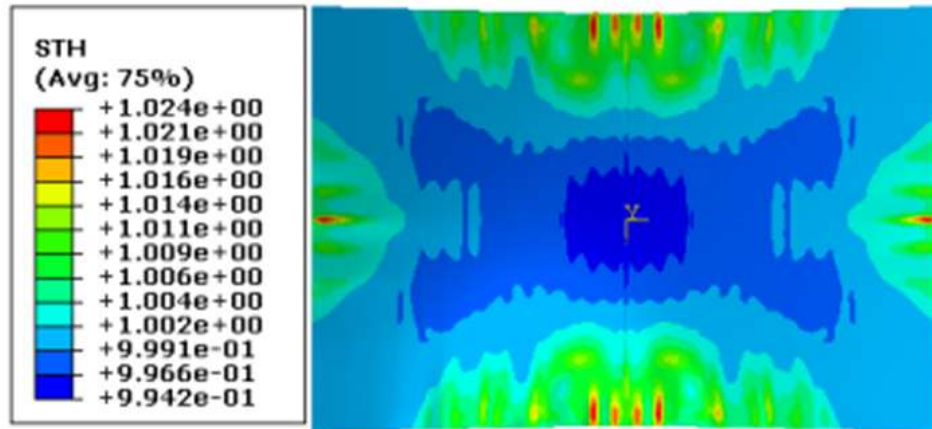


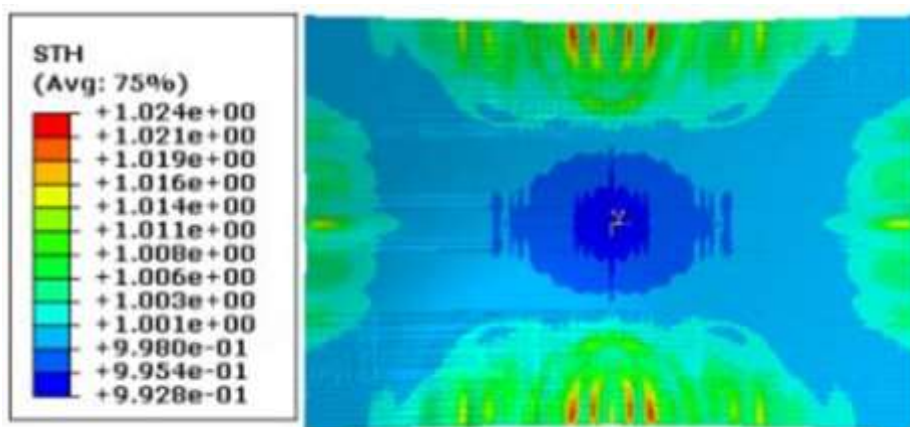
Figure 4.40 Effect of elastic cushion thickness on profile of deformed sheet along paths OA and OC

The general thickness distribution of the deformed sheet is shown in Figure 4.41 a-c.

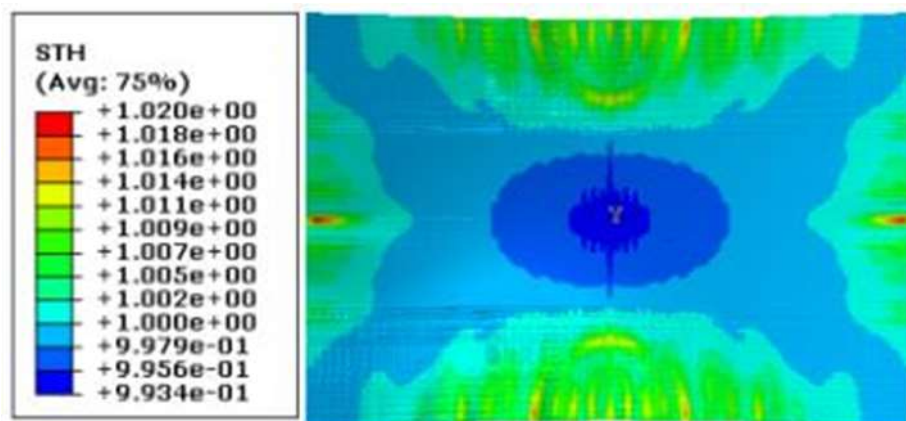
It can be seen that the thickness distribution using elastic cushion thickness of 9 mm is more uniform than for the elastic cushions of thickness 3 mm and 6 mm. Figure 4.42 illustrates the thickness distribution along paths OA and OC and shows that the thickness distribution in the middle of the deformed sheet using different elastic cushion thickness converges.



a-Thickness distribution (elastic cushion thickness=3mm)



b-Thickness distribution (elastic cushion thickness=6mm)



c-Thickness distribution (elastic cushion thickness=9mm)

Figure 4.41 Thickness distribution on deformed sheet using different elastic cushion thickness

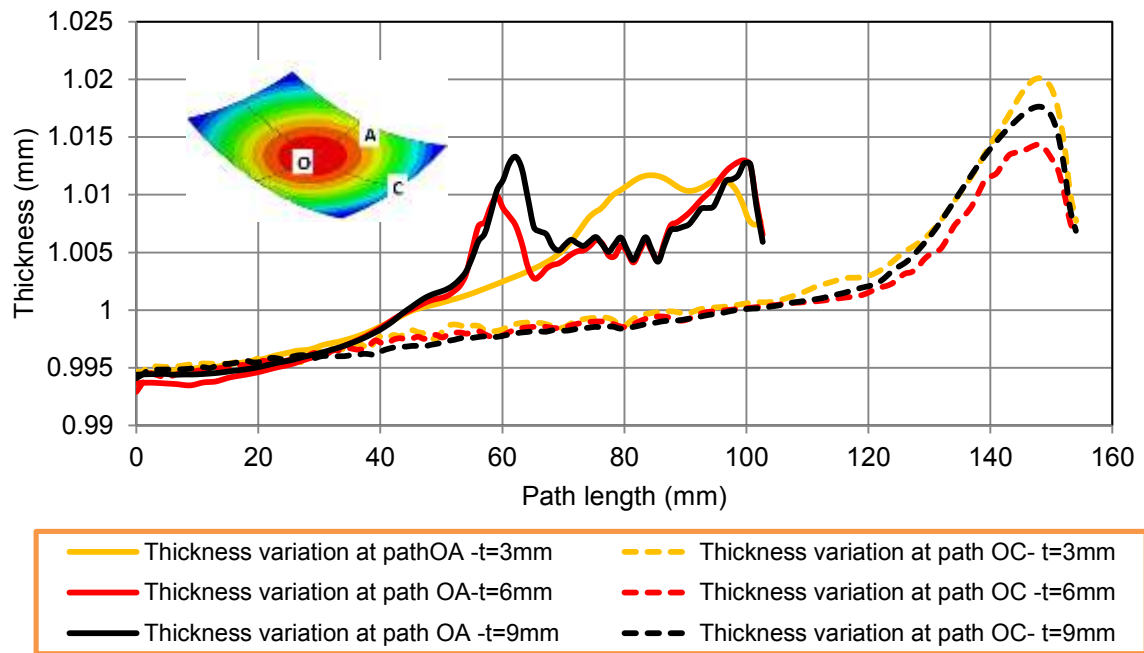


Figure 4.42 Effect of elastic cushion thickness on thickness distribution along paths OA and OC

4.3.4 Effect of coefficient of friction on wrinkling, shape accuracy, and thickness variation

To study the effect of friction between the elastic cushion and the pins, and the elastic cushion and the sheet, several simulations have been performed with coefficient of friction 0.0, 0.05, and 0.1 as used in literature review [102]. Other parameters were maintained constant, pin size 10 mm, radius of curvature 400 mm, and elastic cushion thickness 3 mm. Figure 4.43 shows a very slight decrease of wrinkle height with increasing coefficient of friction, particularly along AB, the long sheet side. Increasing the coefficient of friction leads to reduced sliding of the cushion material between pins and sheet, and this may help to increase the pressure on the sheet in the wrinkled area and reduce the wrinkle height. Figure 4.44 illustrate the effect of friction on the formed profile along the two paths OA and OC. It can be seen that the friction effect on the deformed profile is not significant. There is a variation between target and formed shape after 70% of the path length (about 100 mm) when using a radius of curvature of 400 mm as illustrated in Section 4.3.2 and Figure 4.19.

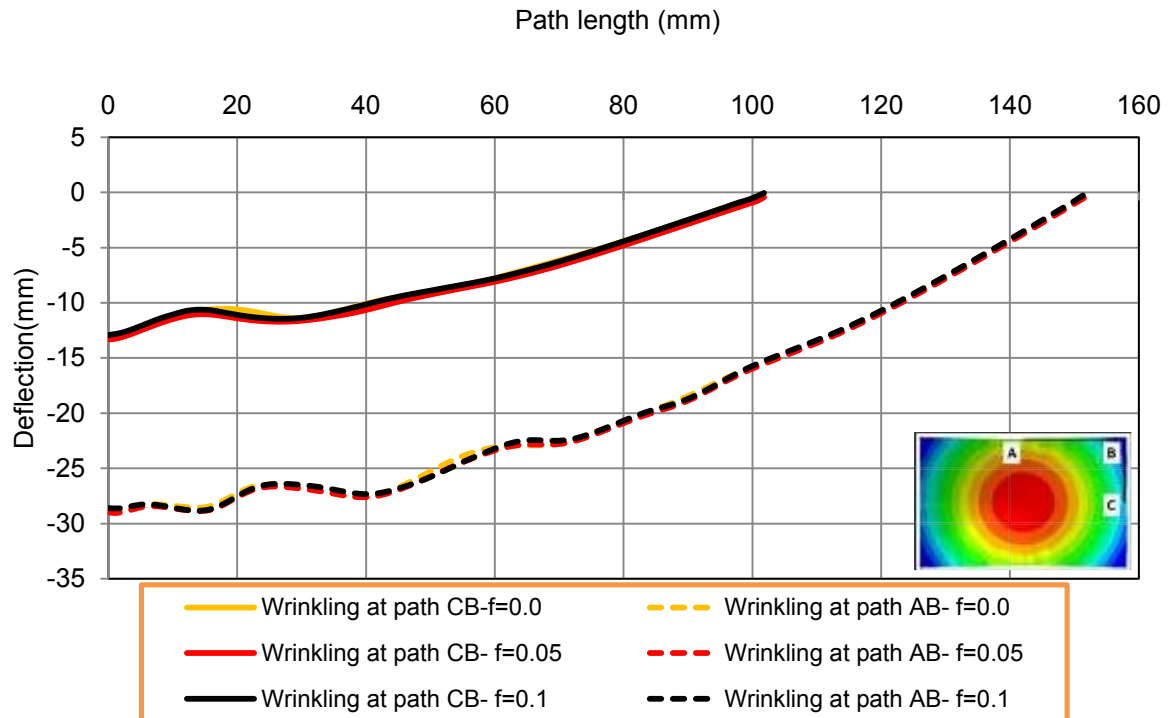


Figure 4.43 Effect of the coefficient of friction on wrinkling along paths AB and CB

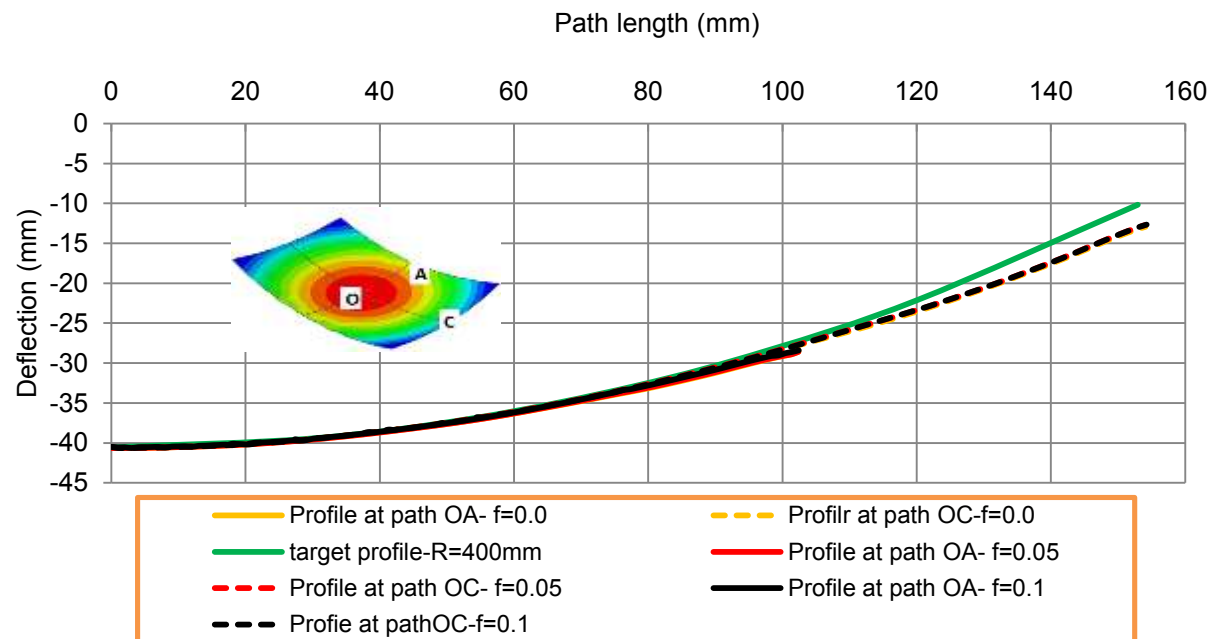
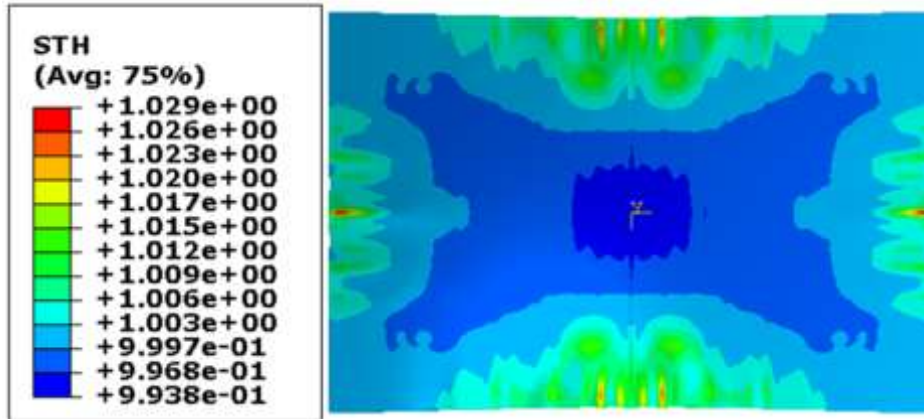


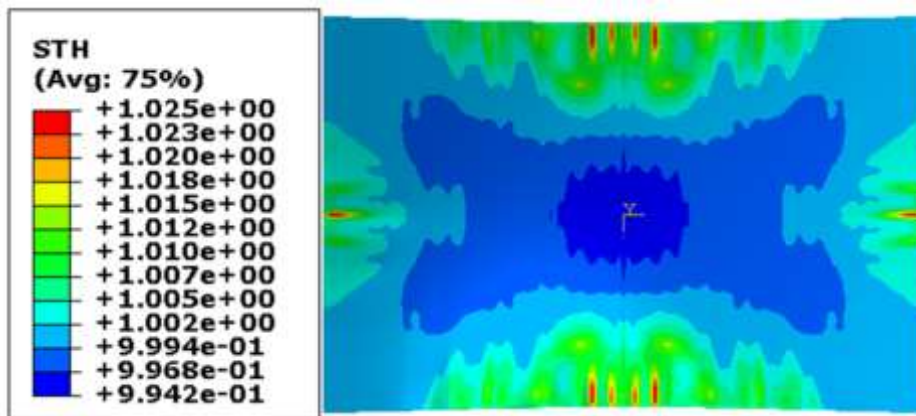
Figure 4.44 Effect of the coefficient of friction on deformed profile over paths OA and OC

Figure 4.45 a, b, and c show general thickness distribution for different coefficients of friction. It can be seen that sheet thickening in the middle of the edges decreased with increase in coefficient of friction, and the thinning in middle area of sheet increased with

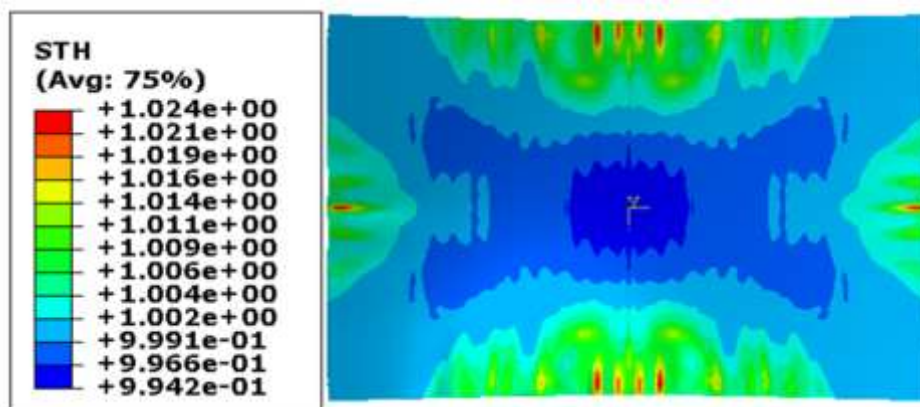
increase in coefficient of friction. The thickness variation along paths OA and OC is shown in Figure 4.46, it can be seen that the effect of friction is not significant for either path, though there is some slight variation when the paths pass through a wrinkled area.



a- Thickness distribution (coefficient of friction=0.0)



b- Thickness distribution (coefficient of friction=0.05)



c-Thickness distribution (coefficient of friction=0.1)

Figure 4.45 Thickness distribution on deformed sheet using different coefficients of friction

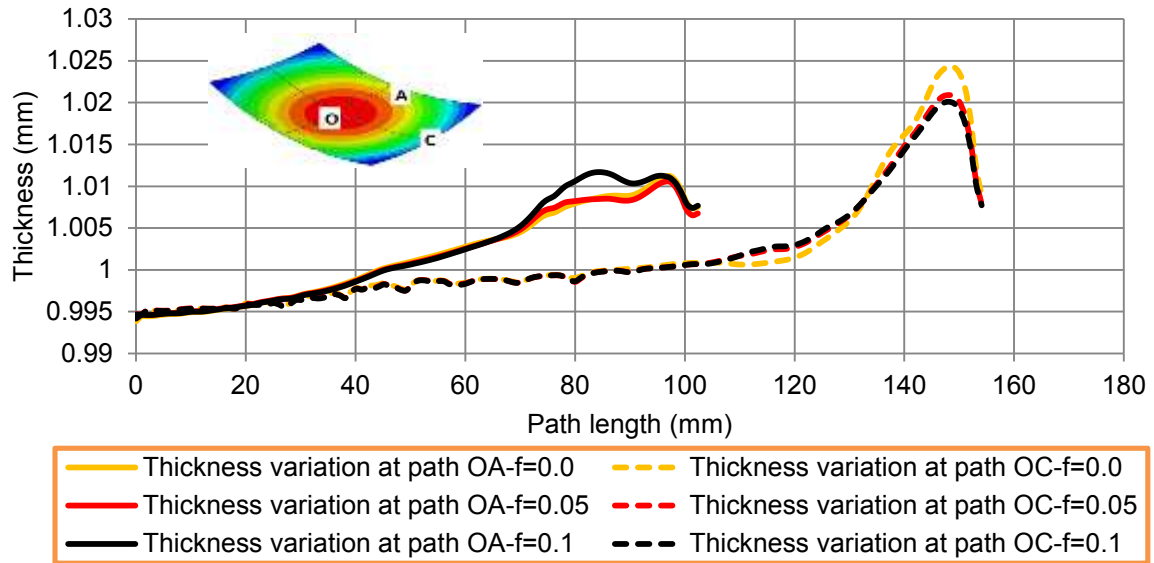


Figure 4.46 Effect of coefficient of friction on thickness distribution along paths OA and OC

4.4 Summary

Many tests have been carried out to determine the mechanical properties of DC05 steel sheet, 5251-O aluminium sheet and polyurethane shore A65 and shore A 90. The samples' preparation and machine setup are explained in Appendix B. The stress-strain curve for DC05 steel sheet, 5251-O aluminium sheet and elastic cushion is shown in Figure 4.2 and Figure 4.5. The plastic anisotropy (r) in three directions and the normal anisotropy coefficient (Ra) of DC05 steel and 5251-O aluminium sheets are illustrated in Table 4.1 and Table 4.2. Comparison between yield stress and ultimate tensile stress for DC05 steel and Aluminium 5251-O at 0° , 45° , and 90° to the rolling orientation are shown in Figure 4.3.

ABAQUS/ Explicit has been used to simulate a multi-point stamping model with and without a blank holder, and simulation time reduced using mass scaling. The experimental results were used to validate the numerical results and showed good agreement. The effect of pin size, curvature of the formed sheet, thickness of elastic cushion, and friction effects on wrinkling, formed profile and thickness variation were investigated using the FE model. The simulated models show the ability for the dynamic explicit FE code to simulate the multi-point forming process successfully. A parametric study was done to study the effect of pin

size, radius of curvature, elastic cushion thickness, and coefficient of friction on wrinkling, deformed profile, and thickness variation. All parameters have important effects on wrinkling, thickness variation and deformed profile, except coefficient of friction which has noticeable effect only on thickness variation.

CHAPTER 5

OPTIMIZATION OF MULTI-POINT FORMING PROCESS PARAMETERS

MPF is subject to many parameters which have been listed previously in this thesis - including tool or workpiece parameters which will include the dimensions of the pin such as tip radius, pin arrangement, and the quality of the tool surface which is directly related to the thickness and elasticity of the cushion. Also of interest are parameters relating to the sheet metal to be formed, its lateral dimensions, its thickness, as well as the properties of the material itself, such as elasticity. To maximise the quality of the part formed by a flexible MPF die it is necessary to carry out an investigation of the effect of the parameters listed, and determine the best possible values of those parameters. Using Design of Experiments (DoE), “a systematic method to determine the relationship between factors affecting a process and the output of that process” [103], and ANOVA (analysis of variance – Design expert 7), the effects of the process parameters listed on sheet metal forming were determined [104-106]. Further, ANOVA and DoE have been used to construct an empirical model relating the listed process parameters to known geometric imperfections of the multi-point stamping process [107]. DoE and numerical simulation were used to determine how variation in the process parameters affected wrinkling, variation in thickness and divergence from the target profile, and hence empirically develop a model for these geometric type errors.

In this study the term “experiment” means an FE simulation using the FE models.

5.1 Methodology of the study

In this study, the DoE included the main MPF process parameters with objective of showing their effect on wrinkling, variation in thickness and divergence from the target profile and to determine which forming parameters had most effect. The next step was to determine those process parameters which gave the best production outcome. The outcomes of the experiment were quantitative measures that can be used to predict the quality of the designated process.

5.2 Procedure for the Design of Experiments

To sensibly design an experiment and analyse the results, one must have a well-defined idea of just what is being studied, what data are of interest, how they are to be collected, and some understanding of how they are to be analysed. The common approach is Design of Experiments (DoE) which is usually follow many steps; chose the response variable, choosen factors and levels, choose the experiment design, implement the experiments, conduct data analysis, and conclude results [108]. The aim of DoE in this study is to determine those factors which have greatest effect on the MPF stamping process and the effect of changing them to better control product quality. DoE was realized using the design of experiment software, DESIGN EXPERT V.7, which is Windows compatible. This software package is designed to identify the most importtant factors that affect a given process or product and has many useful prcedures including a number of experiment design procedures such as factorial design (3 factors each with 3 levels could need as many as 27 tests, so full factorial design tests are generally limited to five variables at most), and response surface method (RSM) which applies statistical tools for analysing the experimental results and modelling them graphically as a response surface [109]. Depending on the number of variables the surface can be plotted in three-dimensional space, or as

contour plots, that allow the shape of the response surface to be “seen”. The surfaces are contours of constant response and the height of each contour corresponds to the magnitude of the response. RSM designs are commonly used to improve or optimise process settings, to make a process of production less sensitive to external, non-controlled influences.

The Central Composite Method (CCM) is a subset of the RSM and has been used in this study. Here each control factor was given one of three values, or levels, and CCM was used to model the likely relationship between input and output parameters. The derived model will determine the output values for any given optimization problem. The response surface is obtained for the design variables using statistical analyses of the experimental results, including, for function approximation, the least square method. All independent variables are assumed to be measurable, continuous and controllable with negligibly small errors. The functional relationship between the response surface and the independent variables is as shown in Equation 5.1:

$$y = f(x_1, x_2, x_3, \dots, x_k) \quad (5.1)$$

where y is the response surface, the response of the system, and x_i the independent variables. The target is to optimize y . Usually, it is necessary to determine an appropriate approximation for y in terms of x_i . Usually, a 2nd order model is used with RSM, see Equation 5.2 [109, 110].

$$y = \beta_0 + \sum_{i=1}^k \beta_i x_i + \sum_{i=1}^k \beta_{ii} x_i^2 + \sum_{i=1}^{k-1} \sum_{j=2}^k \beta_{ij} x_i x_j + \epsilon \quad (5.2)$$

where input parameters x_1, x_2, \dots, x_k affect the response y ;

β_0, β_{ii} ($i = 1, 2, \dots, k$) , β_{ij} ($i = 1, 2, \dots, k; j = 1, 2, \dots, k$) are unknown parameters

where ϵ is the noise or error in y .

In the second order model it is necessary to determine the coefficients, β . This is done by the least square method. Generally, Equation 5.3 is written as:

$$Y = bX + \epsilon \quad (5.3)$$

where ϵ is a matrix of errors, b is a matrix of coefficients, X is a matrix of independent variables, and Y is a matrix of measured values. Matrix manipulation is the usual method for solving Equation 5.3, as shown in Equation 5.4.

$$b = (\hat{X}X)^{-1} \hat{X}Y \quad (5.4)$$

where \hat{X} , is the transpose of the matrix X , and $(\hat{X}X)^{-1}$ is the inverse of the matrix $\hat{X}X$.

5.3 Design of Experiment (DoE)

In Chapter 4, the study showed that the parameters of the Multi-point Forming process that affect product quality are elastic cushion thickness, coefficient of friction, pin dimension, and radius of curvature. The objectives here are to show the effect of these four process factors on wrinkling, deviation from target shape and thickness variation, and to develop a general equation that can predict these selected responses for different process parameters. Central Composite Method design was used to generate a set of experiments for the four process factors where each factor is varied over three levels, high, intermediate and low.

5.3.1 Description of factor levels

Table 5-1 shows the four process factors to be tested, and the physical values assigned to the corresponding levels.

Table 5-1 Process parameters [111]

Parameters	Unit	Levels		
		Low	Intermediate	High
Elastic cushion thickness (A)	mm	3	6	9
Coefficient of friction (B)	----	0	0.05	0.1
Pin dimension (C)	mm	10	15	20
Radius of curvature (D)	mm	400	600	800

5.3.2 Design of experiment (DoE) plan

The DoE RSM design was used to generate a set of experiments for the four process factors with each factor separately assigned three levels, high, intermediate, and low. Table 5-2 presents the results for 27 runs which represent the DoE plan.

Table 5-2 Design of experiment plan [111]

Run	Factor 1	Factor 2	Factor 3	Factor 4
	Cushion thickness (mm)	Friction	Pin dimension (mm)	Radius of curvature (mm)
1	3	0.1	20	400
2	6	0	15	600
3	3	0	20	800
4	9	0	10	400
5	3	0.1	10	400
6	9	0	20	400
7	3	0.1	10	800
8	3	0	10	400
9	6	0.05	15	800
10	3	0	10	800
11	9	0.1	10	800
12	9	0	10	800
13	9	0.1	20	800
14	3	0.05	15	600
15	6	0.05	20	600
16	9	0.1	20	400
17	6	0.05	15	400
18	9	0.05	15	600
19	6	0.1	15	600
20	6	0.05	15	600
21	9	0.1	10	400
22	6	0.05	15	600
23	9	0	20	800
24	3	0.1	20	800
25	6	0.05	15	600
26	3	0	20	400
27	6	0.05	10	600

5.3.3 Quantitative response variable

The forming quality is represented as the quantitative response, which includes wrinkling, deviation between formed and target shape, and thickness variation. The wrinkling was measured as the normal distance between target shape and formed shape as shown in Figure 5.1, and then the root mean square error (RMSE), see Equation 5.5 was used to calculate the equivalent value.

$$RMSE = \sqrt{\frac{1}{n} \sum_{i=1}^n Z_i^2} \quad (5.5)$$

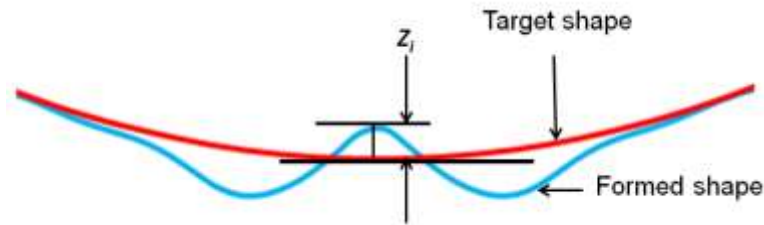


Figure 5.1 Quantification of wrinkling (see Eq. 5.5) [111]

The maximum deviation between the target and formed shape was measured at the centre of the sheet as shown in Figure 5.2.

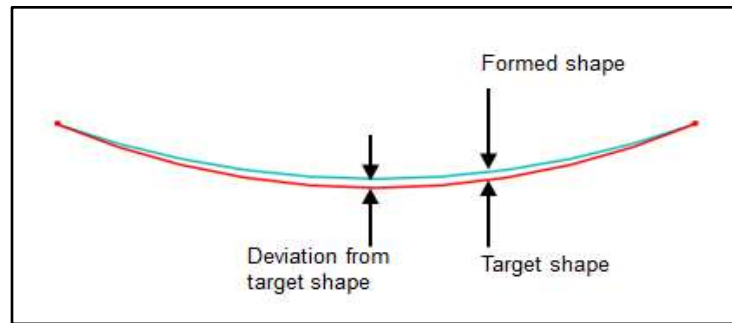


Figure 5.2 Measure of maximum deviation from the target shape [111]

Sheet thickness was measured at different locations across the sheet and the standard deviation (SD), as expressed in Equation 5.6 was used to represent thickness variation.

$$SD = \sqrt{\frac{1}{N} \sum_{i=1}^N (x_i - \bar{x})^2} \quad (5.6)$$

In Equation 5.6; x_i is a value in the i^{th} member of the data set, \bar{x} is the mean of the data set, and N is the number of data points

5.4 Numerical modeling of multi point forming and material data

5.4.1 Model types

FE models were developed for a multi-point forming die, which consists of a pair of pin matrices, a blank sheet and two elastic cushions. Due to symmetry, only a quarter of the die was simulated to reduce computation time. The pins have a hemispherical tip and square cross section. Three pin tip radii were considered, 10 mm, 15 mm and 20 mm. The length of the square cross section was equal to the tip radius. Three pin configurations were simulated: a 10x10 matrix (using a 10 mm pin tip radius), a 6x6 matrix (using a 15 mm pin tip radius) and a 5x5 matrix (using a 20 mm pin tip radius) as shown in

Figure 5.3 (a, b and c). Figure 5.4 shows the pin shapes and dimensions.

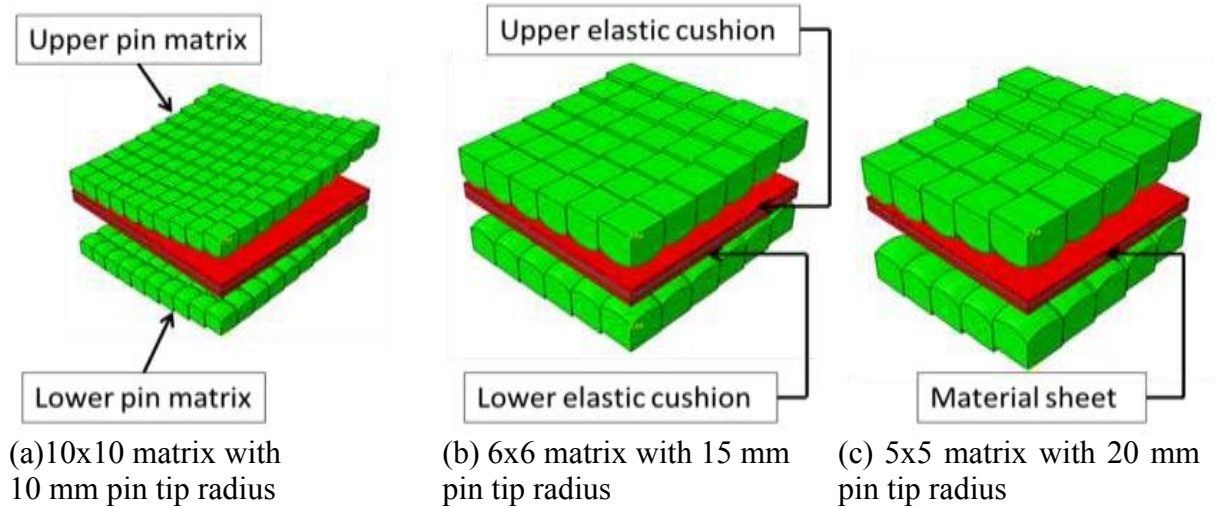


Figure 5.3 Three pin matrix configurations [111]

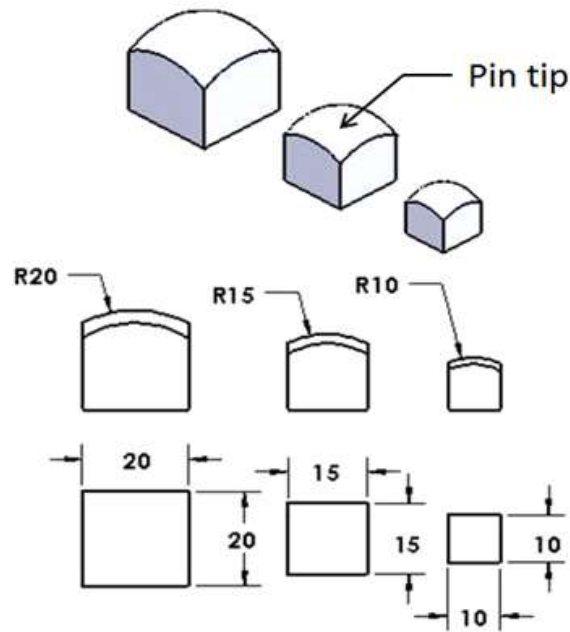


Figure 5.4 The pin shapes and dimensions for the three pin configurations
(All dimensions in mm) [111]

5.4.2 Element types and boundary conditions

The metal sheet and elastic cushion were modelled as deformable bodies using the ABAQUS C3D8R quadratic brick type element [20]. The numbers of mesh elements for the metal sheet and the 3 mm-thick elastic cushion were 288, 300 and 9,248 respectively. The upper and lower dies were modelled as rigid bodies and the element type was the rigid three-dimensional element with four nodes, R3D4. The number of elements for the upper die was equal to that for the lower die in all three models. The mesh elements for the dies with pin sizes 10 mm, 15 mm, and 20 mm were 59,400, 46,080 and 53,550 respectively. Since only a quarter of the model was considered, symmetric boundary conditions were applied to the sheet and elastic cushion. Displacement boundary conditions were used to fix the lower die in the X , Y and Z directions, and the upper die in the X and Z directions. The upper die moved in the Y direction. The FE mesh and boundary conditions are shown in Figure 5.5

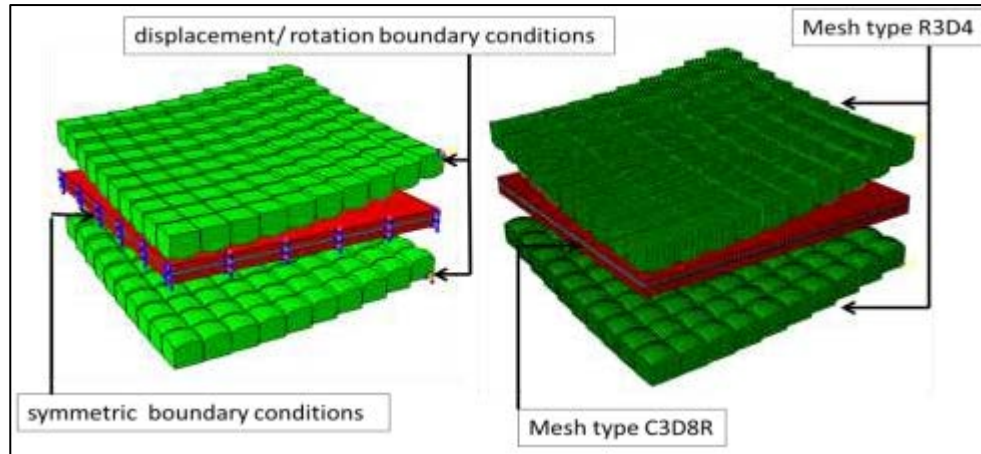


Figure 5.5 Element mesh type and boundary conditions [111]

In common with simulations of other sheet metal forming processes such as conventional deep drawing and stamping, an explicit solver was used to avoid convergence issues because the number of elements was high, and the contact problem was complicated [77, 112].

5.4.3 Material data

The material of the blank sheet used in the numerical simulation is medium strength DC05 steel 1 mm thick, the properties of which were found experimentally, as reported in Chapter 4, see Table 5-3. The material was assumed to be isotropic and the elasto-plastic simulation model was used. A power law equation was selected to represent the flow stress of the material, see Equation 5.7 [113].

$$\sigma = k \cdot \varepsilon^n \quad (5.7)$$

where σ is true stress, k is strength coefficient, ε is true strain, and n is strain hardening.

Table 5-3 Mechanical properties of the sheet metal [111]

Property	Values
Modulus of elasticity (E)	220 GPa
Yield stress (σ)	201.9 MPa
Poisson ratio (ν)	0.3
Density (ρ)	7870 kg/ m ³
Strength coefficient (k)	527.13 MPa
Strain-hardening exponent (n)	0.17

Figure 5.6 shows the stress –strain curve of DC05 sheet steel obtained with a uniaxial tensile test using a Zwick tensile test machine. The curve was generated by fitting a power law to the experimental data.

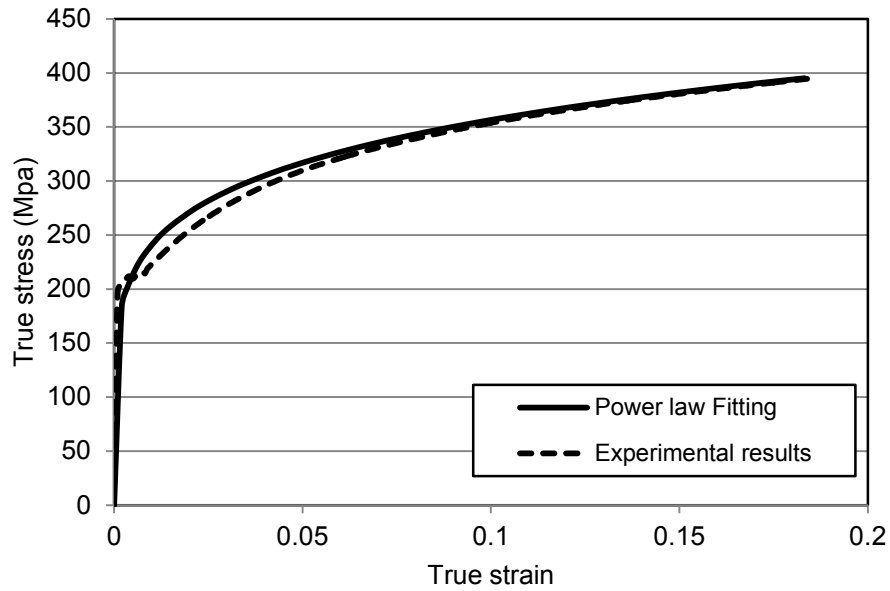


Figure 5.6 Experimental stress-strain results for DC05 sheet steel and fitted curve [111]

An elastic cushion is required in multi-point forming to protect the sheet from dimpling [43, 114]. In this investigation, the material of the elastic cushion was chosen to be Polyurethane A-90 as it is commonly used in this process [43]. Figure 5.7 shows the flow stress for polyurethane A-90 obtained using a Zwick tensile test machine. The experimental results are very similar to those obtained by Seo, et al., [115]. The experimental behaviour of the elastic cushion was also compared against three material models, Mooney-Rivlin, neo-Hooke, and Yeoh. As shown in Figure 5.7, the hyper-elastic model (Mooney-Rivlin model) describes the hyperelastic behaviour of Polyurethane A-90 well. The model can be expressed using Equation 5.8.

$$W = C_{10}(I_1 - 3) + C_{01}(I_2 - 3) \quad (5.8)$$

where W is the strain energy per unit volume, I_1 and I_2 are the first and second invariants of the deviatoric strain tensor and C_{10} and C_{01} are the temperature dependent material

properties obtained from a uniaxial compression test conducted using a material of Shore hardness of 90. The values of C_{10} and C_{01} are 0.861 and 0.354 respectively.

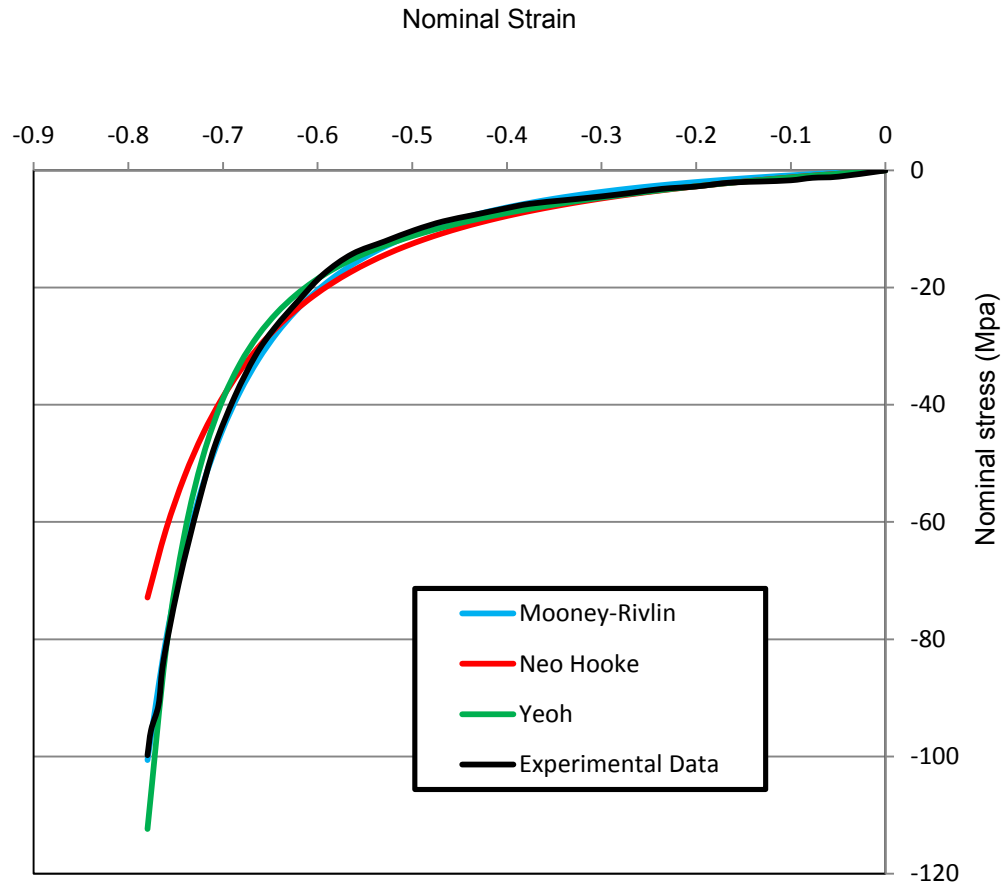


Figure 5.7 Nominal compression stress–strain relationship for polyurethane A-90 compared with Mooney-Rivlin, neo-Hooke , and Yeoh models [111]

5.5 DoE results

Table 5-4 follows the experimental plan based on the RSM, and presents the numerical results for wrinkling, thickness variation, and the deviation between formed and target shapes for all 27 test runs. All the simulation results were statistically analysed using Design Expert 7.0 [116, 117].

Table 5-4 Simulated response results as a function of design parameters [111]

Run	Factor 1 Cushion thickness mm	Factor 2 Friction	Factor 3 Pin dimension, mm	Factor 4 Radius of curvature, mm	Response 1 Wrinkling, m	Response 2 Max. deviation, mm	Response 3 Thickness variation, mm
1	3	0.1	20	400	1.62	2.52	0.002028
2	6	0	15	600	0	0.74	0.000677
3	3	0	20	800	0	0.52	0.000427
4	9	0	10	400	1.64	2.19	0.001187
5	3	0.1	10	400	1.27	1.84	0.001847
6	9	0	20	400	1.79	2.50	0.000935
7	3	0.1	10	800	0	0.37	0.000571
8	3	0	10	400	1.46	2.19	0.001781
9	6	0.05	15	800	0	0.33	0.000420
10	3	0	10	800	0	0.30	0.000543
11	9	0.1	10	800	0	0.46	0.001631
12	9	0	10	800	0	0.62	0.000659
13	9	0.1	20	800	0	0.74	0.000650
14	3	0.05	15	600	0	0.68	0.000682
15	6	0.05	20	600	0.75	1.06	0.000734
16	9	0.1	20	400	1.75	2.48	0.001948
17	6	0.05	15	400	1.10	1.48	0.001197
18	9	0.05	15	600	0	0.77	0.000793
19	6	0.1	15	600	0	0.68	0.001175
20	6	0.05	15	600	0	0.66	0.000838
21	9	0.1	10	400	1.60	2.02	0.004672
22	6	0.05	15	600	0	0.66	0.000838
23	9	0	20	800	0	0.78	0.000424
24	3	0.1	20	800	0	0.55	0.000459
25	6	0.05	15	600	0	0.66	0.000838
26	3	0	20	400	1.69	2.66	0.001879
27	6	0.05	10	600	0	1.09	0.001146

Analysis of Variance (ANOVA) was performed to identify significant process parameters.

In this investigation, the null hypothesis was that the factor under consideration had insignificant effect. A significance level of 5% was used which means that the more the *P*-value falls below 5% the more important the factor [118]. Table 5-5 shows the *P*-value for the main factors and interactions. The ANOVA results suggest that a quadratic model

closely describes the wrinkling and maximum shape deviation while a two-factor interaction model provides a very good prediction of the thickness variation. The *R*-square and adjusted *R*-square values, which are measures of model fit, did not go below 95% for any of the responses.

Table 5-5 Significant factors and corresponding P-values [111]

Response factors Significant factors	Wrinkling	Max. shape deviation	Thickness variation
Cushion thickness (A)	0.2999	0.1691	0.2193
Friction (B)	0.6276	0.2110	0.0071
Pin size (C)	0.0344	0.0010	0.0454
Radius of curvature (D)	<0.0001	<0.0001	<0.0001
Significant interaction	-	-	AB=0.0145 AC=0.0476

The ANOVA results in Table 5-5 indicate that radius of curvature and pin size are the most important factors and have a significant effect on wrinkling, maximum shape deviation, and thickness variation. Friction has a significant effect only on thickness variation, while cushion thickness has no important effects. Additionally, interactions between cushion thickness and friction and between cushion thickness and pin size did significantly affect sheet thickness variation.

5.5.1 Wrinkling

Figure 5.8 shows the effect of pin size and radius of curvature on wrinkling. It can be seen from the surface plot that wrinkling increased noticeably with a decrease in the radius of curvature. Figure 5.9 reveals the stress distribution on both sides of the sheet when a small radius of curvature is used. A small radius of curvature will lead to large bending deformation combined with plane stress, as the sheet surface tries to contract under the pins. This leads to stress instability and wrinkling [47]. Small pins (less than 12.5 mm) or large pins (more than 17.5 mm) will increase wrinkling. Using pins that are too small will reduce

the pin offset (the height difference between two adjacent pins), which forces the elastic cushion to flow towards the sheet edges. As such, the thickness of the elastic cushion at the edges increases, which leads to wrinkling. Too large a pin size will increase the pin offset causing non-uniform stress distribution especially at the edges of the sheet (where wrinkling takes place). Minimal wrinkling can be obtained by using a large radius of curvature (800 mm) with medium size pins (15 mm).

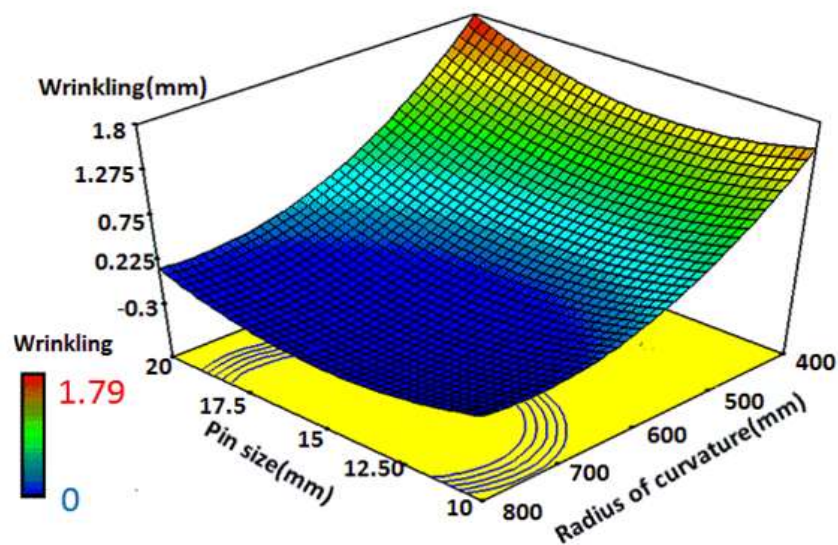


Figure 5.8 Effect of pin size and radius of curvature on wrinkling [111]

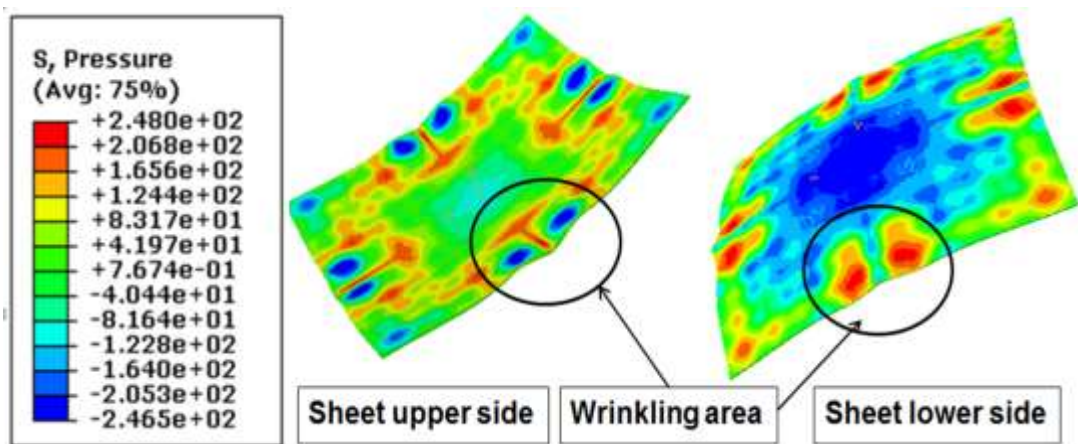


Figure 5.9 Pressure distributions on upper and lower sides of formed sheet (radius of curvature =400mm) [111]

5.5.2 Maximum shape deviation

Figure 5.10 shows the effect of pin size and radius of curvature on the maximum shape deviation. It can be seen from the surface plot that the maximum deviation increases with decrease in the radius of curvature. Using small pins (less than 12.5 mm) or large pins (more than 17.5 mm) will increase the maximum deviation. Figure 5.11 shows the pressure distribution on the deformed sheet when small pins and large pins are used. Too small a pin (less than 12.5 mm) will reduce the contact area which increases stresses. Excessive stresses will over-deform the sheet and increase the maximum deviation from the target shape. Too large a pin (more than 17.5 mm) will increase the contact area, reducing stresses. Having insufficient stresses does not provide the required deformation and increases the deviation from the target. The minimum deviation from the target shape can be obtained when using a large radius of curvature (800 mm) with medium size pins (15 mm).

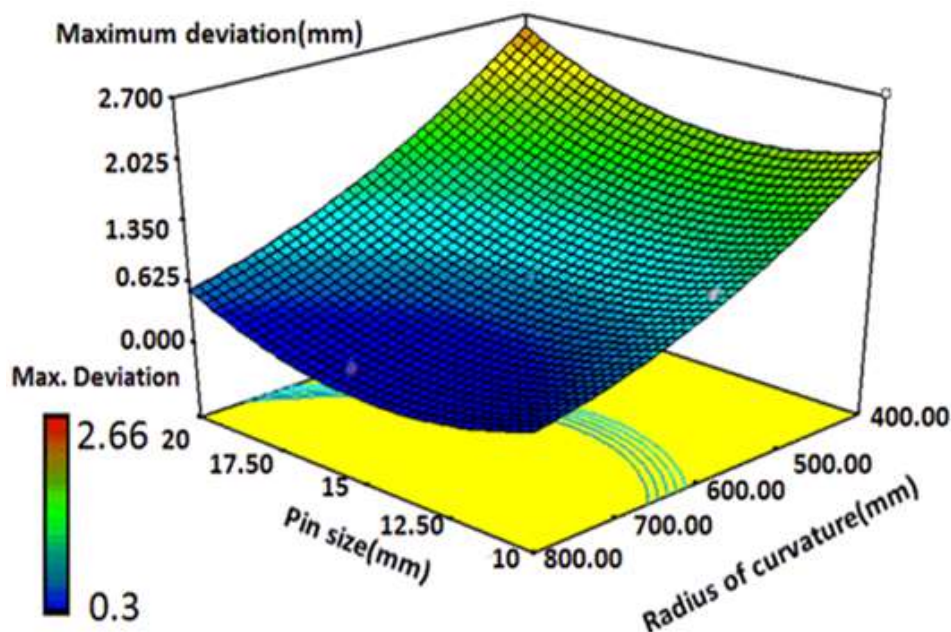


Figure 5.10 Effect of pin size and radius of curvature on maximum shape deviation [111]

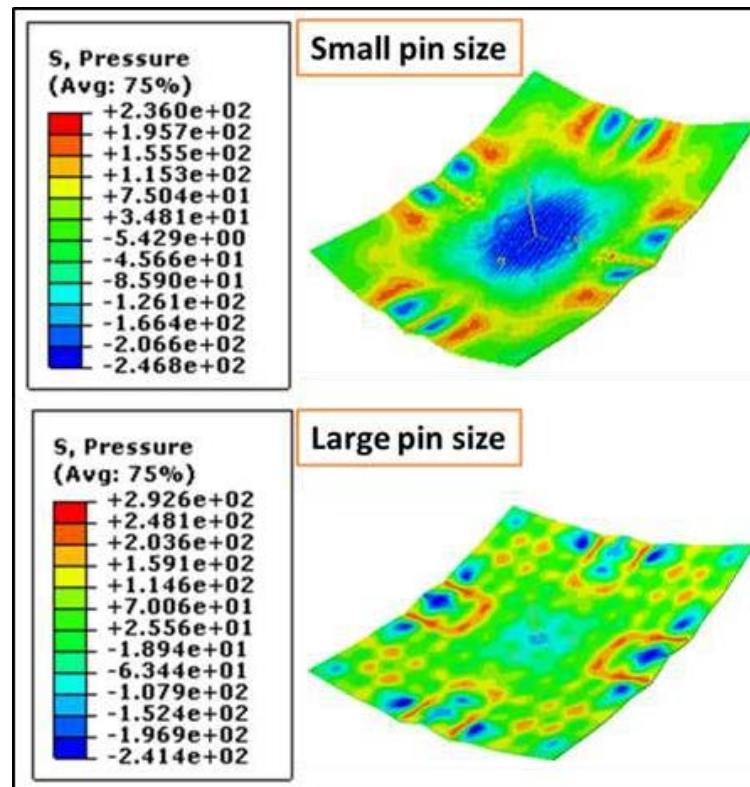


Figure 5.11 Pressure distribution on the formed sheet for small and large pin sizes (radius of curvature =400mm) [111]

5.5.3 Thickness variation

Figure 5.12 show the effect of the coefficient of friction and pin size on thickness variation and, as can be seen, the higher the coefficient of friction, the larger the thickness variation. When the coefficient of friction increases, relative motion between the sheet and the cushion becomes more difficult, this resists material flow which leads to sheet thinning in the middle of the die and thickening at the sheet edges [119]. Additionally, small pin size leads to an increase in the thickness variation. When small pins are used, the spacing between pin tips decreases which causes more resistance to the flow and deformation of the elastic cushion. This leads to non-uniform deformation of the sheet. The minimum thickness variation is obtained with large pins and zero friction.

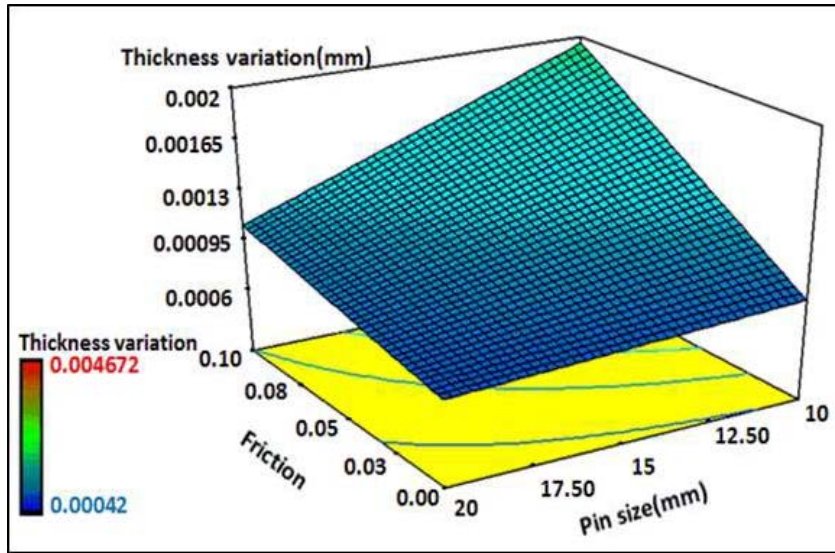


Figure 5.12 Effect of coefficient of friction and pin size on thickness variation [111]

Figure 5.13 shows the effect of friction and radius of curvature on thickness variation, it can be seen that the thickness variation increased with increasing friction and curvature. The maximum thickness variation occurs for the smallest radius of curvature (400 mm) and highest friction (0.1). With small curvature, fewer pins are in contact with the sheet at the beginning of deformation and stress concentrations will occur, leading to localised sheet thinning in the middle of the sheet [120].

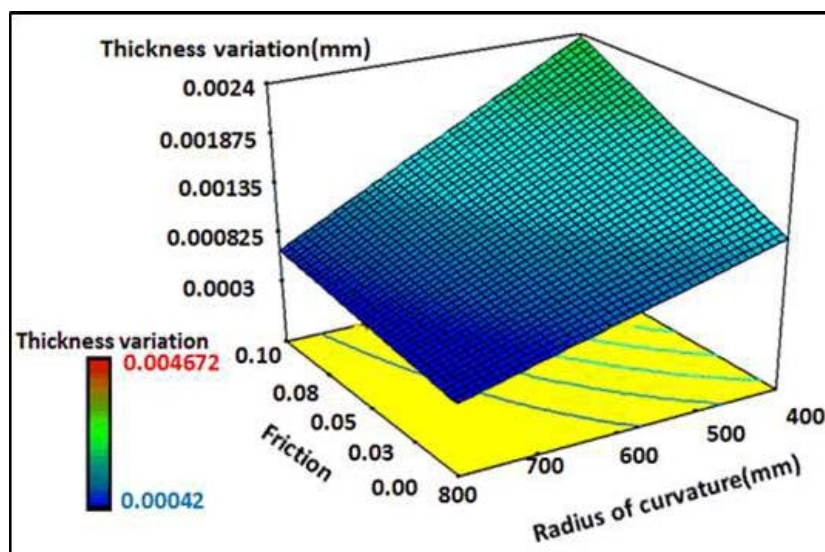


Figure 5.13 Effect of coefficient of friction and radius of curvature on thickness variation [111]

Figure 5.14 shows the effect of interaction between elastic cushion thickness and coefficient of friction on workpiece thickness variation. With no friction, the workpiece thickness variation decreases with increase in elastic cushion thickness. With friction, the variation in the workpiece thickness increases with the elastic cushion thickness. A thick elastic cushion is expected to expand laterally when compressed. However, a high coefficient of friction will resist this movement which leads to non-uniform deformation

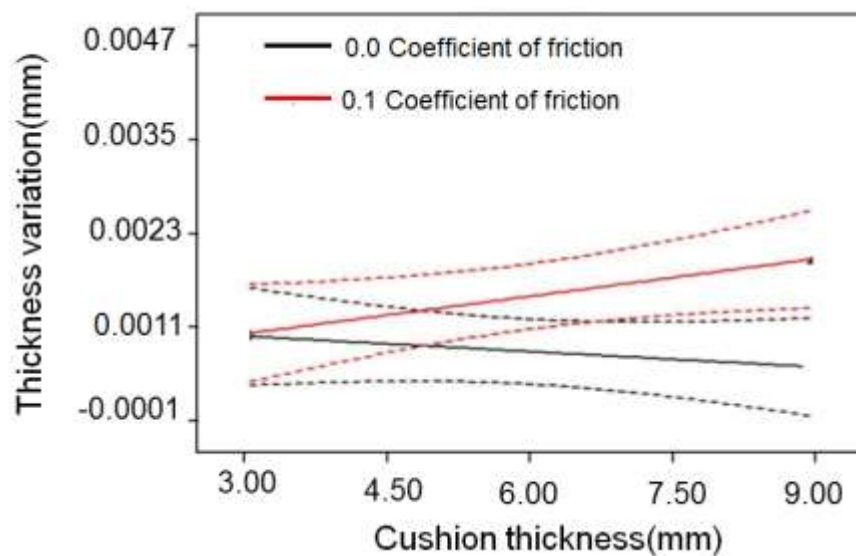


Figure 5.14 Effect of interaction between cushion thickness and coefficient of friction on workpiece thickness variation [111]

Figure 5.15 shows the effect of elastic cushion thickness and pin size on workpiece thickness variation. With large pins, increased cushion thickness decreases workpiece thickness variation. However, when small pins are used, increasing the elastic cushion thickness will lead to an increase in the thickness variation [119]. This is because the gaps between the pins become smaller, which restrains the deformation of the elastic cushion.

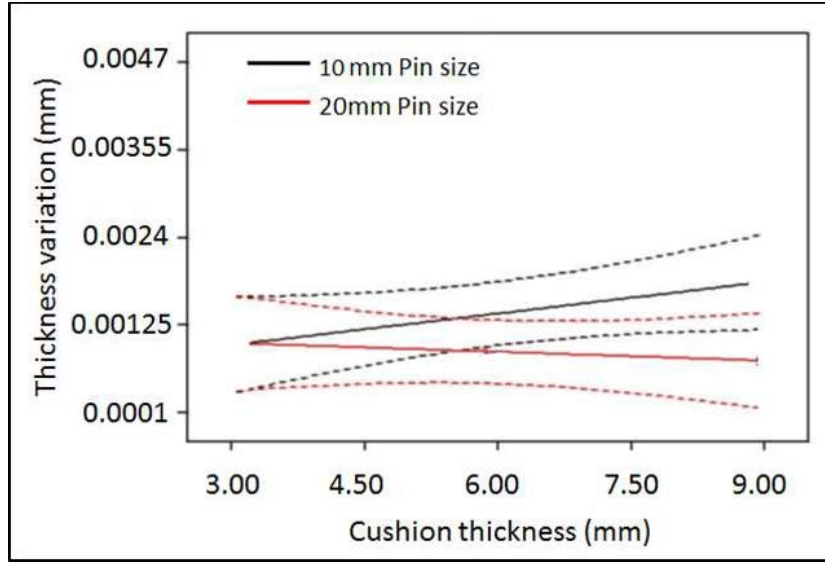


Figure 5.15 Effect of interaction between cushion thickness and pin size on workpiece thickness variation [111]

Thus, the largest variation in workpiece thickness arises with a combination of a thick elastic cushion, small pins and large coefficient of friction.

5.6 Prediction of each quality characteristic

An empirical model has been developed to predict wrinkling, maximum deviation from target and thickness variation using a general second-order polynomial equation (Equation 5.9) [111]. This equation was constructed based on the four process parameters; elastic cushion thickness, coefficient of friction, pin size and radius of curvature. Depending on the response parameter, each process parameter has related coefficients as listed in

Table 5-6

$$\begin{aligned} \text{Response}(q) = & k_0 + k_1 A + k_2 B + k_3 C + k_4 D + k_5 AB + k_6 AC + k_7 AD + k_8 BC + \\ & k_9 BD + k_{10} CD + k_{11} A^2 + k_{12} B^2 + k_{13} C^2 + k_{14} D^2 \end{aligned} \quad (5.9)$$

where q is the response parameter (i.e. wrinkling, maximum deviation from target or thickness variation), A is the elastic cushion thickness, B is the coefficient of friction, C is

the pin size, and D is the radius of curvature; k_0 to k_{14} are model coefficient values corresponding to each response parameter. Table 5.6 shows the values of k_0 - k_{14} .

Table 5-6 Coefficient values corresponding to each response parameter [111]

Coefficient	Wrinkling [mm]	Maximum deviation [mm]	Thickness variation [mm]
k_0	8.72134	8.62860	1.8125E-003
k_1	0.12240	-0.09776	1.9210E-004
k_2	-1.09204	-6.59537	0.018333
k_3	-0.34898	-0.41928	4.7636E-005
k_4	-0.01809	-0.01117	-3.4404E-006
k_5	0.07500	0.00000	2.2588E-003
k_6	-0.00117	-1.4167E-003	-1.7679E-005
k_7	-0.00008	9.1667E-005	1.5235E-007
k_8	0.03632	+0.11000	-7.8275E-004
k_9	0.00215	3.6250E-003	-2.1594E-005
k_{10}	-0.00006	-6.7500E-005	7.8313E-008
k_{11}	-0.00406	6.7696E-003	-
k_{12}	-14.6074	18.3704	-
k_{13}	0.01352	0.016437	-
k_{14}	0.00001	6.02315E-006	-

5-7 Optimisation of process parameters

Optimal working parameters were chosen to yield a spherical shape product that had almost no wrinkling, and minimal shape deviation and thickness variation. The set of process parameters that can achieve this objective was numerically obtained as shown in Table 5-7. The optimal setting is; 10 mm pin size, 3 mm cushion thickness, 0.08 coefficient of friction, and 800 mm radius of curvature. A single experiment was carried out using a MPF die with 10 mm pins (see Figure 5.16 (a)) to validate these results. The fabricated part is shown in Figure 5.16 (b). The sheet was cut into two halves (see Figure 5.16 (c)). The profile of the deformed sheet was measured using a high-resolution 3D Laser Scanner. The data was then used to compare the formed shape with the target shape and to calculate the maximum

deviation from target, as shown in Figure 5.17. The thickness was measured using a high-resolution point type digital micrometre at 17 points across the centre line of the deformed sheet, see Figure 5.17. Table 5-8 shows that predicted results agree well with measurements.

Table 5-7 Optimal work parameters [111]

	Cushion thickness(mm)	Friction	Pin size(mm)	Radius of curvature(mm)
Optimal condition	3	0.08	10	800

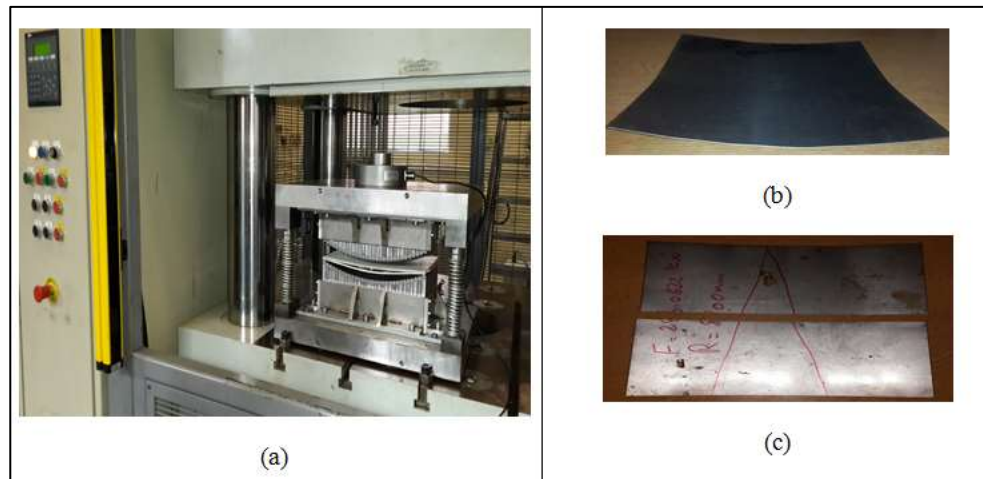


Figure 5.16 [111] (a) Multi-point forming die, (b) Fabricated part, and (c) Part cut into two halves

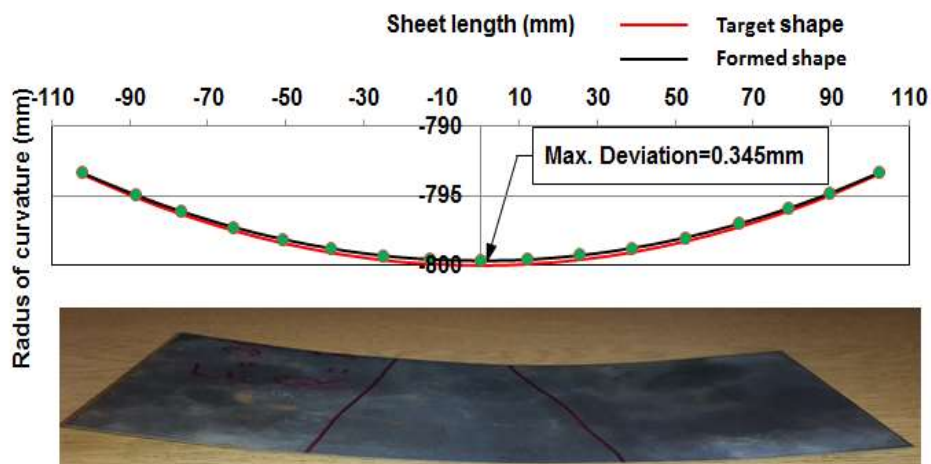


Figure 5.17 Comparison of formed shape with target shape [111]

Table 5-8 Comparison of formed shape with target shape [111]

	Wrinkling [mm]	Max. deviation [mm]	Thickness variation [mm]
Predicted values	(2.019 E-007)≈0	0.3111	0.000575
Observed values	0.00	0.345	0.000560

5-8 Summary

A FE model for multi-point forming has been used to study wrinkling, deviation from target profile, and thickness variation in the forming of a hemispherical shape. DoE was used to generate a set of experiments for four process factors: elastic cushion thickness, coefficient of friction, pin dimension and radius of curvature. Analysis of Variance (ANOVA) was used to identify the most significant of the process parameters on process defects.

This investigation established the following:

1. The pin size and formed radius of curvature have a significant effect on all response parameters, i.e. wrinkling, maximum deviation from target shape, and thickness variation, while the coefficient of friction has a significant effect only on thickness variation.
2. For each of the response parameters, there were significant parametric interactions; a mathematical model was successfully derived to describe the influence of the process parameters on the formed sheet.
3. As the workpiece radius of curvature decreased, wrinkling, maximum shape deviation and thickness variation increased. Both large and small pins lead to increased wrinkling and shape deviation, but using larger pins reduces thickness variation. A high coefficient of friction leads to increased thickness variation.
4. Using the model a doubly curved sheet was produced with no wrinkling, accurate dimensions and high thickness uniformity.

CHAPTER 6

INVESTIGATION OF THE RELATION BETWEEN WRINKLING AND THICKNESS: MODELLING AND EXPERIMENTAL RESULTS

Often a double curved shape is fabricated using the stamping process; this type of shape has two radii of curvature and requires plastic deformation of the sheet metal. As a result of plane stresses, wrinkling occurs when one of the plane stresses (σ_x , σ_z) in an element is compressive above a certain value. In double curved elements, wrinkling appears in the middle of the edges because maximum lateral compressive stress occurs at maximum deflection, see Figure 6.1. There are many parameters that affect the onset of wrinkling; geometric parameters, process parameters and material properties. Thus, to study the relation between wrinkling, radius of curvature and sheet thickness, the geometric and process parameters must be maintained constant. Also, a blank holder is used to show the effect of material stretching on wrinkling.

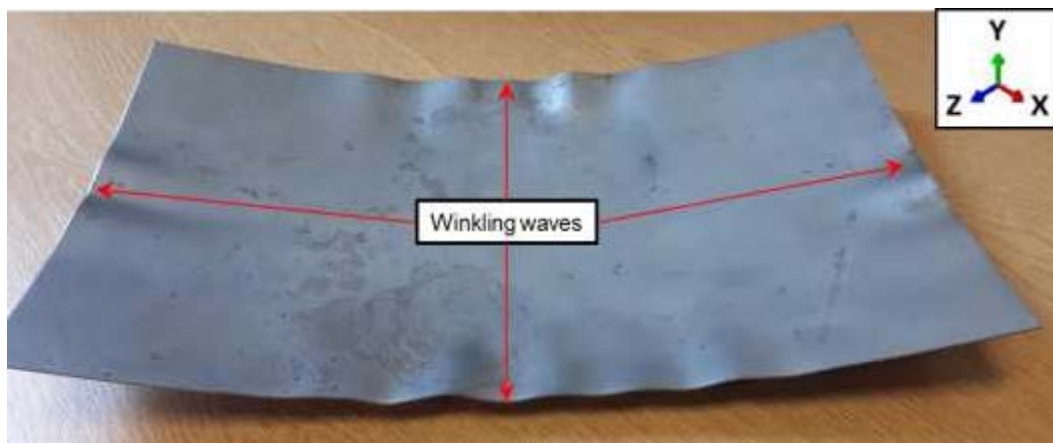


Figure 6.1 Wrinkling on double curved sheet

6.1 Numerical investigation of the relation between wrinkling and thickness variation

In this section, ABAQUS/ dynamic explicit 3-D FE modelling was employed to investigate the relation between wrinkling and thickness variation on hemispherical parts formed by a multi-point stamping die applied to a flat rectangular metal sheet. As can be seen in Figure 6.2 the two FE models (with and without blank holder) developed in Chapter Four are used.

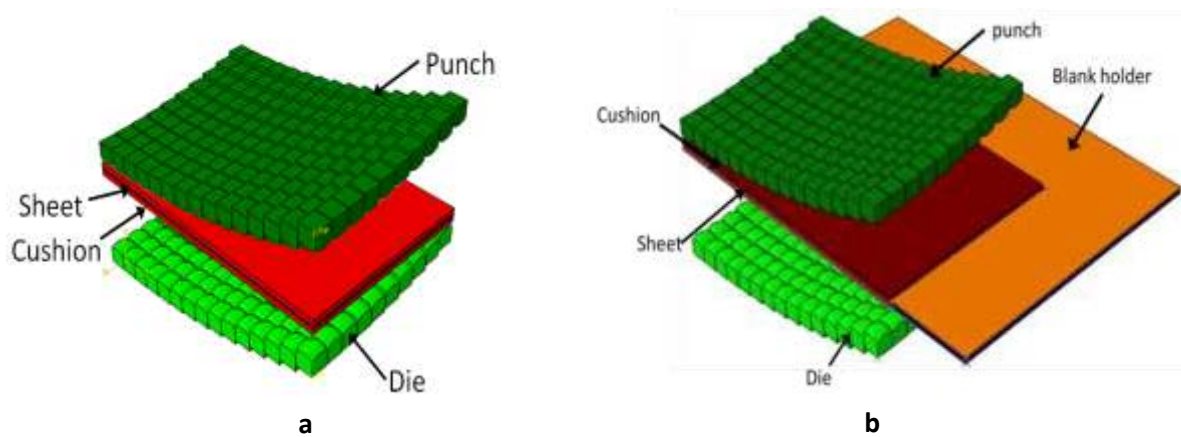


Figure 6.2 3-D FE model a) without blank holder b) with blank holder

The sheet materials used are medium strength DC05 steel and 5251-O aluminium with 1 mm and 1.2 mm thickness respectively, and rectangular shape of 102.25 mm x 153.5 mm in the test without a blank holder, and 162.25 mm x 213.5 mm in the test with a blank holder. The mechanical properties of two materials were determined experimentally, see Appendix B. The geometry of the final formed part is a double curved plate with outer radii of 400 mm and 800 mm, see Figure 6.1.

6.1.1 Stress distribution on deformed sheet without blank holder

During the forming of doubly curved parts with different curvatures, defects can appear as wrinkling in the middle of the sheet edges, which is considered to be due to geometrical factors such as sheet dimensions and radius of curvature. Figure 6.3 to Figure 6.6 show the

stress distribution on the rectangular 5251-O aluminium and DC05 steel sheets formed when the radii of curvature are 400 mm and 800 mm. It can be seen that in both cases the stress concentration occur in the middle of edges of the formed surfaces. When the radius of curvature is increased from 400 mm, to 800 mm, the stress concentration is reduced and becomes more uniform. The values of the stress in the longer sides of the sheet are higher than for the short sides for both aluminium and steel, and both radii of curvature. For aluminium with radii of curvature 400 mm and 800 mm, the maximum stress values were 178 MPa and 123.5 MPa, respectively. For steel the corresponding values were 324.9 MPa and 252.9 MPa.

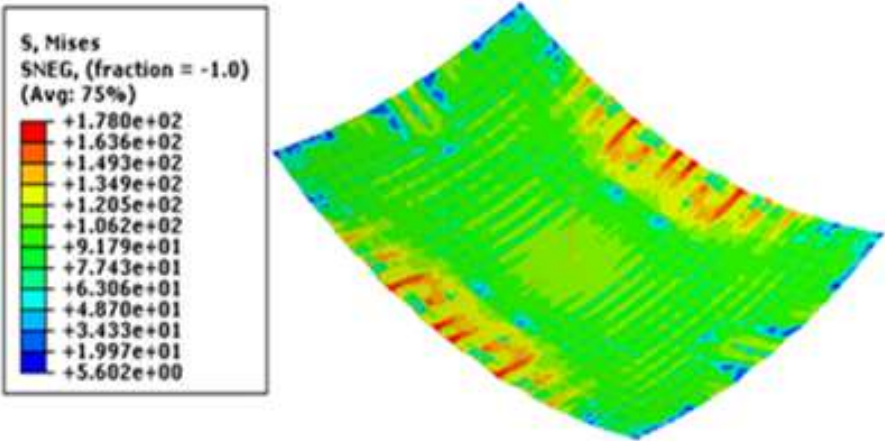


Figure 6.3 Mises stress distribution for 5251-O aluminium sheet (radius of curvature 400 mm)

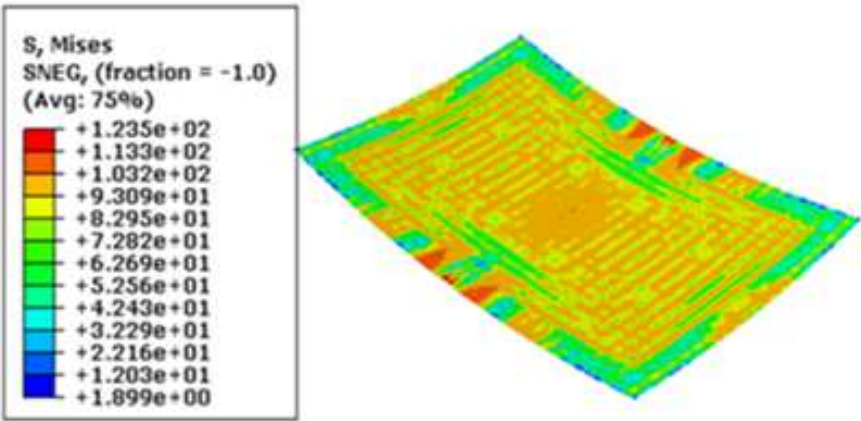


Figure 6.4 Mises stress distribution for 5251-O aluminium sheet (radius of curvature 800 mm)

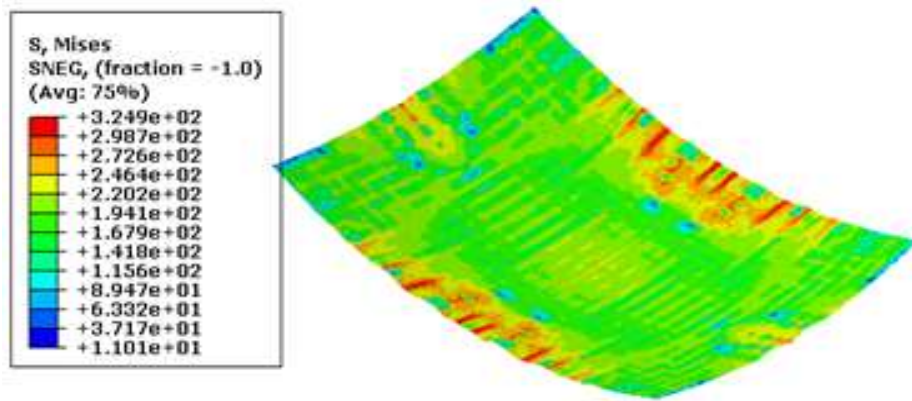


Figure 6.5 Mises stress distribution for DC05 steel sheet (radius of curvature 400 mm)

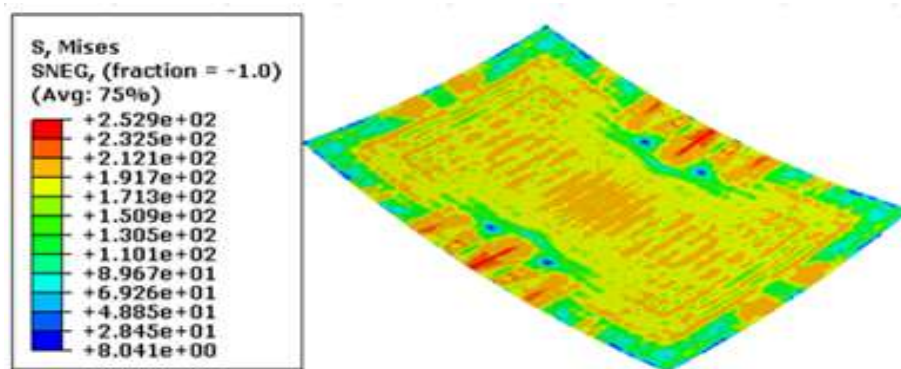
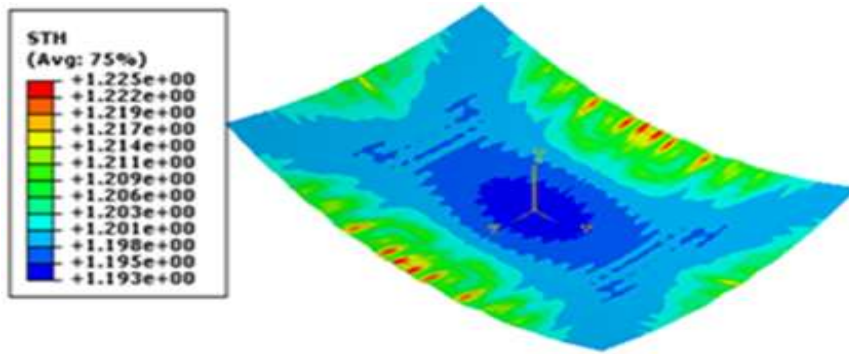


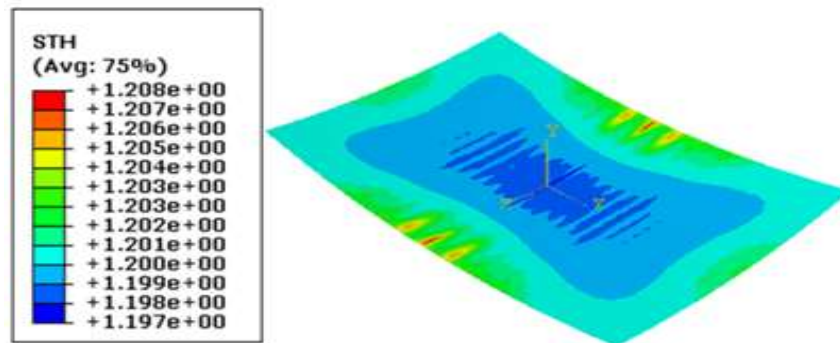
Figure 6.6 Mises stress distribution for DC05 steel sheet (radius of curvature 800 mm)

6.1.2 Thickness distribution and material flow of deformed sheets without blank holder

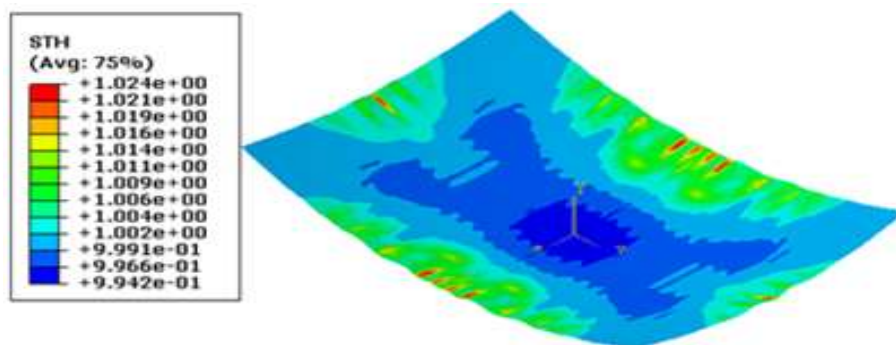
Figure 6.7 a-d shows the thickness of 5251-O aluminium and DC05 steel sheets formed with two different radii of curvature. After analysing the curves representing the mises stress distribution, it was found that the thickness variation is not uniformly related to the stress distribution. It can be seen in Figure 6.8 a and b that the sheet material flows from the centre outwards, this means the thickness of the deformed sheet has minimal value at the centre, and thickness increases towards the sheet edges. This result is in good agreement with published work [121]. With the 400 mm radius of curvature, the thickness of the aluminium sheet ranged from 1.193 to 1.225 mm and for steel from 0.994 to 1.024 mm, the sheet metal flows toward the edges of the sheet increased the thickness noticeably, but inhomogeneously. With the 800 mm radius of curvature the corresponding figures were from 1.197 to 1.208 mm and from 0.9973 to 1.008 mm for aluminium and steel respectively.



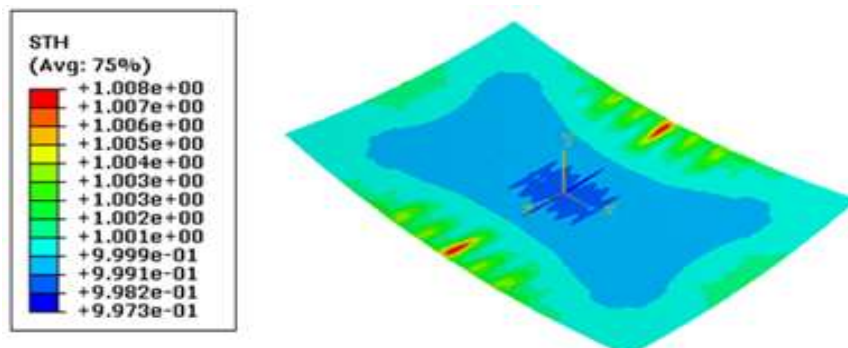
a - Aluminium; R=400 mm



b - Aluminium; R=800 mm

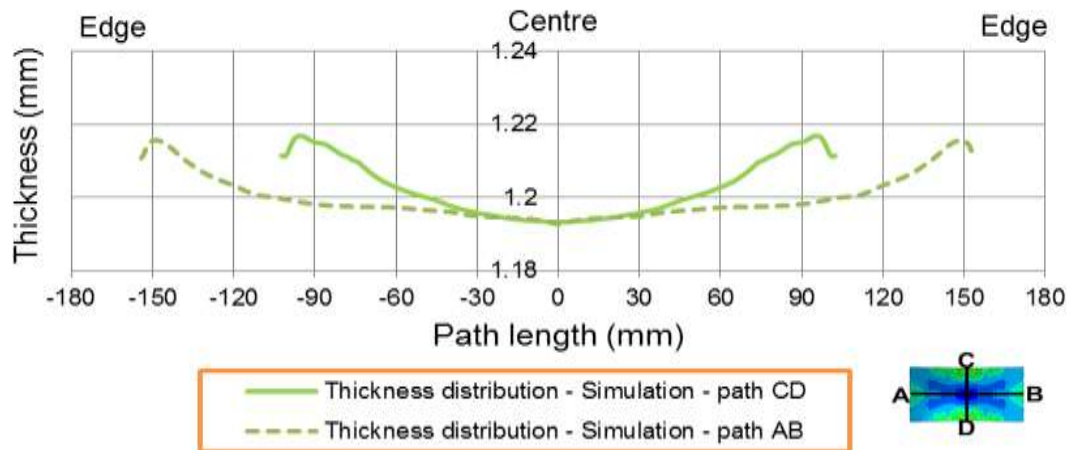


c - Steel; R=400 mm

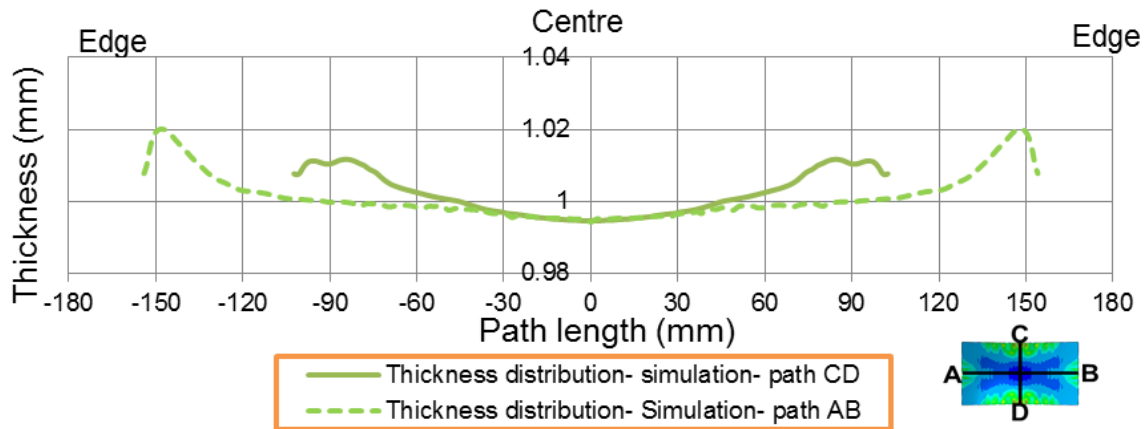


d - Steel; R=800 mm

Figure 6.7 Thickness distribution for 5251-O aluminium and DC05 steel sheets
(R= radius of curvature)



a-Thickness distribution on paths AB and CD for 5251-O aluminium sheet, $R=400\text{mm}$



b-Thickness distribution on paths AB and CD for DC05 steel sheet, $R=400\text{mm}$

Figure 6.8 Simulation results of thickness distribution at centre of deformed aluminium and steel sheets

Figure 6.9 to Figure 6.11, show the logarithmic strain in three planes parallel to the face of the aluminium and steel sheets during the forming process. “Element 1” is the top surface of the plate, “Element 2” is the plane through the centre of the plate and “Element 3” is the bottom surface of the plate. In this case, the radius of curvature of the deformed sheets was 400 mm. Figure 6.9 a shows the logarithmic strain in region A (at centre of the sheet) for each of the three planes. It can be seen that, initially, there is negligible logarithmic strain in any of Element 1, 2 or 3 until half way through the deformation process (1.5 seconds), this is

followed by an increasing negative logarithmic strain until the end of the process, which means thinning of the sheet. Figure 6.10 shows the logarithmic strain in the three elements for region B, between the central region and edge of the sheet. It can be seen that there is a thinning of lower element and thickening of the upper. Figure 6.11 shows the logarithmic strain in the three elements for region C, at edge of the sheet. It can be seen that until about 2 seconds from the start of the process there is no change in logarithmic strain, from 2 to 2.5 seconds there is a slight change in the logarithmic strain which increases both positively and negatively (for elements 1 and 3 respectively), at 2.5 seconds there is a sharp increase in positive logarithmic strain for the upper element 1, and sharp increase in negative logarithmic strain for the lower element 3 until the end of the process.

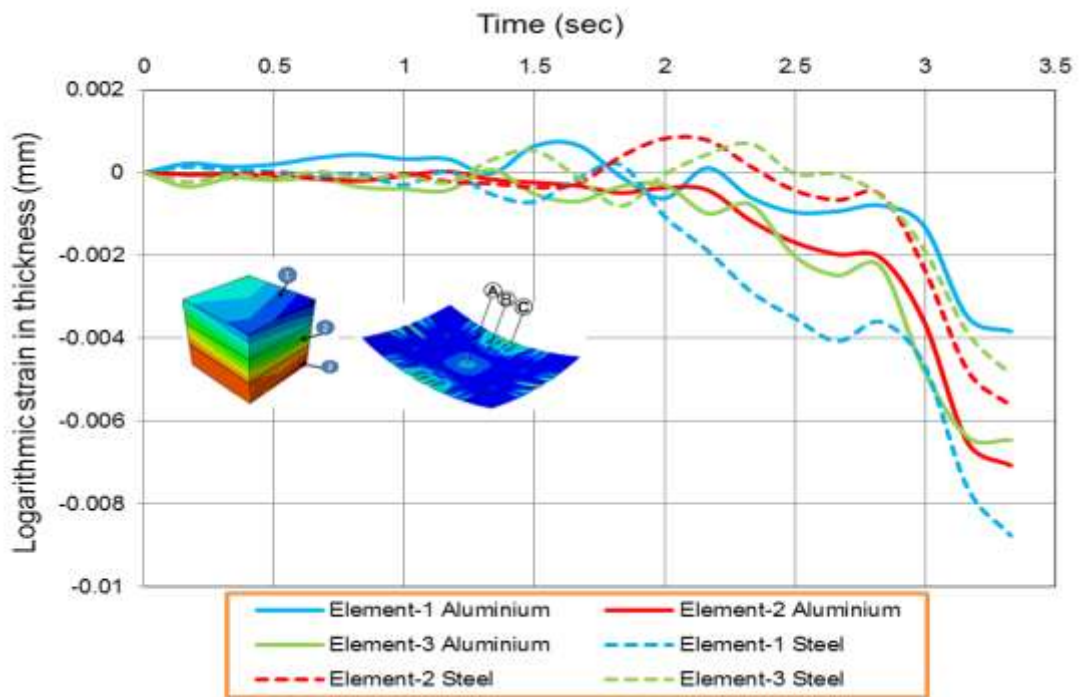


Figure 6.9 Logarithmic strain at centre of the sheet (area A) for deformed DC05 steel sheet and 5251-O aluminium sheet, $R = 400$ mm

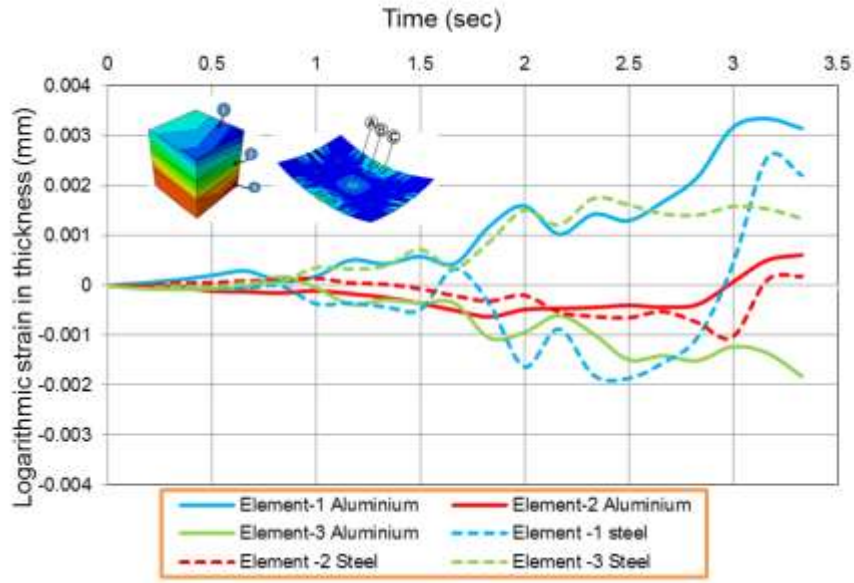


Figure 6.10 Logarithmic strain at between the central region and edge of the sheet (area B) for deformed DC05 steel sheet and 5351-O aluminium sheet, $R = 400$ mm

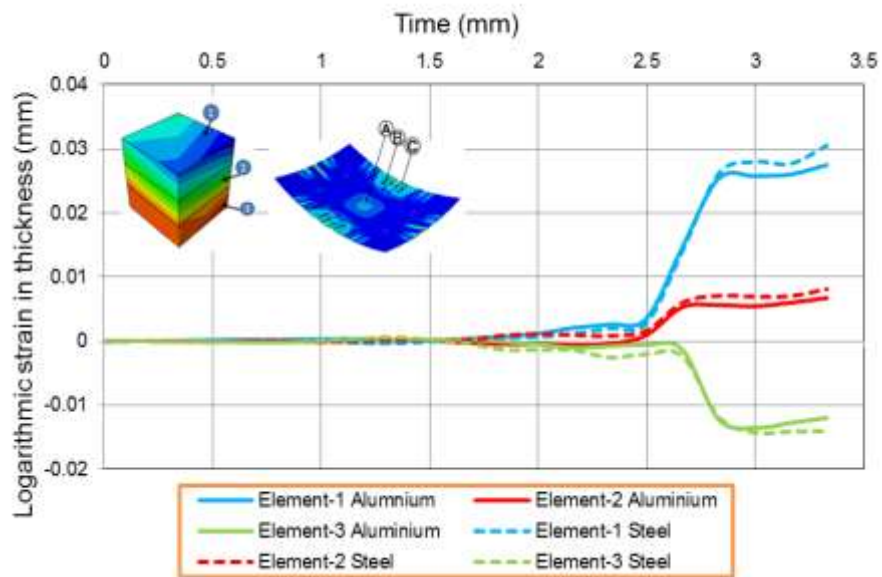


Figure 6.11 Logarithmic strain at edge of the sheet (area C) on deformed DC05 steel sheet and 5251-O aluminium sheet, $R = 400$ mm

6.1.3 Wrinkling and deformed sheets without blank holder

Wrinkling appears on the deformed sheet in the area where thickening occurs as a result of lateral compression stresses. Figure 6.12 and Figure 6.13 show the thickness variation and deformed shapes along the two paths, AB and CB on 5251-O aluminium and DC05 steel

sheets formed with a 400 mm radius of curvature. Comparing formed shapes with the target shape, it can be seen that wrinkling appears in the middle of both short and long sides of the sheet. The amplitude and number of wrinkle waves along AB (long side) are greater than for the short side (CB), which corresponds to the thickness values and thickness variation. The maximum thickening for aluminium and steel are reached about 1.8% and 1.7% respectively from the main thickness on long side(AB), and about 1% and 1.25% respectively from the main thickness on short side (CB) side. From these results, it can be concluded that greater thickening and thickness variation leads to more wrinkling.

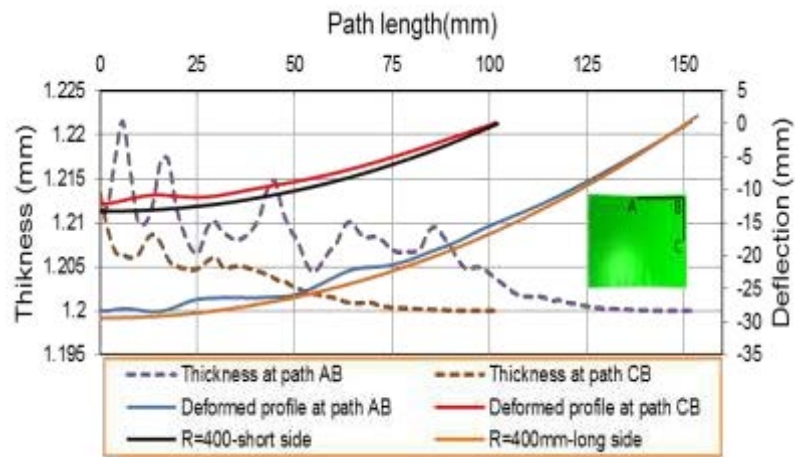


Figure 6.12 Thickness distribution and formed shape for both long and short sides of 5251-O aluminium sheet (radius of curvature, 400 mm)

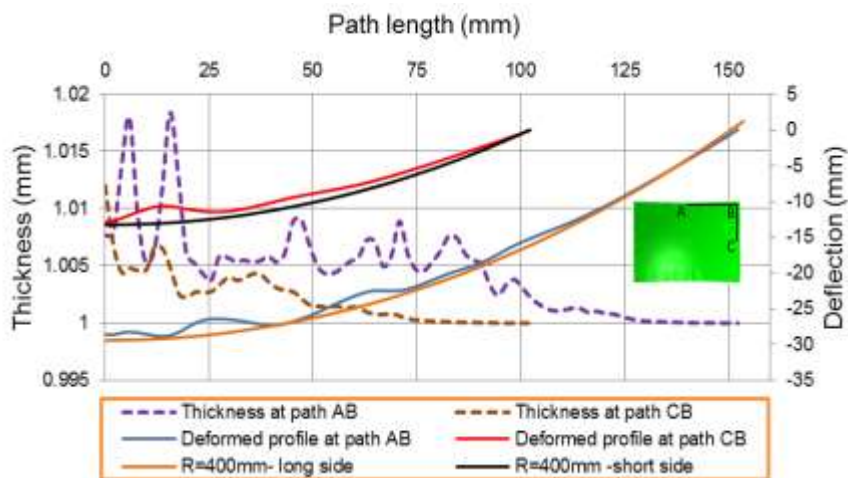


Figure 6.13 Thickness distribution and formed shape for both long and short sides of DC05 steel sheet (radius of curvature, 400 mm)

Figure 6.14 and Figure 6.15 show the thickness variation and deformed shapes along the two paths, AB and CB on 5251-O aluminium and DC05 steel sheets formed with 800 mm radius of curvature. It can be seen the maximum thickening and thickness variation are both less than for the sheet formed with a 400 mm radius of curvature. The maximum thickening for aluminium and steel are reached about 0.55% and 0.6% respectively from the main thickness on long side (AB), and about 0.15% and 0.18% respectively from the main thickness on short side (CB). For that reason, the wrinkling is largely eliminated along the short side and it is negligible on the long side of the sheet.

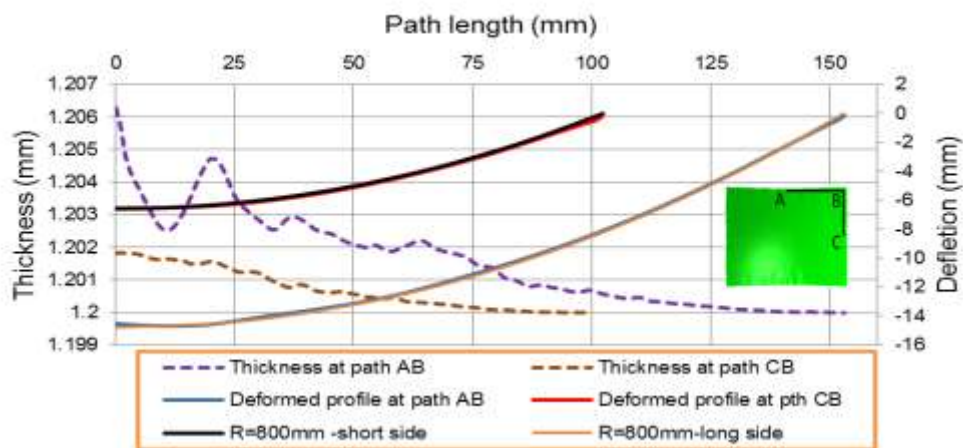


Figure 6.14 Thickness distribution and formed shape on both long and short sides of 5251-O aluminium sheet (radius of curvature, 800 mm)

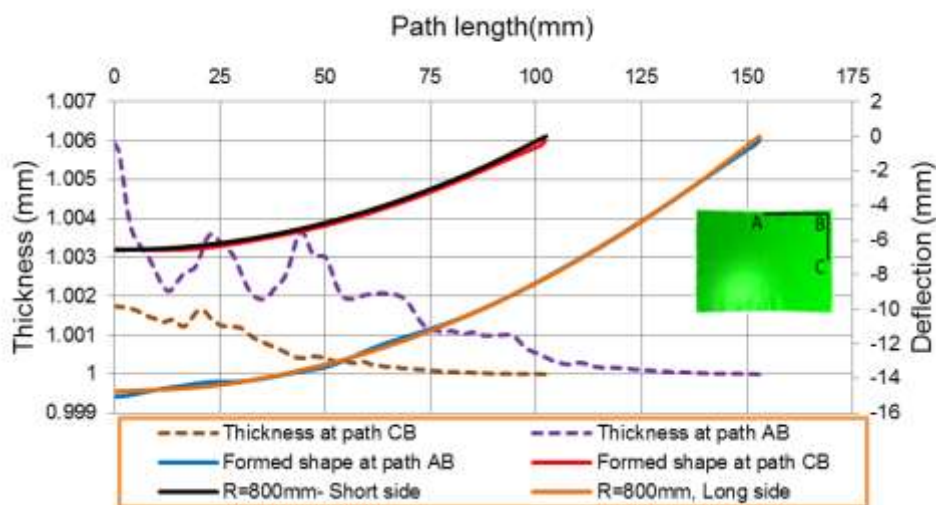
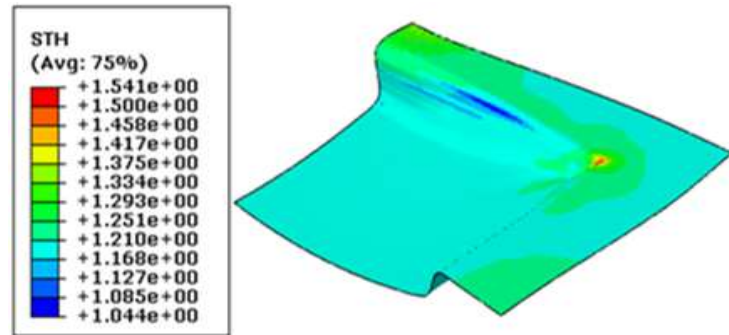


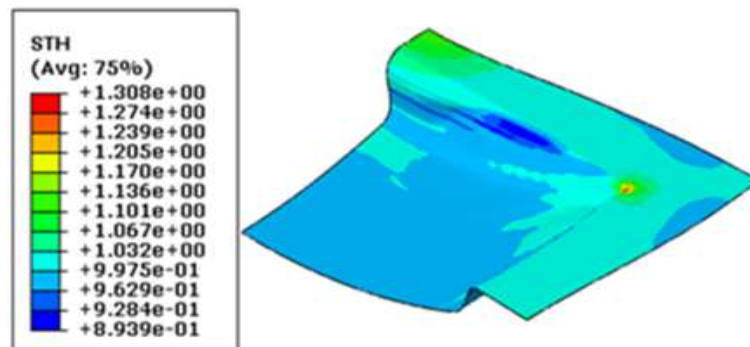
Figure 6.15 Thickness distribution and formed shape on both long and short sides of DC05 steel sheet (radius of curvature, 800 mm)

6.1.4 Simulation results of deformed sheets with blank holder

Figure 6.16 shows the thickness distribution of deformed aluminium and steel sheets using the blank holder to eliminate wrinkling with 400 mm radius of curvature. It can be seen that the thickness distribution using a blank holder is more uniform than without the blank holder, except for the corner defect thickening as a result of stress concentration.



a-Aluminium - R=400mm



b- Steel - R=400mm

Figure 6.16 Thickness distribution for 5251-O aluminium and DC05 steel sheets (R= radius of curvature)

Figure 6.17 and Figure 6.18 show the thickness variation and deformed shapes along the two paths, AB and CB on 5251-O aluminium and DC05 steel sheets, formed with a 400 mm radius of curvature using a blank holder. Thinning can be seen along paths AB and CB as a result of stretching due to using the blank holder. At the end of paths AB and CB, a thickening can be seen which leads to a non-uniform shape at the corner.

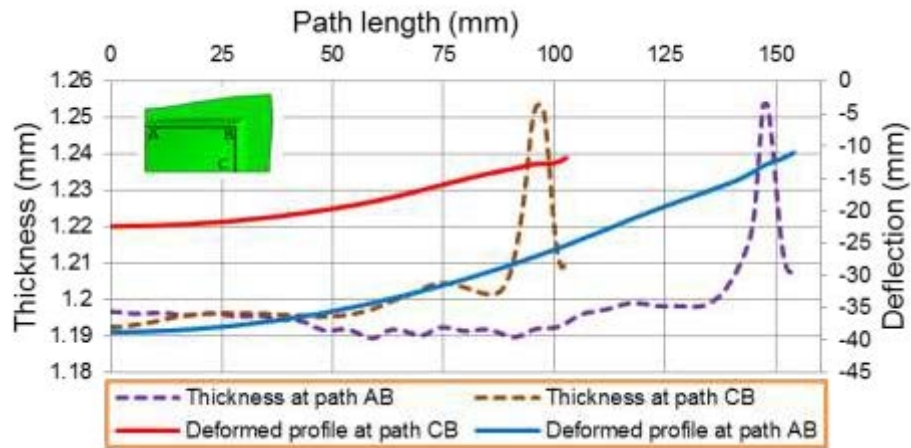


Figure 6.17 Thickness distribution and deformed shape on both long and short sides of aluminium sheet deformed using blank holder (radius of curvature, 400 mm)

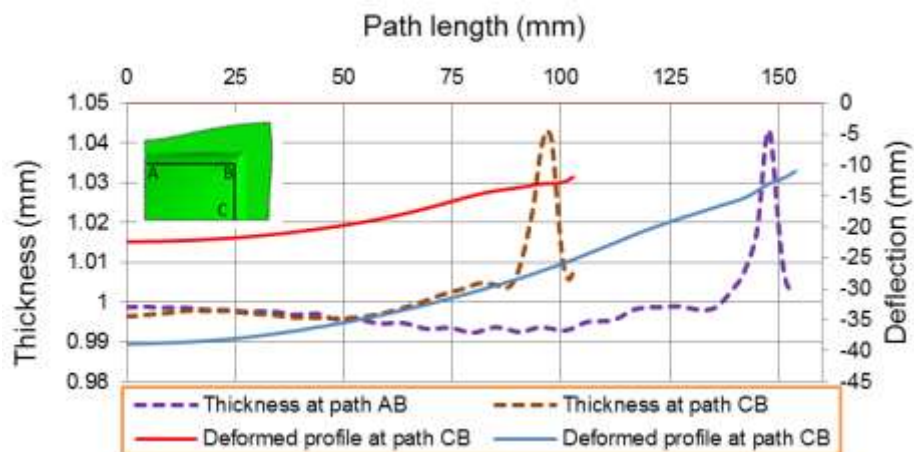


Figure 6.18 Thickness distribution and deformed shape on both long and short sides of steel sheet deformed using blank holder (radius of curvature, 400 mm)

6.2 Experimental work

The aim of the experimental study was to collect geometrical data for the final wrinkled shape for double curved parts. In the experimental study, the press used was a 400 tonnes - down stroke press of four columns construction, with a discrete die with pins of small cross-section (10 mm). A load cell was used to record force value as a function of time during the forming process, and the data collected were saved on the computer. A Microsonic, type

mic+25/IU/TC, ultrasonic distance transducer was used to determine the punch position during the forming process. The Faro Arm (3-D laser scanner) was used to scan the deformed sheets after the multi-point stamping process to build a 3-D model, and then Geomagic control software was used to determine the deformed, wrinkled profile obtained from the forming process. The specifications of the other equipment used are given in Chapter 3. The DC05 steel and 5251-O aluminium sheets were used in the experimental study; the mechanical properties of those materials were experimentally determined and are given in Appendix B. The target shapes were double curved with 400 mm and 800 mm radii of curvature obtained without a blank holder, and 400 mm with the blank holder, Figure 6.19 shows the experimental plan. The results will be used to validate the FE simulations.

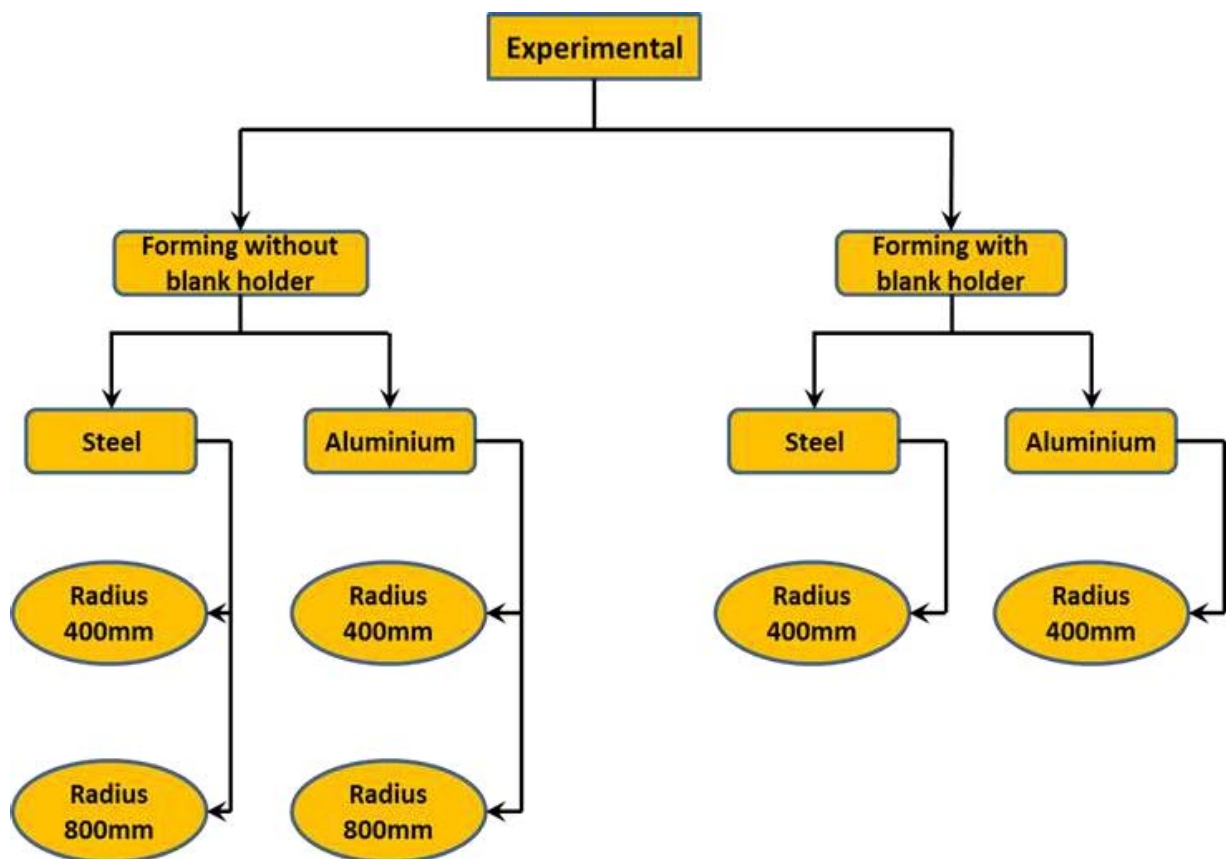


Figure 6.19 Experimental plan

6.2.1 Experimental set-up

The experimental procedure contained five main stages; tooling pins adjustment, calibration of distance transducer, data logger calibration, load cell connection and installing the die on the press.

6.2.1.1 Tooling pins adjustment

Tooling pins adjustment is a crucial step because it has a direct impact on the accuracy of the tool surface. In this study, master curves are used for pin adjustment and to shape the die surface. This curve was fabricated using a 3-D printer as described in Chapter 3. This step begins with adjusting the four pin in the corner of the tool, then adjusting the outer four rows. After that, the pins are adjusted row by row. Figure 6.20 shows the use of the master curve to adjust the pins.



Figure 6.20 Pin adjustment using master curve

6.2.1.2 Distance introducer calibration

The ultrasonic distance transducer has an operating range of 30.0 mm to 250.0 mm; it was used to monitoring the punch movement during the forming process. This sensor connects

with a data logger to record the distance-time relation, for that, the lowest and highest voltages should correspond to the least and greatest distances (30.0 mm and 250.0 mm). A multimeter was connected with a sensor as Figure 6.21 is shown. The lowest value of the voltage at 30.0 mm was 0.061 V and the highest value at 250.0 mm was 10.03 V.



Figure 6.21 Distance transducer calibration using voltmeter

6.2.1.3 Data logger calibration

Before connecting the distance transducer with the data logger, the voltage values corresponding to the lowest and highest distance values were entered. Figure 6.22 shows the logger's window, the lowest and highest values of voltage and distance can be seen, which is the specified working range of the data logger.

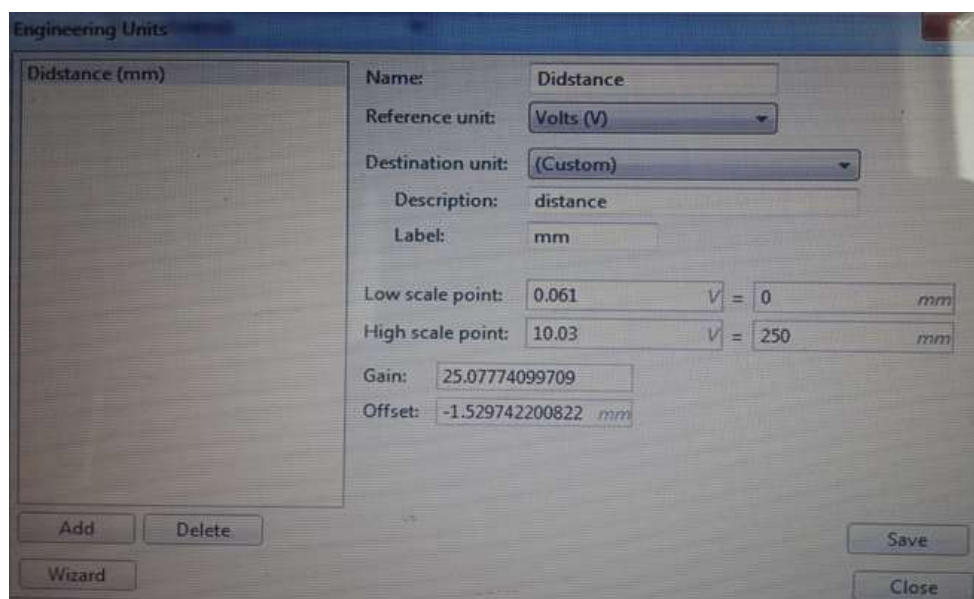


Figure 6.22 Window of data logger setup

6.2.1.4 Load cell connection

As mentioned in Chapter 3 the data logger plugged directly into a computer via a USB port using in Line Load Cell Amplifiers and Load Cell USB interface. Figure 6.23 shows the main window for data logger software. It can be seen that many facilities can be added to the screen, such as data rates and filters, plots of force-time, and the save and restore icon.



Figure 6.23 Load cell – software main window

6.2.1.5 Installation of die on the press

The complete assembly of the multi-point forming tool used for the experimental work is shown in Figure 6.24. It consisted of a die, punch and blank holder. The complete tool was installed on a Press machine. The distance transducer was fixed on the tool and connected to the data logger, and the data logger connected to the computer. The load cell was fixed on the punch and connected directly to the computer.

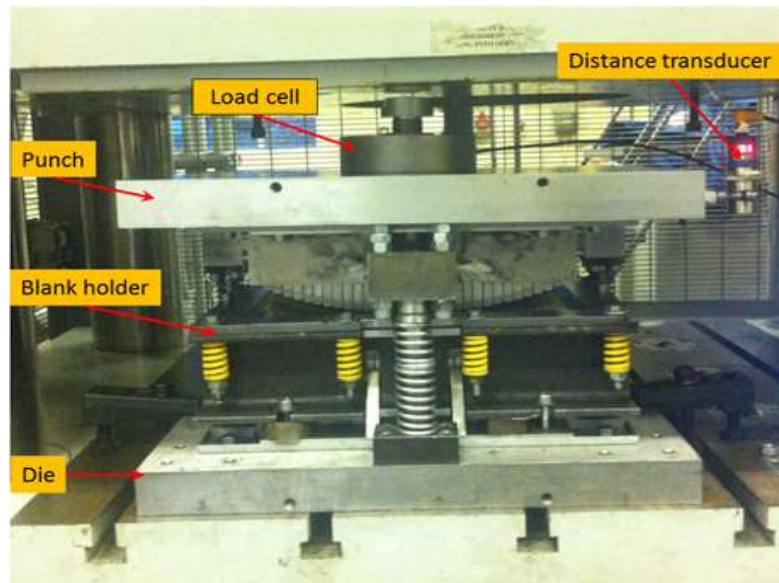


Figure 6.24 Tool setup on the press

6.2.2 Experimental forming without blank holder

The area of DC05 steel, 5251-O aluminium, and polyurethane A90 sheets used in the experimental work without a blank holder was 204.75 mm x 307.25 mm. The pins were adjusted according to the radius of curvature required. The metal sheet was placed between two polyurethane sheets as a sandwich and then put in the tool between the punch and die as shown in Figure 6.25. The punch moved, pushing the sheet to take the shape of the die cavity. The forming process was applied to the steel and aluminium sheets using 400 mm and 800 mm radii of curvature. Figure 6.26 shows deformed sheets of steel and aluminium.

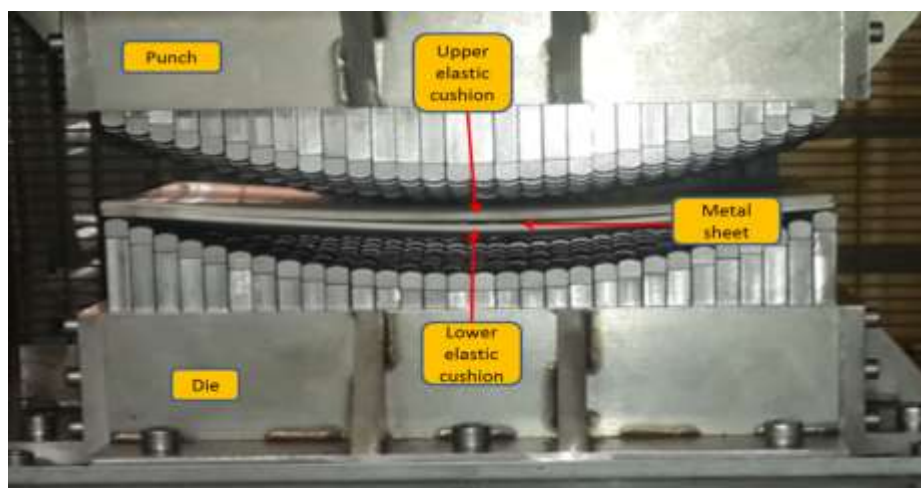


Figure 6.25 Position of metal and elastic cushion sheets in discrete tool

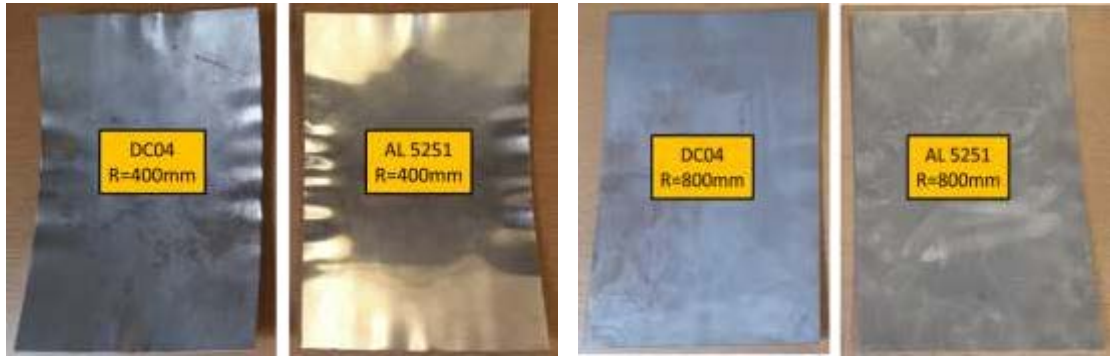


Figure 6.26 Deformed sheets with different curvatures (without blank holder)

6.2.3 Experimental forming with blank holder

In the experimental work with the blank holder, the dimensions of the DC05 steel and 5251-O aluminium sheets were 324.75 mm x 427.25 mm, and the dimensions of polyurethane sheet were 224.75 mm x 327.25 mm. The first step was fixing the metal sheet using the blank holder force 20 kN. This force was generated by 10 springs, with each spring compressed 8.19 mm, generating 2 kN/spring. Figure 6.27 shows the sheet after being fixed into the blank holder and installed onto the lower part of the tool. After completing the die assembly, as shown in Figure 6.24, the punch was pushed using the press to form the sheet and the final deformed parts are shown in Figure 6.28.

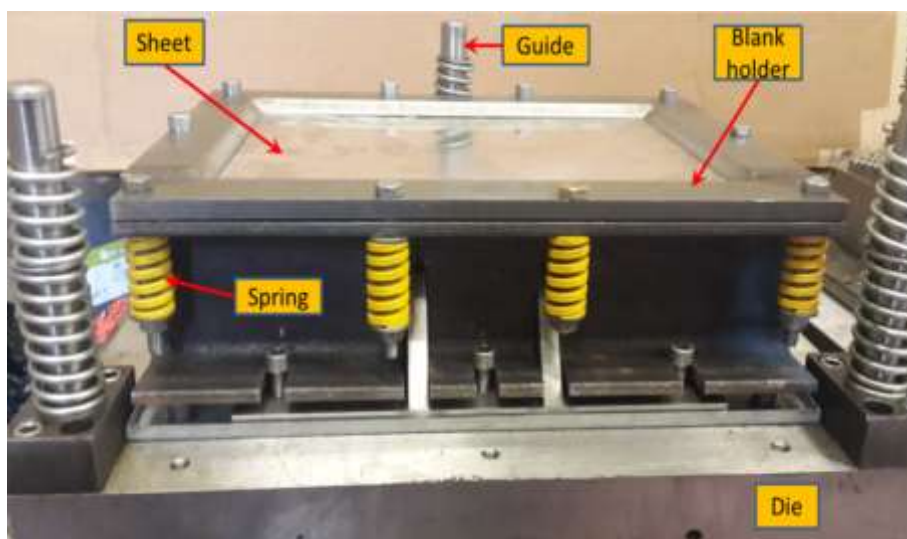


Figure 6.27 Sheet fixing into the blank holder



Figure 6.28 Aluminium and steel deformed sheets using blank holder

6.3 Comparison of simulation and experimental results with target profile

The aim of this section is to compare experimental and simulation results with the target profile. To extract the wrinkle wave profile, deformed shape profile and thickness at specific profiles of deformed parts, the Faro arm and Geomagic control software were used.

6.3.1 Results for deformed parts without blank holder

Figure 6.29 to Figure 6.32 show the target profile, simulation profile and deformed profile for 400 mm double curved aluminium and steel sheets along paths AB and CD. Clearly there is a very good match between simulation and target profiles along both paths, but there is a small deviation of the deformed profile from the target. This deviation might be due to spring back after the forming stage, during the unloading stage, which was about 1 mm and 1.5 mm for the 5251-O aluminium and DC05 steel sheets respectively.

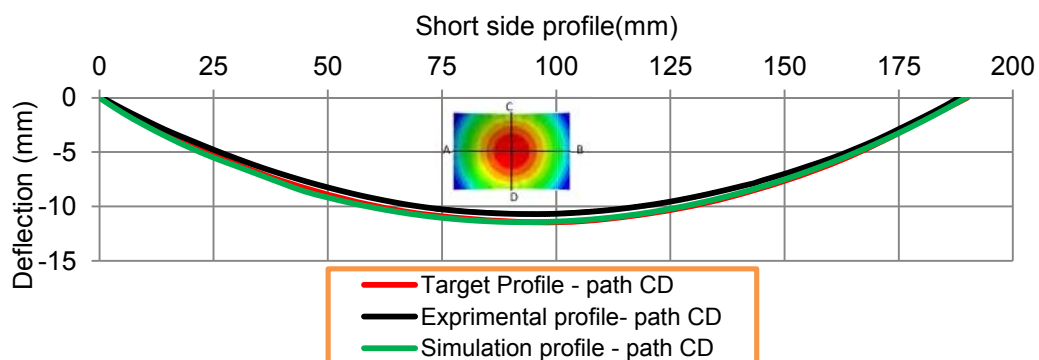


Figure 6.29 Target, simulated and deformed profiles over the section CD for 5251-O aluminium sheet (radius of curvature, 400 mm)

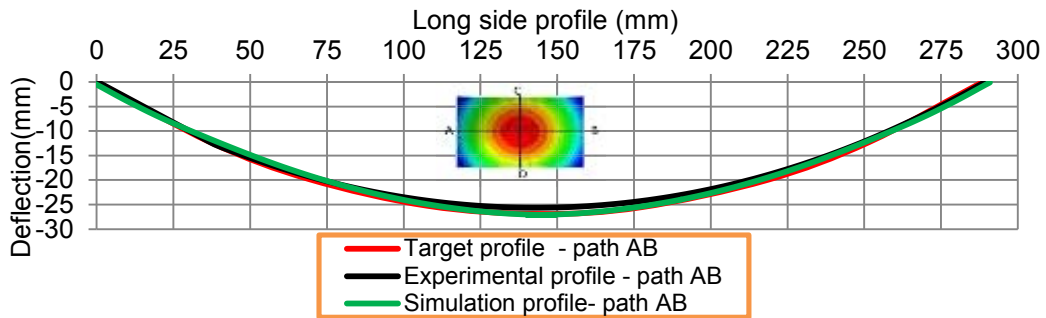


Figure 6.30 Target, simulated and deformed profiles over the section AB for 5251-O aluminium sheet (radius of curvature, 400 mm)

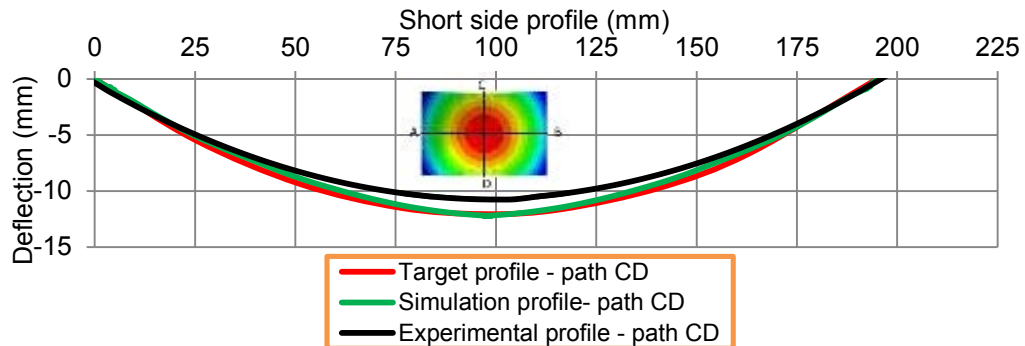


Figure 6.31 Target, simulated and deformed profiles over the section CD for DC05 steel sheet (radius of curvature, 400 mm)

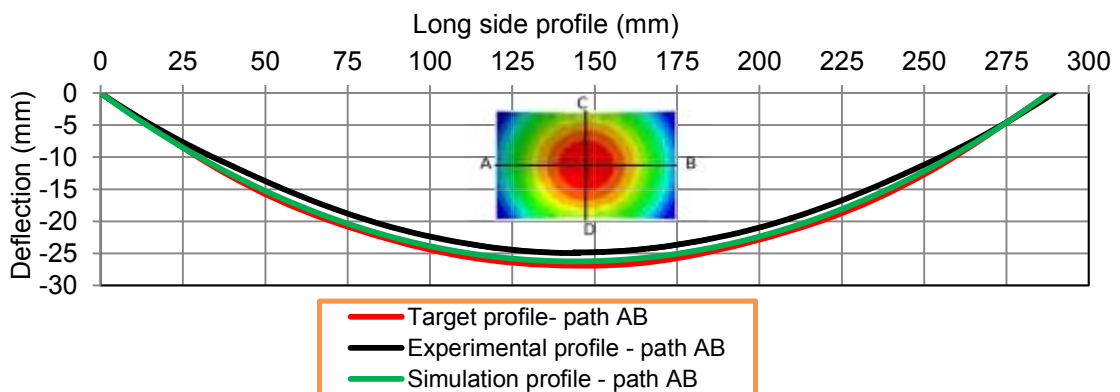


Figure 6.32 Target, simulated and deformed profiles over the section AB for DC05 steel sheet (radius of curvature, 400 mm)

Figure 6.33 to Figure 6.36 show simulated wrinkled profile, experimentally deformed shape (taken using the 3-D laser scan), and target profile over the sections AB and BC for double curved aluminium and steel sheets with radius of curvature 400 mm. It can be seen that the

wrinkling wave on the experimentally deformed sheets along path BC for both steel and aluminium sheets show strong similarity to the simulated results in terms of the number and shape of the waves, but they are not identical. Along path AB, there is a difference in the number of wrinkling waves between simulated and experimental shapes, but the simulated and experimental profiles of both are closer to target profile than the profiles along path BC.

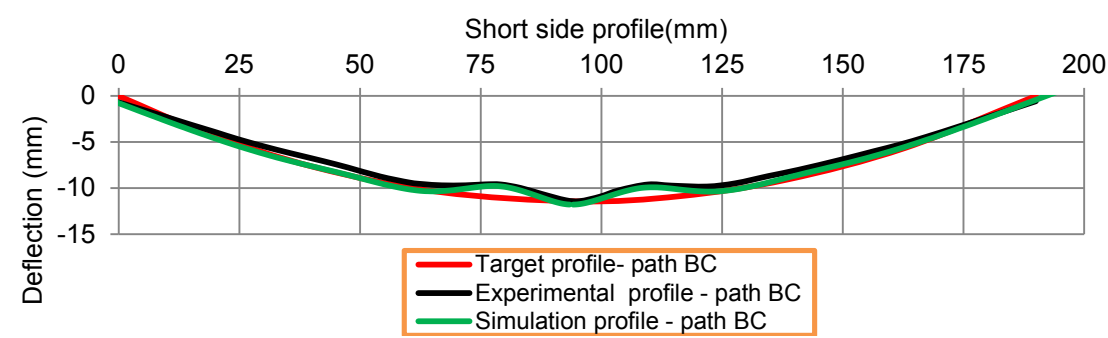


Figure 6.33 Simulated wrinkled profile, deformed shape and target profile over the section BC for aluminium sheet (radius of curvature, 400 mm)

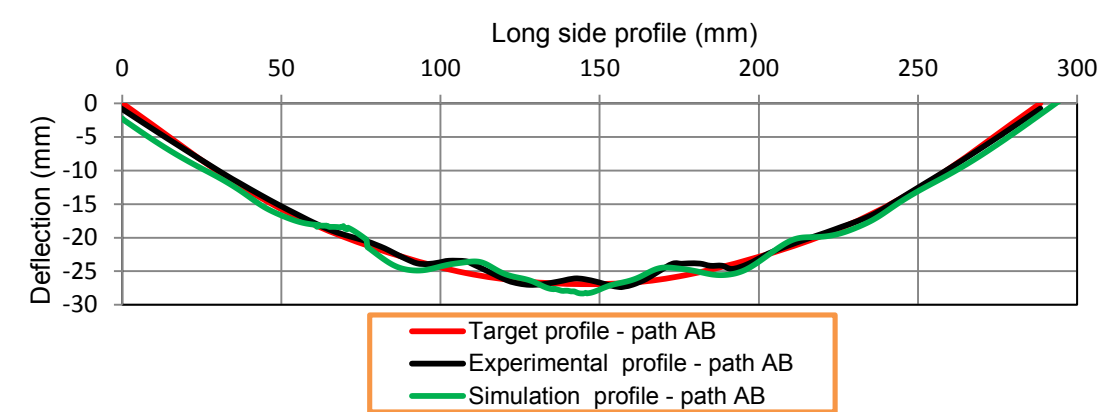


Figure 6.34 Simulated wrinkled profile, deformed shape and target profile over the section AB for aluminium sheet (radius of curvature, 400 mm)

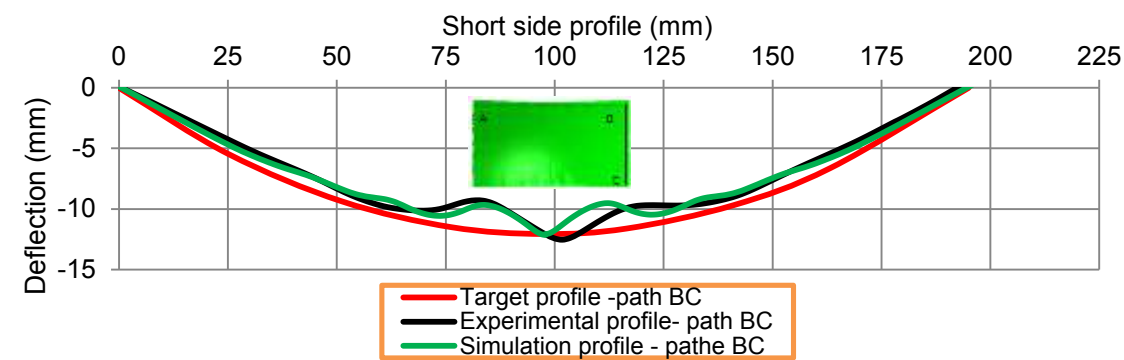


Figure 6.35 Simulated wrinkled profile, deformed shape and target profile over the section BC for steel sheet (radius of curvature, 400 mm)

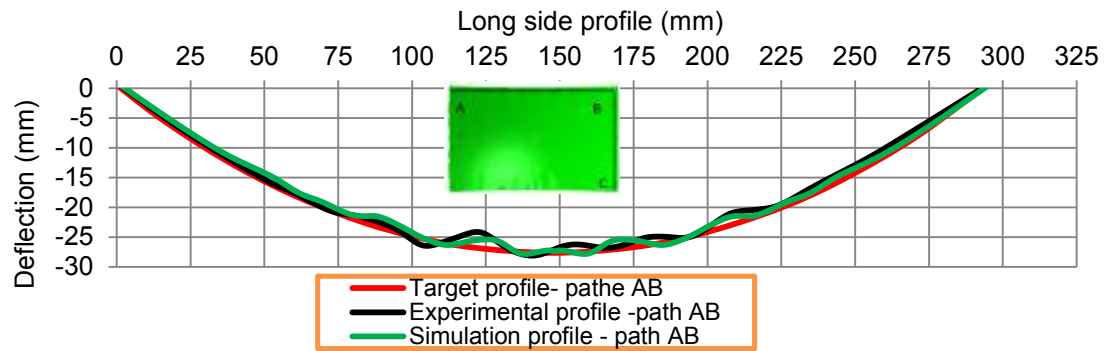


Figure 6.36 Simulated wrinkled profile, deformed shape and target profile over the section AB for steel sheet (radius of curvature, 400 mm)

Figure 6.37 to Figure 6.40 show the simulated, experimentally measured and target profiles for 800 mm doubly curved aluminium and steel sheets along paths AB and CD. In all cases it can be seen that the simulated and target profiles are almost identical. However, there is noticeable variation between experimental and target profiles. This variation reaches its maximum value at the middle of the deformed sheet and its value ranges between about 1.5 mm and 2.6 mm for both aluminium and steel sheet, being larger along AB.

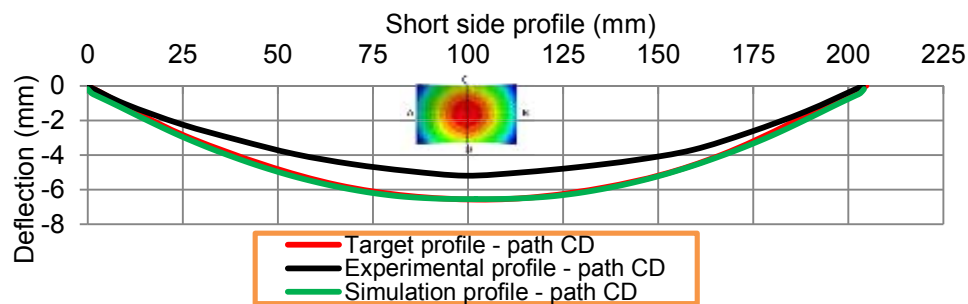


Figure 6.37 Target, simulated and deformed profiles over the section CD for aluminium sheet (radius of curvature, 800 mm)

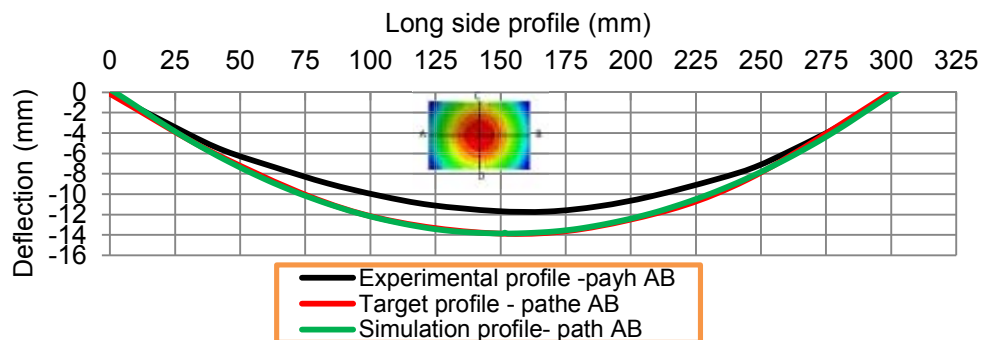


Figure 6.38 Target, simulated and deformed profiles over the section AB for aluminium sheet (radius of curvature, 800 mm)

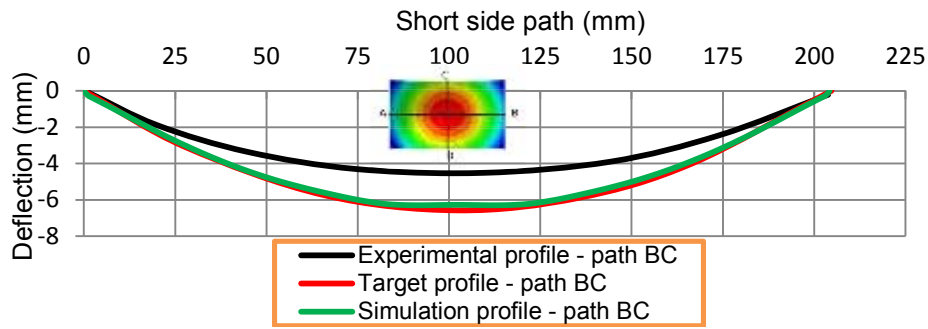


Figure 6.39 Target, simulated and deformed profiles over the section CD for steel sheet (radius of curvature, 800 mm)

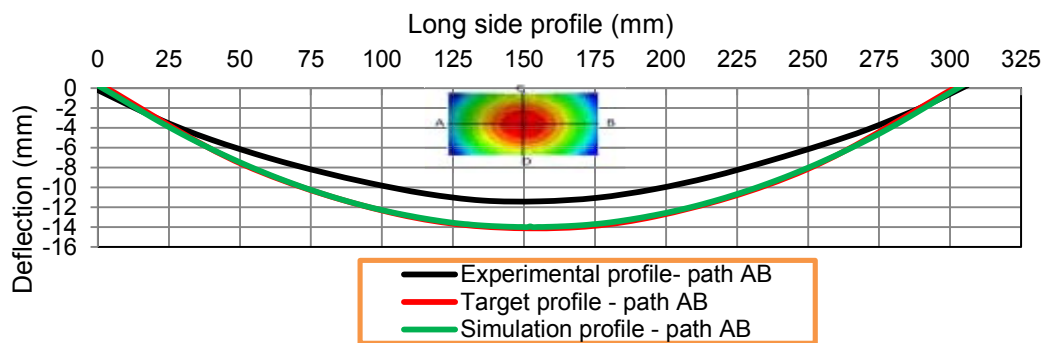


Figure 6.40 Target, simulated and deformed profiles over the section AB for steel sheet (radius of curvature, 800 mm)

Figure 6.41 to Figure 6.44 show the wrinkling wave along edges AB and BC for 800 mm double curved aluminium and steel sheets. It can be seen that the amplitudes of the wrinkling waves on the aluminium sheet are smaller than on the steel sheet for both paths AB and BC. Along paths AB and BC, for aluminium and steel sheets, the difference between the experimental and target profiles with a radius of curvature 800 mm is bigger than the variation obtained when using 400 mm as the radius of curvature.

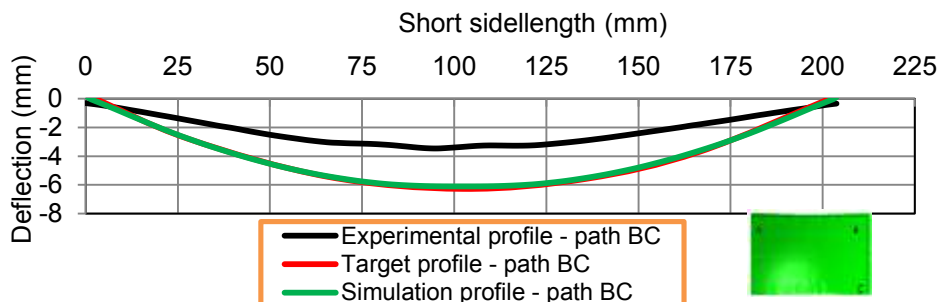


Figure 6.41 Wrinkling profile obtained from simulation results and deformed shape over the section BC for aluminium sheet (radius of curvature, 800 mm)

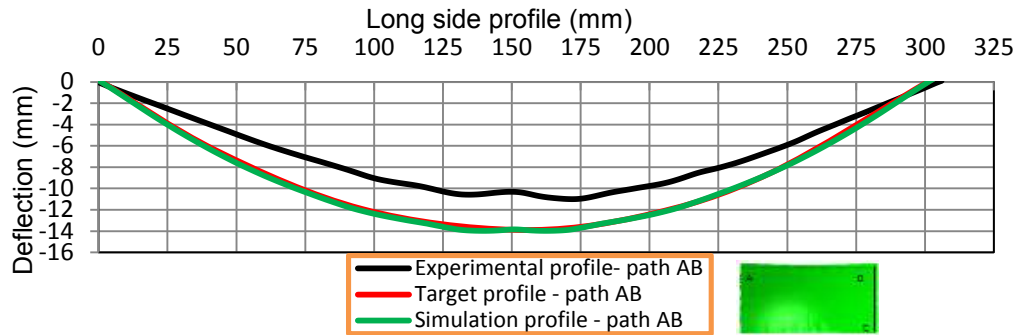


Figure 6.42 Wrinkling profile obtained from simulation results and deformed shape over the section AB for aluminium sheet (radius of curvature, 800 mm)

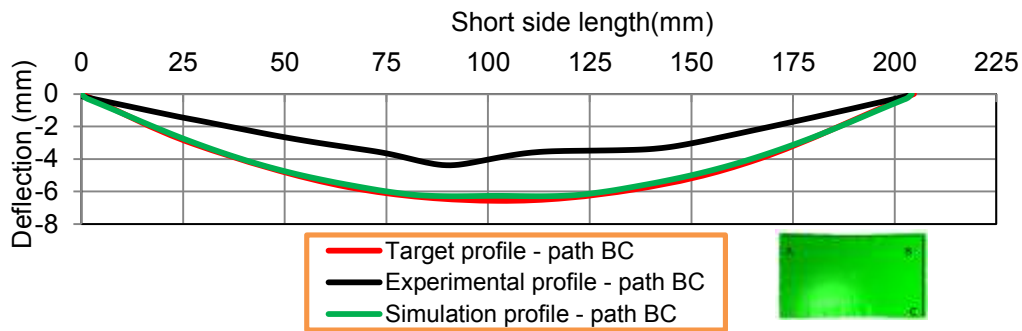


Figure 6.43 Wrinkling profile obtained from simulation results and deformed shape over the section BC for steel sheet (radius of curvature, 800 mm)

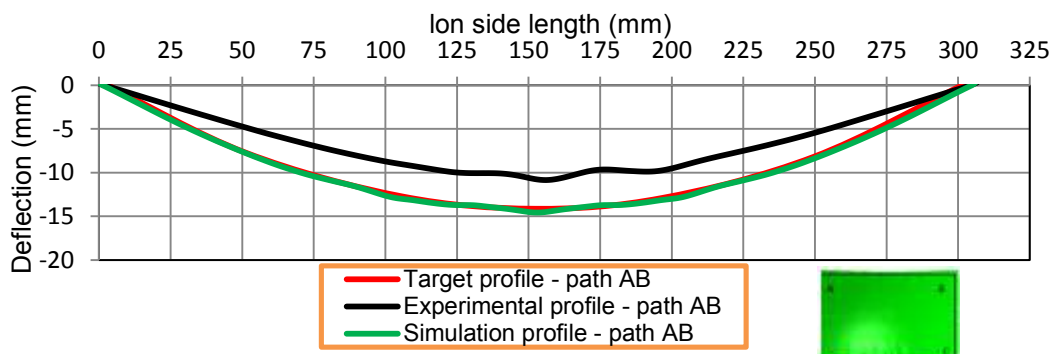


Figure 6.44 Wrinkling profile obtained from simulation results and deformed shape over the section AB for steel sheet (radius of curvature, 800 mm)

6.3.2 Results for deformed parts using blank holder

In the forming process using a blank holder, the sheet is clamped at the edges. The two part blank holder, see Figure 6.27, generates a holding force that opposes the movement of the

sheet. The magnitude of any resulting movement will depend on the blank holder area, blank holder force, and coefficient of friction between blank holder and sheet. This holding force generates the required tension to stretch the sheet during the stamping process, and can eliminate wrinkling. Figure 6.45 to Figure 6.48 show simulated, experimental and target profiles for 5251-O aluminium and DC05 steel sheets using a blank holder with radius of curvature 400 mm. It can be seen that all three profiles along path CD are almost identical over the range “b” for both aluminium and steel sheets, as shown in Figure 6.45 and Figure 6.47. Along path AB, see Figure 6.45 and Figure 6.48, there is a small deviation of the experimental profiles from the target shape. This difference is due to the forming depth at the sheet edge along path CD being about twice the forming depth along path AB, this leads to the stretching in the direction CD being more than in direction of path AB, which makes the spring back along path AB more than a long path CD. Over the ranges a and c, there is a variation of the experimental profile as a result of elastic cushion compression from the pin edges, also a variation of simulation profile near to the flange as a result of decreasing the contact area between the sheet and blank holder in the of deformed stage.

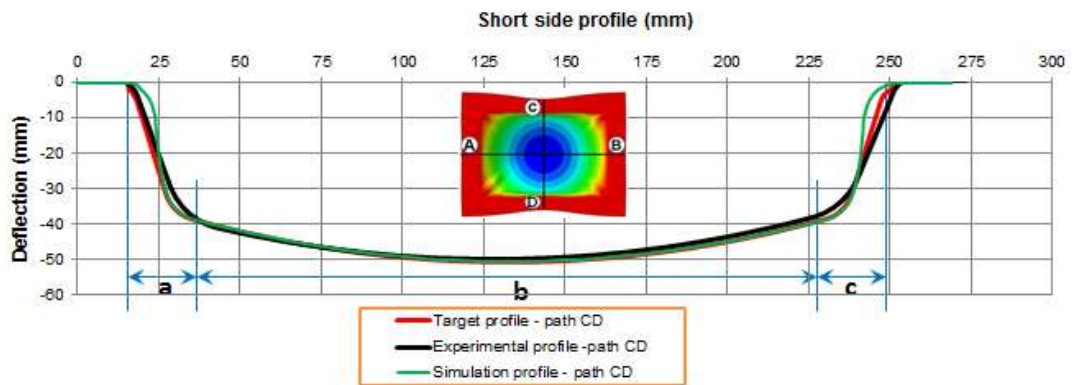


Figure 6.45 Target, simulated and deformed profiles over the section CD for aluminium sheet (with blank holder, and radius of curvature, 400 mm)

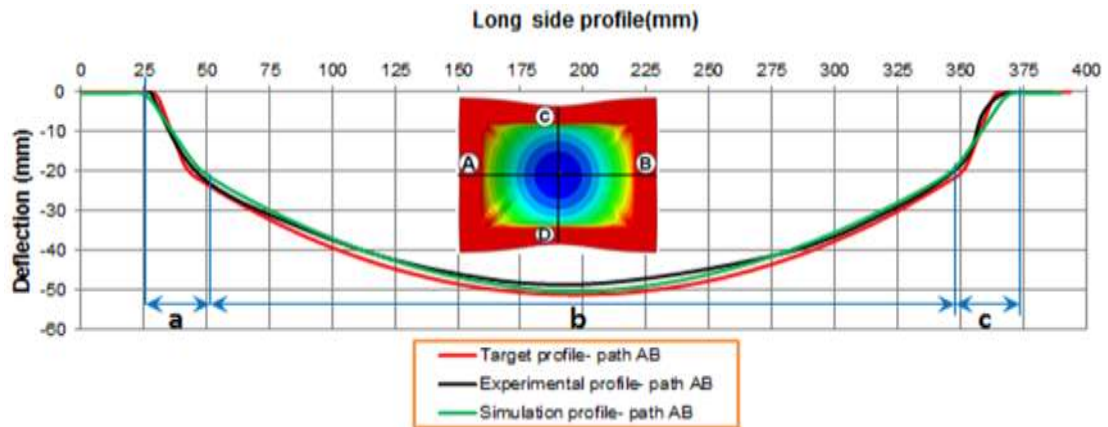


Figure 6.46 Target, simulated and deformed profiles over the section AB for aluminium sheet (with blank holder, and radius of curvature, 400 mm)

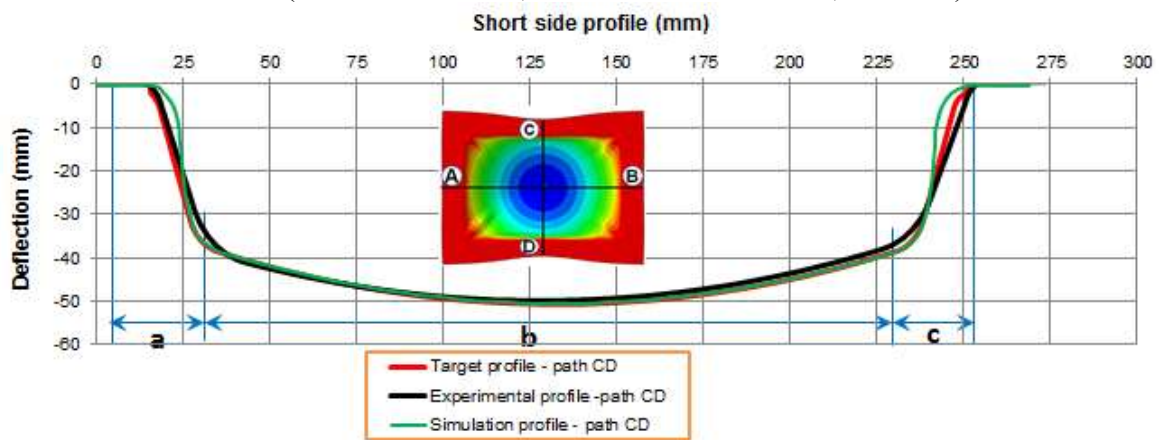


Figure 6.47 Target, simulated and deformed profiles over the section CD for steel sheet (with blank holder, and radius of curvature, 400 mm)

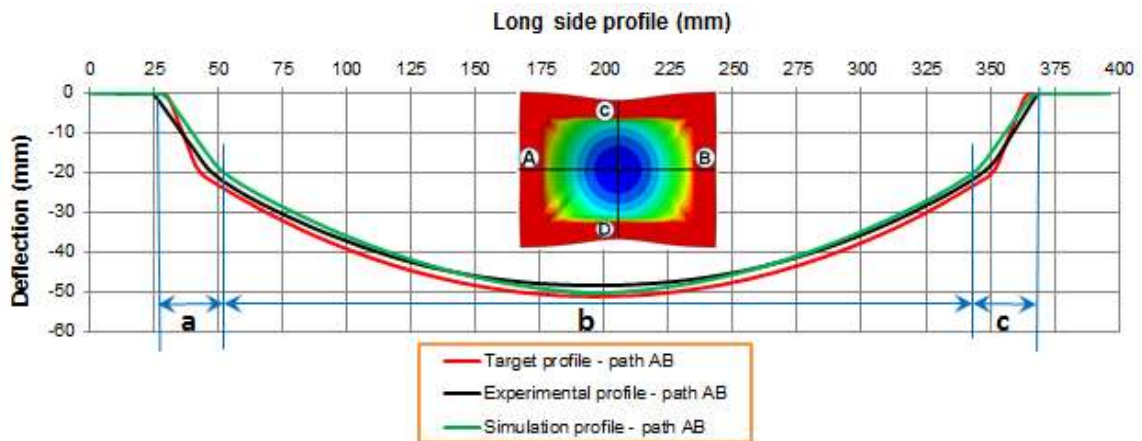


Figure 6.48 Target, simulated and deformed profiles over the section AB for steel sheet (with blank holder, and radius of curvature, 400 mm)

6.3.3 Thickness distribution on deformed parts without and with blank holder

The numerically simulated thickness distribution, as predicted in Section 6.2.2, for the deformed aluminium and steel sheets along the longitudinal path AB and transfers path CD using a 400 mm radius of curvature, without and with blank holder are shown with experimentally measured thickness distributions in Figure 6.49- Figure 6.51.

From Figure 6.49 and Figure 6.51 in case without blank holder, it can be seen that the simulated and experimental results of deformed aluminium and steel parts without blank holder show much the same minimum thickness at the centre of the deformed parts, and then show thickness increases towards the edges of both deformed sheets. From Figure 6.50 and Figure 6.52 in case with blank holder, it can be seen that thinning occurs in all deformed areas between the punch and die as a result of the blank holder stretching force for aluminium and steel deformed sheets. The maximum thinning occurs at the beginning and end of the overhanging sheet length between the die and blank holder, and the maximum thickening occurs under the blank holder.

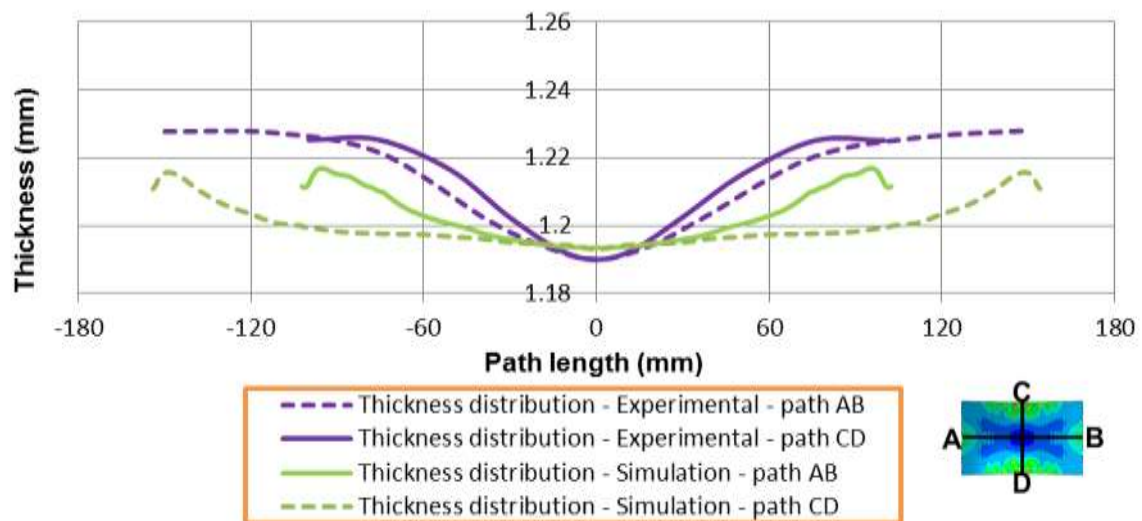


Figure 6.49 Experimental and simulated thickness distribution profiles over the sections AB and CD for aluminium sheet (without blank holder, and radius of curvature, 400 mm)

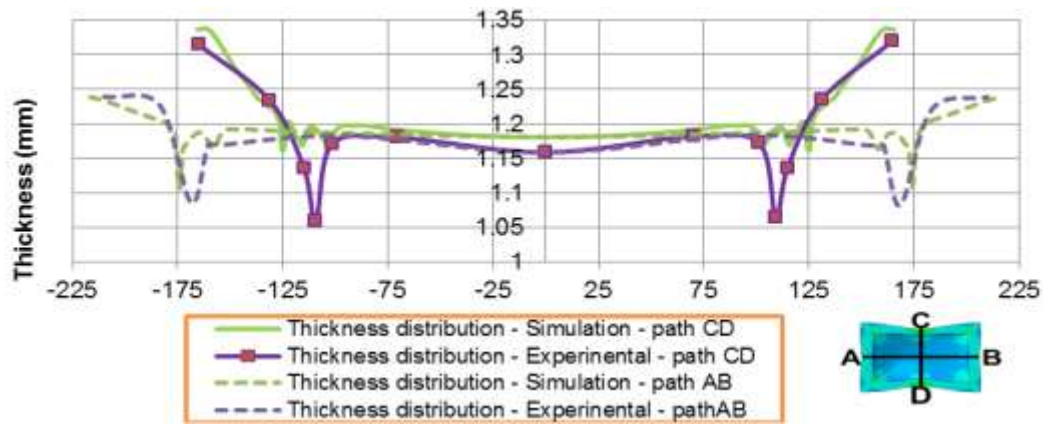


Figure 6.50 Experimental and simulated thickness distribution profiles over the sections AB and CD for aluminium sheet (with blank holder, and radius of curvature, 400 mm)

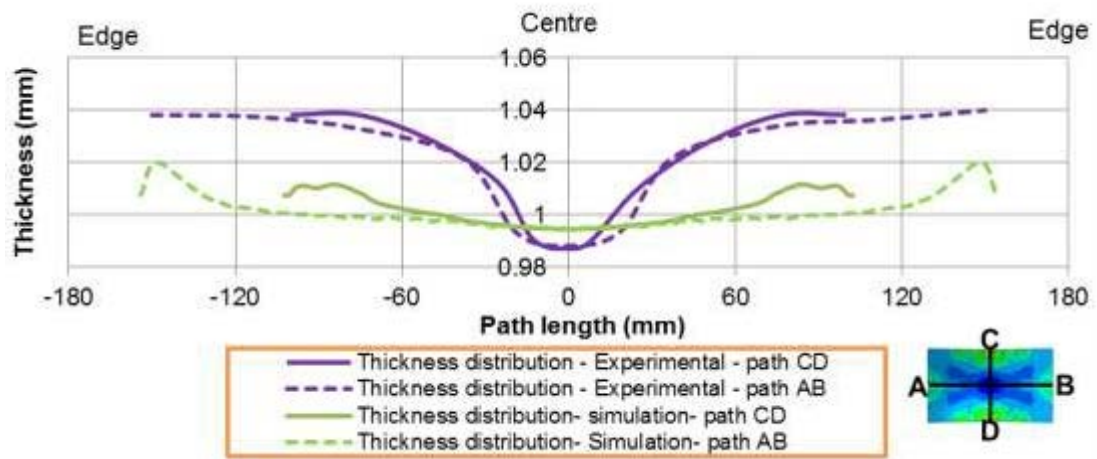


Figure 6.51 Experimental and simulated thickness distribution profiles over the sections AB and CD for steel sheet (without blank holder, and radius of curvature, 400 mm)

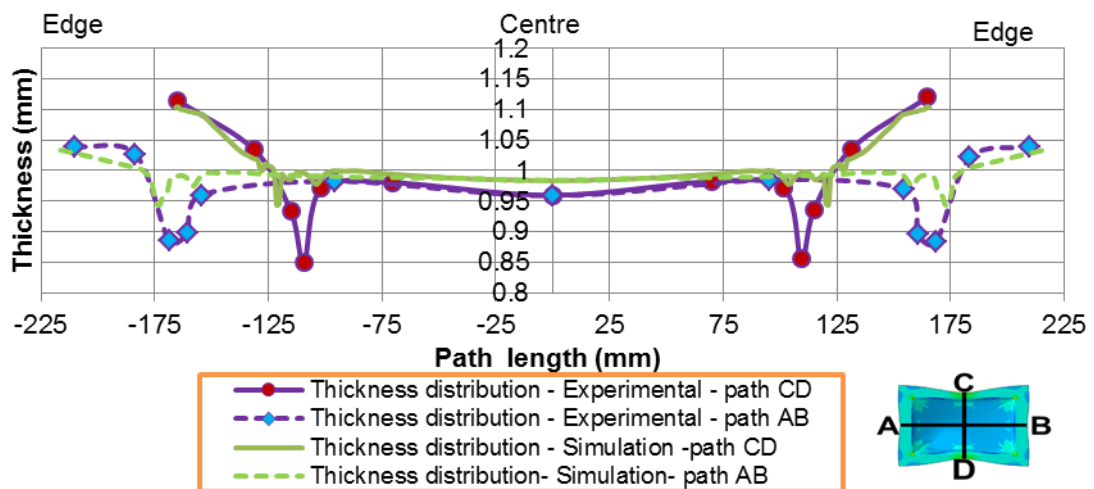


Figure 6.52 Experimental and simulated thickness distribution profiles over the sections AB and CD for steel sheet (with blank holder, and radius of curvature, 400 mm)

6.4 Summary

In this chapter, a numerical investigation of the relation between wrinkling and thickness variation has been undertaken for two materials (5152-O aluminium sheet and DC05 steel sheet) using the MPF models developed in Chapter 4. The experimental forming of doubly curved products from the two materials have been outlined. The Faro Arm (3-D laser scanner) was used to scan the deformed parts after the multi-point stamping process to build a 3-D model and then Geomagic control software was used to determine the deformed and wrinkled profiles. The results of the numerical investigation showed that the wrinkling appears in the thickened areas of deformed parts as a result of lateral compression stress. Thus, the use of a blank holder to control the sheet material flow helped eliminate wrinkling. There is an acceptable agreement between simulation and experimental results for both deformed shape and wrinkling. For the thickness distribution, both sets of results show the same general trends but with a difference in absolute values.

CHAPTER- 7

CONCLUSIONS AND PROPOSALS FOR FUTURE WORK

7.1 Conclusions

Due to growing demands on batch production, multi-point forming is becoming increasingly important in sheet metal forming processes. To perform this process with minimal defects is highly dependent on certain parameters such as pin size, elastic cushion thickness, coefficient of friction and radius of curvature of the formed component. These parameters effect the quality of the deformed sheets and failure to use the optimum values can lead to defects such as wrinkling, deviation from target shape, and excessive thickness variation.

The results of this study have been concluded as following:

- 1- A 10 mm pin size test rig has been developed and constructed to carry out the experimental work.
- 2- The results and findings obtained from the mechanical tests are summarised as follows;
 - a- Mechanical properties, such as, yield stress, ultimate tensile stress; elastic modulus and elongation have been determined for DC05 steel sheet and 5251-O aluminium sheet, see Section 4.1 and are presented in Appendix B.
 - b- Anisotropy coefficients, and r_0 , r_{45} , and r_{90} have been determined to calculate normal anisotropy, R_a , for both sheet materials, see Section 4.1
 - c- The behaviour of elastic cushion materials under compression test were determined, see Section 4.1 and are presented in Appendix B
- 3- After determining the relevant materials properties experimentally, a 3-D FE model of the multi-point forming stamping process was developed using explicit solver/ABAQUS software through the following steps;

- a- The die, punch and blank holder were considered as the discrete rigid body, the sheet metal was simulated as an elastic-plastic material, and the elastic cushion was simulated as a hyper-elastic material
 - b- Displacement boundary conditions were used to fix the die and lower part of a blank holder in the x, y and z directions, and then the punch and upper part of blank holder in the x and z directions. Symmetric boundary conditions were applied to the elastic cushion and sheet metal.
 - c- The die, punch, and blank holder were meshed using linear quadrilateral elements (R3D4). The metal sheet and elastic cushion sheet were meshed using 3-D 8-node linear elements (C3D8R).
 - d- The effect of number of elements representing sheet thickness, on the forming force was evaluated.
 - e- The relation between artificial strain energy, kinetic energy and internal energy was used to determine the reliability of the FE model.
 - f- A blank holder was used to eliminate the wrinkling, and to determine a suitable blank holder force. Also, the effect of the gap between the die and blank holder (overhang sheet length) on sheet thickness distribution was investigated
 - g- Reduction of the corner defect in double curved shapes was investigated
 - h- Effect of radii of curvature on sheet thickness distribution was investigated.
 - i- Two FE models (with and without blank holder) were developed and experimentally validated.
- 4- A parametric study was done to study the effect of pin size, radius of curvature, elastic cushion thickness, and coefficient of friction on wrinkling, deformed profile, and thickness variation. All parameters have important effects on wrinkling, thickness

variation and deformed profile, except coefficient of friction which has noticeable effect on thickness variation.

- 5- Optimisation of process parameters using the response surface method were undertaken using the validated numerical models, which studied the effect of pin size, cushion thickness, coefficient of friction, and radius of curvature on the response parameters - which included wrinkling, deviation from target profile and thickness variation. It was shown that;
 - a- The pin size and part radius of curvature have a significant effect on the response parameters.
 - b- All response parameters increased with decreasing radius of curvature, and the use of pins either larger and smaller than 15 mm led to increased wrinkling and increased shape deviation.
 - c- Using large pins reduces thickness variation.
 - d- An empirical model has developed to predict wrinkling, maximum deviation from target shape and thickness variation for doubly curved sheet forming.
- 6- The relation between wrinkling phenomena and thickness variation was numerically and experimentally studied with double curved sheet forming. DC05 steel, and 5251-O aluminium sheets were used in the experimental work and polyurethane A90 was used as an elastic cushion to protect the deformed sheets from dimpling. The CAD models for the deformed sheets were built using a Faro arm (3-D laser scan) and measurements were taken using Geomagic control software and it was shown that;
 - a- During deformation the sheet material flows outwards from the centre towards the edges, this means the thickness of the deformed sheet had a minimal value at the centre, while the thickness increased towards the sheet edges.
 - b- The compressive stresses are concentrated in the middle of the sheet edges.

- c- Wrinkling occurs in thickened areas.
 - d- Using a blank holder causes sheet stretching, thickening is prevented which reduces or eliminates wrinkling.
- 7- Using the multi-point forming die geometrical data was obtained representing the formed profile, wrinkling profile and thickness variation. These results were compared with simulation results and it was shown that;
- a- Without a blank holder, the experimental and simulation results for the central area of the formed profile were almost identical for those parts with a 400 mm radius of curvature, with some small variation at the middle point. The variation was larger for those parts with a 800 mm radius of curvature.
 - b- With a blank holder, the profile of the middle of the formed parts was identical for experimental and simulated results, with some small variation at the ends where there was overhang between blank holder and die, especially at along the shorter side of the deformed sheet.
 - c- For a wrinkled profile, the number of wrinkling waves and their amplitude on the short side of deformed sheets showed excellent agreement between simulated and experimental results for the parts with radius of curvature of 400 mm. However there is a difference in the number of waves along the longer sides. For the parts with 800 mm radius of curvature, there is excellent agreement in wave shapes and wave numbers between experimental and simulated results, however there was a difference between profiles shapes.
 - d- For thickness variation, the experimental curves were general slightly higher than predicted by the numerical model with or without the blank holder.

7.2 Suggestions for future work

As a result of this study, together with the conclusions that have been reached, the following further work is recommended to help improve the multi-point stamping process:

- 1- The effect of using a discrete blank holder on the stress distribution and the quality of deformed parts should be investigated.
- 2- Using a variable blank holder force and its effect on wrinkling phenomenon should be investigated.
- 3- Manual adjustment of the pins takes a large amount of time, but automatic systems have difficulties because the distance between the pin centres is small. Alternative methods should be developed to reduce setup time and improve the accuracy of this process.

APPENDIX A

THE MAIN PARTS DIMENSIONS OF DEVELOPED MULTI-POINT FORMING TOOL

Appendix A explains the main parts dimensions of multi-point forming tool that have been developed.

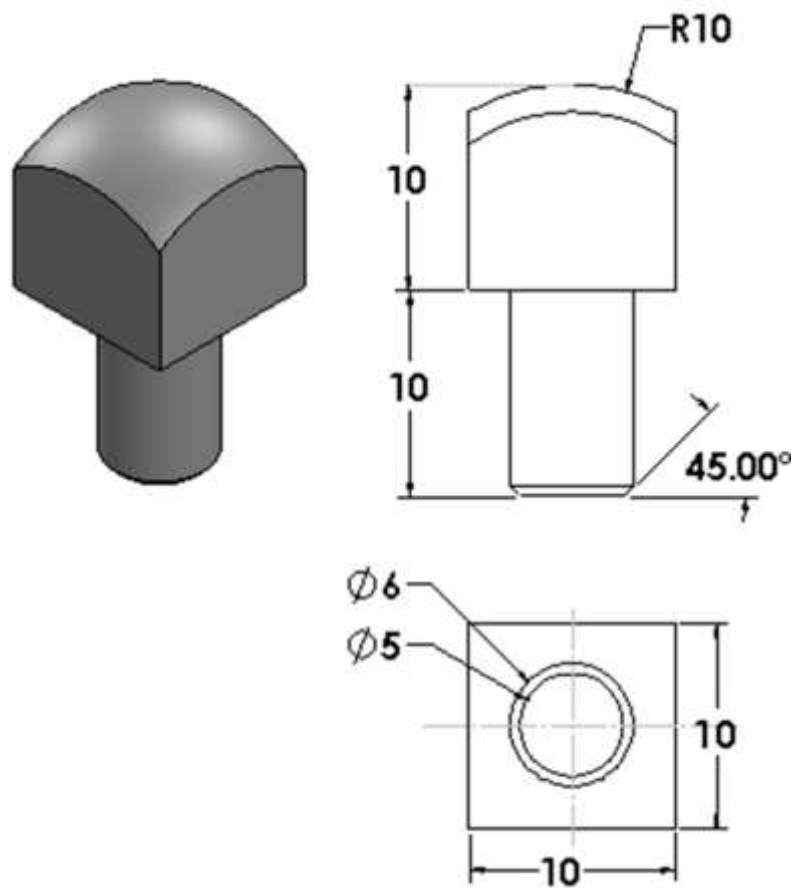


Figure A.1 Pin tip

(All dimensions mm)

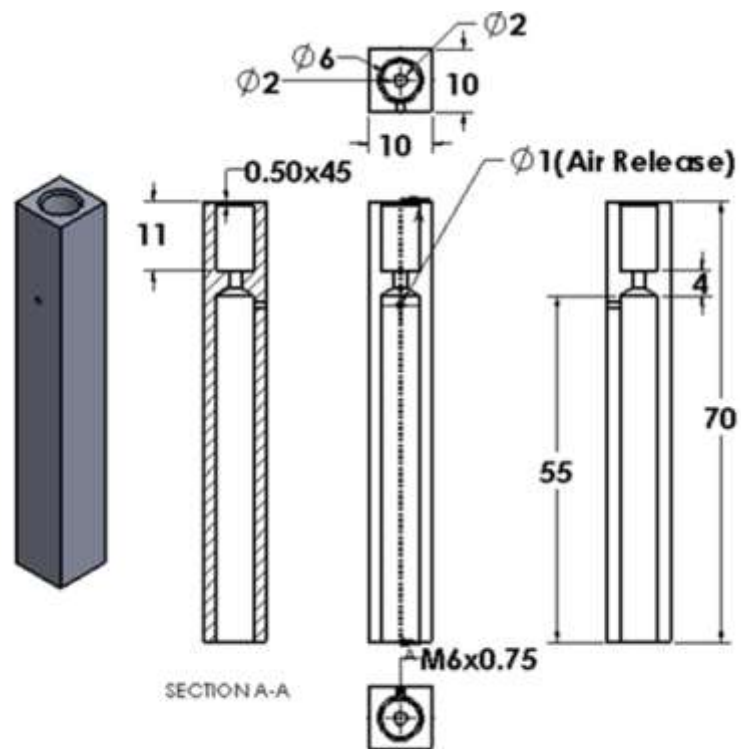


Figure A.2 Pin cap
(All dimensions mm)

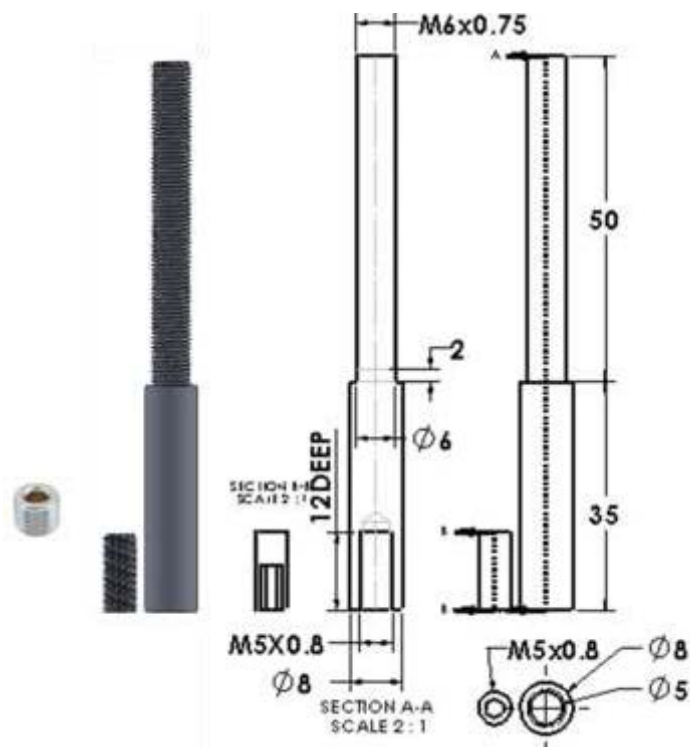


Figure A.3 Pin screw
(All dimensions mm)

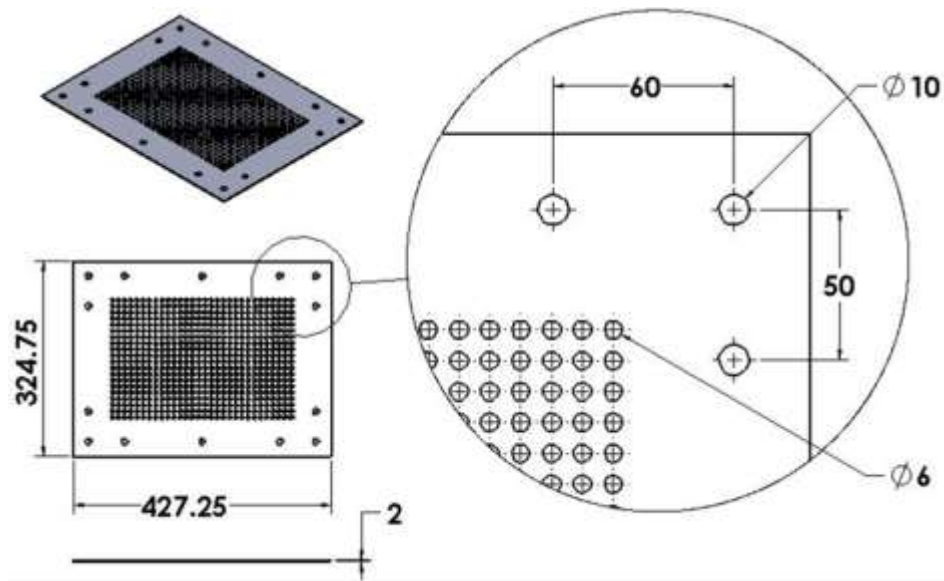


Figure A.4 Fixing sheet
(All dimensions mm)

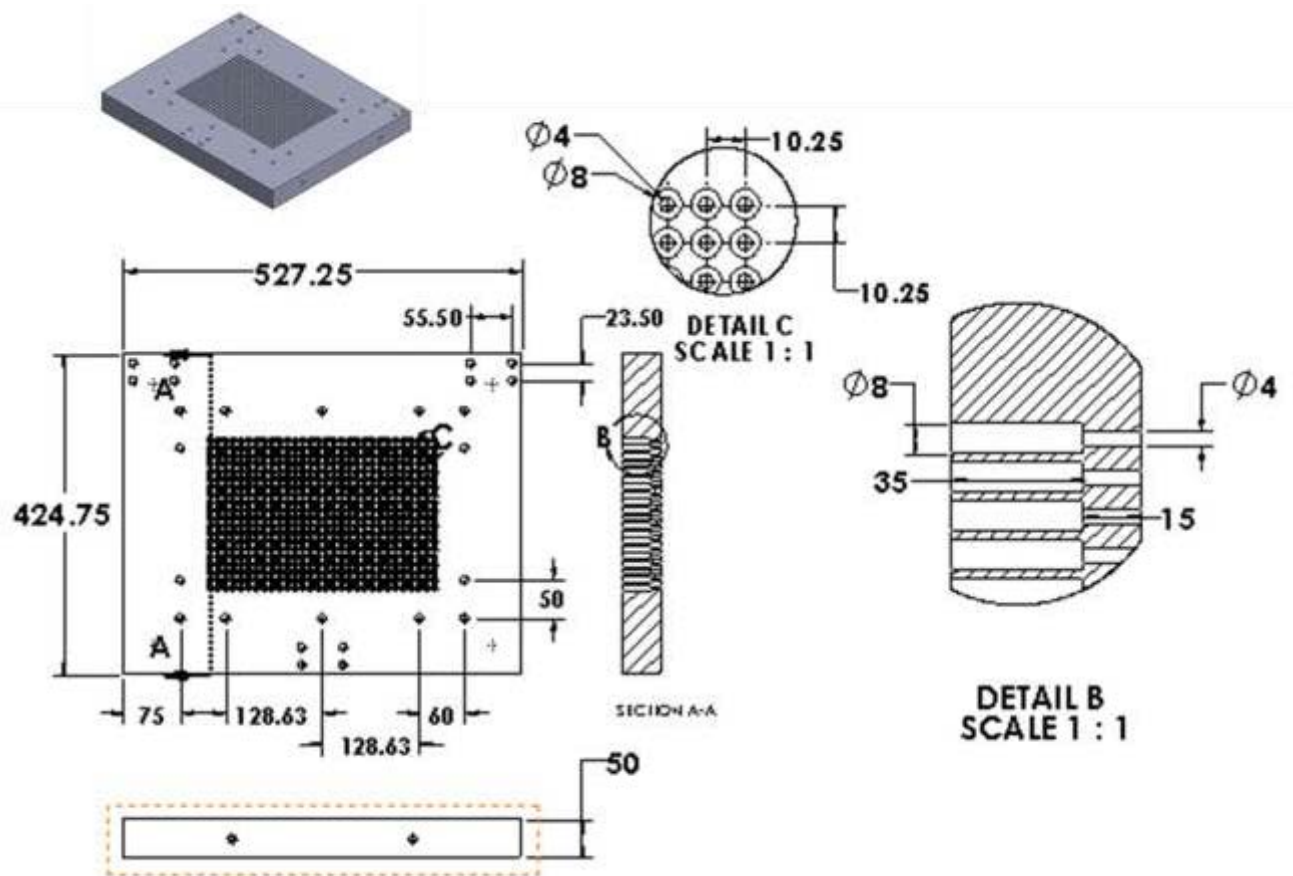


Figure A.5 Main plate
(All dimensions mm)

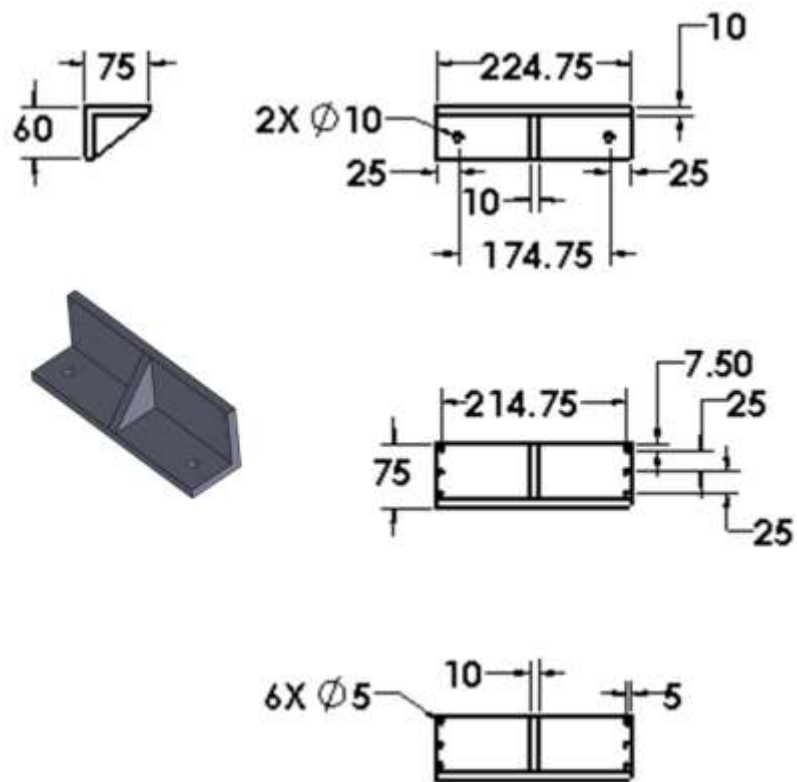


Figure A.6 Pins support- Short side
(All dimensions mm)

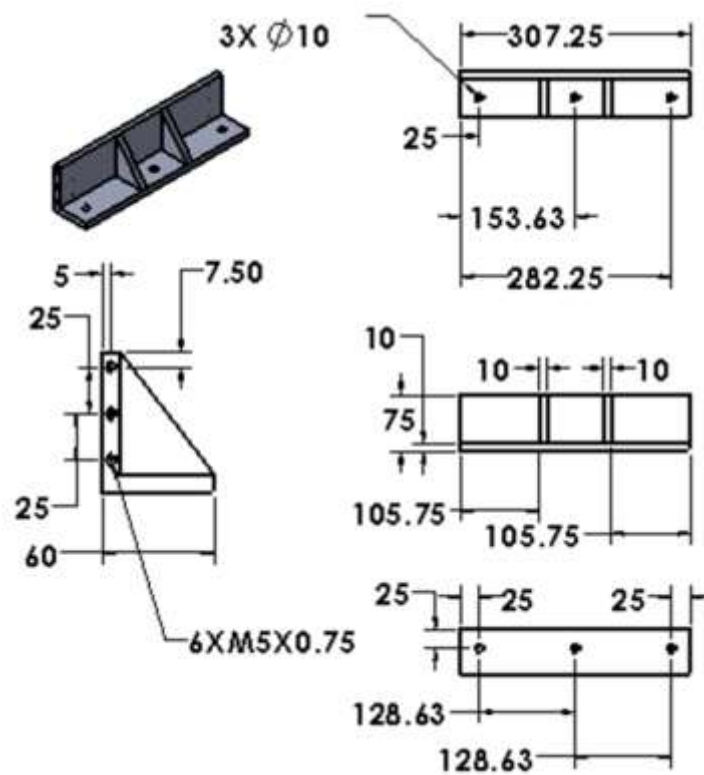


Figure A.7 Pins support – long side
(All dimensions mm)

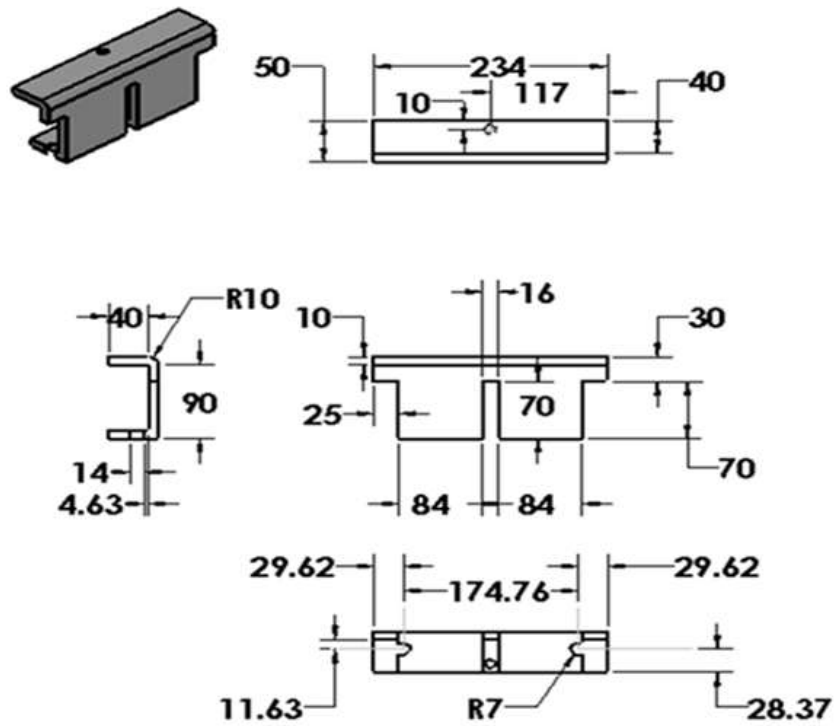


Figure A.8 Blank holder (Lower part –short side)
(All dimensions mm)

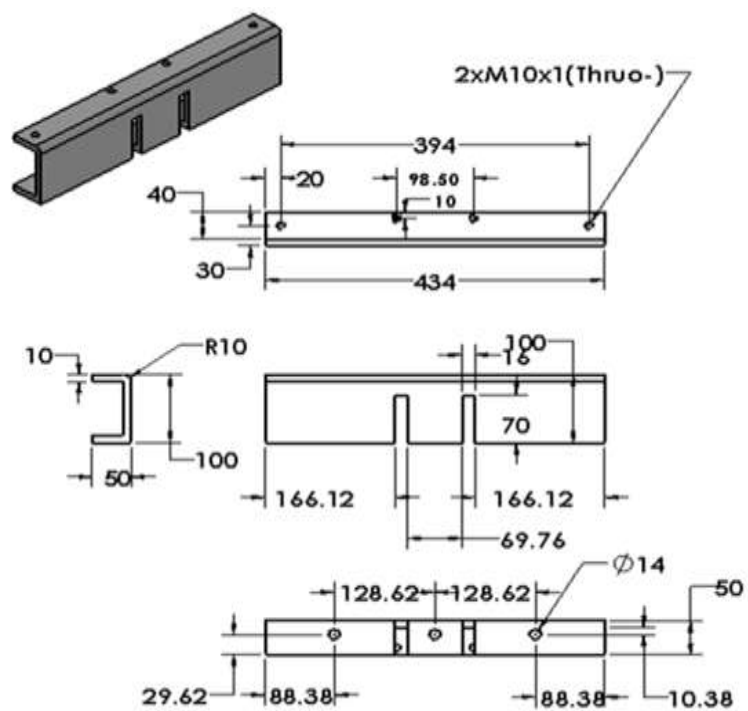


Figure A.9 Blank holder (Lower part –long side)
(All dimensions mm)

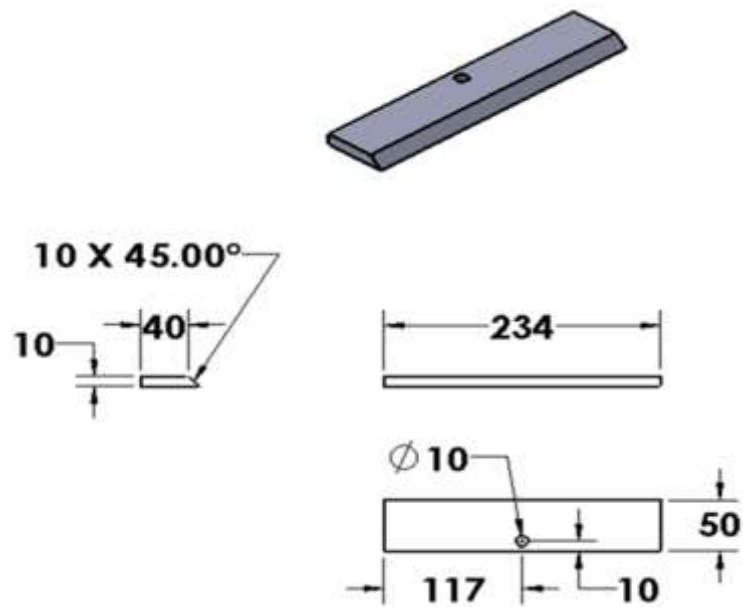


Figure A.10 Blank holder (upper part –short side)
(All dimensions mm)

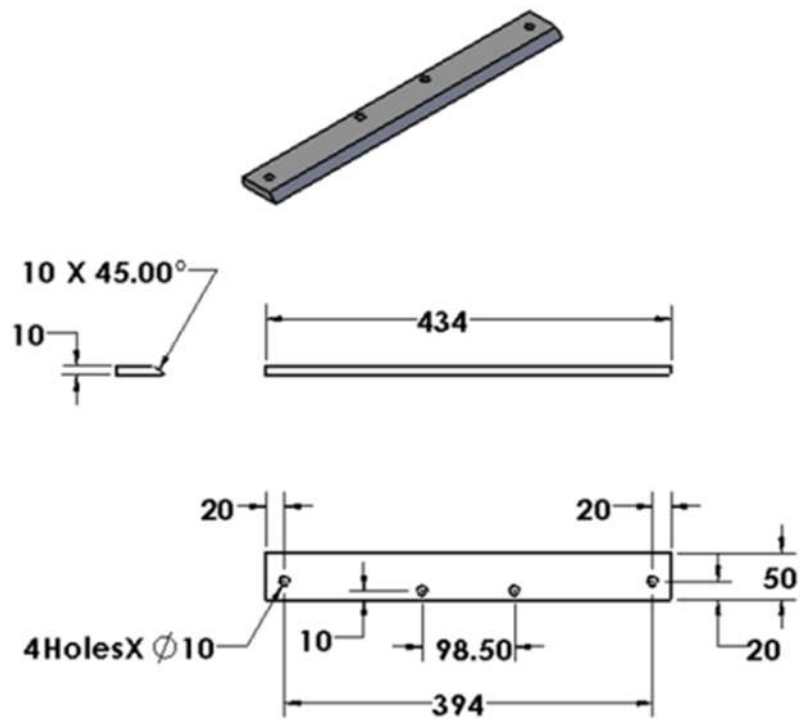


Figure A.11 Blank holder (upper part –long side)
(All dimensions mm)

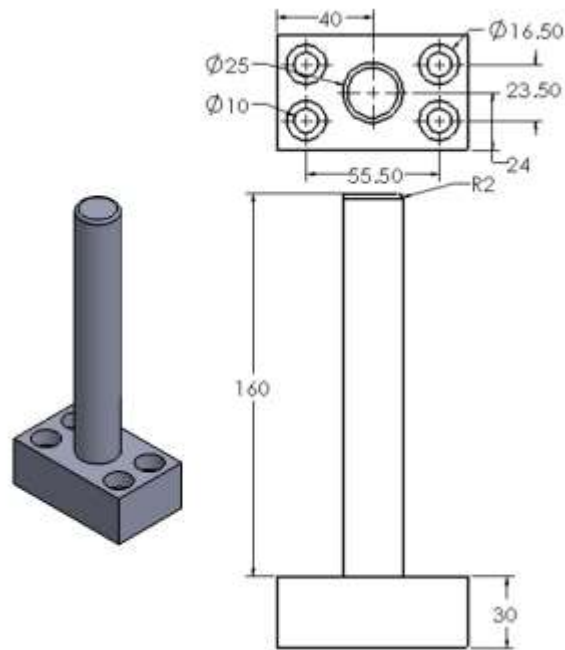


Figure A.12 Guide pin
(All dimensions mm)

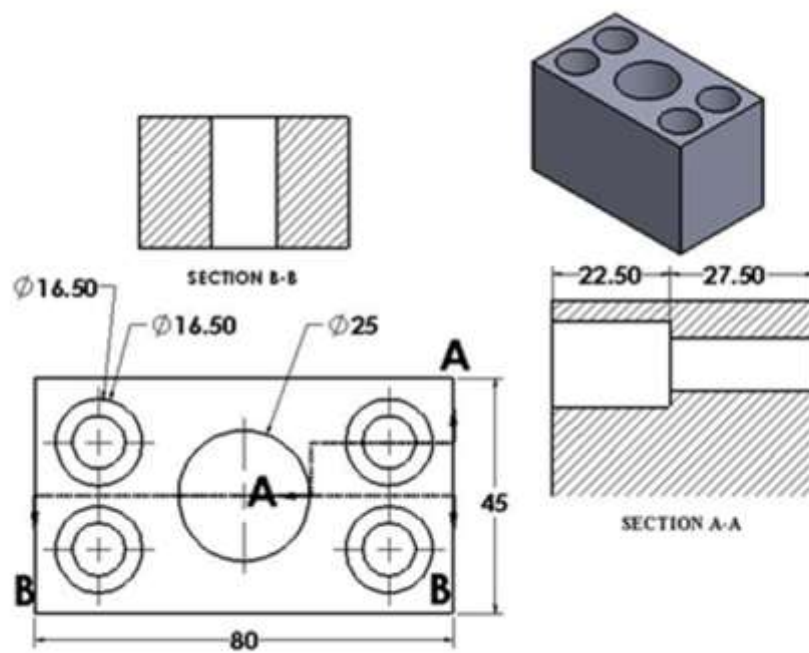


Figure A.13 Guide pin trapped
(All dimensions mm)

APPENDIX B

DETERMINATION OF THE MECHANICAL PROPERTIES OF SHEET MATERIALS

Appendix B explains the tests that have been attempted to determine the material behaviour under tensile load, plastic anisotropy, and uniaxial compression test for elastic cushion material.

B.1 Determination of the mechanical properties of sheet materials

B.1.1 Machine description

Figure B.1 shows the tensile test machine which is used for experimental work. The capacity of the test machine is 100kN, and the velocity of cross-head is 0.005 to 200 mm/min within ± 0.1 %. To control the machine functions and collect the data of tests, dedicated computer with specialist testing software is used [1].



Figure B.1 Tensile test machine in Metallurgy and Materials Department at the University of Birmingham

B.1.2 Specimen preparation

To determine the mechanical properties of the selected sheet materials which are used in this investigation, the samples were cut regarding the material orientation (0° , 45° , and 90°). The standardised specimen dimensions and orientations are shown in Figure B.2.

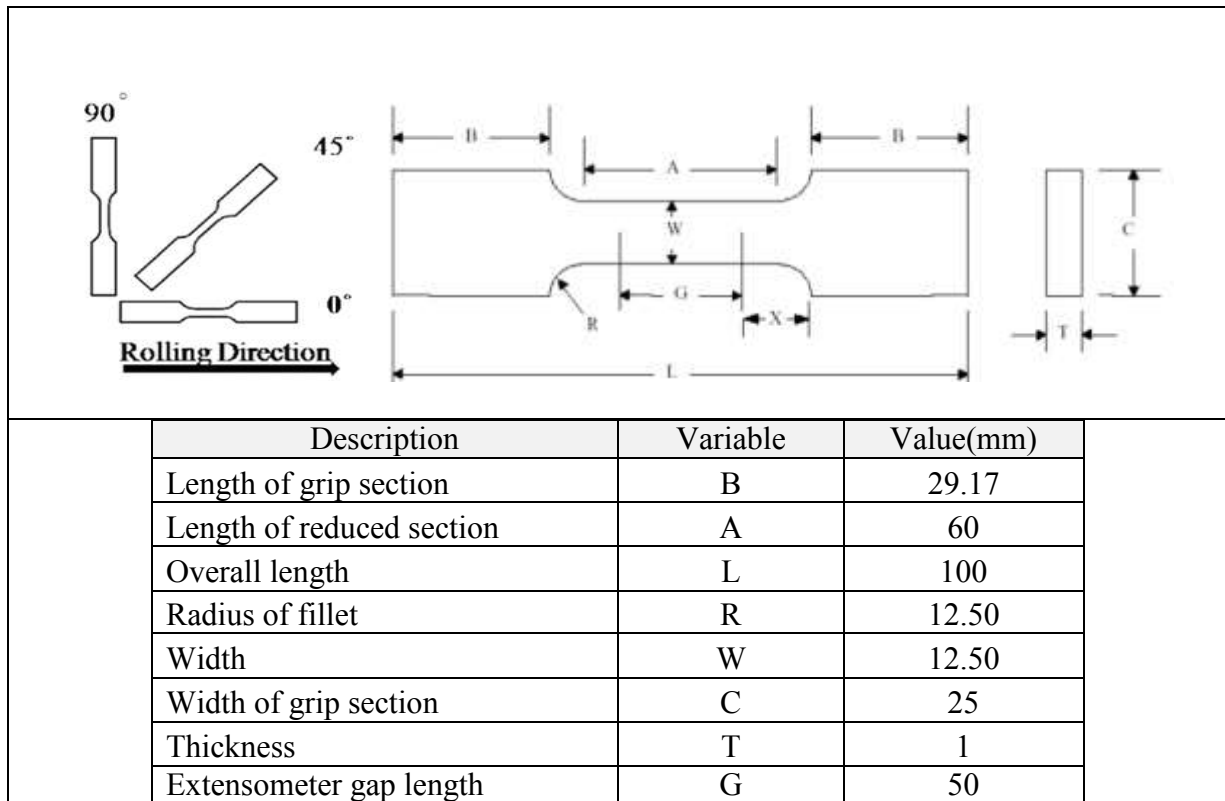


Figure B.2 Dimensions of the tensile test specimen

The wire cut (electric discharge machine EDM) is used to produce the testing samples. For each DC05 steel sheet and 5251-“O” aluminium sheet, 12 samples were cut, 6 samples at 0° , 4 samples at 45° , and 4 samples at 90° . All samples were cleaned from impurities after wire cut and then measured width and thickness using micrometre before testing. The measurement was taken on the two ends of gauge length and on the centre to calculate the average dimension. Figure B.3 shows the marks on the sample.



Figure B.3 Specimen geometry- all dimensions in mm

B.1.3 Uniaxial tensile test to failure

B.1.3.1 Methodology

Two samples in each direction 0^0 , 45^0 , and 90^0 were used to perform the uniaxial tensile test. The Zwick tensile test machine illustrated in section B.1.1 was used. This test is done to determine the yield stress (σ_Y), ultimate tensile stress (UTS), elongation at failure (ΔL), and it will save the main data of anisotropy test. The first step of the uniaxial tensile test was clamped the sample as shown in Figure B.4, and second step, the tensile load was applied with 0.5 mm/min as constant speed till the sample reached UTS and failed.

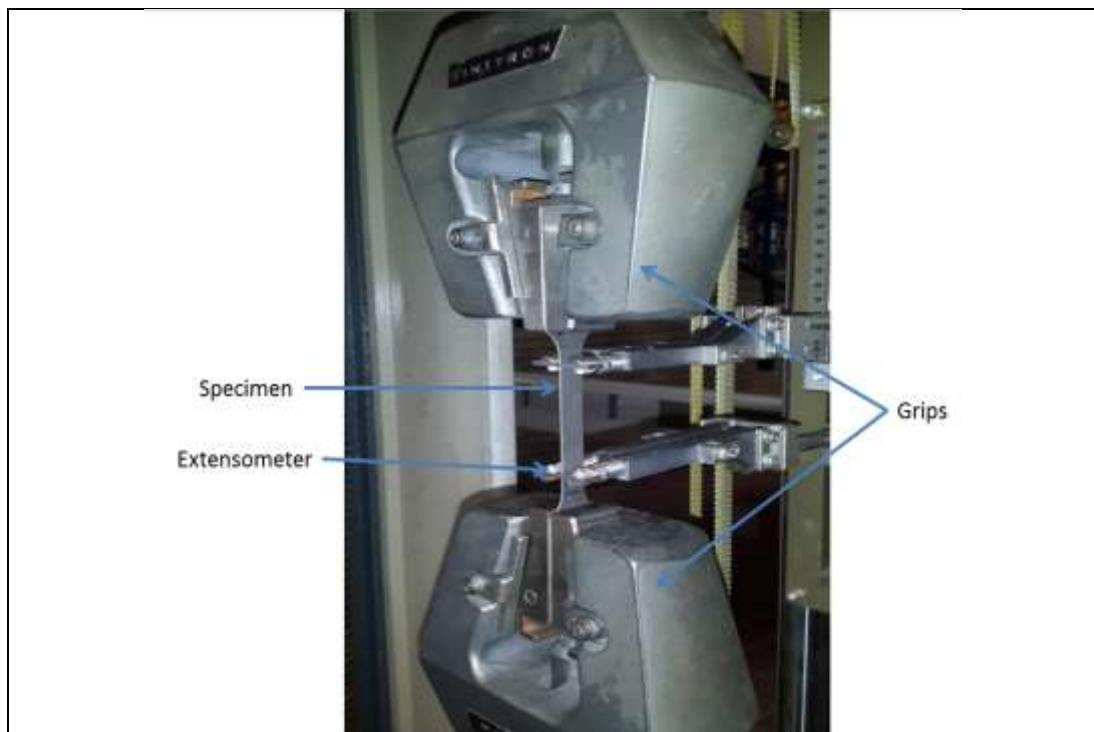


Figure B.4 Clamped specimens on the tensile machine

In order to determine the stress –strain curve for the samples, the test is done for six samples, two in orientation direction (0^0), two inclined directions (45^0) direction, and two in the normal direction (90^0). The results of previous tests were used in equations B.1 and B.2 to calculate engineering stress (σ_{eng}), and engineering strain (ϵ_{eng})

$$\sigma_{eng} = P/A_o \quad (B.1)$$

$$\epsilon_{eng} = \frac{\Delta L}{L_o} \quad (B.2)$$

Where P is the applied load, A_o is the initial sample cross section area, ΔL is a change of the length, and L_o is the gauge length of the sample. The values of engineering stress and engineering strain were used in equation B.3 and B.4 to calculate true stress (σ_T) and true strain (ϵ_T).

$$\sigma_T = \sigma_{eng}(1 + \epsilon_{eng}) \quad (B.3)$$

$$\epsilon_T = \ln(1 + \epsilon_{eng}) \quad (B.4)$$

As the ASTM E-8 [122] recommended, the yield stress was determined at 0.002 strain offset and modulus of elasticity as the curve slope after yield stress.

B.1.3.2 Results

Figure B.5 a, b, and c shows true stress-strain curves for the DC05 steel sheet in 0^0 , 45^0 , and 90^0 regarding material orientation, which is drawn using the data from equations B.3 and B.4. These curves show approximately identical in three directions. Figure B.5 d shows the true stress –strain curve for three directions. It can be seen that the true stress-strain curve at 45^0 slightly more than true stress-strain curves for 0^0 and 90^0 .

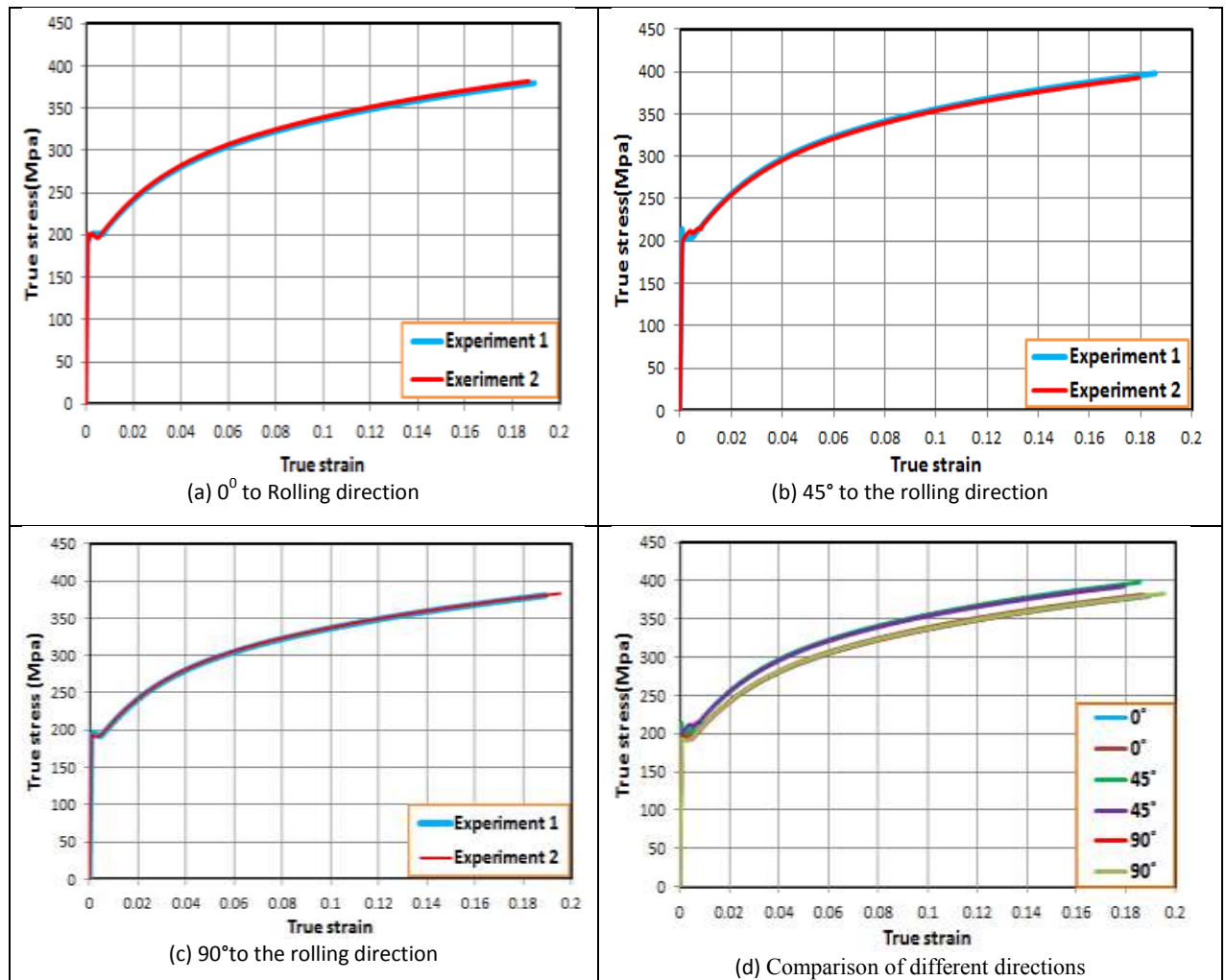


Figure B.5 True stress-strain curves for DC05 steel material

The comparison between mechanical properties in three directions of the DC05 material is shown in Figure B.6 and Figure B.7. It can be observed that the variation in the mechanical properties in three directions is not significant. From Figure B.6, the highest value of yield stress and ultimate tensile stress at 45° samples were 210 Mpa and 330 Mpa respectively. Also, the lowest value of yield stress and ultimate tensile stress at 90° samples were 195 Mpa and 315 Mpa respectively.

From Figure B.6 and Figure B.7, it can be observed that the minimum elongation was with maximum yield stress for 45° samples. In contrast, the maximum elongation was found with minimum yield stress for the 90° samples

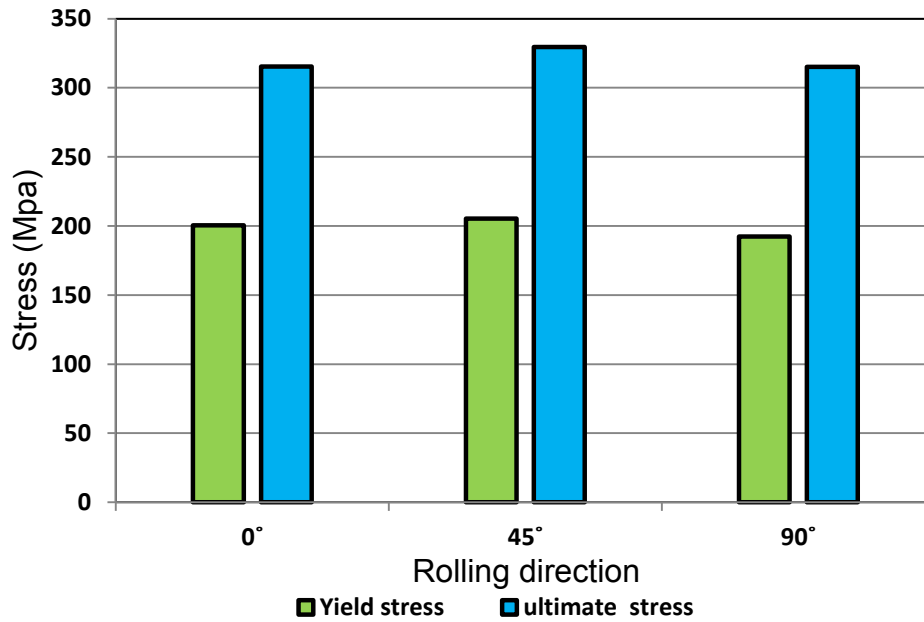


Figure B.6 Yield stress and ultimate tensile stress for the DC05 at 0°, 45°, and 90°

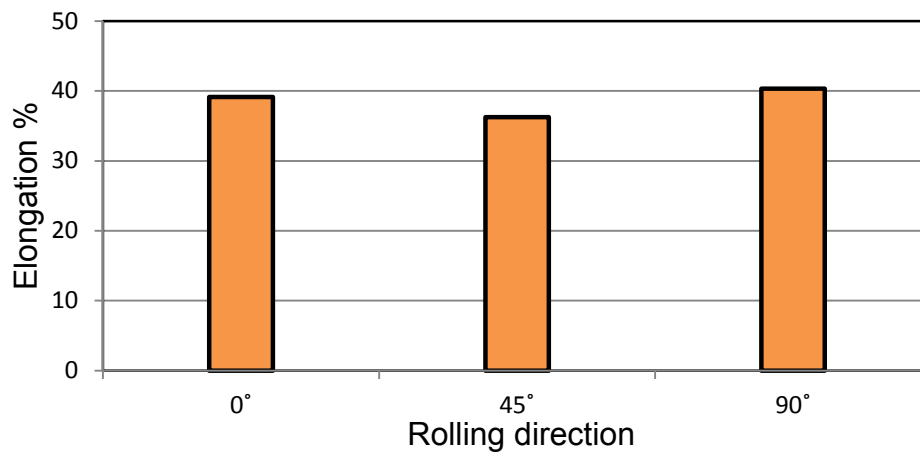


Figure B.7 Elongation of the DC05 at different orientations

Figure B.8 shows the stress –strain curves for the AL 5251-“O” material in 0°, 45°, and 90° directions regarding material orientation. It can observe that the stress-strain curves for two samples in the three directions are nearly similar. Likewise, Figure B.8 d shows the stress – strain curve for 45° samples is slightly different comparing with other two directions, and the difference between stress-strain curves for 0° and 90° is not significant.

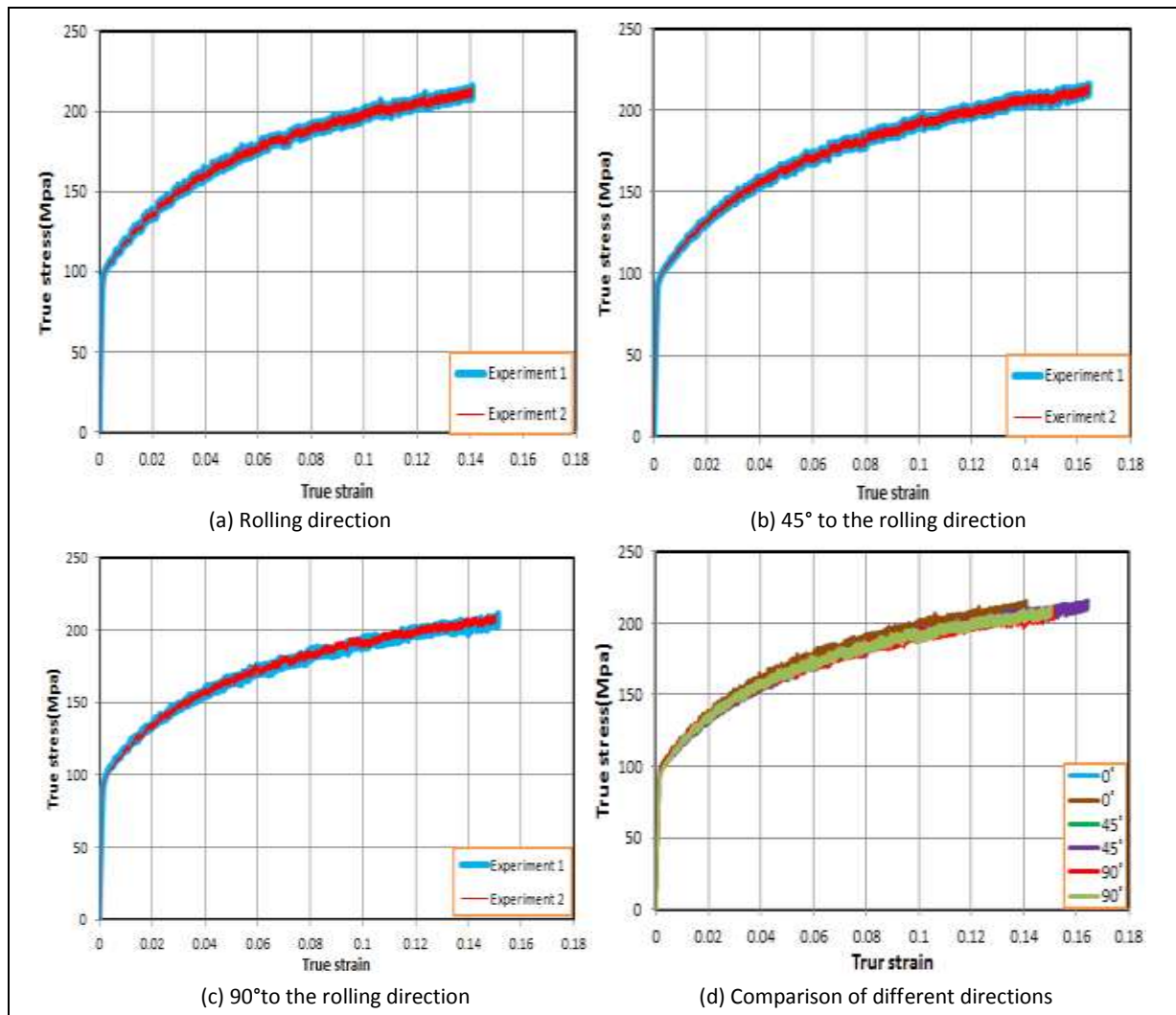


Figure B.8 True stress-strain curve for the AL 5251-"O" material

The comparison between mechanical properties in three directions of the AL 5251-"O" material is shown in Figure B.9 and Figure B.10. It can be observed that the variation in the mechanical properties in three directions is not significant. From Figure B.9, the highest value of yield stress and ultimate tensile stress at 0° samples were 105 Mpa and 190 Mpa respectively. Also, the lowest value of yield stress and ultimate tensile stress at 90° samples were 100 Mpa and 180 Mpa respectively. From Figure B.9 and Figure B.10, it can be observed that the minimum elongation was with maximum yield stress for 0° samples. In contrast, the maximum elongation was found with minimum yield stress for the 90° samples

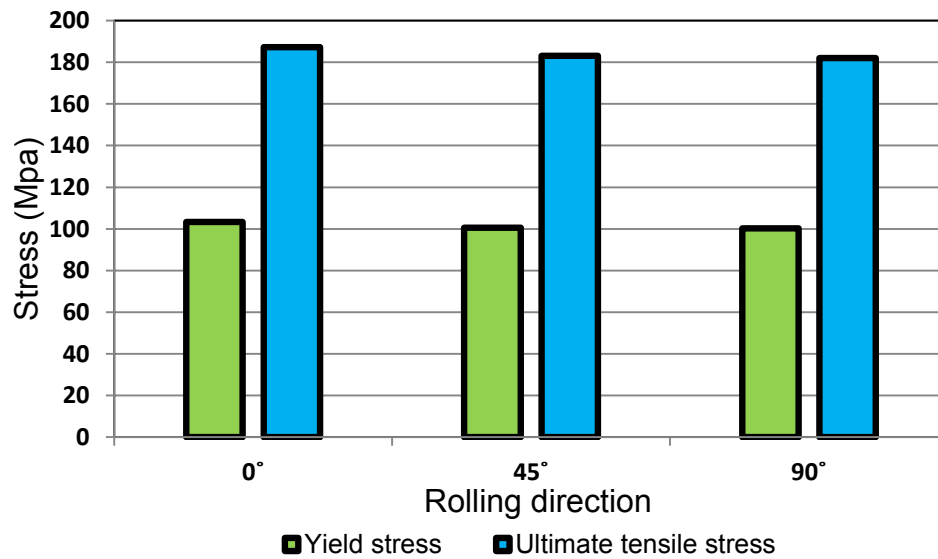


Figure B.9 Yield stress and ultimate tensile stress for the AL 5251-“O” at 0°, 45°, and 90°

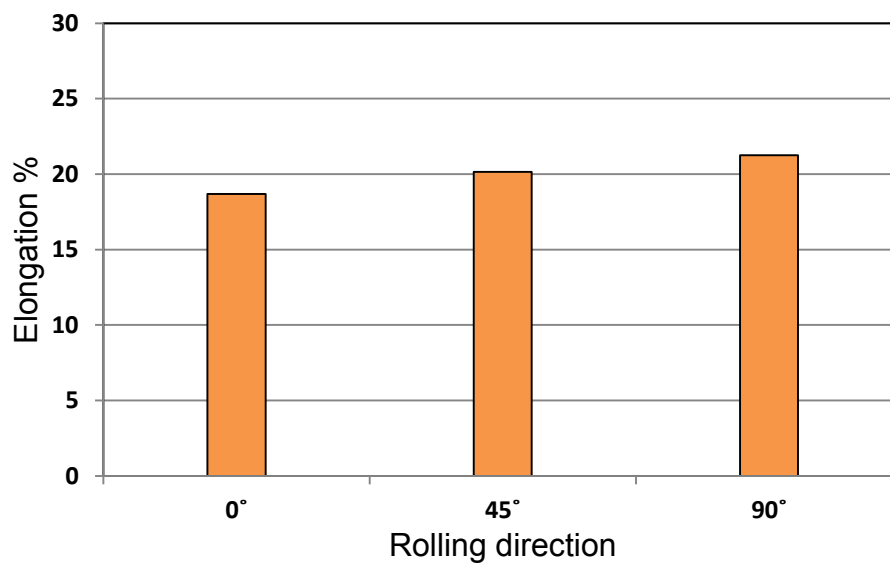


Figure B.10 Elongation of the AL 5251-“O” at different orientations

B.1.4 Uniaxial compression test to determine of polyurethane properties

Polyurethane is considered flexible material and has a high tensile strength which is reached till 650% [123, 124]. The main characteristics of polyurethane are representing in high

resistance to abrasion, tearing, oils effect and has wide work temperature range (-30°C to $+100^{\circ}\text{C}$), the polyurethane is available in a wide hardness range 10 shores “OO” to 90 shores [123]. From the previous characteristics, polyurethane can combine the rubber elasticity and toughness of metals, for that, it is suitable to protect the sheet during the forming process using multi-point forming tool. In this investigation, Polyurethane shore A75 and A90 were chosen as the material of the elastic cushion as it is commonly used in this process. To perform a uniaxial compression test, Zwick machine in Figure B.11 is used with a 100kN load cell. Regarding the standard ASTM D575 [125], the specimens dimensions were $28.6 \pm 0.1\text{mm}$ is a diameter, and $12.5 \pm 0.5\text{mm}$ is a height as Figure B.12 is shown. For each type of polyurethane, two specimens are tested to get the more accurate results. The force applied on each specimens using compression rate 12.5mm/min .



Figure B.11 Zwick machine

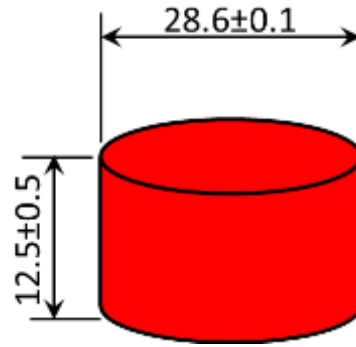
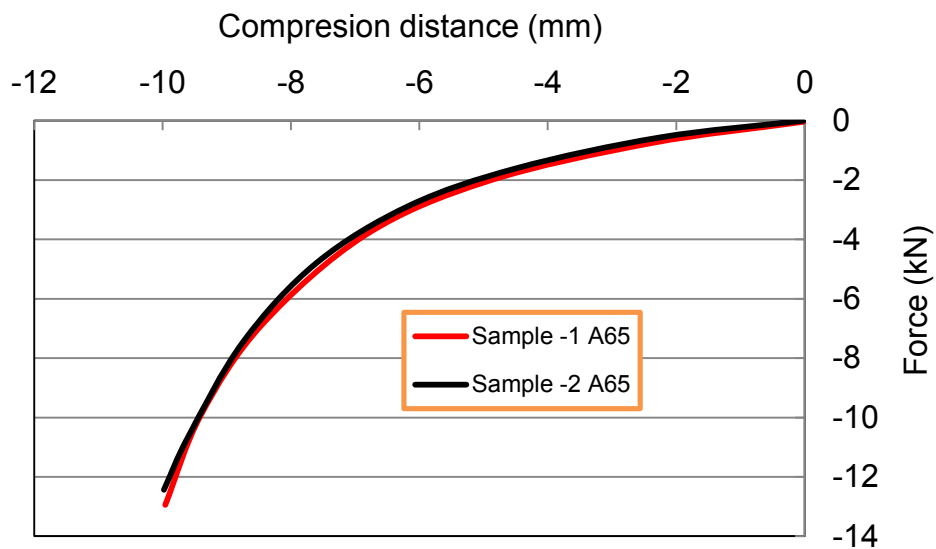
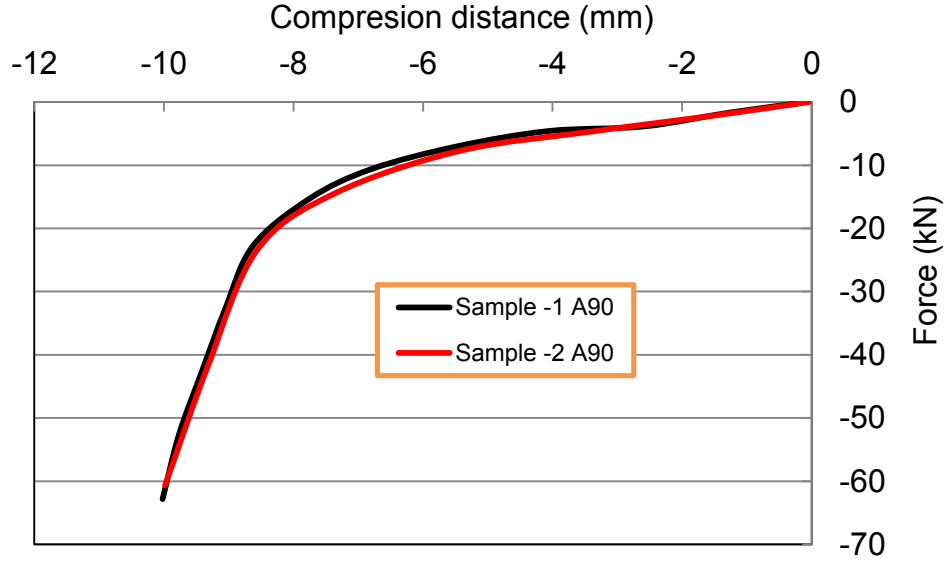


Figure B.12 Specimen dimensions (All dimensions mm)

Figure B-13 a, and b presents the experimental testing result of Polyurethane A65 and A90. It can be observed that as the polyurethane A90 is required more force from polyurethane A65 to achieve the compression ratio.



a- Uniaxial compression Force – distance of polyurethane A65



b-Uniaxial compression Force – distance of polyurethane A90

Figure B.13 Uniaxial compression test results

B.1.5 Anisotropy test

The metal properties become non-homogeneous; if the plastic deformation was different for the 0° , 45° , and 90° directions to the rolling direction [126]. For that, determination of plastic anisotropy to know the type of material behaviour becomes important. The anisotropy coefficient (r_a) is used to defined plastic anisotropy, which is represented in equation B.6.

$$r_a = \frac{\varepsilon_2}{\varepsilon_3} = \frac{\varepsilon_w}{\varepsilon_t} = \frac{-\varepsilon_w}{(\varepsilon_w + \varepsilon_t)} \quad (\text{B.6})$$

Where r_a is the anisotropy coefficient, $\varepsilon_2 = \varepsilon_w$ is the strain in width, and $\varepsilon_3 = \varepsilon_t$ is the strain in thickness direction. Figure B.14 shows the main parameters in equation B.6.

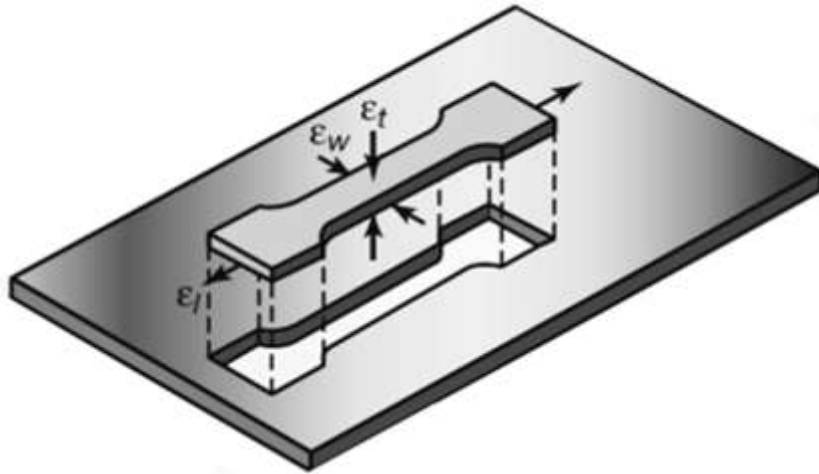


Figure B.14 The main dimensions of changing directions

Where thickness strain of sample (ϵ_t) is the summation of length strain (ϵ_l) and width strain (ϵ_w) as equation B.6 is shown. The anisotropy coefficient is as indicator to thinning defect, if r_a of the material greater than 1, then the material is strained in thickness direction less than in width direction, and the risk of thinning becomes low. This may help to know if the sheet material is suitable for process forming.

B.1.4.1 Methodology

The main steps of this test are same in the tensile test, except in the anisotropy test the sample is stretching up to 15% of gage length. The sample before and after stretching is shown in Figure B.15.



Figure B.15 Sample before and after stretching until 15% gage length.

After stretching the sample, it is removed from the tensile machine and the length and width were measured at three regions 1,2, and 3 into gage length as Figure B.3 is shown, and then calculate the average. Equation B.6 is used to calculate the plastic anisotropy in 0^0 , 45^0 , and 90^0 to the rolling direction. And then put the plastic anisotropic r_0 , r_{45} , r_{90} in Equation B.7, to determine the normal anisotropy coefficient (R_a).

$$R_a = \frac{r_0 + 2r_{45} + r_{90}}{4} \quad (B.7)$$

References

- [1] C. LI MZ, Z. SUI, and Q. YAN, "Multi-point forming technology for sheet metal parts," *Journal of Materials Processing Technology*, vol. 129, pp. 333-338, 2002.
- [2] D. Hardt, B. Olsen, B. Allison, and K. Pasch, "Sheet metal forming with discrete die surfaces," in *Ninth North American Manufacturing Research Conference Proceedings*, 1981, pp. 140-144.
- [3] J. M. Papazian, "Tools of change," *Mechanical Engineering*, vol. 124, p. 52, 2002.
- [4] Q. L. Liu, Cheng Fu, Wenzhi Tieu, Kiet Li, Mingzhe Gong, Xuepeng, "Optimization of cushion conditions in micro multi-point sheet forming," *Journal of Materials Processing Technology*, vol. 212, pp. 672-677, 2012.
- [5] B. A. Olsen, "Die forming of sheet metal using discrete surfaces," Massachusetts Institute of Technology, 1980.
- [6] G. F. Eigen, "Smoothing methods for discrete die forming," Massachusetts Institute of Technology, 1992.
- [7] S. Socrate and M. C. Boyce, "A finite element based die design algorithm for sheet-metal forming on reconfigurable tools," *Journal of engineering materials and technology*, vol. 123, pp. 489-495, 2001.
- [8] E. L. Anagnostou, "Optimized tooling design algorithm for sheet metal forming over reconfigurable compliant tooling," *State University of New York at Stony Brook*, 2002.
- [9] P. Mossedale, "The use of avothane for sheet metal forming, J," *Sheet Metal Industries*, vol. 4, pp. 257-267, 1965.
- [10] H. Al-Qureshi, "Analytical investigation of ram movement in piercing operation with rubber pads," *International Journal of Machine Tool Design and Research*, vol. 12, pp. 229-248, 1972.
- [11] D. F. Walczyk and D. E. Hardt, "Design and analysis of reconfigurable discrete dies for sheet metal forming," *Journal of Manufacturing Systems*, vol. 17, pp. 436-454, 1998.
- [12] C. R. Peterson, "Vise for irregularly shaped objects," ed: Google Patents, 1956.
- [13] P. L. Hoffman, "Reconfigure modular tooling," ed: Google Patents, 1998.
- [14] E. Haas, R. C. Schwarz, and J. M. Papazian, "Design and test of a reconfigurable forming die," *Journal of Manufacturing processes*, vol. 4, pp. 77-85, 2002.
- [15] V. Păunoiu, D. Nicoară, B. Mihaela, C. Maier, O. Ciocan, and A. Epureanu, "Design an experimental reconfigurable die for sheet metal forming," ed: Analele Universității Dunărea de Jos din Galați, Fasc. V, ISSN, 2006.
- [16] P. Beecherl, P. Szuba, J. Manjunathaiah, K. McGaffey, F. Crelley, and S. Melkote, "Flexible fixturing apparatus," ed: Google Patents, 2002.
- [17] J. Moore and N. Gindy, "Work piece holding arrangement," ed: Google Patents, 2006.
- [18] T. Schroeder and R. Stevenson, "Surface generating device suitable for generating a die, mold or fixture surface," ed: Google Patents, 1996.
- [19] S.-C. Heo, Y.-H. Seo, T.-W. Ku, and B.-S. Kang, "A study on thick plate forming using flexible forming process and its application to a simply curved plate," *The International Journal of Advanced Manufacturing Technology*, vol. 51, pp. 103-115, 2010.
- [20] S. Wang, Z. Cai, and M. Li, "Numerical investigation of the influence of punch element in multi-point stretch forming process," *The International Journal of Advanced Manufacturing Technology*, vol. 49, pp. 475-483, 2010.
- [21] B. Charles P. Trudell, N. Y., "Sheet metal forming apparatus," ed: Google Patents, 1942.
- [22] E. G. Haas, R. C. Schwarz, and J. M. Papazian, "Modularized reconfigurable heated forming tool," ed: Google Patents, 2000.
- [23] J. M. Papazian, E. G. Haas, R. C. Schwarz, J. A. Nardiello, and J. Melnichuk, "Pin tip assembly in tooling apparatus for forming honeycomb cores," ed: Google Patents, 2001.

- [24] Z. Wang, "Rapid manufacturing of vacuum forming components utilising reconfigurable screw pin tooling," University of Nottingham, 2010.
- [25] A. Al-Habaibeh, N. Gindy, and R. M. Parkin, "Experimental design and investigation of a pin-type reconfigurable clamping system for manufacturing aerospace components," *Proceedings of the Institution of Mechanical Engineers, Part B: Journal of Engineering Manufacture*, vol. 217, pp. 1771-1777, 2003.
- [26] W. Rivai, P. Suwarta, B. L. Sanjoto, H. Nur, and S. Hari, "Numerical Simulation of Multipoint Forming with Circular Die Pins in Hexagonal Packing," in *Applied Mechanics and Materials*, 2014, pp. 589-593.
- [27] T. Skinner, "Spring-forming device," ed: Google Patents, 1923.
- [28] W. H. WAKEFIELD, "Die and method of making same," ed: Google Patents, 1943.
- [29] N. NAKAJIMA, "A newly developed technique to fabricate complicated dies and electrodes with wires," *Bulletin of JSME*, vol. 12, pp. 1546-1554, 1969.
- [30] G. T. Pinson, "Apparatus for forming sheet metal," ed: Google Patents, 1980.
- [31] C. Liu, M. Li, and W. Fu, "Principles and apparatus of multi-point forming for sheet metal," *International Journal of Advanced Manufacturing Technology*, vol. 35, pp. 1227-1233, 2008.
- [32] E. G. Haas and M. Kesselman, "Adjustable form die," ed: Google Patents, 1996.
- [33] R. C. Boas, "Sequential setup mechanism design for a reconfigurable sheet metal forming die," Massachusetts Institute of Technology, 1997.
- [34] D. F. Walczyk and Y.-T. Im, "A hydraulically-actuated reconfigurable tool for flexible fabrication: implementation and control," *Journal of manufacturing science and engineering*, vol. 122, pp. 562-568, 2000.
- [35] Y.-T. Im, D. F. Walczyk, R. C. Schwarz, and J. M. Papazian, "A comparison of pin actuation schemes for large-scale discrete dies," *Journal of Manufacturing Processes*, vol. 2, pp. 247-257, 2000.
- [36] E. L. Anagnostou and J. M. Papazian, "Optimized tooling design algorithm for sheet metal forming over reconfigurable compliant tooling," in *AIP Conference Proceedings*, 2004, pp. 741-748.
- [37] D. F. Walczyk, *Rapid fabrication methods for sheet metal forming dies*: Massachusetts Institute of Technology, 1996.
- [38] O. O. Owodunni, J. Diaz-Rozo, and S. Hinduja, "Development and evaluation of a low-cost computer controlled reconfigurable rapid tool," *Computer-Aided Design and Applications*, vol. 1, pp. 101-108, 2004.
- [39] D. F. Walczyk, J. F. Hosford, and J. M. Papazian, "Using reconfigurable tooling and surface heating for incremental forming of composite aircraft parts," *Journal of manufacturing science and engineering*, vol. 125, pp. 333-343, 2003.
- [40] J.-J. Chen, M.-Z. Li, W. Liu, and C.-T. Wang, "Sectional multipoint forming technology for large-size sheet metal," *The International Journal of Advanced Manufacturing Technology*, vol. 25, pp. 935-939, 2005.
- [41] M. F. Alfaidi, L. Xiaoxing, and M. A. Nwir, "Effect of rubber pad on forming quality in multi point forming process," in *Computer and Automation Engineering (ICCAE), 2010 The 2nd International Conference on*, 2010, pp. 728-731.
- [42] L. Li, Y.-H. Seo, S.-C. Heo, B.-S. Kang, and J. Kim, "Numerical simulations on reducing the unloading springback with multi-step multi-point forming technology," *International Journal of Advanced Manufacturing Technology*, vol. 48, pp. 45-61, 2010.
- [43] G.-Z. Quan, T.-W. Ku, and B.-S. Kang, "Improvement of formability for multi-point bending process of AZ31B sheet material using elastic cushion," *International Journal of Precision Engineering and Manufacturing*, vol. 12, pp. 1023-1030, 2011.
- [44] D. E. Sherrill and K. G. Young, "Method for constructing a composite structure," ed: Google Patents, 2004.
- [45] "Surface Generation Ltd <http://www.surface-generation.com>," 2006.

- [46] C.-g. LIU, Z.-y. CAI, and M.-z. LI, "Dimple formation and its elimination in multi-point forming for sheet metal [J]," *Journal of Jilin University of Technology (Natural Science Edition)*, vol. 1, p. 019, 2004.
- [47] Z.-Y. Cai, S.-H. Wang, and M.-Z. Li, "Numerical investigation of multi-point forming process for sheet metal: Wrinkling, dimpling and springback," *International Journal of Advanced Manufacturing Technology*, vol. 37, pp. 927-936, 2008.
- [48] M. Li, Z. Cai, Z. Sui, and X. Li, "Principle and applications of multi-point matched-die forming for sheet metal," *Proceedings of the Institution of Mechanical Engineers, Part B: Journal of Engineering Manufacture*, vol. 222, pp. 581-589, 2008.
- [49] T. Yu, W. Johnson, and W. Stronge, "Stamping and springback of circular plates deformed in hemispherical dies," *International journal of mechanical sciences*, vol. 26, pp. 131-148, 1984.
- [50] T. Yu, W. Johnson, and W. Stronge, "Stamping rectangular plates into doubly-curved dies," *Proceedings of the Institution of Mechanical Engineers, Part C: Journal of Mechanical Engineering Science*, vol. 198, pp. 109-125, 1984.
- [51] J. Hutchinson and K. Neale, "Wrinkling of curved thin sheet metal," *Plastic Instability*, pp. 71-78, 1985.
- [52] J. Cao and M. Boyce, "Wrinkling behavior of rectangular plates under lateral constraint," *International Journal of Solids and Structures*, vol. 34, pp. 153-176, 1997.
- [53] J. Cao and X. Wang, "An analytical model for plate wrinkling under tri-axial loading and its application," *International Journal of Mechanical Sciences*, vol. 42, pp. 617-633, 2000.
- [54] M. Kawka, L. Olejnik, A. Rosochowski, H. Sunaga, and A. Makinouchi, "Simulation of wrinkling in sheet metal forming," *Journal of Materials Processing Technology*, vol. 109, pp. 283-289, 2001.
- [55] J. B. Kim, J. W. Yoon, and D. Y. Yang, "Investigation into the wrinkling behaviour of thin sheets in the cylindrical cup deep drawing process using bifurcation theory," *International Journal for Numerical Methods in Engineering*, vol. 56, pp. 1673-1705, 2003.
- [56] M. Yasar, Z. Korkmaz, and M. Gavas, "Forming sheet metals by means of multi-point deep drawing method," *Materials & design*, vol. 28, pp. 2647-2653, 2007.
- [57] N. Liu, H. Yang, H. Li, and S. Yan, "Plastic wrinkling prediction in thin-walled part forming process: A review," *Chinese Journal of Aeronautics*, vol. 29, pp. 1-14, 2016.
- [58] S. P. Timoshenko and J. M. Gere, *Theory of elastic stability*: Courier Corporation, 2009.
- [59] X. Wang, J. Xiao, and Y. Zhang, "A method for solving the buckling problem of a thin-walled shell," *International Journal of pressure vessels and piping*, vol. 81, pp. 907-912, 2004.
- [60] R. Peek, "Wrinkling of tubes in bending from finite strain three-dimensional continuum theory," *International journal of solids and structures*, vol. 39, pp. 709-723, 2002.
- [61] X. Wang and J. Cao, "On the prediction of side-wall wrinkling in sheet metal forming processes," *International Journal of Mechanical Sciences*, vol. 42, pp. 2369-2394, 2000.
- [62] M. Morovvati, B. Mollaei-Dariani, and M. Asadian-Ardakani, "A theoretical, numerical, and experimental investigation of plastic wrinkling of circular two-layer sheet metal in the deep drawing," *Journal of Materials Processing Technology*, vol. 210, pp. 1738-1747, 2010.
- [63] M. A. Shafaat, M. Abbasi, and M. Ketabchi, "Investigation into wall wrinkling in deep drawing process of conical cups," *Journal of Materials Processing Technology*, vol. 211, pp. 1783-1795, 2011.
- [64] E. Kowsarinia, Y. Alizadeh, and H. S. S. Pour, "Theoretical and experimental study on the effects of explosive forming parameters on plastic wrinkling of annular plates," *The International Journal of Advanced Manufacturing Technology*, vol. 67, pp. 877-885, 2013.
- [65] S. Timoshenko and J. Gere, "Theory of elastic stability. New York: McGraw-Hill, 1961," 1961.
- [66] R. Peek and A. Hilberink, "Axisymmetric wrinkling of snug-fit lined pipe," *International Journal of Solids and Structures*, vol. 50, pp. 1067-1077, 2013.

- [67] S. Kyriakides and E. Corona, *Mechanics of offshore pipelines: volume 1 buckling and collapse* vol. 1: Elsevier, 2007.
- [68] J. Hutchinson and M. He, "Buckling of cylindrical sandwich shells with metal foam cores," *International Journal of Solids and Structures*, vol. 37, pp. 6777-6794, 2000.
- [69] W. Wong and S. Pellegrino, "Wrinkled membranes I: experiments," *Journal of Mechanics of Materials and Structures*, vol. 1, pp. 3-25, 2006.
- [70] W. Wong and S. Pellegrino, "Wrinkled membranes III: numerical simulations," *Journal of Mechanics of Materials and Structures*, vol. 1, pp. 63-95, 2006.
- [71] E. Riks, "An incremental approach to the solution of snapping and buckling problems," *International Journal of Solids and Structures*, vol. 15, pp. 529-551, 1979.
- [72] M. Zhan, H. Yang, Z. Jiang, Z. Zhao, and Y. Lin, "A study on a 3D FE simulation method of the NC bending process of thin-walled tube," *Journal of Materials Processing Technology*, vol. 129, pp. 273-276, 2002.
- [73] J.-B. Kim, D.-Y. Yang, J.-W. Yoon, and F. Barlat, "The effect of plastic anisotropy on compressive instability in sheet metal forming," *International Journal of Plasticity*, vol. 16, pp. 649-676, 2000.
- [74] I. ABAQUS, "ABAQUS User Manuals, Version 6.7," vol. Version 6.7, 2007.
- [75] J. D. M. Correia and G. Ferron, "Wrinkling of anisotropic metal sheets under deep-drawing: analytical and numerical study," *Journal of Materials Processing Technology*, vol. 155, pp. 1604-1610, 2004.
- [76] M. Watson and H. Long, "Wrinkling failure mechanics in metal spinning," *Procedia Engineering*, vol. 81, pp. 2391-2396, 2014.
- [77] A. Documentation, "Getting started with Abaqus: Interactive Edition," <http://abaqusdoc.ucalgary.ca/v6.9/books/gsa/default.htm>, 2013.
- [78] I. Suchy, *Handbook of die design*: McGraw-Hill New York, 1998.
- [79] <https://www.cromwell.co.uk/shop/fasteners/die-springs/die-springs-extra-heavy-load-springs-colour-coded-yellow/f/11638>.
- [80] S. N. S. Mackey Bowley International Limited. Manual 4Columan Downstrokw.
- [81] <http://www.omega.com/das/pdf/OM-CP-QUADVOLT.pdf>.
- [82] <http://www.loadcellshop.co.uk/load-cell-amplifiers-and-load-cell-usb>.
- [83] <http://www.loadcellshop.co.uk/load-cells/low-profile-load-cell/low-profile-load-cell-100kn-200kn-300kn-detail?showall=1>.
- [84] http://www.automation24.co.uk/position-sensors/ultrasonic-sensor-microsonic-mic25/iu/tc-i7-193-0.htm?refID=adwords_product-number_UK&gclid=Cln81dzZtdICFW0A0wodtZsKEQ.
- [85] <http://www.faro.com/en-us/products/metrology/measuring-arm-faro-scanarm/applications#main>.
- [86] M. Abbadi, P. Hähner, and A. Zeghloul, "On the characteristics of Portevin–Le Chatelier bands in aluminum alloy 5182 under stress-controlled and strain-controlled tensile testing," *Materials Science and Engineering: A*, vol. 337, pp. 194-201, 2002.
- [87] F. Klose, A. Ziegenbein, F. Hagemann, H. Neuhäuser, P. Hähner, M. Abbadi, *et al.*, "Analysis of portevin-le chatelier serrations of type bin Al–Mg," *Materials Science and Engineering: A*, vol. 369, pp. 76-81, 2004.
- [88] M. Mazière and H. Dierke, "Investigations on the Portevin Le Chatelier critical strain in an aluminum alloy," *Computational Materials Science*, vol. 52, pp. 68-72, 2012.
- [89] A. Benallal, T. Berstad, T. Børvik, O. S. Hopperstad, I. Koutiri, and R. N. de Codes, "An experimental and numerical investigation of the behaviour of AA5083 aluminium alloy in presence of the Portevin–Le Chatelier effect," *International Journal of Plasticity*, vol. 24, pp. 1916-1945, 2008.
- [90] D. Banabic, *Formability of metallic materials: plastic anisotropy, formability testing, forming limits*: Springer Science & Business Media, 2000.

- [91] X. W. Dong, S. P.; Nakamachi, E.: Dynamic explicit finite element analysis. In: 1996 Nakamachi Lab. Report, Osaka Institute of Technology, Osaka 1996.
- [92] K. Schewizerhof and J. Hallquist, "Explicit Integration Scheme and Contact Formulation for Thin Sheet Metal Forming In: FE-Simulation of 3D sheet metal forming processes in automotive industry," *VDI-Ber*, vol. 894, pp. 405-439, 1991.
- [93] Q. Zhang, Z. Wang, and T. Dean, "Multi-point sandwich forming of a spherical sector with tool-shape compensation," *Journal of Materials Processing Technology*, vol. 194, pp. 74-80, 2007.
- [94] <https://www.pes-performance.com/analysis-and-simulation/finite-element-analysis>.
- [95] A. J. ABAQUS Theory Manual (v6.5.1), "Access Jun 2017."
- [96] Q. Zhang, Z. R. Wang, and T. A. Dean, "The mechanics of multi-point sandwich forming," *International Journal of Machine Tools & Manufacture*, vol. 48, pp. 1495-503, 10/2008.
- [97] <http://www.intrinsys.com/blog/2016/using-general-contact-in-abacus-cae>.
- [98] ["http://www.colorado.edu/engineering/CAS/courses.d/IFEM.d/IFEM.Ch07.d/IFEM.Ch07.pdf."](http://www.colorado.edu/engineering/CAS/courses.d/IFEM.d/IFEM.Ch07.d/IFEM.Ch07.pdf)
- [99] B. Qian, Y. He, and Z. Mei, "Finite element modeling of power spinning of thin-walled shell with hoop inner rib," *Transactions of Nonferrous Metals Society of China*, vol. 18, pp. 6-13, 2008.
- [100] L. Huang, Y. He, Z. Mei, and L.-j. Hu, "Numerical simulation of influence of material parameters on splitting spinning of aluminum alloy," *Transactions of Nonferrous Metals Society of China*, vol. 18, pp. 674-681, 2008.
- [101] Y. Lim, R. Venugopal, and A. G. Ulsoy, *Process control for sheet-metal stamping*: Springer, 2014.
- [102] Y.-H. S. Seong-Chan Heo, Jung-Won Park, Tae-Wan Ku, Jeong Kim and Beom-Soo Kang, "<2-Application of flexible forming process to hull structure forming.pdf>," 2009.
- [103] K. Sundararajan, ", <https://www.isixsigma.com>," accessed DATE: May 2017.
- [104] G. Hussain, L. Gao, and N. Hayat, "Empirical modelling of the influence of operating parameters on the spifability of a titanium sheet using response surface methodology," *Proceedings of the Institution of Mechanical Engineers, Part B: Journal of Engineering Manufacture*, vol. 223, pp. 73-81, 2009.
- [105] M. Ham and J. Jeswiet, "Forming limit curves in single point incremental forming," *CIRP Annals-Manufacturing Technology*, vol. 56, pp. 277-280, 2007.
- [106] L. Filice, G. Ambrogio, and F. Micari, "On-line control of single point incremental forming operations through punch force monitoring," *CIRP annals-Manufacturing technology*, vol. 55, pp. 245-248, 2006.
- [107] G. Ambrogio, V. Cozza, L. Filice, and F. Micari, "An analytical model for improving precision in single point incremental forming," *Journal of Materials Processing Technology*, vol. 191, pp. 92-95, 2007.
- [108] R. L. Mason, R. F. Gunst, and J. L. Hess, *Statistical design and analysis of experiments: with applications to engineering and science* vol. 474: John Wiley & Sons, 2003.
- [109] J.-S. Kwak, "Application of Taguchi and response surface methodologies for geometric error in surface grinding process," *International journal of machine tools and manufacture*, vol. 45, pp. 327-334, 2005.
- [110] K. Palanikumar, "Application of Taguchi and response surface methodologies for surface roughness in machining glass fiber reinforced plastics by PCD tooling," *The International Journal of Advanced Manufacturing Technology*, vol. 36, pp. 19-27, 2008.
- [111] M. Abosaf, K. Essa, A. Alghawail, A. Tolipov, S. Su, and D. Pham, "Optimisation of multi-point forming process parameters," *The International Journal of Advanced Manufacturing Technology*, pp. 1-11, 2017.

- [112] M. Abebe, K. Lee, and B.-S. Kang, "Surrogate-based multi-point forming process optimization for dimpling and wrinkling reduction," *The International Journal of Advanced Manufacturing Technology*, pp. 1-13, 2015.
- [113] W. F. Hosford and R. M. Caddell, *Metal forming: mechanics and metallurgy*: Cambridge University Press, 2011.
- [114] Z.-Y. W. Cai, Shao-Hui Xu, Xu-Dong Li, Ming-Zhe, "Numerical simulation for the multi-point stretch forming process of sheet metal," *Journal of Materials Processing Technology*, vol. 209, pp. 396-407, 2009.
- [115] Y.-H. Seo, B.-S. Kang, and J. Kim, "Study on relationship between design parameters and formability in flexible stretch forming process," *International Journal of Precision Engineering and Manufacturing*, vol. 13, pp. 1797-1804, 2012.
- [116] H. M. Hassanin, Francesco El-Sayed, Mahmoud Ahmed Liu, Jian Essa, Khamis, "Manufacturing of Ti-6Al-4V micro-implantable parts using hybrid selective laser melting and micro-electrical discharge machining," *Advanced Engineering Materials*, vol. 18, pp. 1544-1549, 2016.
- [117] L. N. Carter, K. Essa, and M. M. Attallah, "Optimisation of selective laser melting for a high temperature Ni-superalloy," *Rapid Prototyping Journal*, vol. 21, pp. 423-432, 2015.
- [118] D. A. Lind, Marchal, W.G., and Wathen, S.A, *Statistical techniques in business and economics* 12 ed.: Year:McGraw Hill Irwin Edition/2005, 2005.
- [119] Y. Liu, M. Li, and F. Ju, "Research on the process of flexible blank holder in multi-point forming for spherical surface parts," *The International Journal of Advanced Manufacturing Technology*, pp. 1-8, 2016.
- [120] S. Lemes and N. Zaimovic-Uzunovic, "Using buckling analysis to predict wrinkling in incremental sheet metal forming," *STROJNISKI VESTNIK*, vol. 54, p. 115, 2008.
- [121] B. Zareh-Desari, B. Davoodi, and A. Vedaiei-Sabegh, "Investigation of deep drawing concept of multi-point forming process in terms of prevalent defects," *International Journal of Material Forming*, pp. 1-11, 2015.
- [122] W. Soboyejo, *Mechanical properties of engineered materials* vol. 152: CRC press, 2002.
- [123] Custom Molded Urethane C.U. E. Inc., "<http://www.cue-inc.com/urethane-benefits.html>".
- [124] Eriks, "<http://rubbertechology.info/en/products/overview-rubberqualities/different-compounds/polyurethane-rubber-au-eu/>".
- [125] D. S. t. m. f. r. p. i. c. American Society for Testing and Materials (Astm), *Annual Book of ASTM Standards* vol. 91, 2007.
- [126] D. Koistinen, *Mechanics of Sheet Metal Forming: Material Behavior and Deformation Analysis*: Springer Science & Business Media, 2012.